UNIVERSITÀ DEGLI STUDI DI PALERMO

PhD Course in Chemical, Environmental, Biomedical, Hydraulic and Materials Engineering
Dipartimento di Ingegneria
Settore Scientifico Disciplinare ICHI-01/A (ex ING-IND/23)

Combined biomass valorization and hydrogen production in (photo)electrochemical cells

PhD Candidate:
CLAUDIO MARIA PECORARO

Phd Course Coordinator:
PROF. GIORGIO D. M. MICALE

Supervisors:
PROF. MONICA SANTAMARIA

Co-Supervisors:
PROF. MARIANNA BELLARDITA

XXXVII CYCLE
GRADUATION YEAR 2024

Index

1. Introduction

1.1. Green hydrogen

The world is experiencing a significant transformation in how energy is produced, transformed, stored, and utilized. There is a growing awareness of the need to shift towards a society where energy no longer contributes to climate change, i.e., CO_2 emissions, and local pollution [1,2], moving away from fossil fuels to renewable low carbon energy sources [3]. As renewable energy deployment increases globally [4–7], especially in the power sector, there is a need to introduce solutions that use renewable electricity to decarbonize end-use sectors through power-to-gas strategies or use electricity to produce high-value chemicals or fuels. Additionally, since electricity consumption needs to rise from about 20% of final energy consumption to approximately 50% by 2050, it's crucial to decarbonize applications where direct electrification is more challenging, known as "hard-to-abate" sectors upstream. For instance, bioenergy is suitable as biofuels for transport sectors with limited fuel alternatives, such as aviation but also as a carbon source for synthetic fuels.

Direct electrification is more efficient from a systems perspective and is already commercially deployed in many areas, like heating and passenger vehicles. Carbon capture and storage (CCS) might be attractive for existing assets early in their lifespan and process emissions (e.g., from cement production). However, even with the most ambitious scenarios, these technological solutions might not be sufficient, and behavioral changes may be needed to further reduce energy demand. Thus, hydrogen is one solution among many and should be pursued alongside others since it can be used in the so-called hard-to-abate sectors, for the transport industry, for heating and power generation, and as a chemical (Figure 1.1) [8–10] and, in general, in the decarbonization of chemical processes [1,3,11–13]. Notably, hydrogen is a clean energy carrier [14–17], whose combustion with oxygen only produces water [12,13,18].

Hydrogen is primarily utilized in crude oil refining and the synthesis of ammonia and methanol, which account for nearly 75% of the total demand for pure and mixed hydrogen. Currently, most hydrogen production relies on natural gas and coal, contributing to 95% of the output whilst about 5% of global hydrogen is obtained as a by-product of the electrolytic chlorine production. At present, there is no substantial hydrogen production from renewable sources; green hydrogen remains largely confined to demonstration projects [19–21]. Commonly color code is used in nomenclature to simplify discussions (see Figure 1.2), impacting life-cycle greenhouse gas (GHG) emissions, despite

in some cases not neatly fitting into a single color category (e.g., mixed hydrogen sources or electrolysis using grid electricity) [22,23].

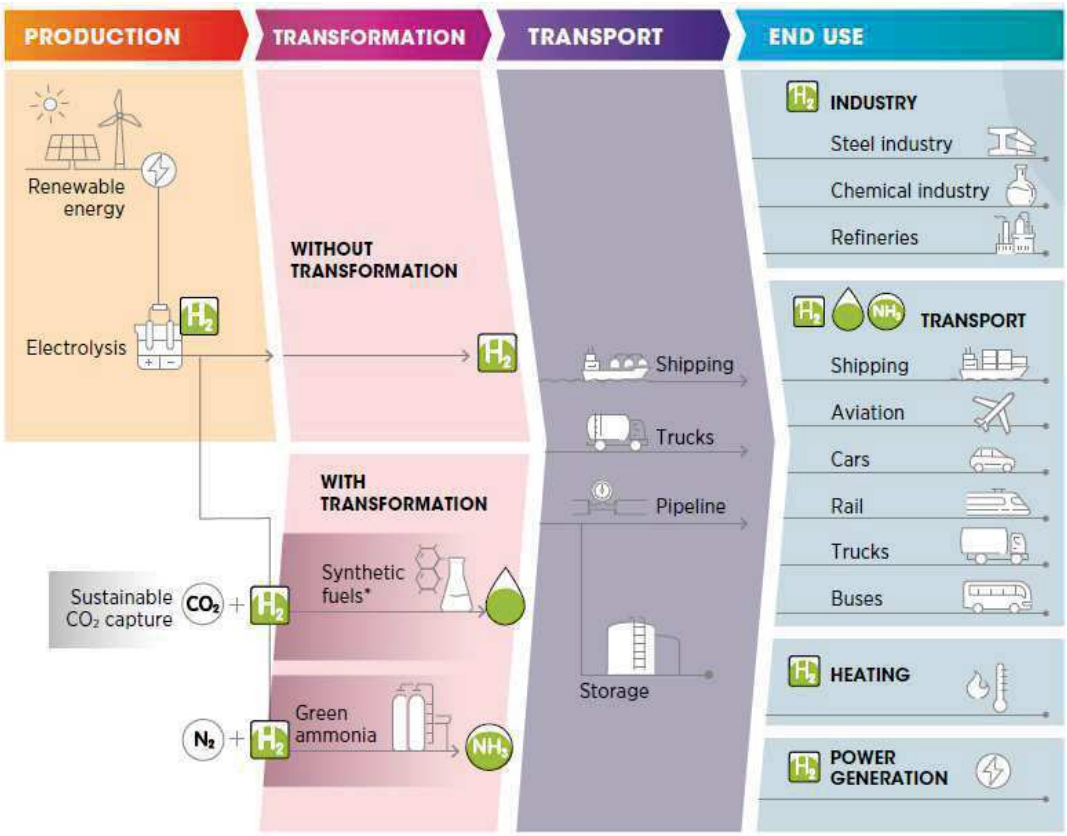

Source: IRENA (2020f).

Note: N_2 = nitrogen; NH_3 = ammonia

** The term synthetic fuels refers here to a range of hydrogen-based fuels produced through chemical processes with a carbon source (carbon monoxide (CO) and CO_2 captured from emission streams, biogenic sources or directly from the air). They include methanol, jet fuels, methane and other hydrocarbons. The main advantage of these fuels is that they can be used to replace their fossil fuel-based counterparts and in many cases be used as direct replacements – that is, as drop-in fuels. Synthetic fuels produce carbon emissions when combusted, but if their production process consumes the same amount of CO_2, in principle it allows them to have net-zero carbon emissions.*

Figure 1.1. Green hydrogen production, conversion and end uses across the energy system

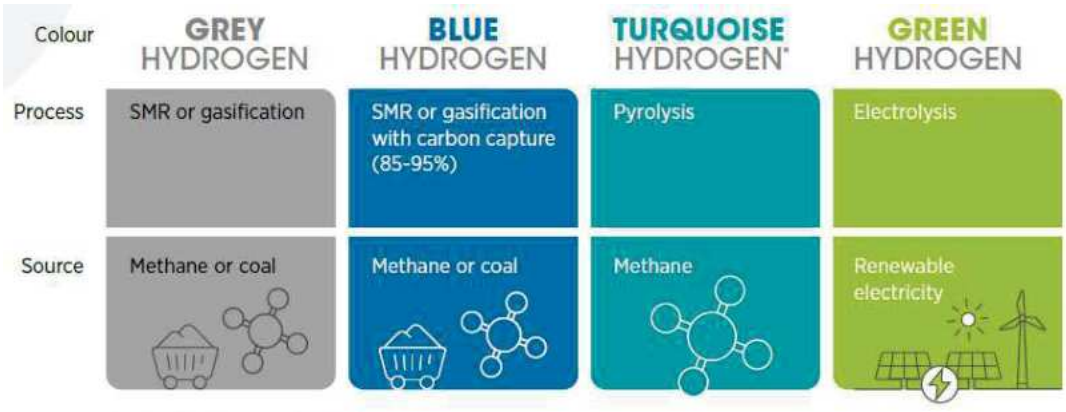

Note: SMR = steam methane reforming.

** Turquoise hydrogen is an emerging decarbonisation option.*

Figure 1.2. Main shades to indicate the origin of hydrogen

Green hydrogen, produced through the redox splitting of water from renewable electricity emerged as a promising alternative [24–27]. It links renewable electricity with various end-use applications, complementing electrification, bioenergy, and direct renewable energy. The potential for green hydrogen surpasses that of fossil fuels due to its connection to solar and wind energy, which far exceeds the current and the future global energy demand scenario [28,29]. Remarkably, green hydrogen is the only zero-carbon option for hydrogen production, as CCS captures only 85%-95% [30,31] of carbon at best and currently achieves even lower rates [32]. However, there are still some challenges that need to be addressed to make green hydrogen sustainable from an economic and environmental point of view. For instance, one of them is the use of Platinum Group Metal (PGM) free catalysts, since Pt manufacturing is energy-demanding and responsible for GHG emissions. Others are the improvement of the Oxygen Evolution Reaction (OER) anode side, mainly due to the high thermodynamic barrier and its sluggish kinetics [33–36], and the minimization of the energy consumption of the overall system [8,37–39]. Indeed, OER is a slow reaction that needs a very high overvoltage to be activated even in the presence of catalysts and poses several restrictions in catalyst selection due to the very positive operating voltage which could cause very severe corrosion issues at this electrode [40–42]. Adding in the solution species that can compete with water oxidation and have a less demanding kinetic can be an effective strategy to minimize the overall energy consumption during the electrolysis [43–46]. Biomass is a good candidate since the corresponding oxidation products could be high-value-added chemicals [47–50] that find application as intermediates for plastics, pharmaceuticals, and textiles [16,46,51–56]. This process is known as biomass reforming [44,52,57–60].

Once produced at scale and competitive costs, green hydrogen can be converted into other energy carriers, such as ammonia, methanol, methane, and liquid hydrocarbons. Hydrogen can be used in fuel cells, which combine hydrogen with oxygen to produce electricity and can also be used in engines and turbines. Fuel cells are used for stationary applications, such as large-scale power plants, microgrids, backup generation (e.g., data centers), and various transport applications, including fuel cell electric vehicles (FCEVs), trucks, light-duty vehicles, forklifts, buses, ferries, and ships. As a chemical, green hydrogen can reduce GHG emissions in sectors where hydrogen from fossil fuels is widely used today, such as oil refining and methanol and ammonia production [61–63]

Low-carbon hydrogen can also be produced from methane pyrolysis, where carbon ends up as solid rather than CO_2, consuming 4-5 times less electricity than electrolysis and potentially lowering hydrogen production costs. However, each pathway has limitations. Bioenergy might be better suited

for other applications due to its limited nature and low inherent hydrogen yield. CCS does not lead to zero emissions, requires significant CO_2 infrastructure, does not enable sector coupling, remains exposed to fossil fuel price fluctuations, and may face social acceptance issues. Additionally, methane leakages during gas production and transportation are significant contributors to climate change, as methane has 86 times the global warming potential of CO_2 over a 20-year period [64].

Given the sector, green hydrogen is one of the most attractive options due to its renewable nature. Nonetheless, green hydrogen also faces challenges, including its current high cost across the entire value chain, from electrolysis to transport and fuel cells; lack of existing infrastructure for transport and storage; high energy losses requiring higher wind/solar deployment rates; and the lack of valuation for its primary benefit of lower GHG emissions [32,65]. Nonetheless, renewables are becoming the cheapest source of electricity globally, with considerable potential for further cost reductions. This trend creates the long-term opportunity to trade low-cost green hydrogen worldwide, from regions with abundant renewable resources to areas with limited land or renewable potential. This trade could involve transporting liquid hydrogen, using hydrogen carriers that increase energy density, or converting it into commodities like chemicals [66–68].

Table 1.1. Near- (approx. 5–10 years) and long-term (approx. 20–30 years) electrolysis cost and efficiency values CAPEX, capital expenditures; OPEX, operational expenditures.

		Near term	Long term
AEL	CAPEX (€ W^{-1})	800 (400-1300)	470 (380-560)
	OPEX (% of CAPEX)	2%-9%	2%-5%
	Efficiency	67% (63%-71%)	68% (66%-70%)
PEMEL	CAPEX (€ W^{-1})	1040 (500-2400)	545 (400-950)
	OPEX (% of CAPEX)	2%-11%	2%-5%
	Efficiency	64% (58%-69%)	68% (62%-71%)
SOEL	CAPEX (€ W^{-1})	1280 (450-4250)	380 (300-450)
	OPEX (% of CAPEX)	2%-3%	2%-3%
	Efficiency	78% (58%-69%)	79% (75%-83%)

One of the main key components for this transition is the electrolyzer, a device that produces hydrogen using electricity and water. Electrolysis, already widely used in the chemical industry, needs to further reduce costs. Technological innovations, such as new catalysts, improved configurations, standardized designs, and mass production, are essential for enhancing the efficiency and lifespan of electrolyzers. To keep the resulting gases apart, the reacting compartments are

separated by an electrolyte, which classifies the main technologies: alkaline electrolysis (AEL), polymer electrolyte membrane electrolysis (PEMEL), and solid oxide electrolysis (SOEL). Table 1.1 [69] provides an overview of available costs and efficiency ranges from the analyzed literature, which vary significantly. The low and high capital expenditures (CAPEX) values represent the most optimistic data from the reviewed papers but should not be directly compared as not all authors assess all technologies [70–74].

Notably, in some regions, green hydrogen is nearing competitiveness, particularly where favorable conditions align, allowing a green hydrogen production cost of about USD 2.5/kg, comparable to blue hydrogen costs. However, in most areas, green hydrogen remains 2-3 times more expensive than blue hydrogen. Its cost depends on electricity prices, investment costs, fixed operating expenses, and the operating hours of electrolyzer facilities (Figure 1.3) [75,76].

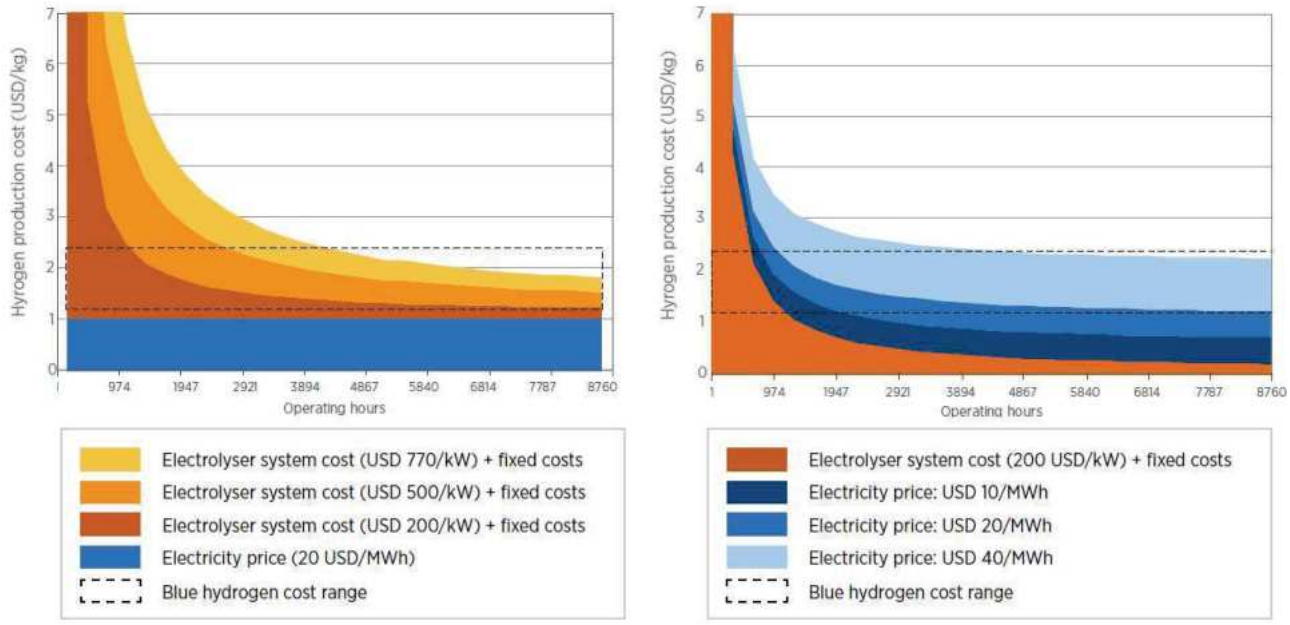

Figure 1.3. Hydrogen production cost as a function of investment, electricity price

When operating hours are low, investment costs dominate because they are spread over less hydrogen. This scenario can occur when using only curtailed electricity or coupling with photovoltaic (PV) without storage or backup. As operating hours increase, electricity costs become more significant. Solar projects in countries like Brazil, Portugal, the UAE, and the USA have achieved electricity costs as low as USD 13.5-20/MWh due to supportive policies, which ensure stable payments and reduce investment risk. The efficiency of the current process means that any power cost translates to roughly

1.5 times this value in final production costs. Therefore, a power cost of USD 20/MWh results in a hydrogen production cost of around USD 31/MWh, or just over USD 1/kg H_2 [77,78].

With optimal conditions—low-cost renewable electricity, reduced investment costs, and high operating hours—green hydrogen could become cost-competitive with fossil-based hydrogen. Achieving the largest reduction in investment contribution may only require about 3000-4000 operating hours per year. This can be accomplished with large-scale hybrid PV-wind plants, which in the best locations can achieve capacity factors above 5000 hours. Green hydrogen, produced via water electrolysis, contributes less than 0.02% of today's global pure hydrogen production. Most projects are in the single-digit MW scale, with the largest operational project being a 20 MW PEM electrolyzer in Becancour, Canada, by Air Liquide. Despite the small scale, the technology is already commercial and ready for scaling up, with projects announced between 2020 and 2025 totaling more than 25 GW [79,80].

Previous waves of interest in hydrogen were sparked by oil supply shocks, positioning hydrogen as a means to diversify energy sources and enhance energy security. In recent years, the focus has shifted towards achieving net-zero emissions and capitalizing on falling renewable energy costs, leading to growing interest in hydrogen across various sectors. Consequently, most existing policy support for hydrogen has centered on fuel-cell electric vehicles and refueling stations. However, this is expected to change as attention shifts towards sectors with existing hydrogen demand, such as industry, and the replacement of fossil-based hydrogen [81].

Promoting hydrogen uptake across different end-use sectors requires an integrated policy approach. The main pillars of this approach include: developing national hydrogen strategies that unify various elements and set a long-term vision shared with industry; establishing policy priorities for sectors where hydrogen can add the most value based on national conditions; creating governance systems and enabling policies to remove barriers and facilitate growth; and implementing guarantees of origin systems to track production emissions and value lower GHG emissions [32,65].

In recent years, a growing number of countries have adopted hydrogen policies and strategies. These vary in scope, with some focusing on green hydrogen, others on fossil-based hydrogen, or a combination of both, and in scale, ranging from no targets to very ambitious, quantified targets for hydrogen and electrolyzers. This rapid increase in hydrogen policies and their ambition reflects the widespread recognition that green hydrogen is crucial for achieving the Paris Agreement's objectives and reaching zero emissions in the energy sector [65].

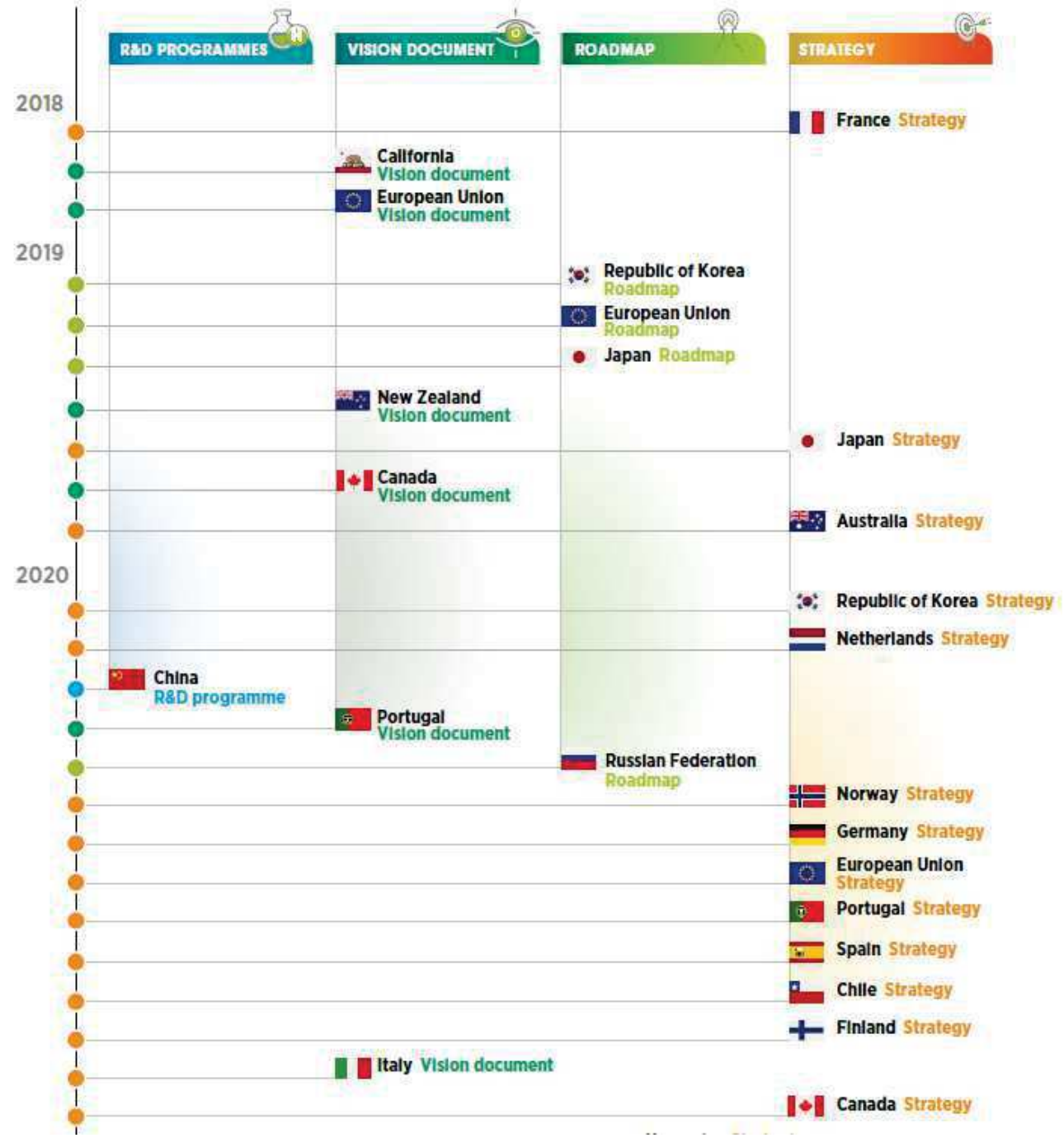

Figure 1.4. Recent hydrogen policies and strategies.

While some strategies support fossil-based hydrogen as a transitional technology for scaling up in the short term, there is a broad consensus that green hydrogen is the long-term, sustainable solution. Support for green hydrogen is more prevalent today, with more countries endorsing green hydrogen compared to blue hydrogen. A few jurisdictions worldwide announced hydrogen strategies, and more are expected to follow. These strategies are not the beginning or end of hydrogen's role in decarbonizing energy but are the result of decades of investment in energy application research and

development (R&D) since the 1970s. This investment has fostered technological progress and close cooperation between private and public sectors through partnerships, culminating in vision documents and roadmaps that pave the way for concrete policy actions by aligning long-term views. These strategies must be followed by impact assessments, policy design, financial viability assessments, and implementation. In the past years, there has been a significant increase in public efforts towards achieving these goals (see Figure 1.4) [82–84].

Currently, most countries are at the strategy stage for hydrogen development and have yet to implement concrete policy measures. Explicit capacity targets for electrolysis are the most common measure for green hydrogen, particularly in Europe. Specific policy instruments to achieve these targets will be developed in the future. For instance, Japan, an early supporter of hydrogen, has already set concrete cost and efficiency targets for application and has initiated multiple international trade projects, including the first liquid hydrogen shipment in December 2019 and the first blue ammonia shipment in September 2020. Conversely, Australia and Chile have set ambitious cost targets. Australia's "H_2 under 2" target aims for a production cost below AUD 2/kg of hydrogen, prompting AUD 370 million in state support, while Chile aims for USD 1.5/kg of hydrogen by 2030, aspiring to be the world's cheapest producer [11].

Beyond capacity and cost targets, governments have various policy options, such as incentives for domestic electrolyzer production (e.g., tax breaks), direct grants, conditional and convertible loans, feed-in tariffs, auctions, and contracts for difference. However, these measures have been limited in the announced strategies [81].

The European Union (EU) has the most ambitious strategies for green hydrogen, with a collective target of 40 GW by 2030, supported by national targets from France, Germany, the Netherlands, Portugal, and Spain, aiming for 6.5 GW, 5.0 GW, and 3.0-4.0 GW respectively. The EU strategy also targets 10 million tonnes of hydrogen per year (MtH_2/year) by 2030, necessitating 40 GW of electrolysis capacity in neighboring countries (North Africa). Beyond the EU, Chile aims for 25 GW by 2030, and Australia has multiple proposals. Both countries plan to meet local demand initially and target exports in the long term [11].

Collectively, these targets could meet the 2030 goal of 100 GW [85]. However, this is insufficient for a well-below 2°C trajectory, which requires at least 270 GW of capacity by 2030, as outlined in the Transforming Energy Scenario (TES). The TES scenario still results in about 9.5 gigatonnes of carbon dioxide ($GtCO_2$) emissions by 2050. Achieving a net-zero world by 2050 would necessitate an even larger role for hydrogen and a faster deployment pace. Positively, 14 of 17 strategies already focus on green hydrogen by 2030, although only the EU, Chile, and Australia have set specific electrolysis

targets. The gap before the more ambitious scenario could close rapidly once other green hydrogen-supporting countries set specific electrolysis capacity targets.

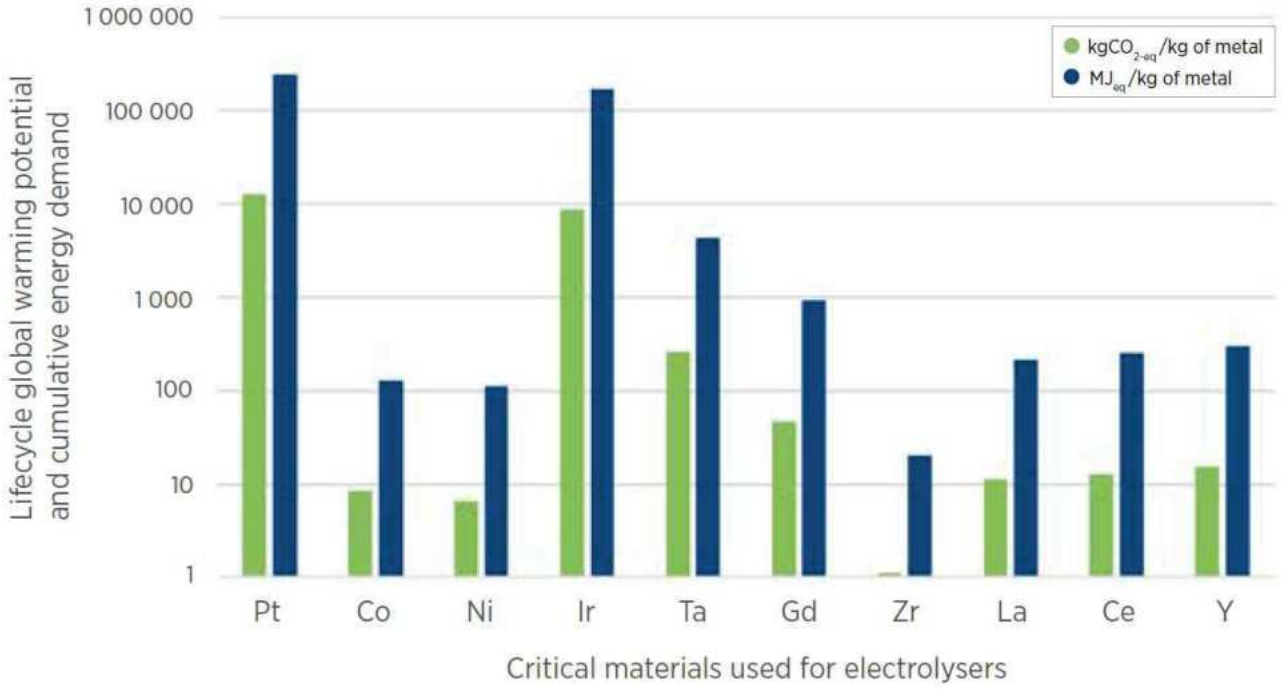

Figure 1.5. Global warming potential and cumulative energy demand for critical materials.

Setting hydrogen production targets into specific electrolyzer capacity targets is a crucial component of a national hydrogen strategy. This approach signals the industry to invest in electrolyzer manufacturing plants and demonstrates how such targets can be achieved through government policies, which are essential for meeting green hydrogen policy targets. Electrolyzer costs will benefit from global deployment, necessitating coordinated national efforts through international platforms to ensure knowledge transfer. Additionally, green hydrogen production requires substantial additional renewable electricity generation, necessitating investment in renewable power generation manufacturing capacity. Without clear government policies, especially regarding how hydrogen will be produced (using clean electricity or fossil fuels), businesses won't know how much hydrogen will be needed. This uncertainty will slow down the growth of the green hydrogen industry, which already faces ambitious production goals. Announced plans call for a massive increase in water electrolysis capacity, from 0.2 gigawatts in 2020 to 85 gigawatts by 2030. That's an incredible growth rate of nearly 83% per year. For comparison, solar panels achieved a similar growth rate between 2008 and 2011, but that industry had a skilled workforce, government support, and easier-to-install technology. To meet these ambitious hydrogen goals, investments need to happen quickly to expand electrolyzer

manufacturing [32,65]. Two main challenges regarding electrolyzers development can be considered: the data availability, often limited due to its confidential nature and the desire to maintain a competitive advantage, and the inconsistent boundaries of cost estimates (e.g., stack, balance of plant, full system) often not specified, making comparisons across studies difficult. However, key limitation factors include the increase in module size, the reduction of specific energy, and the use of critical materials, like Platinum and Iridium. These are two of the scarcest, most energy-intensive and emission-intensive metals (see Figure 1.5) but can allow long-term operation under low overpotential conditions [11,86].

Overall, global interest in green hydrogen is surging as it emerges as a key solution for transitioning towards zero or net-zero emissions. Unlike previous waves of interest, this new wave emphasizes the connection between renewable electricity and hard-to-electrify end uses. The drivers behind this trend include decreasing renewable electricity costs, advancements in relevant technology, benefits for power system flexibility, national commitments to achieving net-zero emissions, and a growing base of stakeholders. In the last years, the momentum for green hydrogen increased significantly, with many countries developing national hydrogen strategies or declaring their intentions to do so.

Despite the unprecedented interest in green hydrogen, several barriers hinder its full contribution to the energy transition. The primary challenge is its high cost compared to grey hydrogen and fossil fuels. Other obstacles include a lack of dedicated infrastructure, insufficient recognition of the value of reduced GHG emissions, and issues related to the development of an emerging industry.

Although the hydrogen sector has gained attention from governments, more dedicated policy support is needed to ensure technology readiness, market penetration, and growth. There are four pillars for green hydrogen policymaking: national hydrogen strategies, policy priorities for green hydrogen, guarantee of origin systems, and enabling policies.

National hydrogen strategies define a country's ambition for hydrogen and outline the support needed to achieve it. They serve as a reference for private actors in the hydrogen industry, encouraging increased financing. Effective strategies should provide a clear pathway for increasing hydrogen uptake.

Green hydrogen can be utilized in a wide range of applications. To maximize impact, national policymakers should identify the applications with the highest value and prioritize them. This approach ensures that policy efforts yield immediate benefits and create a higher demand for green hydrogen.

Guarantee-of-origin schemes should be based on life-cycle greenhouse gas emissions. These schemes help policymakers and end users understand the impact of green hydrogen, ensure consistency with emissions standards for other commodities, and facilitate comparison with other energy sources.
Enabling policies are economy-wide measures designed to level the playing field between hydrogen and fossil fuels. These policies should allow hydrogen actors to contribute value to the entire energy system as well as broader economic and social systems [11].

1.2. Biomass oxidation

Throughout history, biomass has been used not only for food and energy, but also for extracting valuable products such as medicinal drugs, flavors and fragrances. However, large-scale industrial conversion of biomass to chemicals and materials began in the latter half of the 19th century with the production of cellulose esters (nitrate and acetate) and oxidized linseed oil (linoleum). In the 20th century, flavors and fragrances were produced through the catalytic conversion of terpenes, lubricants, and surfactants were derived from vegetable oils in the oleochemical industry, and various industrial products were obtained from the conversion of carbohydrates from different crops. However, bio-based chemicals faced significant economic competition from cheaper products synthesized from hydrocarbons, which had been optimized over more than a century manufacturer worldwide have become interested in using renewable feedstocks for producing bulk and specialty chemicals, while start-ups and small and medium-sized enterprises (SMEs) have developed innovative processes for niche markets.
The chemical industry's interest in the biomass-to-chemical supply chain has grown with the development of sustainable production processes, driven by two global issues:

- The need to use renewable carbon sources to compensate for the anticipated decline in petroleum production and to address concerns about volatile oil market prices. While this is a strong argument for transportation fuels, it is less so for the manufacture of chemicals, as only about 5% of total oil production is currently needed to supply the carbon for organic chemicals and polymers.
- The need to reduce GHG emissions, which can negatively impact the global climate, by using renewable carbon from biomass. However, this argument is weaker for chemicals compared to the significant GHG emissions associated with energy and fuel consumption. GHG emissions depend on many factors, including agricultural practices, biomass collection, and conversion processes, making the extent of GHG reduction debatable.

The current trend of the chemical industry to increasingly substitute fossil feedstocks with renewable carbon is driven not only by concerns about dwindling fossil resources or global warming but also by other factors:

- Sustainable production of chemicals from biomass can improve public confidence in the chemical industry.
- Industrial agencies in developed countries have actively promoted the use of renewable resources to manufacture innovative products, maintaining the chemical industry's competitiveness in the global market.
- Bio-based bulk chemicals have significant market potential, and bio-based products like surfactants, lubricants, and plasticizers already hold a substantial market share.
- Beyond replicating existing fossil-based products, renewable chemistry opens opportunities to develop new products that have no equivalents among those currently produced from hydrocarbons.
- Developing bio-products requires fewer legislative constraints. For instance, biopolymers, even when chemically modified, are currently exempt from the European REACH registration.

Among the production of chemicals and materials from biomass, thermochemical processes like gasification, pyrolysis, and aqueous phase reforming of biomass can offer opportunities for chemical production. For example, biomass gasification produces syngas, which can be selectively converted to hydrocarbons, dimethyl ether, methanol, and higher alcohols depending on the catalysts used. Fast pyrolysis produces a complex mixture of oxygenates that can be used to extract chemicals, although recovering pure compounds is costly. Hydro-processing of pyrolysis oils on Ru/C and Pt/C catalysts increases the yield of polyols and alcohols. Aqueous phase reforming of carbohydrates has primarily focused on alkane and hydrogen production, but dehydration and coupling reactions during this process can lead to valuable oxygenates. Catalytic transesterification of triglycerides can be employed to produce biodiesel, as well as various combined depolymerization/fermentation processes to produce bioethanol or biobutanol. Bio-catalytic processes are crucial for producing platform molecules from carbohydrates, and many biomass conversions require a combination of bio- and chemo-catalytic processes, either separately or in one-pot processes, as demonstrated by the concept of cascade catalysis [58,59,87–90].

Among the various definitions over the past decade, biorefining can be identified as the sustainable processing of biomass into a range of marketable products and energy. However, a biorefinery can sometimes be limited to a single process, such as sugar fermentation to ethanol.

Biorefineries processing starch, sucrose, or vegetable oils into bioproducts existed long before the biorefinery concept was named. Large starch biorefineries, established decades ago, have been converting millions of tons of corn, wheat, or potato starch annually into hundreds of different products. For instance, Roquette company currently processes 6 million tonnes of starch-containing crops per year, producing over 700 different products. Cognis, a company established 150 years ago in Germany, produces hundreds of wellness, nutritional, and functional products from vegetable oils. Today, numerous start-ups and SMEs are emerging to exploit new resources such as microalgae and seaweeds and to develop optimized fermentation processes for producing platform molecules used as building blocks for chemistry. New biorefineries are being set up to process lignocellulosic materials from forestry products, various types of grasses like miscanthus and switchgrass, and agricultural residues. A notable trend in Nordic countries is the transformation of paper pulp mills into lignocellulose biorefineries, which collect raw materials and extract various wood components such as lignin, cellulose, hemicellulose, tall oil, and turpentine.

Cost-effective processes adapted to the molecular structure of highly functionalized biomass molecules are necessary to make the quality and price of chemicals competitive with those produced from fossil fuels. Robust and easily regenerable catalysts need to be developed because natural raw materials often contain impurities that can affect selectivity and decrease activity, thus hindering catalyst recycling or continuous processes. Combining homogeneous and heterogeneous catalytic processes for multi-step biomass conversion is desirable.

Two strategies can be adopted for biomass conversion to chemicals:

- A target-driven approach using process analysis methodology to find the most efficient synthetic routes to produce a specific chemical from well-identified platform molecules. This approach might lead to uneconomical chemical production compared to optimized conventional synthesis routes from hydrocarbons.
- A process-driven approach converts biomass through one or more catalytic processes (e.g., hydrogenation, hydrogenolysis, oxidation), yielding a family of valuable products. This approach does not aim to duplicate chemicals currently produced from fossil resources but may more effectively identify new valuable bioproducts.

In 2004, the US Department of Energy published a list of the "Top 10 chemicals" (actually 15) that could serve as platform molecules or building blocks for the synthesis of bio-based chemicals. Among these, certain chemicals have seen significant research and development in recent years, while others, such as fumaric, malic, aspartic, glutamic, and itaconic acids, have received comparatively less

attention. Platform molecules are also derived from terpenes and proteins. For instance, α-pinene and β-pinene, extracted from turpentine oil (350,000 tonnes per year), and limonene, extracted from citrus oil (30,000 tonnes per year), serve as platform molecules for synthesizing flavors, fragrances, and pharmaceuticals. Furthermore, vegetable proteins or distiller grains, available in large quantities as by-products of carbohydrate fermentations, could become a major source of amino acids with high potential as building blocks for fine and specialty chemicals.

With 100% atom economy in aqueous solutions using heterogeneous catalysts that can be recycled multiple times, some biomass conversion processes are indeed highly efficient. However, the green nature of other biomass conversion processes is compromised by using toxic reagents and solvents, which generate significant waste and have a modest atom economy. The sustainability of these processes can be evaluated through life cycle analysis (LCA) using a cradle-to-grave or cradle-to-gate approach. This method requires a comprehensive inventory and environmental impact assessment of all inputs and outputs of the production system, but it is often impractical due to the complexity of the numerous raw materials, processes, and chemicals involved in biomass conversion [52,91–94].

1.3. Green hydrogen and biomass for e-fuel and high value-added products, traditional and emerging technologies

1.3.1. E-fuel feasibility, cost, and environmental impact

In the past years, the transportation sector, e.g., road, rail, air, and marine transport, accounted for about 27% of global GHG emissions from energy use. Additionally, this sector contributes to local health and environmental problems through the emission of particulate matter, NO_x, and other pollutants. Reducing GHG emissions can be achieved by lowering energy demand, decreasing the emission intensity of that energy, or both. In this sense, it is possible to reduce GHG emissions by decreasing the emission intensity of transport-related energy using electrofuels. Electrofuels are liquid or gaseous hydrogen-containing fuels produced by combining energy from electricity, hydrogen from water (via electrolysis), and carbon or possibly nitrogen. Capturing carbon to produce electrofuels typically involves additional costs. However, a special case arises when externally provided hydrogen reacts with surplus CO or CO_2 from a biofuel production process (e.g., biomass gasification or anaerobic digestion), resulting in products referred to as bio-electrofuels. Depending on the production technology, the resulting electrofuels and bio-electrofuels can be either liquid or

gaseous, including electro-methane, electro-methanol, electro-gasoline, electro-diesel, and electro-ammonia (Figure 1.6). For brevity, these terms are denoted as e-fuels, e-methanol, bio-e-fuels, bio-e-methanol, and so on.

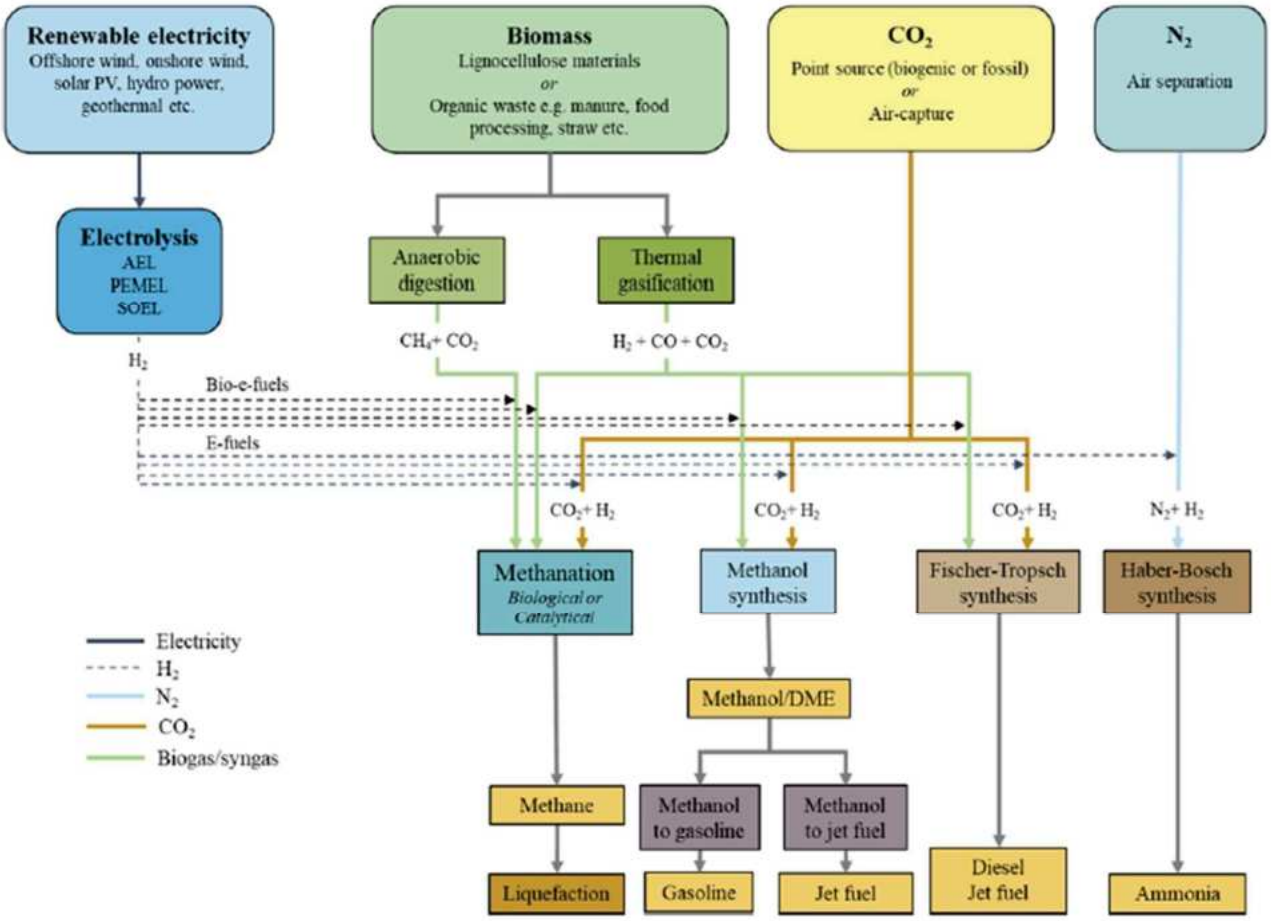

Figure 1.6. Production pathways, for the main fuel options. All carbon-based fuels can be produced either as e-fuels or bio-e-fuels. E-fuels are formed from H_2 and CO_2 or N_2. Both energy flows and material flows are illustrated, i.e. electricity and biomass (energy inputs), CO_2, N_2 and biomass (material inputs) and hydrocarbons, methanol, and ammonia (energy carrier outputs). PV, photovoltaic solar panels; AEL, alkaline electrolysis; PEMEL, polymer electrolyte membrane electrolysis; SOEL, solid oxide electrolysis; DME, dimethyl ether.

E-fuels are of interest for all modes of transport, as many hydrocarbon e-fuels could be used in existing vehicles without significant investment in new distribution and fueling infrastructure. They are particularly relevant in sectors like long-distance aviation and deep-sea shipping, where electrification opportunities are limited due to the need for liquid fuels with high energy density. Additionally, e-fuels could help balance intermittent electricity production by utilizing excess or very low-cost electricity and generating marketable by-products such as high-purity oxygen and heat. However, the combined efficiency of energy conversion and utilization presents a challenge compared to options that use electricity directly. Nonetheless, over the past few years, the concept of

e-fuels has gained increased attention from both research and industries, including automotive, fuel production, and energy utilities [95–97].

Carbon can be sourced by capturing CO_2 from point sources such as ethanol production, bioenergy power plants, cement production, or other industrial processes. Capture technologies include absorption, membrane filtering, or cryogenic capture. Direct air capture (DAC) involves removing CO_2 from ambient air, a challenging process due to low CO_2 concentrations but increasingly attractive for achieving negative emissions when combined with carbon storage, offsetting past and future CO_2 emissions [98]. Table 1.2 presents the reported costs for capturing CO_2 and nitrogen [69].

Table 1.2. Carbon and nitrogen production costs in $€_{2019}$ /tCO_2/N_2. Values are shown for near-term (approx. 5–10 years) and long-term (approx. 20–30 years).

	Near-term	Long-term
Point-source carbon	50 (20–260)	25 (10–100)
Air-sourced carbon	300 (25–778)	90 (15–105)
Nitrogen capture	9 (8–10)	7 (5–14)

While carbon-based e-fuels are the most researched, ammonia is also considered a hydrogen carrier or a fuel itself. E-ammonia is advantageous as it does not produce CO_2 when used, making it attractive if CO_2 emissions are restricted. Pure gases like N_2 can be separated from air by cooling it until it liquefies, then distilling the components based on their boiling points using an air separation unit (ASU) or expansion turbines for cooling. Pressure swing adsorption (PSA) is another method for separating oxygen or nitrogen from air without liquefaction, though it carries a risk of high gas losses due to pressure release.

Hydrogen and carbon can be combined to produce a variety of fuel products using three technologies: methanation, methanol synthesis, and Fischer–Tropsch (FT) synthesis. Additionally, hydrogen can be combined with nitrogen to produce ammonia via the Haber–Bosch synthesis. Methanation can be achieved through catalytic methanation, using catalysts, or biological methanation, using methanogenic microorganisms. Biological methanation, which operates at relatively low temperatures, can be added to biogas plants. In contrast, catalytic methanation operates at high temperatures and is highly exothermic, with excess heat potentially used for purposes like district heating or as a heat source for high-temperature electrolysis, thereby increasing overall plant efficiency [99].

Methanol synthesis is similar to catalytic methanation, where CO_2 and CO in syngas combine with H_2 to produce methanol. This exothermic reaction operates at high temperatures and pressures, with

the resulting methanol further processed into dimethyl ether (DME), gasoline, diesel, or jet fuel [100–102].

FT synthesis involves a series of reactions where CO and H_2 react to form hydrocarbons at high temperatures and pressures. Typically, a reverse water-gas shift reaction precedes FT synthesis to optimize the H_2/CO stoichiometry. The resulting FT liquids, a mixture of paraffins, olefins, and alcohols, are not highly selective, with the final products usually being gasoline, diesel, jet fuel, and high-quality lubricants, while alcohols can also be produced [103]

Ammonia synthesis via the Haber–Bosch process uses a catalyst under high temperature and pressure. This exothermic reaction is typically designed for continuous production. However, future dynamic operation of ammonia synthesis might be economically feasible to utilize hydrogen from intermittent renewable electricity, thus avoiding the high costs of hydrogen storage [104].

Bioenergy sources such as animal manure, organic waste from food processing, straw, and other energy crops may serve as feedstocks for anaerobic processes like digestion or fermentation (Figure 1.6). Anaerobic digestion plants convert biodegradable organic material into biogas, primarily composed of methane (CH_4) and CO_2. Lignocellulosic feedstocks (e.g., wood chips, wood pellets, straw, tops, and branches, or biogas plant residues) are suitable for thermal gasification or other deconstructive processes. Gasification endothermically converts solid biomass into syngas (a mixture of H_2, CO, CO_2, CH_4, water, and light hydrocarbons) in the presence of an oxidizing agent like oxygen or steam, which can then be synthesized into other fuels [105].

In both gasification to syngas and anaerobic digestion, biofuels are produced through the reaction of hydrogen and carbon (CO or CO_2). These processes do not utilize all the carbon in the biomass, with excess carbon typically released as biogenic CO_2. To make use of this excess biogenic carbon, additional hydrogen can be inserted into the production process (e.g., into the syngas or biogas, see Figure 1.6), generating additional fuel without the need for carbon capture. This special hybrid of biofuels and e-fuels is termed bio-e-fuels. Bio-e-fuel production costs encompass gasification/anaerobic digestion, biomass feedstock/biogas substrate, electrolyzer, electricity, fuel synthesis, and potential liquefaction, spread over the entire volume of fuel produced. Literature estimates for gasifier CAPEX range from €1100–1700 per kWsyngas in the near term [105] and €350–1300 per kWsyngas in the long term [106,107], while anaerobic digestion plant costs are €200–235 per kWhbiogas in the near term and €160–205 per kWhbiogas in the long term [108], depending on the biomass type, with lower costs for manure-based feedstocks and higher costs for straw or industrial waste feedstocks.

A main challenge for renewable e-fuel production is the need for continuous synthesis while utilizing low-cost renewable electricity, which is often variable and intermittent. Depending on the e-fuel plant's operating profile, hydrogen storage might be necessary. Additionally, depending on the e-fuel type, additional processing might be required post-synthesis. For road transportation, gaseous fuels (methane and hydrogen) need compression or liquefaction for improved volumetric density and storage. LNG is also used in heavy-duty vehicles and is a potential aircraft fuel [109]. Liquefied hydrogen has been suggested for heavy road vehicles, shipping [68], and aviation [110]. Notably, e-fuel production generates by-products that could create additional revenue streams, potentially enhancing business models for fuel producers. Different electrolysis types generate varying amounts of excess heat at different temperatures, which can be adjusted for district heating levels or used within the process to enhance e-fuel production efficiency, particularly with SOEL [111].

The environmental impacts of e-fuel utilization in the transport sector vary based on the technology used, influencing material requirements, energy demand, and emissions. These factors significantly affect the outcomes of environmental assessments for different e-fuel production pathways. Different materials lead to varying environmental impacts, including GHG emissions and "up-stream emissions" from electricity generation or metal mining operations. Environmental assessments focus on various issues, which review current knowledge on the environmental impacts of e-fuels and identify key influencing factors on the environmental performance of e-fuel production and usage.

Climate change/global warming is the most investigated environmental impact, considered in all reviewed assessments, where emissions from electricity production and carbon supply are primary contributors. E-fuels generally offer emission reductions if produced from low-carbon renewable electricity. However, if fossil energy sources are used, GHG emissions can be higher than those from fossil fuels [69].

Methodological choices and the choice of electricity source can cause significant variations in the carbon footprint of e-fuels. Two main methods for modeling GHG flows can be used: one tracing all emissions and feedstocks upstream and calculating impacts based on the overall sum of flows, and the other considering only fossil-origin CO_2 flows while treating non-fossil CO_2 as having zero climate impact. The choice of carbon capture technology, system boundary assumptions, and how CO_2 emissions are treated in calculations explain the variations in reported impacts.

Water is essential in the e-fuel life cycle, particularly in the electrolyzer and some carbon capture processes. Most studies assume stoichiometric water consumption, but the type of electrolyzer may influence water demand.

Transforming the global energy sector to e-fuels would require significant land, but less than a fully biomass-based system. The land use for facilities like electricity production appears lower than for biogenic fuels. However, further investigations are needed to assess land use connected to carbon capture and other factors.

Health impacts are mainly assessed through emissions causing respiratory issues and toxic emissions. Particulate emissions from combustion processes are a primary source, but e-fuels produce cleaner combustion profiles due to the absence of contaminants. Some studies investigate specific health-related emissions, such as formaldehyde from DME production, but further studies are needed to determine the overall health impacts of e-fuels.

Acidification and eutrophication are secondary impacts linked to material requirements and emissions from electricity production. The choice of chemicals in CO_2 capture and electricity sources influences these impacts. The reviewed assessments did not include noise pollution, social aspects, or other environmental factors.

E-ammonia, produced from hydrogen and nitrogen, has different environmental impacts compared to carbon-based e-fuels. Life cycle assessments of ammonia production highlight the significance of the electricity source used in the electrolyzer. Use phase impacts of e-ammonia include potential emissions of ammonia slip, NO_x, CO, N_2O, and hydrocarbons, but detailed assessments are lacking.

Overall, the environmental impacts of e-fuels depend on several factors, including technology, material requirements, energy demand, and methodological choices in assessments. Renewable electricity sources and efficient carbon capture technologies are crucial for minimizing these impacts. Further studies are needed to explore specific environmental aspects and improve the understanding of e-fuels' overall sustainability [69,112,113].

1.3.2. High value-added products from biomass

To create a sustainable environment, it is crucial to produce biopower, biofuels, and bioproducts from sustainable biomass sources. While standalone processes like the production of charcoal, ethanol, and fuel pellets are well established, using biomass to produce multiple products through biorefineries is a relatively new concept. Researchers have categorized biorefineries based on the generation of feedstock into first-generation (energy crops, edible oil seeds, food crops, animal fats), second-generation (lignocellulosic biomass), and third- or fourth-generation (algae and other microbes) biorefineries. Biorefineries can also be classified by feedstock type, such as corn-based, wood-based, forest-based, palm-based, and algae-based [114].

All these definitions can be generalized into two categories: energy-driven and product-driven biorefineries. Energy-driven biorefineries primarily produce biofuel and bioenergy, while product-driven biorefineries focus on producing bioproducts (food, feed, chemicals, materials) along with bioenergy.

There are multiple pathways to convert biomass into various value-added products, necessitating the integration of diverse biomass conversion platforms (thermal, biological, catalytic, and physical) to produce a broad range of products. The concept of an integrated biorefinery, which combines multiple platforms, has been proposed to enhance overall process and economic performance.

A sustainable integrated biorefinery efficiently converts biomass to produce biofuels, energy, bulk, and fine chemicals. Such facilities are gaining attention due to their potential to improve economic, environmental, and social sustainability. Regardless of the biomass input, an integrated biorefinery typically includes multiple conversion platforms/technologies with varying levels of integration. According to Koukios et al. [115], a sustainable integrated biorefinery must:

- Minimize energy consumption and environmental impact through material and energy integration across platforms.
- Accommodate variable seasonal and annual feedstock patterns by integrating multiple biomass conversion platforms (thermal and biological).
- Depolymerize target macromolecules (e.g., biomass) to intermediates that meet the specifications for further processing steps.
- Maximize the yield and quality of target molecules.

Additionally, due to the inconsistent nature of biomass, pretreatment is essential before conversion. Pretreatment methods include biological, physical, chemical, and physicochemical processes. In biological pretreatment, microorganisms deconstruct lignin and alter the lignocellulose structure. But, although eco-friendly, biological pretreatment is time-consuming. Physical pretreatment typically involves chopping and grinding biomass to ensure uniform feed rates at the biorefinery. To improve transportation, handling, and storage, biomass can be pelletized or briquetted into a densified form. To do that, biomass is pulverized and dried to the required size and then extruded. Hot densified biomass must cool off to reduce moisture content. Chemical pretreatments, such as acid, and alkaline, are also common. Physicochemical pretreatment combines physical and chemical effects. Common methods include hot water and steam. Hot water dissolves biomass and removes part of the lignin and hemicellulose. In steam exposure, high-pressure steam rapidly heats the biomass, promoting hemicellulose hydrolysis, followed by rapid pressure release [116].

Once pretreated, biomass can be processed in conversion platforms.

Biological or biochemical conversion involves degrading biomass with microorganisms. Common strategies include fermentation and digestion. Fermentation utilizes yeast or other microorganisms to produce alcohols or organic acids. Lignocellulose from biomass can also be converted into sugars, typically using mineral acids. Once simple sugars are formed through acid or enzymatic hydrolysis, they are fermented by adding yeast or other microorganisms.

Continuous fermentations are employed in commercial biofuel production due to their ability to achieve higher productivity and yields compared to batch fermentations [117].

Anaerobic digestion is a biological process where microbes convert solid biomass into methane and carbon dioxide CO_2 in the absence of oxygen. This process, widely used for recycling and treating wet organic waste and wastewater in biorefineries, involves three main stages: hydrolytic, acidogenic, and methanogenic. Biogas, composed mainly of methane (approximately 60%) and carbon dioxide (approximately 40%), is produced through digestion. Anaerobic digestion can process various biomass feedstocks with high conversion efficiency (65%-81%), making it feasible for methane production as an intermediate for methanol. However, it has limitations such as a slow conversion rate and the challenge of maintaining an optimal environment for microbes. Biogas can be used directly for cooking or heating after appropriate treatment, or in secondary conversion devices like internal combustion engines for electricity production.

Thermal conversion systems, e.g., combustion, gasification, and pyrolysis, use heat to chemically transform biomass into potential energy products or intermediates like fuels or chemicals for further synthesis. Thermal conversion systems can be used also to produce electricity via combustion, gasification, and pyrolysis, generating intermediate such as steam, syngas, and bio-oil.

Combustion involves a complete oxidation reaction where biomass reacts with excess oxygen at high temperatures (700–1400°C) to generate heat, steam, and by-products like carbon dioxide (CO_2) and water (H_2O), along with NO_x and SO_x emissions. The steam produced can be expanded in steam turbines to generate electricity.

Gasification produces syngas, containing carbon monoxide and hydrogen, through partial oxidation, steam reforming, and other reactions. The process operates at high temperatures in an oxygen-lean environment with a gasifying medium like air, steam, or oxygen. Stages of gasification include drying (100–200°C), pyrolysis (~500°C), gasification (800–1000°C), and combustion (~1300°C). Apart from syngas, char, and tar are also produced and require rigorous cleaning. Common gasifiers include fixed beds, fluidized beds, and entrained bed reactors.

FT synthesis produces synthetic fuel from syngas, generating straight-chain hydrocarbons that can be processed into diesel via hydrocracking. FT synthesis reactions involve paraffin and olefin production, as well as the water-gas shift reaction. The process typically operates at 25–60 bar under low or high temperatures, depending on the reactor type. Iron and cobalt-based catalysts are used, with syngas feed requiring specific H_2/CO ratios. The final product distribution is influenced by the reactor configuration and the chain growth probability.

Catalytic conversion technologies offer high selectivity and yield under mild conditions and can be integrated with other conversion technologies.

Given the numerous pathways available for converting biomass into value-added products, a systematic approach is necessary for the design and screening of integrated biorefineries, facilitating process optimization. In hierarchical-based approaches, engineers use rules derived from their knowledge and experience to create a baseline design [118].

Mathematical optimization-based approaches have been widely used in screening and synthesizing integrated biorefineries These methods develop a superstructure connecting all possible unit operations, model their behavior and performance mathematically, and optimize the system by searching for solutions that maximize or minimize an objective function. These models also include process integration for biomass utilization for heat and power. Notably, sustainable integrated biorefineries must consider multiple conflicting objectives, such as economic, environmental, and social aspects. A highly integrated biomass processing strategy ensures maximum resource utilization and energy efficiency while minimizing environmental impact [119,120].

In general, it is possible to convert biomass into value-added products through integrated biorefineries considering economic analysis, e.g., capital cost estimation, operating cost evaluation, and profitability analysis, promoting sustainability. Various process design approaches can be used for synthesizing, designing, and optimizing these biorefineries.

1.4. Photocatalysis, electrocatalysis and photoelectrocatalysis

This study explores hydrogen production and biomass valorization using photocatalysis and photoelectrocatalysis in aqueous solution and mild operative conditions.

Heterogeneous photocatalysis (PC) relies on the capacity of certain solids, known as photocatalysts, to generate electron (e^-) and positive hole (h^+) pairs when exposed to light of suitable energy. These e^-/h^+ pairs can directly or indirectly induce oxidation and reduction reactions on the surface of the semiconductor through radical formation [121–123]. Historically, heterogeneous photocatalysis has been employed in many applications in the last few years, like organic synthesis [124,125],

decomposition of pollutants [126,127], water splitting [128,129], and photo reforming [130,131]. However, its industrial application has been limited [132,133]. Recently, the focus has shifted towards synthesizing high-value molecules, such as the partial oxidation of alcohols to aldehydes, ketones, and carboxylate species [134–136], reduction reactions, biomass conversion, C-C bond cleavage, CO_2 activation, and H_2 production. Despite its versatility, photocatalysis faces challenges like low solar energy utilization due to high band-gap values of photocatalysts and significant recombination rates of photogenerated e^-/h^+ pairs [137]. Electrocatalysis, on the other hand, facilitates redox reactions in electrochemical cells, converting electrical energy into chemical energy efficiently if powered by renewable sources. Nonetheless, it also has limitations, including high overpotential for some reactions, and often poor Faradic Efficiency due to competitive reactions (FE).

Combining photocatalytic and electrochemical methods, known as photoelectrocatalysis (PEC), offers a synergistic approach to enhance process efficiency. PEC involves applying an external bias, improving the separation and longevity of photogenerated e^-/h^+ pairs [138–140]. Unlike photocatalysis, PEC allows a higher photon to chemical conversion, avoiding catalyst separation issues from the reaction medium [141]. In PEC systems, photo-produced electrons (e^-) and holes (h^+) migrate to the cathode and the photoanode surfaces respectively, triggering reduction and oxidation reactions at these spots [142]. This results in reduction and oxidation reactions occurring at these respective electrodes [142–144]. Although PEC research primarily focuses on water-splitting [145–147], and degradation of organic pollutants [148–150], it is a sustainable way to oxidize organic compounds [151–158], producing valuable chemicals [159] and promoting cathodic H_2 production [22,57,71,134,138,141,160,161], potentially making this process more economical than fossil fuel-based alternatives [162,163].

The great challenge in PEC oxidation of organic compounds is to achieve high selectivity towards desired products and high faradic efficiency (FE) [134,152,155,161,164].

In organic syntheses using water as a solvent, PEC can improve conversion and selectivity towards target compounds by spatially separating oxidation and reduction processes at the electrodes, enhancing reaction efficiency. The primary mechanisms involve the formation of reactive species like $\bullet O_2^-$, $HO_2\bullet$, $HO\bullet$, and h^+ on cathode and anode surfaces under aerobic conditions. Material selection for electrodes must consider the oxidation and reduction potentials of substrates to ensure selectivity toward desired products [161]. Therefore, there is a photoanode where the anodic half-cell reaction can occur and a cathode where the reduction half-cell reaction takes place [142,143,165–169]. This method represents a sustainable and energy-saving way for the production of value-added chemicals by partial oxidation of cheap organic molecules and simultaneously promotes cathodic H_2

production [159,170]. The selection of a photoanode with a suitable valence band (VB) potential is crucial to enhance the selectivity towards high value added (HVA) products, while Pt-based cathodes are usually employed to get a good H_2 evolution rate with low overvoltage [16,171–174].

The foundational principles of photoelectrochemistry were established by Gerischer and other eminent scientists during the latter half of the last century, which greatly advanced the understanding of electrode/electrolyte interface phenomena. The concept of PEC methods was first introduced by Fujishima and Honda in 1972 [175], and interest in semiconductor photoelectrochemistry surged in the 1970s, spurred by the development of efficient liquid-junction solar cells using semiconductors like CdS or CdSe with redox electrolytes and the ability to split water into H_2 and O_2 by illuminating semiconductor/electrolyte junctions. The field experienced various phases of progress, notably revitalized by the advent of dye-sensitized solar cells. Today, PEC is regarded as a promising method for CO_2 conversion, degradation of persistent organic pollutants, and sustainable synthesis of organic molecules, transitioning from bulk to nanostructured materials. Chemical transformations in photoelectrochemical devices typically occur at the semiconductor-electrolyte interface. First, we consider water without any redox species in the dark. The potential distribution at this interface is illustrated in Figure 1.7 [176].

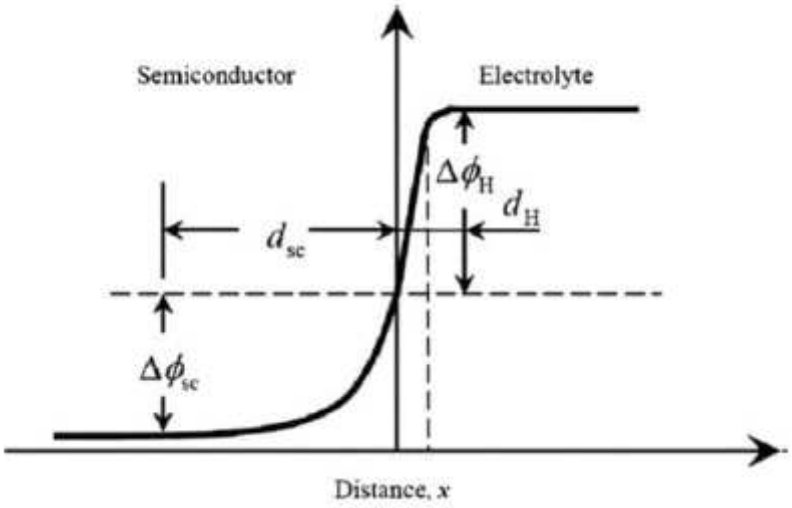

Figure 1.7. Potential trend at the semiconductor-electrolyte interface.

Semiconductor electrodes have a much lower density of charge carriers compared to metal electrodes. Consequently, when in contact with the semiconductor, a region called the Helmholtz layer forms on the solvent side, where a potential drop of $\Delta\Phi_H$ over a distance d_H occurs. On the semiconductor side,

a countercharge corresponding to a potential drop of $\Delta\Phi_{SC}$ forms to a depth of d_{SC} (called space charge region).

The potential distribution within the space charge region along the x-axis in the semiconductor can be described by the Poisson equation (Equation 1.1),

$$Eqn\ 1.1) \qquad \frac{d^2\Delta\Phi_{SC}}{dx^2} = \frac{1}{\varepsilon\varepsilon_0}\,\rho(x)$$

where ε_0 is the permittivity of free space, ε is the dielectric constant of the material, and $\rho(x)$ is the charge density along the distance from the surface, expressed by Equation 1.2.

$$Eqn\ 1.2) \qquad \rho(x) = e[N_d - N_a - n(x) + p(x)]$$

in which N_d and N_a represent the densities of ionized donors and acceptors introduced by the semiconductor's doping, while n(x) and p(x) are the electron and hole densities, respectively, which depend on x according to Equations 1.3 and 1.4.

$$Eqn\ 1.3) \qquad n(x) = N_c\, exp\left(-\frac{E_c\,(x) - E_F}{kT}\right)$$

$$Eqn\ 1.4) \qquad p(x) = N_v\, exp\left(\frac{E_v\,(x) - E_F}{kT}\right)$$

where N_c and N_v are the density of states at the lower edge of the conduction band and the upper edge of the valence band, respectively, $E_c(x)$ and $E_v(x)$ represent the energies of these band edges, while E_F is the Fermi level energy of the semiconductor, defined as the highest occupied energy level within the crystal at 0 K. The position of the Fermi level for an intrinsic semiconductor can be calculated using Equation 1.5:

$$Eqn\ 1.5) \qquad E_F = \frac{E_c + E_v}{2} + \frac{kT}{2}\, ln\left(\frac{N_v}{N_c}\right) = \frac{E_c + E_v}{2} + \frac{kT}{2}\, ln\left(\frac{m_h^*}{m_e^*}\right)$$

where m_h^* and m_e^* are the effective masses of electrons and holes, respectively.

Within the space charge region, the E_F is expected to remain constant, but the positions of the energy bands $E_c(x)$ and $E_v(x)$ vary with distance x. If the charge-carrier densities in the bulk of the semiconductor are n_0 for electrons and p_0 for holes, their densities vary according to a Boltzmann distribution in the space charge region according to Equations 1.6 and 1.7.

$$Eqn\ 1.6) \qquad n(x) = n_0\, exp\left(-\frac{E_c\,(x) - E_c^b}{kT}\right) = n_0\, exp\left(-\frac{e\,\Delta\Phi_{SC}(x)}{kT}\right)$$

$$Eqn\ 1.7) \qquad p(x) = N_v\, exp\left(\frac{E_v\,(x) - E_v^b}{kT}\right) = p_0\, exp\left(\frac{e\,\Delta\Phi_{SC}(x)}{kT}\right)$$

where E_c^b and E_v^b are the conduction and valence bands energy levels in the bulk. Charge neutrality must be maintained in the semiconductor bulk, as expressed by Equation 1.8.

$$Eqn\ 1.8) \qquad N_d - N_a = n_0 - p_0$$

By combining Equations 1.2, 1.6, 1.7, and 1.8 with Equation 1.1, the Poisson-Boltzmann equation is obtained (Equation 1.9).

$$Eqn\ 1.9) \qquad \frac{d^2\Delta\Phi_{SC}}{dx^2} = \frac{1}{\varepsilon\varepsilon_0}\left[n_0 - p_0 - n_0\, exp\left(-\frac{e\,\Delta\Phi_{SC}(x)}{kT}\right) - p_0\, exp\left(\frac{e\,\Delta\Phi_{SC}(x)}{kT}\right)\right]$$

Solving this equation provides the space charge region capacity C_{sc} (Equation 1.10),

$$Eqn\ 1.10) \qquad C_{SC} = \frac{\varepsilon\varepsilon_0}{L_D}\cosh\left(\frac{e\,\Delta\Phi_{SC}(x)}{kT}\right)$$

where C_{sc} is a function of the potential drop $\Delta\Phi_{sc}$. The Debye length, L_D, is defined by Equation 1.11,

$$Eqn\ 1.11) \qquad L_D = \left(\frac{\varepsilon\varepsilon_0 kT}{2n_i e^2}\right)^{1/2}$$

with n_i representing the intrinsic carrier density equivalent to the square root of the product n_0 and p_0.

To calculate the dependence of d_{SC} on $\Delta\Phi_{SC}$ we need to solve the Poisson equation in Equation 1.1, considering the boundary conditions of zero electric field and zero Galvani potential in the bulk of semiconductor ($d\Phi/dx(\infty) = 0$ and $\Phi_{SC}(\infty)=0$). By this assumption, it follows that $\Phi_{SC}(x) = \{ \Phi_{SC}(x) - \Phi_{SC}(\infty) \}$ has the opposite sign to the electrochemical scale of potential. The width of the space charge region, d_{SC}, as well as the potential distribution inside the semiconductor under reverse polarization of the junction, can be easily found by using the Schottky barrier model of the junction and by solving the Poisson in Equation 1.1 under depletion approximation and in the hypothesis of homogeneously doped semiconductor with fully ionized donors N_d (for n-type SC) or acceptors N_a (for p-type SC) [177,178]. The depletion approximation implies that the net charge density varies from the zero value of the bulk to the value $+eN_d$ for a n-type SC (or $-eN_a$, for a p-type SC) at the depletion edge.

As a consequence of such a charge distribution, a linear variation of the electric field is obtained according to the Gauss equation, which relates the electric field E_s intensity at the surface of the SC, to the charge density Equation 1.12:

$$E_s = \frac{eN_d d_{SC}}{\varepsilon\varepsilon_0} \qquad Eqn\ 1.12)$$

For an electric field varying linearly inside the space-charge region, the potential drop inside the SC can be calculated as Equation 1.13:

$$\Delta\Phi_{SC} = \frac{E_s d_{SC}}{2} = \frac{\varepsilon\varepsilon_0 E_s^2}{2eN_d} \qquad Eqn\ 1.13)$$

from which a dependence of E_s on $(\Delta\Phi_{SC})^{1/2}$ is derived.

By relaxing the depletion approximation and by considering a more gradual drop of the electron density at the depletion edge, we get for E_s the expression (Equation 1.14).

$$E_s = \left(\frac{2eN_d}{\varepsilon\varepsilon_0}\right)^{1/2} \left(\Delta\Phi_{SC} - \frac{k_B T}{e}\right)^{1/2} \qquad Eqn\ 1.14)$$

showing that the depletion approximation differs from the contribution k_BT/e.

The dependence of the width on the space-charge region from the potential drop Equation 1.15, can be obtained by using Equation 1.12 and Equation 1.14:

Eqn 1.15) $$d_{SC} = \left(\frac{2\varepsilon\varepsilon_0}{eN_d}\right)^{1/2} \left(\Delta\Phi_{SC} - \frac{k_B T}{e}\right)^{1/2}$$

This expression can be used for deriving also the dependence of the space-charge capacitance from $\Delta\Phi_{SC}$ Equation 1.16.

Eqn 1.16) $$C_{SC} = \frac{\varepsilon\varepsilon_0}{d_{SC}} = \left(\frac{\varepsilon\varepsilon_0 eN_d}{2}\right)^{1/2} \left(\Delta\Phi_{SC} - \frac{k_B T}{e}\right)^{1/2}$$

The previous relationship is the Mott-Schottky (M-S) equation, which can be employed to derive the flat band potential, U_{FB}, of the junction. For this aim, we need to relate the Galvani potential drop within the semiconductor to the measured electrode potential, U_E.
By defining the flat band potential of the junction as the electrode potential at which $\Delta\Phi_{SC} = 0$, in absence of surface states we can write Equation 1.17:

Eqn 1.17) $$\Delta\Phi_{SC} = U_E - U_{FB}$$

where U_E and U_{FB} are measured to the same reference electrode. By substituting Equation 1.17 in Equation 1.16 we get the final form of the M-S equation (Equation 1.18), usually employed for getting the flat band potential and the energetics of the n-junction.

Eqn 1.18) $$\left(\frac{1}{C_{SC}}\right)^2 = \left(\frac{2}{\varepsilon\varepsilon_0 eN_d}\right)\left(U_E - U_{FB} - \frac{k_B T}{e}\right)$$

The determination of the flat-band potential is the first step in the location of the energy levels at the semiconductor/electrolyte interface. Once U_{FB} is known, it is possible to locate the Fermi level of the semiconductor to the electrochemical scale through the relationship $E_F = -|e|U_{FB}$

When a redox couple is present in the solution, the equilibrium between the oxidized (Ox) and reduced (Red) species (Equation 1.19) is influenced by the semiconductor.

Eqn 1.19) $$Ox + e^- \leftrightarrows Red$$

If the Fermi level of the semiconductor differs from the redox potential of the couple, charge-carrier transfer occurs from the valence or conduction band across the liquid-solid interface to establish equilibrium. At equilibrium, the electrochemical potential of electrons in the semiconductor equals the difference between the electrochemical potentials of Red and Ox. This allows us to define a redox Fermi energy (Equation 1.20),

$$Eqn\ 1.20) \qquad E_{F,redox} = E^0_{F,redox} - kT\ ln\left(\frac{C_{ox}}{C_{red}}\right) = -4.44 - e\ E^0_{F,redox} - kT\ ln\left(\frac{C_{ox}}{C_{red}}\right)$$

where the standard reduction potential is measured on the standard hydrogen scale (SHE) according to the recommended estimation of the position of the H^{+}/H_2 redox Fermi level as -4.44eV on the vacuum scale. The charge transfer at the electrolyte-semiconductor interface can be described by the Gerischer model [179,180], schematically described in Figure 1.8. The redox system is depicted as an array of occupied states for the reduced species, whose charge density maximum is centered at the E_{red}^0 value, and of unoccupied states for the oxidized species centered at E_{ox}^0. The density of the occupied and empty states is D_{red} and D_{ox}, respectively, which are proportional to the concentration of the reduced (C_{red}) and oxidized (C_{ox}) species in the redox system according to Equations 1.21 and 1.22.

$$Eqn\ 1.21) \qquad D_{red}(\check{E}) = C_{red} W_{red}(\check{E})$$

$$Eqn\ 1.22) \qquad D_{ox}(\check{E}) = C_{ox} W_{ox}(\check{E})$$

In the text, Ě was used as a generic energy symbol when it represents a function of a certain physical quantity (in Figure 1.8, energy is still denoted by E).

$W_{red}(\check{E})$ and $W_{ox}(\check{E})$ account for the distribution of occupied and empty levels, respectively. The energy distribution of reduced and oxidized species differs due to their distinct solvation. Assuming a harmonic oscillation of the solvation shell, $W_{red}(\check{E})$ and $W_{ox}(\check{E})$ are Gaussian-type functions. This relationship is expressed by the reorganization energy λ (Figure 1.8a), which appears in the distribution functions' expressions (Equation 1.23 and 1.24) along with the thermal energy kT.

$$Eqn\ 1.23) \qquad W_{red}(\check{E}) = (4kT\lambda)^{1/2}\ exp\left[-\frac{(\check{E} - E^0_{F,redox} - \lambda)^2}{4kT\lambda}\right]$$

$$Eqn\ 1.24) \qquad W_{ox}(\check{E}) = (4kT\lambda)^{-1/2}\ exp\left[-\frac{(\check{E} - E^0_{F,redox} - \lambda)^2}{4kT\lambda}\right]$$

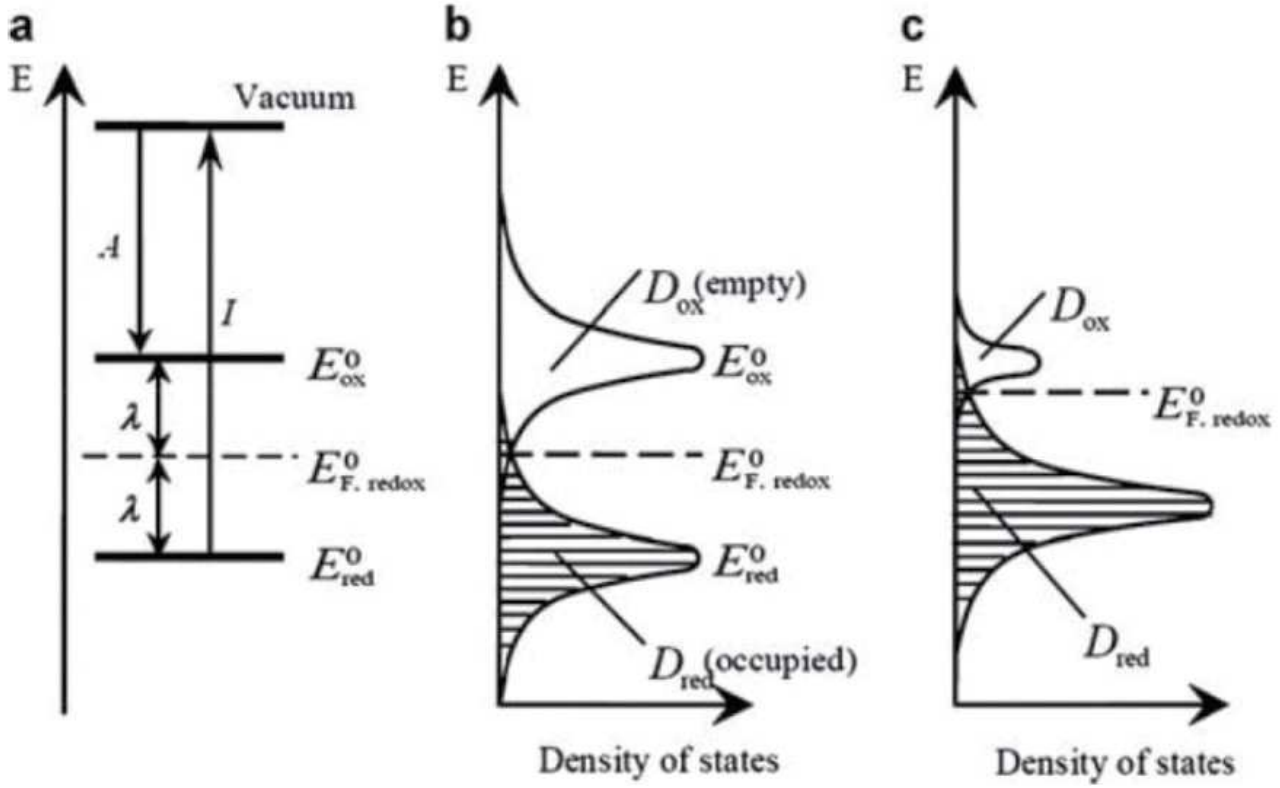

Figure 1.8. Electron energies of a redox system vs. density of states: (a) E_{red}^0 for occupied states, E_{ox}^0 for empty states, an electron affinity and *I* ionization energy of the redox system; (b) the corresponding distribution functions at C_{ox}=C_{red}; (c) the distribution functions at $C_{ox} \ll C_{red}$.

When the concentrations of the redox species vary (Figures 1.8b-c), the standard electrochemical potential of the redox couple, $E^0_{F,redox}$, shifts according to the Nernst equation. When the semiconductor contacts the electrolyte, equilibrium must be established on both sides [179,181–184], meaning the E_F of the semiconductor must align with that of the redox couple $E_{F,redox}$, which remains virtually constant due to the higher number of states per unit energy in solution compared to the semiconductor. If the potential of the redox couple is more positive than the semiconductor's Fermi level, equilibration occurs through electron transfer from the semiconductor to the redox couple. This results in the depletion of majority carriers (electrons) in the semiconductor's surface region, forming a “depletion layer” on the semiconductor side. This process continues until the negative charges in

the solution side prevent further charge transfer, reaching equilibrium. The resulting band bending forms a potential barrier that hinders charge transfer at the semiconductor-electrolyte interface [158]. The height of this barrier represents the potential drop in the space charge layer and is the difference between the conduction band edge energy in the bulk and at the surface.

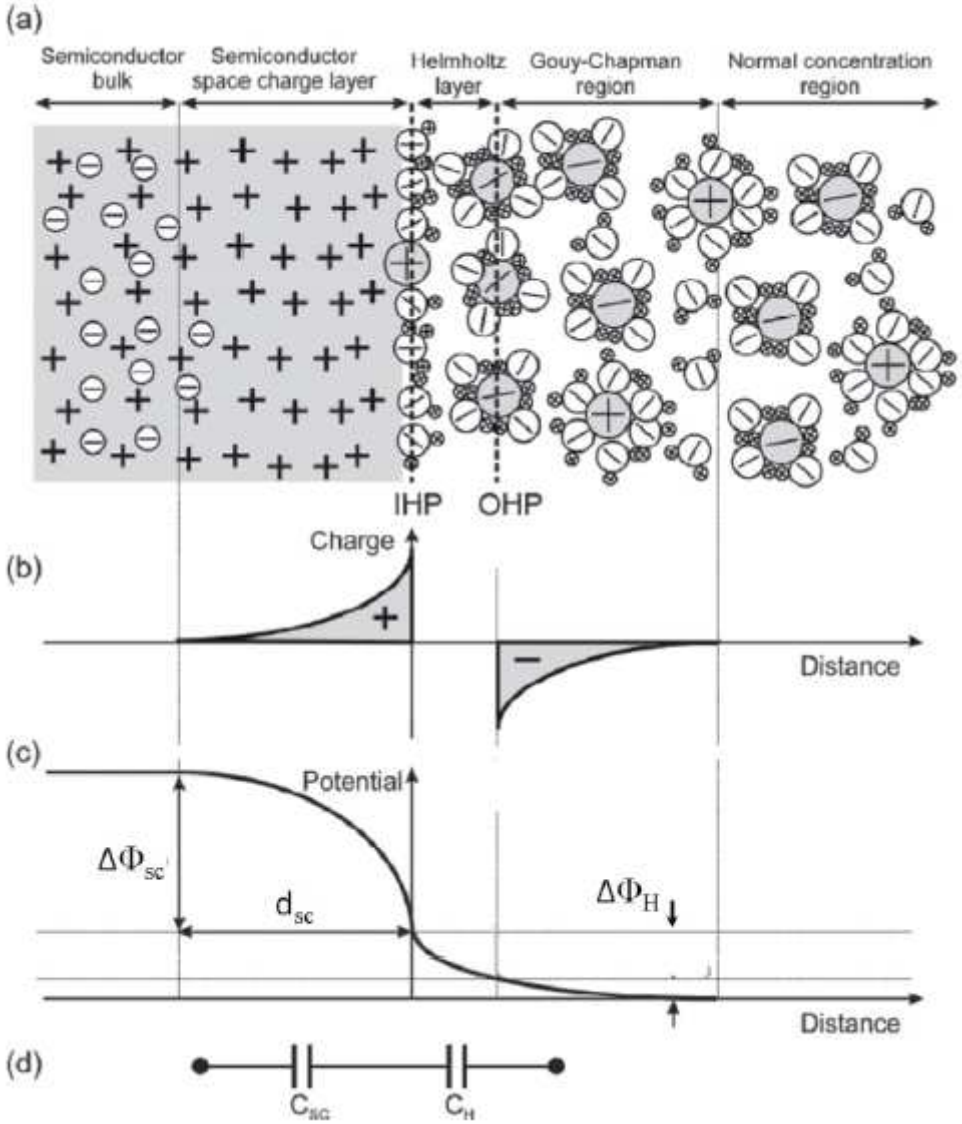

Figure 1.9. Schematic view of the electric double layers at the n-type semiconductor-aqueous electrolyte interface (a) with corresponding charge (b) and potential (c) distributions. ΔΦsc is the potential drop across the space charge layer, $\Delta\Phi_H$ is the potential drop in the solvent side; (d) the equivalent circuit for the interface

Figure 1.9 illustrates the n-type semiconductor-electrolyte interface as a series of three double layers between the semiconductor bulk and the electrolyte. Starting from the left, the space charge layer in the semiconductor is depleted of electrons (positive region) with counter-negative charges at the surface. Next, on the electrolyte side, the Helmholtz double layer consists of the inner Helmholtz

plane (IHP) at the semiconductor interface and the outer Helmholtz plane (OHP), which marks the nearest approach of hydrated mobile ions. Finally, the Gouy-Chapman layer is an extended region with an excess of free ions of one sign. For high concentrations of electrolyte (> 0.1M), the potential drop in the Gouy-Chapman region can be neglected. Thus, the interface region can be modeled as two parallel-plate capacitors in series, with capacitances C_{SC} and C_H, respectively.

The simplest quantitative interpretation of the semiconductor-electrolyte interface [158,185,186] assumes an ideal crystalline semiconductor without surface states. Notably, the potential drop in the electrode is negligible for metal electrodes but significant in the Helmholtz layer. Conversely, for semiconductor electrodes, the largest potential drop occurs in the semiconductor's space charge region. If electron transfer from the redox system to the semiconductor occurs, it generates an anodic current contribution (j_c^+), where the subscript "c" indicates the current is generated through the conduction band and the superscript "+" indicates oxidation occurring at the electrolyte side (Equation 1.25).

$$Eqn\ 1.25) \qquad j_c^+ = ek^0\, C_{red} \int_{E_F}^{\infty} \left(1 - f(\check{E})\right)\, \rho(\check{E})\, exp\left[-\frac{\left(\check{E} - E_{F,redox}^0 - \lambda\right)^2}{4kT\lambda}\right]$$

where E_F is the Fermi level of the semiconductor, $\rho(\check{E})$ represents the distribution of energy states in the semiconductor, k^0 is the standard electron transfer rate constant, and $f(\check{E})$ is the Fermi-Dirac energy state distribution (Equation 1.26).

$$Eqn\ 1.26) \qquad f(\check{E}) = \frac{1}{1 + \exp\left(\frac{E - E_F}{kT}\right)}$$

Electron transfer occurs when the orbitals of the redox species overlap with those of the semiconductor. Since this overlap is typically confined to a narrow energy range, it can be assumed that $d\check{E} = kT$ and $\check{E} = E_c^s$, where E_c^s is the lower edge of the conduction band at the surface. Under this assumption, Equation 1.27 can be obtained.

$$Eqn\ 1.27) \qquad j_c^+ = ek^0\big(1 - f(E_c)\big)\,\rho(E_c)\left\{ C_{red}\ exp\left[-\frac{\big(E_c^s - E_{F,redox}^0 - \lambda\big)^2}{4kT\lambda} \right] \right\}$$

where the density of states in the semiconductor at the lower edge of the conduction band, $\rho(E_c)$, can be approximated as equal to the density of energy states a few kT above the conduction band edge (N_c), and can be expressed by Equation 1.28.

$$Eqn\ 1.28) \qquad \rho(E_c) = N_c = \frac{2(2\pi m_e^* kT)^{3/2}}{h^3}$$

Since most of the energy states in the conduction band are empty, $f(E_c) \approx 0$, and therefore Equation 1.29.

$$Eqn\ 1.29) \qquad \big(1 - f(E_c)\big)\,\rho(E_c) \approx N_c$$

By applying this assumption to Equation 1.27, it is possible to obtain Equation 1.30:

$$Eqn\ 1.30) \qquad j_c^+ = ek^0 N_c C_{red}\ exp\left[-\frac{\big(E_c^s - E_{F,redox}^0 - \lambda\big)^2}{4kT\lambda} \right]$$

Since Equation 1.30 contains only constant parameters for a given system at equilibrium, the anodic contribution to the current is independent of the electrode potential.
Similarly, it can be shown that the cathodic contribution to the current, resulting from electron transfer from the semiconductor's conduction band to the empty states of the redox system, is given by Equation 1.31.

$$Eqn\ 1.31) \qquad j_c^- = ek^0 f(E_c)\,\rho(E_c) C_{ox}\ exp\left[-\frac{\big(E_c^s - E_{F,redox}^0 + \lambda\big)^2}{4kT\lambda} \right]$$

The density of occupied states at the bottom of the conduction band on the surface is given by the product of $(E_c)\rho(E)$ at $\check{E}=E_c^s$. This is equivalent to the surface density of free electrons n_s, which depends on the potential drop $\Delta\Phi_{sc}$ according to Equation 1.32.

Eqn 1.32)
$$n_s = n_0 exp\left[-\frac{e\,\Delta\Phi_{SC}}{kT}\right]$$

The net current due to charge transfer involving the conduction band is the sum of the anodic (j_c^+) and cathodic (j_c^-) contributions. This net current reaches zero when the electrochemical potentials on both sides of the interface are equal. This results in a modification of the energy distribution within the space charge layer compared to the scenario where no redox system is present in the electrolyte. The band bending observed near the interface on the semiconductor side, shown in Figure 1.10, is plotted as energy vs. distance. It illustrates the curvature induced in the space charge region due to the charge transfer occurring to establish thermodynamic equilibrium at the semiconductor-electrolyte interface.

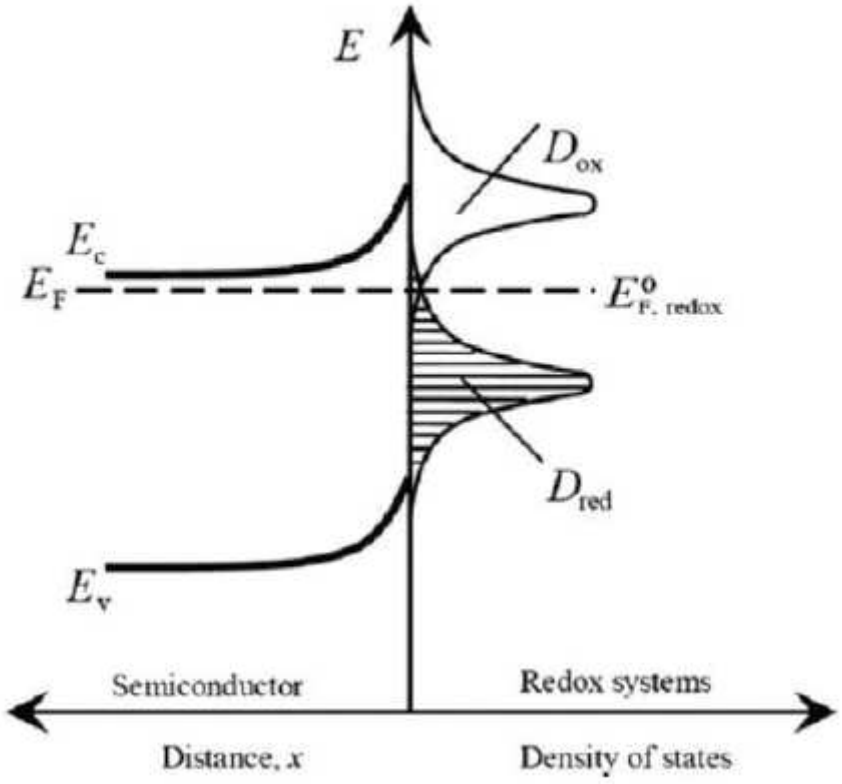

Figure 1.10. Electron energies of a semiconductor electrode in contact with a redox system

To fully understand the behavior of electrons within a conductor, and consequently the electronic transfer between an electron conductor and an ionic conductor, it is essential to investigate the energy levels of the electrons. The energy of the electrons primarily depends on the electric potential within the phase. This potential, known as the internal potential (Galvani potential, ϕ), is divided into two components: the external potential (ψ), which arises from any excess electrical charges present in the

phase, and the surface potential (χ), which is due to the surface dipolar layer. For the i^{th} phase (Equation 1.33):

$$Eqn\ 1.33) \qquad \phi_i = \psi_i + \chi_i$$

where ψ_i is a measurable quantity, whereas ϕi and χi are not measurable. The chemical potential (μ) is thermodynamically defined as the work needed to introduce a j^{th} particle into the i^{th} phase at constant temperature and pressure. This is equivalent to the change in free energy resulting from the addition of the species N_j and is expressed as (Equation 1.34):

$$Eqn\ 1.34) \qquad \left(\mu_j\right)_i = \left(\frac{\partial G}{\partial N_j}\right)_{T,p} = \left(\frac{\partial G}{\partial n_j}\right)_{T,p}$$

where $n_j=N_AN_j$ and N_A is Avogadro's number. If the particle N_j is charged, the electrochemical potential is defined as the work required to introduce 1 mole of the j^{th} species into the i^{th} phase and is expressed as (Equation 1.35)

$$Eqn\ 1.35) \qquad \left(\tilde{\mu}_j\right)_i = \left(\mu_j\right)_i + z_jF\phi_i = \left(\mu_j\right)_i + z_jF\psi_i + z_jF\chi_i = \left(\alpha_j\right)_i + z_jF\psi_i$$

where the term $\left(\tilde{\mu}_j\right)_i$ represents the electrochemical potential of the j^{th} species in the i^{th} phase, $\left(\mu_j\right)_i$ is the chemical potential of the j^{th} species in the i^{th} phase, and the term $z_jF\phi_i$ accounts for the electrical work needed to add the charge against the internal potential. The term $(\alpha_j)_i$, known as the real potential, can also be seen as the energy required to transfer the particle from a point in front of the surface (in contact with the vacuum) across the dipole layer. For a metal phase and electrons, $-\alpha$ corresponds to the electron work function (Φ_M) in Equation 1.36.

$$Eqn\ 1.36) \qquad (\alpha_e)_M = -FV_0 + E_F - F\chi_M = -\Phi_M$$

where E_F is the energy of the Fermi level and $-FV_0$ is the potential energy of a mole of electrons inside the metal. The metal (M) surface potential χ_M depends on the crystallographic orientation and, like the work function, increases with the surface atom density.

When two different phases come into contact, such as an electrode (M) in contact with an electrolyte solution (S), an equilibrium condition is established (Equation 1.37).

Eqn 1.37) $$\left(\tilde{\mu}_j\right)_M = \left(\tilde{\mu}_j\right)_S$$

Within each phase, the electrochemical potential remains constant, but an electrochemical potential gradient is created at the interphase ${}^{M}\Delta^{S}\phi$. Consequently, the ability of a charged particle "j" to move between the two phases is dependent on this potential difference ${}^{M}\Delta^{S}\phi$.
Under equilibrium conditions, the potential difference across the double layer is determined by the difference in the chemical potentials of the species in the two phases (Equation 1.38).

Eqn 1.38) $$ {}^{M}\Delta^{S}\phi = \phi_M - \phi_S = \frac{{}^{S}\Delta^{M}\phi(\mu_e)}{F}$$

Notably, ϕ for each phase is not directly measurable, neither is $\Delta\phi$ since the experimental setup for measuring $\Delta\phi$ introduces at least one additional interphase potential, making the absolute value of $\Delta\phi$ experimentally inaccessible. What can be measured is the electrode potential, which is not equal to the interfacial potential drop.

In a typical two-electrode cell composed of two electrodes immersed in the same electrolyte solution and connected by an external conductor (Figure 1.11a), at least three different interfaces are created: (M_1:S_1), (S_1:M_2), and (M_2:M_1'). Here, M_1' refers to the M_1 metal in contact with M_2, whose electrostatic potential will generally differ from that of M_1 at the other pole. The measured voltage V (Equation 1.39) is the sum of the potential drops at these three interfaces (Figure 1.11b).

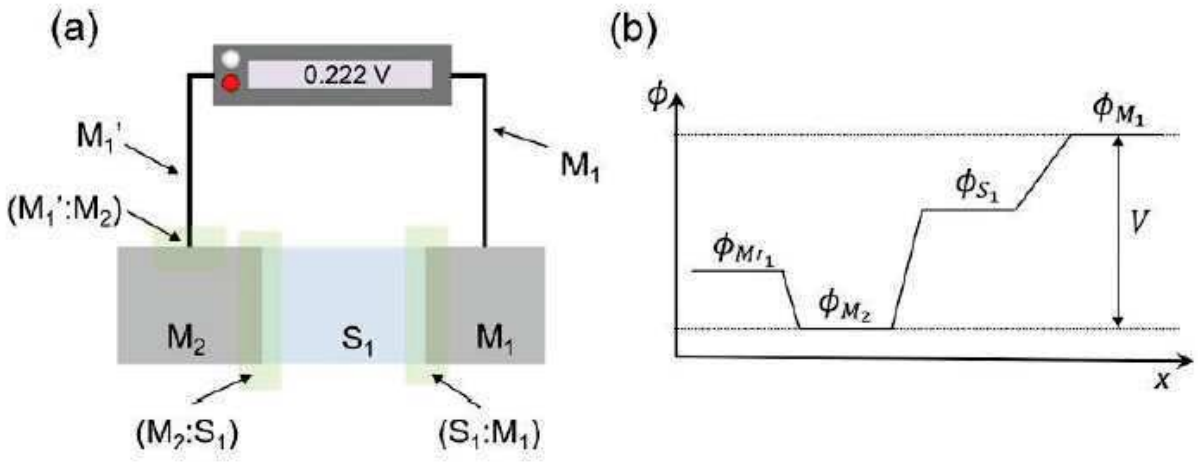

Figure 1.11. (A) Scheme of an electrochemical cell with the interfaces of interest. (B) Potential drops at each interphase and graphical definition of the measured voltage V in an electrochemical cell.

$Eqn\ 1.39)$ $$V = RI = \left(\phi_{M_1} - \phi_{S_1}\right) + \left(\phi_{S_1} - \phi_{M_2}\right) + \left(\phi_{M_2} - \phi_{M_1'}\right)$$
$$= {}^{M_1}\Delta^{S_1}\phi + {}^{S_1}\Delta^{M_2}\phi + \left(\phi_{M_2} - \phi_{M_1'}\right)$$

Explicating in terms of electrochemical potentials and applying the condition of equilibrium Equations 1.40-1.42 can be obtained:

$Eqn\ 1.40\ )$ $$(\tilde{\mu}_e)_{M_1} = (\mu_e)_{M_1} - e\phi_{M_1'}$$

$Eqn\ 1.41)$ $$(\tilde{\mu}_e)_{M_2} = (\mu_e)_{M_2} - e\phi_{M_2}$$

$Eqn\ 1.42)$ $$(\tilde{\mu}_e)_{M_1} = (\mu_e)_{M_1} - e\phi_{M_1'} = (\mu_e)_{M_2} - e\phi_{M_2} = (\tilde{\mu}_e)_{M_2}$$

Consequently, voltage V can be measured based on the chemical potentials of an electron in the two metals (Equations 1.43-1.44).

$Eqn\ 1.43)$ $$V = {}^{M_1}\Delta^{S_1}\phi + {}^{S_1}\Delta^{M_2}\phi + \left(\frac{(\mu_e)_{M_2}}{e} - \frac{(\mu_e)_{M_1}}{e}\right)$$

$Eqn\ 1.44)$ $$V = \left({}^{M_1}\Delta^{S_1}\phi + \frac{(\mu_e)_{M_1}}{e}\right) + \left({}^{S_1}\Delta^{M_2}\phi + \frac{(\mu_e)_{M_2}}{e}\right) = E_1 - E_2$$

where E_i is defined as the electrode potential. Since the absolute value of the electrode potential cannot be measured directly, the values reported in the literature always represent the differences between two electrode potentials: the working electrode and the reference electrode. If the standard hydrogen electrode (SHE) is used as a universal reference, any other electrode potential can be placed within the electrochemical series. The electrode potential is related to the concentrations of the oxidized and reduced species involved in the electrode process (even if the reaction does not occur at the electrode surface) by the well-known Nernst equation, which reads (Equation 1.45).

$Eqn\ 1.45)$ $$E_{eq} = E^0 + \frac{RT}{nF} ln \frac{a_O}{a_R}$$

For instance, if we consider the equilibrium for the H^+/H_2 redox couple as shown in Equation 1.46, the equilibrium potential can be defined using Equation 1.47.

Eqn 1.46) $$2H^+ + 2e^- \rightleftarrows H_2$$

Eqn 1.47) $$E_{eq} = E^0_{H^+/H_2} + \frac{RT}{nF} ln \frac{(a_{H^+})^2}{p_{H^2}}$$

where, E^0 is the standard electrode potential of the redox system, which is conventionally zero for the H^+/H_2 redox couple. n is the number of electrons involved in the reaction (2 in this case), R is the universal gas constant, and F is the Faraday constant. a_{H^+} is the activity of the hydrogen ions, which can be approximated by the H^+ molar concentration $[H^+]$ in dilute solutions, while p_{H^2} is the partial pressure of the hydrogen gas [187].

The electrode potential E (vs. SHE), multiplied by nF, represents the relative value of $\Delta_r G^0$, i.e., the $\Delta_r G$ of the redox process occurring at the interface, considering that $\Delta_r G^0$ for the reference interphase is zero at any temperature and pressure Equation 1.48. This is the only thermodynamic information accessible, but it is significant, even though it does not provide any information on the value of $\Delta\phi$.

Eqn 1.48) $$nFE_{eq} = -\Delta_r G^0 = RTlnK$$

It is possible to state that at the equilibrium potential (E_{eq}), no net process occurs in either the cathodic or anodic direction. By definition, the equilibrium electrode potential is the value at which no net current flows in the circuit and the system is in complete equilibrium.

To initiate a process, it is necessary to move toward more positive potentials to favor oxidation or more negative potentials to favor reduction. This introduces a new quantity called overpotential (η), which is defined as the difference between the applied potential and the equilibrium potential (Equation 1.49).

Eqn 1.49) $$\eta = E - E_{eq}$$

Considering the definition of equilibrium potential, overpotential is required to move the reaction from equilibrium, favoring either the oxidation (formation of H^+) or the reduction (formation of H_2),

resulting in a net current flowing in the external circuit. Overpotential represents the energy loss needed to overcome kinetic barriers, mass transfer resistance, and ohmic drops. The ohmic drop accounts for energy losses due to the non-ideal conductivity of the electrolyte and electrodes. Both overpotential and ohmic drop depend on current density; as current increases, both overpotential and ohmic drop also increase.

Processes where the unidirectional flow of electrons has a low overvoltage are kinetically fast, while those with high overvoltage are kinetically slow. The applied potential's role is to accelerate the electrode process in either the anodic or cathodic direction of the reaction. Whether this can be achieved at high or low voltages depends on the electrode material, which acts as the catalyst for the electrode reaction.

Whenever a new catalyst is proposed or optimized, it needs to be characterized. Multiple electrochemical and electrochemically enhanced techniques can be used for this purpose. Cyclic voltammetry is a versatile and invaluable technique for investigating redox processes of chemical species and electron transfer-initiated chemical reactions, including catalysis. These experiments are conducted in a three-electrode cell, involving the linear scanning of the working electrode's potential (Equation 1.50) at a specific rate (v) while recording the resulting current [187–189].

$Eqn\ 1.50)$ $$E(t) = E_i + vt$$

The resulting graph of current versus applied potential is called a voltammogram. In the simplest case, a reversible (fast/Nernstian) n-electron reduction of a species R generates O. During the forward scan, R is oxidized to O, and in the reverse scan, O is reduced back to R (Figure 1.12a). The voltammogram is characterized by anodic and cathodic peaks for the oxidation and reduction processes.

However, in electrocatalysis, reversible processes are not typically of interest; instead, irreversible processes are usually encountered. The voltammogram for an irreversible electron transfer typically displays only a forward peak, characterized by a less intense and more stretched profile (Figure 1.12b). Notably, by using voltammetry, is it possible to assess an electrode's electrocatalytic activity for a certain reaction, helping us choose the best material.

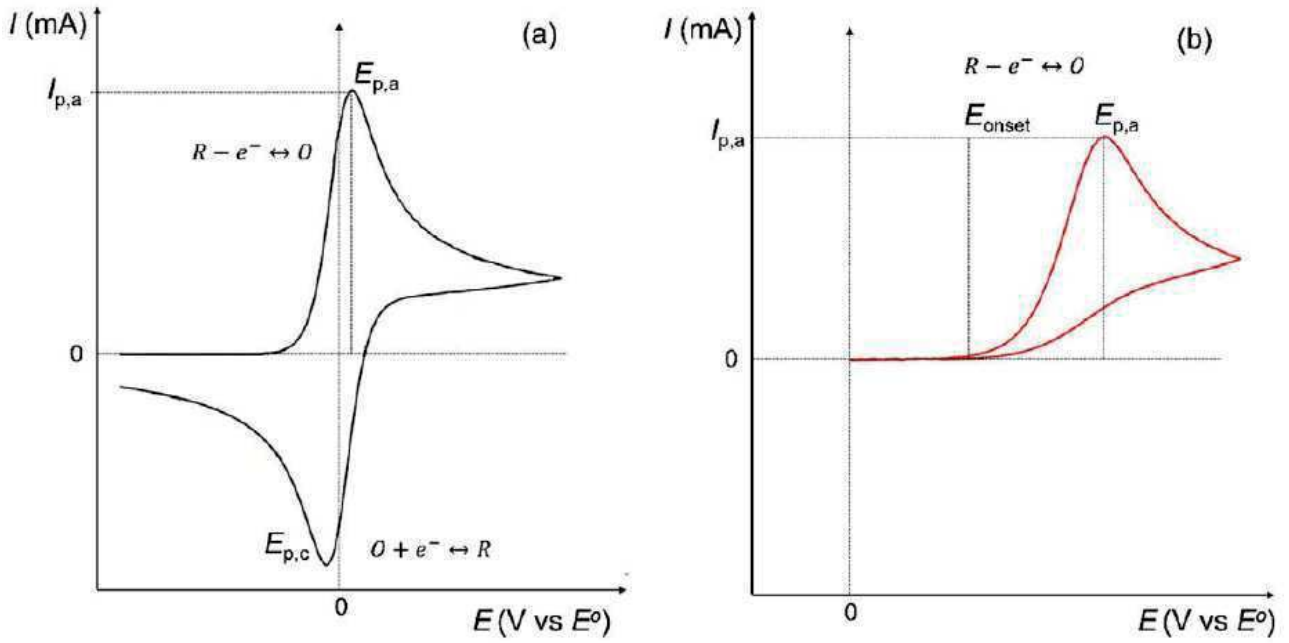

Figure 1.12. Cyclic voltammetric for (A) reversible and (B) irreversible electron transfer process with the same formal potential, E^0, on a microelectrode in the assumption of a semi-planar diffusion process and a triangular potential ramp applied to the working electrode

In contradistinction to the conventional approach of continuous current application, electrochemical investigations can be undertaken within the frequency domain. Electrochemical Impedance spectroscopy offers an alternative strategy, employing a small-amplitude sinusoidal potential perturbation (or, less frequently, a current perturbation) applied to the interface. The consequent response of the current (or potential) is then measured. The potential can be expressed using complex notation, where i denotes the imaginary unit (Equation 1.51).

$$V(t) = V_0 e^{i\omega t} \qquad Eqn\ 1.51)$$

Provided that the amplitude, V_0, remains sufficiently small, the interfacial response exhibits linearity. Consequently, the current, I, can be expressed in the following form, where the angular frequency, ω, remains unaltered (Equation 1.52).

$$I(t) = I_0 e^{i\omega t} = |I_0| e^{-i\varphi} e^{i\omega t} \qquad Eqn\ 1.52)$$

The observed phase shift, denoted by φ, is directly correlated with the system's impedance, Z. In essence, it reflects the system's response characteristics to the applied oscillating potential (Equation 1.53).

$Eqn\ 1.53)$ $$Z(\omega) = \frac{V}{I} = \frac{V_0}{I_0} e^{i\varphi} = |Z|e^{i\varphi} = |Z|(cos\varphi + isin\varphi)$$

To obtain a comprehensive picture of the system's behavior, the modulation frequency, ω, is typically swept across a broad range. This process generates an impedance spectrum, denoted as Z(ω). These spectral data are then visualized through two primary methods: Nyquist Plot: this plot depicts both components of the impedance (real and imaginary parts) on a single graph and Bode Plot: This plot presents the frequency (ω) on the x-axis and the phase angle of the impedance on the y-axis.

For accurate impedance spectroscopy measurements, several critical conditions must be met:

- Linearity: The applied signal's amplitude must be sufficiently small to ensure the system's response remains linear. This implies that the measured impedance is independent of the input signal's amplitude.
- Steady State: The transfer coefficient measurements must be independent of the time at which the measurement is performed. Long measurement times can potentially alter the observed system.
- Finite Impedance: Both the real and imaginary parts of the impedance must possess finite values across the entire investigated frequency range.
- Single Input, Single Output: Throughout the measurement, all external parameters (temperature, concentration, bias, pH) must remain constant. Additionally, there should be no output without a corresponding input.
- Absence of Memory Effects: The system's response should not be influenced by prior experiments.
- Observability: The phenomena of interest must be sufficiently prominent within the chosen frequency range for reliable detection.
- Current Additivity: The faradaic current (resulting from electron transfer reactions) and the capacitive current (associated with charging/discharging processes) must be additive.
- Electroneutrality: The electrolyte solution must maintain a charge-neutral state overall.
- Minimal Convection and Migration: Ideally, there should be minimal changes in local concentrations beyond those caused by diffusion and charge transfer processes. This minimizes the influence of convection and migration phenomena.
- Lateral Current/Charge Flow Absence: No net mass or charge flow should occur laterally across the electrode surface.

The total impedance of an electrochemical system often arises from the collective contributions of various electrode processes. In many instances, it proves beneficial to represent the system using an equivalent circuit. These circuits typically consist of basic electrical components like resistors (representing resistive elements) and capacitors (representing capacitive elements) arranged in parallel and series configurations. However, for complex systems, there might exist multiple equivalent circuits with identical overall impedance, making interpretation challenging.

Both Nyquist and Bode plots are often fitted based on a chosen equivalent circuit model to extract pertinent parameters. Generally, the real part of the impedance signifies the system's resistive behavior (e.g., solution resistance). Conversely, the imaginary part reflects the capacitive nature (e.g., double-layer capacitance) and inductive behavior (if present).

The Randles circuit (depicted in Figure 1.13) offers a simplified model of an electrochemical interface where diffusion limitations are minimized (kinetic control prevails). This model assumes a polarizable electrode with charge transfer processes occurring. The impedance expression for this system is presented in Equation 1.54.

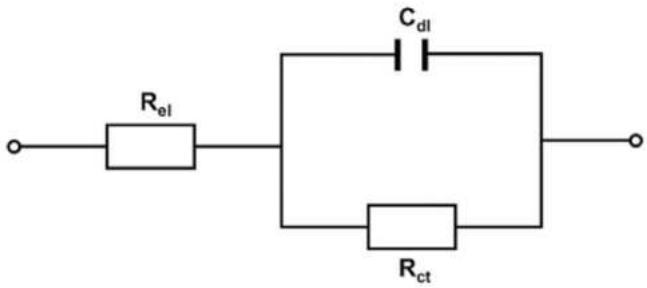

Figure 1.13. Randles circuit

$$Z(\omega) = \frac{1}{1/R_{CT} + i\omega C_{dl}} + R_{el} \qquad Eqn\ 1.54)$$

where R_{CT}, charge transfer resistance, quantifies the resistance associated with electron transfer reactions occurring at the electrode surface; R_{el}, solution resistance, represents the resistance of the electrolyte solution to the flow of current; C_{dl}, double layer capacitance signifies the capacitance of the electrical double layer formed at the interface between the electrode and the electrolyte solution.

The key aspect of impedance spectroscopy lies in its ability to extract these parameters by analyzing the impedance response across a range of frequencies. At very high frequencies, the capacitive reactance (imaginary component of impedance) approaches zero. Consequently, the measured

impedance (Z) converges towards the sum of R_{el} and R_{CT}. Conversely, at very low frequencies, the capacitive behavior dominates, and the impedance primarily reflects C_{dl} [187,190].

As mentioned before, thanks to its unique band structure, a semiconductor can absorb light with sufficient energy. This band structure is characterized by a filled valence band, an empty conduction band, and a forbidden energy gap (bandgap) separating them. Light absorption excites electrons from the valence band to the conduction band, creating electron-hole pairs [191]. Light-induced transitions between bands in a semiconductor can be categorized as either direct or indirect, depending on the relative positions of the valence band maximum (VBM) and conduction band minimum (CBM) in momentum space (k-space).

- Direct Transitions: These occur when the VBM and CBM lie at the same k-value. Direct transitions require only the absorption of a photon with sufficient energy to bridge the bandgap. This makes them more probable events.
- Indirect Transitions: These occur when the VBM and CBM reside at different k-values. To conserve momentum during the transition, indirect transitions necessitate both photon absorption and the emission or absorption of a phonon (lattice vibration) along with the photon. This additional requirement makes them less likely compared to direct transitions.

Therefore, direct semiconductors generally exhibit higher absorption coefficients due to the prevalence of direct transitions. The most fundamental method to explore a semiconductor's band structure involves measuring its absorption spectrum. This technique analyzes the amount of light absorbed at various wavelengths, offering insights into the energy transitions available.
Recently, advancements have combined spectroscopic and photoelectrochemical methods for a more detailed investigation of the intricate electronic structure within a semiconductor [192,193]. These combined techniques provide a deeper understanding of the material's electronic properties [194,195]. When light interacts with a semiconductor, the absorption of a photon can induce various electronic transitions, resulting in the formation of different excited states. The specific type of transition that occurs depends on the photon's energy and the material's electronic band structure (Figure 1.14A).

- Band-to-Band Transitions: Photons with energy equal to the bandgap of the semiconductor can directly excite an electron from the filled valence band to the empty conduction band. This process creates an electron-hole pair, where the "hole" refers to the vacancy left behind in the valence band (Figure 1.14A(a)).

- Supra-Bandgap Excitation: Photons possessing energy exceeding the bandgap can excite electrons to states beyond the lower edge of the conduction band. These excited electrons rapidly lose this excess energy through interactions with the lattice (thermalization) within a femtosecond timescale (10^{-15} s to 10^{-12} s), relaxing to the conduction band minimum (Figure 1.14A(b)).
- Intraband Transitions: If the semiconductor's band structure possesses discrete energy levels within the forbidden bandgap, photons can excite electrons between these levels. This can bring them closer either to the conduction band minimum or the valence band maximum (Figures 1.14A(c) and (d)).
- Low-Energy Excitation: In certain instances, even photons with relatively low energy can induce the excitation of electrons within the same band (intraband excitation) (Figure 1.14A(e)).
- Exciton Formation: Under specific conditions, the Coulombic attraction between the photogenerated electron and hole can lead to the formation of a bound state known as an exciton. This exciton can subsequently dissociate into a free electron and hole through thermal processes (Figure 1.14A(f)).

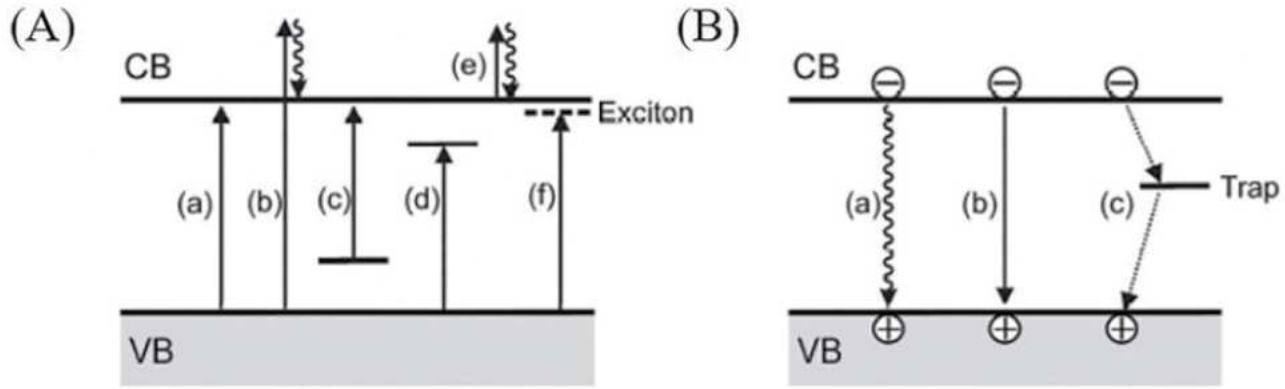

Figure 1.14. Various electronic transitions (A) and recombination mechanisms (B) in irradiated semiconductors

The absorption of light by a semiconductor creates electron-hole pairs in a non-equilibrium state characterized by high energy. These energetic charges can undergo recombination if the charges are not efficiently trapped or transferred elsewhere. During recombination, the energy initially absorbed by the photon is released, often in the form of heat (thermal recombination) or light (radiative recombination). Recombination can also occur through pathways involving intermediate energy states within the bandgap (Figure 1.14B).

The Fermi level (E_F) in a semiconductor at thermal equilibrium represents the energy level at which the probability of finding an electron is 50%. However, under light irradiation, the population distribution of electrons and holes deviates significantly from the equilibrium condition. To account for this non-equilibrium situation, the concept of quasi-Fermi levels is introduced [196]. These represent the Fermi level for electrons ($^*E_{Fn}$) and holes ($^*E_{Fp}$) under illumination (Figure 1.15).

In n-type semiconductors, where electrons are the majority charge carriers, the electron density changes minimally upon irradiation. Consequently, the quasi-Fermi level for electrons remains relatively constant. In contrast, p-type semiconductors, dominated by holes, experience a significant increase in hole density under light. This phenomenon leads to a quasi-Fermi level for holes positioned near the valence band edge.

The splitting of the Fermi level into quasi-Fermi levels depends on the size of the semiconductor particle relative to the depth of light penetration within the material. In small particles where the light penetration depth encompasses the entire particle, the quasi-Fermi levels are spatially uniform throughout the material (Figure 1.15b). In larger particles, the generation of electron-hole pairs is concentrated near the surface where light enters the material. As a result, the quasi-Fermi level for holes varies across the particle, with a higher value near the surface due to the higher concentration of photogenerated holes (Figure 1.15c).

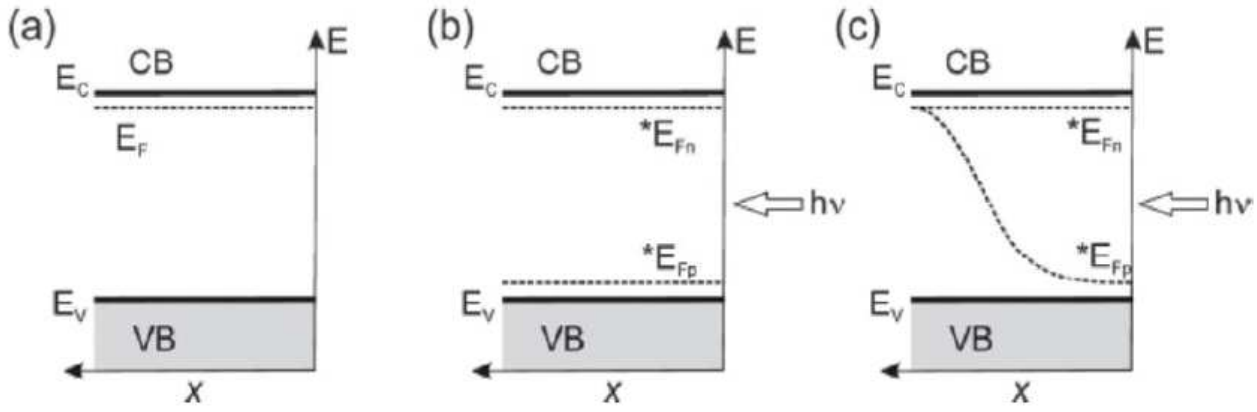

Figure 1.15. Fermi levels and Quasi-Fermi levels of electrons and holes for an n-type semiconductor: (A) at thermodynamic equilibrium (in the dark); (B) and (C) under illumination; (C) local excitation; x is the distance from the semiconductor surface

The concept of the quasi-Fermi level for holes is particularly important because it reflects the driving force for oxidation reactions that can occur at the semiconductor surface. This parameter is crucial for understanding the behavior of both n-type semiconductors under light irradiation and p-type semiconductor electrodes subjected to an external electrical bias.

When photons with energy exceeding the bandgap of a semiconductor irradiate the material, the resulting photoexcitation alters the equilibrium established at the semiconductor-electrolyte interface under dark conditions. This photoexcitation can involve band-to-band transitions or transitions from impurity states within the semiconductor. The absorption of a photon generates an electron-hole pair. The excited electron occupies the conduction band, while the vacancy left behind (hole) resides in the valence band.

Considering an n-type semiconductor, where electrons are the majority carriers, light irradiation dramatically changes the density of holes (minority carriers). This density can increase by several orders of magnitude compared to dark conditions. The electric field existing under dark conditions, arising from band bending, plays a crucial role in carrier movement. This field drives the photogenerated holes within the space-charge layer (SCL) towards the semiconductor-electrolyte interface. Similarly, holes generated in the bulk of the semiconductor first diffuse towards the SCL and then undergo the same transport to the interface.

In contrast, for p-type semiconductors, the situation is reversed. Light irradiation excites electrons, which are then driven towards the surface. Conversely, holes are driven towards the bulk of the semiconductor.

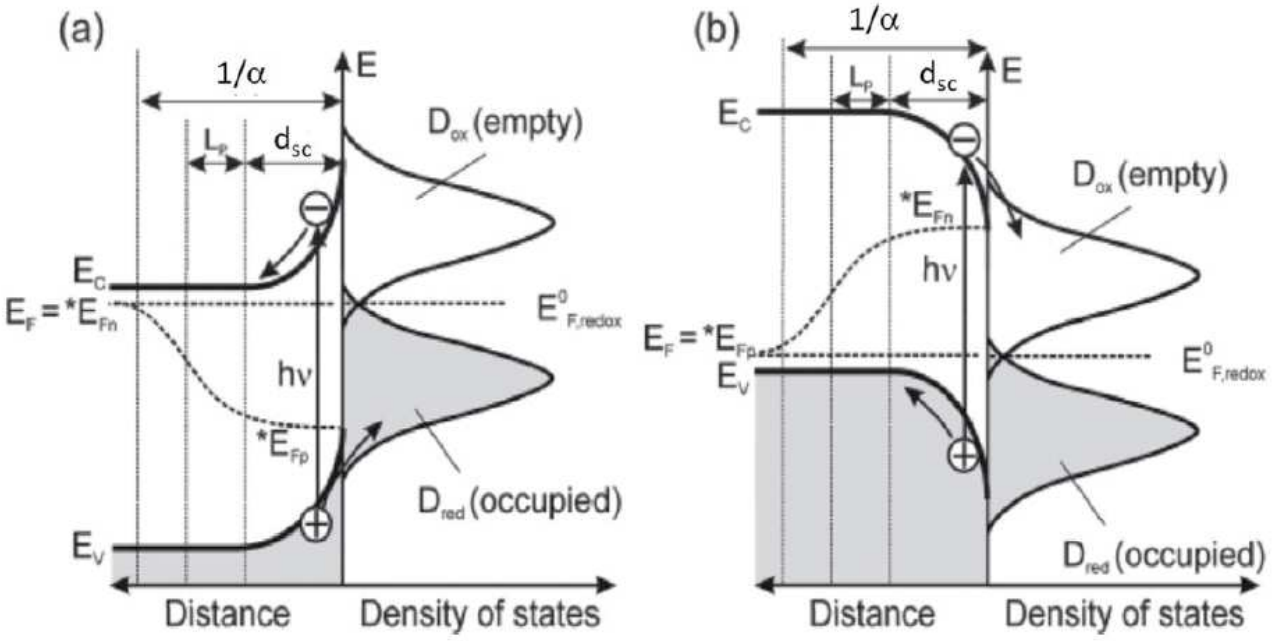

Figure 1.16. Charge transfer at the (a) n-type and (b) p-type semiconductor-solution interface under illumination.

Because of these carrier transport behaviors, n-type semiconductors typically exhibit anodic (positive) photocurrents under light irradiation. Conversely, p-type semiconductors generate cathodic (negative) photocurrents.

A critical parameter in this process is the hole diffusion length (L_p). This length defines the region within the bulk where photogenerated holes can effectively diffuse towards the space-charge region (SCR) and reach the surface under the influence of the built-in electric field.

Assuming negligible charge recombination, Figure 1.16 depicts this mechanism for irradiated n-type (Figure 1.16a) and p-type (Figure 1.16b) semiconductors. To accurately model the current density under light irradiation (photocurrent density), it becomes necessary to solve the hole diffusion equation (Equation 1.55). This equation, i.e., Butler-Gartner derivation, incorporates three terms in its balance equation, accounting for diffusion, recombination, and generation of holes under irradiation, respectively.

$Eqn\ 1.55)$ $$D\frac{d^2p}{dx^2} - \frac{p - p_0}{\tau} + \bar{I}\alpha\ exp(-\alpha x) = 0$$

where D is the diffusion coefficient, p and p_0 are the hole density in a certain position and the bulk at equilibrium, respectively, τ is the lifetime of holes, $\bar{I}$ the monochromatic photon flux absorbed by the semiconductor, obviously depending on the distance from the surface, α is the absorption coefficient of the semiconductor, defined as in Equation 1.56.

$Eqn\ 1.56)$ $$\alpha = \frac{1}{d} ln \frac{\bar{I}_0}{\bar{I}}$$

where d is the semiconductor thickness, and $\bar{I}_0$ and $\bar{I}$ are the incident and transmitted photon flux, respectively. α generally vary with wavelength between 10^3 and 10^6 cm^{-1}. The depth of penetration, inversely proportional to α, is defined as the distance at which the radiant power is reduced of 1/e times its incident value and varies in the range of 10^{-8}-10^{-6} m for different semiconductors.

The diffusion current density j_{diff} at the interface between the hole diffusion length and the space charge layer, resulting from the irradiation of an n-type semiconductor, is described by Equation 1.57.

$Eqn\ 1.57)$ $$j_{diff} = -j_0 \left(\frac{p_d}{p_0} - 1\right) + \frac{eI_0\alpha L_p}{1 + \alpha L_p} exp(-\alpha d_{SC})$$

where j_0 (Equation 1.58) is a saturation current density in the bulk representing the generation/recombination rate of holes in the bulk

Eqn 1.58) $$j_0 = \frac{eDn_i^2}{N_D L_p}$$

Furthermore, p_0 is the hole density in the bulk and p_d is the hole density at $x=d_{SC}$. The p_d value is related to the hole density at the irradiated surface (p_s) (Equation 1.59).

Eqn 1.59) $$p_s = p_d exp\left(\frac{e\Delta\Phi_{SC}}{kT}\right)$$

d_{SC} can be estimated by using Equation 1.60:

Eqn 1.60) $$d_{SC} = \frac{1}{e}\left(\frac{2\Delta E_F \varepsilon\varepsilon_0}{N_D}\right)^{1/2}$$

Assuming charge recombination is negligible within the space charge layer, the value of the hole photocurrent in the space charge region can be determined using Equation 1.61.

Eqn 1.61) $$j_{SC} = eI_0[1 - exp(-\alpha d_{SC})]$$

By also neglecting recombination at the semiconductor-electrolyte interface, the total hole-induced current (j_v, where the subscript indicates charge transfer through the valence band) is the sum of the diffusion current (j_{diff}) and the current generated in the space charge region (j_{SC}) (Equation 1.62).

Eqn 1.62) $$j_v = j_{diff} + j_{SC} = -j_0\left(\frac{p_d}{p_0} - 1\right) + \frac{eI_0\alpha L_p}{1+\alpha L_p} exp(-\alpha d_{SC}) + eI_0[1 - exp(-\alpha d_{SC})]$$

$$= -j_0\left[\frac{p_s}{p_0} exp\left(-\frac{e\Delta\Phi_{SC}}{kT}\right) - 1\right] + \frac{eI_0\alpha L_p}{1+\alpha L_p} exp(-\alpha d_{SC}) + eI_0[1 - exp(-\alpha d_{SC})]$$

This current must be equal to the hole current derived from the cathodic (j_v^+) and anodic (j_v^-) hole densities at the surface of the semiconductor, analogous to Equations 1.63 and 1.64 for the valence band.

Eqn 1.63) $$j_v^+ = ek_0 p_s C_{red} exp\left[-\frac{\left(E_v^s - E_{F,redox}^0 - \lambda\right)^2}{4kT\lambda}\right]$$

Eqn 1.64) $$j_v^- = ek_0 N_v C_{ox} exp\left[-\frac{\left(E_v^s - E_{F,redox}^0 - \lambda\right)^2}{4kT\lambda}\right]$$

where E_v^s is the energy of the upper edge of the valence band at the semiconductor surface. Anodic and cathodic currents at the equilibrium and in the dark are equal to the saturation current density j_v^0 in Equation 1.65.

Eqn 1.65) $$j_v^0 = j_{v,equilibrium}^+ = ek_0 p_s^0 C_{red} exp\left[-\frac{\left(E_v^s - E_{F,redox}^0 - \lambda\right)^2}{4kT\lambda}\right] =$$

$$= j_{v,equilibrium}^- = ek_0 N_v C_{ox} exp\left[-\frac{\left(E_v^s - E_{F,redox}^0 - \lambda\right)^2}{4kT\lambda}\right]$$

At equilibrium, $p_s = p_s^0$. N_v, the density of states at the upper edge of the valence band, can be assumed constant since the valence band is full by definition. However, the current density resulting from hole transfer from the irradiated (non-equilibrium) semiconductor to the electrolyte is given by Equation 1.66.

Eqn 1.66) $$j_v = j_v^+ - j_v^- = j_{v,equilibrium}^+ \frac{p_s}{p_s^0} - j_{v,equilibrium}^- = j_v^0\left(\frac{p_s}{p_s^0} - 1\right)$$

where again the hole density at the surface (p_s^0) depends on that in the bulk (p^0) through a Boltzmann distribution function Equation 1.67:

Eqn 1.67) $$p_s^0 = p_0 exp\left(\frac{e\Delta\Phi_{SC}^0}{kT}\right)$$

where $\Delta\Phi_{SC}^0$ is the drop of potential across the space charge layer under dark conditions at the equilibrium. By combining Equations 1.62 and 1.63, the ratio can be obtained from Equations 1.68 and 1.69

Eqn 1.68)
$$\frac{p_s}{p_s^0} = \left(\frac{j_v}{j_v^0} + 1\right) exp\left(\frac{e\Delta\Phi_{SC}^0}{kT}\right)$$

Eqn 1.69)
$$j_v = \frac{j_0 + eI_0\left[1 - \frac{exp(-\alpha d_{SC})}{1+\alpha L_p}\right] - j_0 exp\left(-\frac{e\eta}{kT}\right)}{1 + \frac{j_0}{j_v^0} exp\left(-\frac{e\eta}{kT}\right)}$$

where $\eta = \Delta\Phi_{SC} - \Delta\Phi_{SC}^0$ is the overpotential generated under irradiation. Consequently, the generation current (j_g) is given by Equations 1.70:

Eqn 1.70)
$$j_v = j_0 + eI_0\left[1 - \frac{exp(-\alpha d_{SC})}{1+\alpha L_p}\right] = j_0 + j_{ph}$$

where j_{ph} is the photocurrent density.

Typical parameters used to unambiguously compare the efficiency of a photoinduced process are photonic efficiency and quantum yield.

Photonic efficiency is defined as the ratio between the reacted molecules and the incident photons of a certain wavelength striking the system. While this parameter is relevant for engineering purposes, quantum yield is more powerful as it provides mechanistic insights.

Quantum yield is the ratio between the reacted molecules and the absorbed photons of a given wavelength. Evaluating this parameter in heterogeneous photocatalysis is challenging due to scattering phenomena, which complicate the measurement of absorbed radiation. Several methods have been proposed for this evaluation, utilizing numerical approaches or simplified experimental setups.

In the context of PEC systems, the incident photon-to-current efficiency (IPCE) is a typical parameter used to describe efficiency. IPCE represents the number of electrons in the circuit per incident photon at a given wavelength. It essentially constructs the action spectrum of the semiconductor in terms of photocurrent response per incident photon at each wavelength.

Practically, an external bias is applied to the semiconductor electrode in a three-electrode system, and the photocurrent is measured for each wavelength. Equation 1.71 is used to calculate the IPCE.

$Eqn\ 1.71)$ $$IPCE(\%) = \frac{I_{ph}\ h\ c}{\lambda\ \ P\ e} x100$$

where I_{ph} is the measured photocurrent, h is the Planck's constant, c is the speed of light, λ is the wavelength, P is the light power density, and e is the elementary charge.

Overall, PEC processes involve applying either an appropriate current (I) or a constant bias potential (E) while irradiating a semiconductor deposited or grown on an electrode. This method leverages the advantage of separating photo-generated electron-hole pairs (e^-/h^+) through a potential gradient [197,198].

Semiconductors can function as photoanodes (n-type semiconductors) for oxidation reactions or as photocathodes (p-type semiconductors) for reduction reactions [157,198]. Recently, PEC applications have expanded in areas such as the degradation of persistent organic pollutants, organic syntheses, CO_2 reduction, H_2 production, and inorganic ion reduction [199–201].

By adjusting experimental conditions—such as the type of photoelectrodes, the applied potential, light source and intensity, solution pH, and the type and concentration of supporting electrolyte—it is possible to fine-tune the degree of substrate conversion, selectivity towards target compounds, and their typology. Additionally, as mentioned before, depositing or growing the photocatalyst on a solid substrate eliminates the need for catalyst separation post-reaction.

To be effective, photoelectrodes must exhibit good mechanical, optical, electronic, catalytic, and electrochemical properties [202,203]. They need to maintain mechanical, chemical, and electrochemical stability under reaction conditions, ensure high mobility of photogenerated charges, and minimize recombination by reducing the diffusion path. For optimal performance, electrodes should have high catalytic activity for the desired oxidation or reduction reactions. Energetically, the conduction band (CB) and valence band (VB) edges of the semiconductors must align with the redox potentials of the involved species [204,205]. For water splitting, for example, the CB potential should be more negative than the reduction potential of the H^+/H_2 couple, and the VB potential more positive than the O_2/H_2O redox couple. Various semiconductors, including metal oxides, sulfides, metal chalcogenides, carbon, and metal nitrides, meet these requirements and are used to prepare photoelectrodes for different reactions. Among them, TiO_2 has been established as the most widely used photoanode [125,191,206–208] due to its high photocatalytic activity, excellent stability, scalability, low cost, and non-toxic nature [16,209–211]. Consequently, these electrodes can be used many times without being damaged, and the recovery of the catalyst from the reaction medium is very easy [207,212–214].

Finally, the applied potential is a crucial parameter that significantly impacts the performance of a PEC process. It controls the redox reactions occurring at the electrode surfaces, influencing both substrate conversion and product selectivity. Additionally, the applied potential helps manage the Fermi level in a semiconductor, enhancing charge separation and directly affecting the energy consumption and overall costs of the process.

For wide band gap materials (i.e., E_g > 2 eV), where the minority carrier concentration in the bulk is minimal, Equation 1.55 can be simplified by ignoring the diffusion term. In this case, when the product of the absorption coefficient and semiconductor thickness, αd_{SC}, is much less than 1 (indicating weak light absorption), and the product of the absorption coefficient and minority carrier diffusion length, αL_p, is much less than 1 (indicating short diffusion length for minority carriers), the photocurrent passing through the n-type semiconductor/electrolyte interface can be described by Equation 1.72.

$$I_{ph} = e\Phi_0 \alpha d_{SC}^0 \left(U_E - U_{FB} - \frac{K_B T}{e}\right)^{0.5} \quad Eqn.\ 1.72)$$

Consequently, the photocurrent is expected to have a quadratic dependence on the electrode potential. Measuring photocurrent as a function of U_E is referred to as a photocharacteristic and can be used to determine the flat band potential of the junction. Specifically, neglecting the k_BT/e term in Equation 1.72, a plot of $(I_{ph})^2$ versus U_E should intersect the potential axis at the flat band potential (U_{FB}), provided that the $\alpha d_{SC} << 1$ condition holds, regardless of the irradiating wavelength (λ).
It's important to note that these equations apply to the steady-state d.c. photocurrent, and they remain valid under chopped light conditions, as long as the measured signal is proportional to the steady-state chopped value [215].
According to Equation 1.72, the measured photocurrent is directly proportional to the light absorption coefficient. Near the optical absorption threshold of the semiconductor [216], the relationship tween the absorption coefficient and the optical band gap (E_g^{opt}) can be expressed as Equation 1.73

$$\alpha = A\frac{\left(h\nu - E_g^{opt}\right)^{n/2}}{h\nu} \quad Eqn.\ 1.73)$$

From this, the following expression can be derived (Equation 1.74):

$Eqn.\ 1.74)$ $$Q\ h\nu\ \propto \left(h\nu - E_g^{opt}\right)^{n/2}$$

where $Q = (I_{ph})/e\Phi_0$ is the photocurrent collection efficiency, and E_g^{opt} represents the optical threshold for the onset of photocurrent at the illuminated electrode. Based on Equation 1.74, at constant electrode potential, the optical band gap of the material can be determined from the dependence of I_{ph} on the wavelength of the incident light, maintaining a constant photon flux. This measurement is typically referred to as the photocurrent spectrum. The result is a plot of I_{ph} vs hν, and by plotting $(Qh\nu)^{2/n}$ versus hν (at constant electrode potential), the characteristic photon energy, that is E_g^{opt} can be extrapolated by determining where $(Qh\nu)^{2/n}$, in accordance with Equation 1.74.

For an ideal semiconductor/electrolyte junction, E_g^{opt} corresponds to the minimum energy gap between the filled states in the valence band (VB) and the empty states in the conduction band (CB), which is the band gap, E_g. Assuming a parabolic electronic density of states (DOS) distribution ($N(E) \propto E^{1/2}$) near the band edges, in the case of direct transitions, the value of n in Equation 1.74 is either 1 or 3, depending on whether the optical transitions involved are allowed or forbidden in the quantum mechanical sense [216]. In the case of indirect transitions, n is equal to 4. It is important to highlight that, in addition to determining the band gap, photocurrent spectra can also be used to identify optical transitions related to electron states localized within the material's band gap [217].

1.5. Thesis objectives and synopsis

This Ph.D. project aims to advance the application of photocatalysis and photoelectrocatalysis for biomass valorization and hydrogen production while addressing scalability, material sustainability, and efficiency improvements.

One of the primary objectives is to harness the photocatalytic properties of TiO_2 for biomass valorization and hydrogen production. We transitioned from small-scale batch experiments to a continuous, pilot-scale process, i.e., flow-through (PEC) system (Figure 1.17). Scaling up we enhanced the practical applicability of the technology, making it feasible for large-scale hydrogen production and biomass conversion.

Improving the PEC cell design to increase output gas pressure is another crucial objective. Higher gas pressures facilitate more efficient hydrogen collection and storage, making the system more practical for real-world applications. This involves optimizing electrode geometry, enhancing gas

separation, and using materials that can withstand higher pressures without compromising performance.

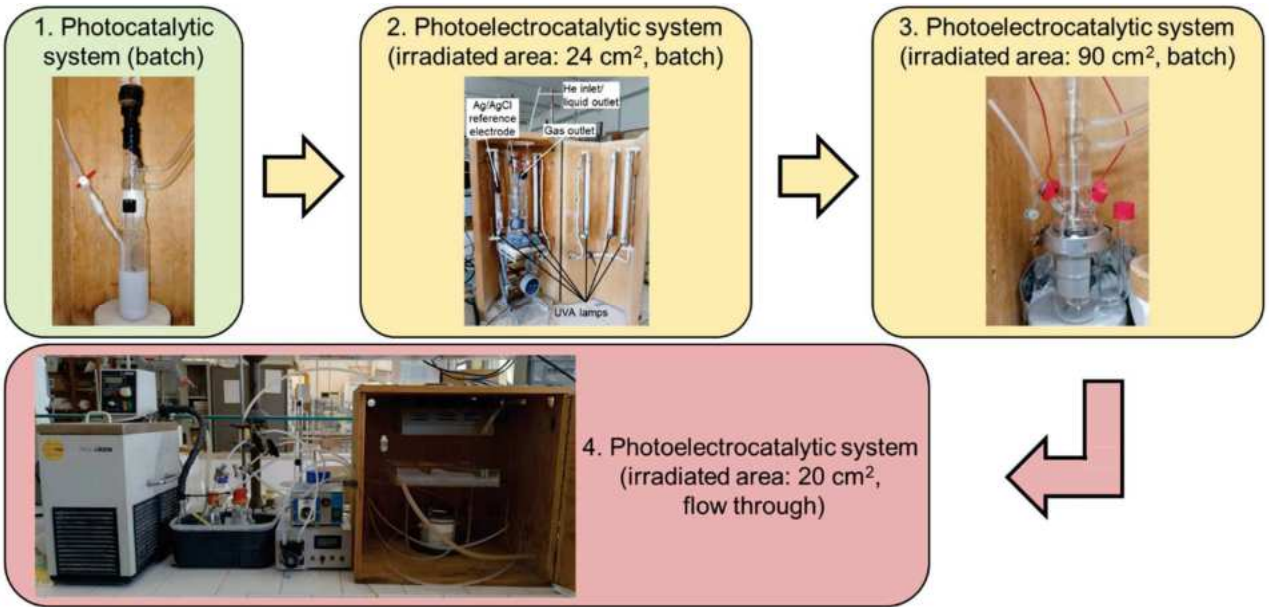

Figure 1.17. Experimental setups employed during the Ph.D. project.

The reliance on PGMs poses significant cost and supply challenges. Therefore, another objective is to develop and utilize PGM-free materials that offer comparable catalytic performance. Ensuring the stability and reusability of the materials used in the PEC system is crucial for long-term operation and economic viability. The objective is to identify and employ materials that are chemically and physically stable under operating conditions, allowing for repeated use after proper cleaning steps. This will enhance the durability and reduce the operational costs of the PEC system. Additionally, to improve PEC performance, mechanically and chemically stable TiO_2 nanotubes (NTs) photoanodes were modified with Cu_2O or Bi_2O_3 through electrodeposition. However, this approach did not yield satisfactory results. Furthermore, TiO_2's applications were extended beyond energy production and biomass oxidation, i.e., TiO_2-based photocatalysts were also employed to degrade organic pollutants. While TiO_2 is effective, alternative materials such as $ZnIn_2S_4$ and CuBiO-based materials were explored to address its limitations, such as its wide band gap requiring UV light for activation. These alternatives might offer advantages like narrower band gaps, allowing better utilization of visible light. The objective is to evaluate these materials for their photocatalytic efficiency and stability to potentially enhance the performance of PEC systems beyond what is achievable with TiO_2 [214,218]. Achieving these objectives will advance the field of photoelectrochemical systems, making significant strides in sustainable hydrogen production, biomass valorization, and environmental

remediation. By addressing scalability, material sustainability, and efficiency, this work aims to develop practical and economically viable solutions that contribute to sustainable and clean energy and chemical production.

The following steps outline the key activities undertaken to achieve the objectives of the PhD project:

a) A PGM-free photocatalyst for combined glycerol oxidation and hydrogen production was synthesized using a PC batch system (picture 1 of Figure 1.17). In this published work [219], Pt was successfully replaced with Cu_2O as a cocatalyst on commercial P25 (Aeroxide) TiO_2, which consists of a mixture of anatase/rutile polymorphs.

b) The same PC batch system was used to get insight into the effect of home-prepared TiO_2 polymorph on the HER, using Pt cocatalyst, with the glycerol oxidation reaction serving as a model reaction [220].

c) In this step, furfuryl alcohol (FuA), along with simultaneous HER was carried out in both a PC batch system and a PEC batch system using TiO_2 NTs photoanode with an irradiated area of 24 cm^2 (picture 2 of Figure 1.17) [16]. The results were compared, revealing that the PEC system showed better performance and enhanced photon-to-chemical conversion than the PC system.

d) The influence of operational conditions, such as pH and applied bias, on glycerol oxidation and H_2 production in the PEC system was deeply investigated to enhance the overall system performances [221].

e) The PEC system was successfully scaled up, achieving a photoanode irradiated area up to 90 cm^2 (picture 3 of Figure 1.17). This setup was employed for the simultaneous H_2 evolution and glycerol oxidation [155].

f) To improve FE toward HVA products, TiO_2 NTs photoanodes were successfully subjected to N-doping, producing holes in the valence band with suitable energy for the production of HVA by glycerol partial oxidation. Despite the improved FE toward HVA, the N-doped TiO_2 NTs showed lower photoactivity compared to the bare ones, as evidenced by a decrease in photocurrent and a slower reaction rate [222]. As a result, this approach was not pursued further. This work was carried out at Prof. Dr. Patrik Schmuki's group (Department of Materials Science of Friedrich Alexander University, Erlangen, Germany).

g) Bare TiO_2 NTs photoanodes with different features and 90 cm^2 of irradiated area were investigated in a PEC cell for the partial oxidation of glucose and fructose, alongside H_2 evolution, to examine the effect of pH and optimize HER and HVA production [223].

h) The photoelectrolysis of glycerol, glucose, and fructose, with simultaneous H_2 evolution, was explored using the continuous PEC cell in a flow-through configuration (picture 4 of Figure 1.17, article in preparation).

2. Experimental

Unless otherwise specified, the materials in all the work were characterized using the following techniques.

Analytical tecniques

XRD (X-ray diffraction) patterns were acquired by means of a PANalytical Empyrean diffractometer at room temperature. The PIXcel1D (tm) detector worked under a current of 40 mA and a voltage of 40 kV by using the CuKa emission tube. The 2h investigated scan range was set from 20 to 60° with a scan rate of 3°/min.

Raman spectra were recorded by a Raman Microscope coupled with a Leica DMLM microscope. The laser was focused on the sample by a 5x magnification lens in order to obtain an analyzing spot diameter around 50 microns, with a maximum power of 133mW on the sample. Only the 10% of maximum power was used in these measurements, the power was reduced by holographic filters, three for each sample, and the spectra recorded using a 532 nm laser coupled with a 2400 lines per millimeter grating resulting in a spectral resolution equal to 0.5 cm^{-1}. Each measurement consisted of two accumulations.

A Shimadzu UV-2401 PC spectrophotometer was utilized to record the Diffuse Reflection Spectra (DRS) in the 200–800 nm region at ambient conditions and by using $BaSO_4$ as a reference.

The specific surface areas (SSA) of the samples were evaluated by a Micromeritics Flow Sorb 2300 instrument by employing the single-point (Brunauer–Emmett–Teller) BET method.

The SEM (Scanning electron microscopy) images were taken by mean of a FEI Quanta 200 ESEM microscope operated at an accelerating voltage of 30 kV. The elementary composition of the samples was investigated by an electron microprobe used in an energy dispersive mode (EDX).

To follow the concentration of the species, aliquots of the reaction mixture were withdrawn at fixed times, filtered by using a 0.2 μm PTFE filter in the case of photocatalytic tests, and analyzed by an HPLC instrument (Thermo Scientific Dionex UltiMate 3000) equipped with a REZEK ROA Organic acid H^+ column. The eluent consisted of a 2.5 10^{-3} M H_2SO_4 solution with a flow rate of 0.6 mL min^{-1}.

CO_2 and H_2 accumulated in the head space gaseous phase were collected by a gas-tight syringe and quantified by a TCD (thermal conductivity detector) installed on a gas chromatograph HP 6890.

The compounds were separated by a packed 60/80 Supelco GC column and analyzed at 523 K.

The Equations 2.1 – 2.3 were used for the determination of X (conversion), S (selectivity) and Y (yeld):

$$Eqn.\,2.1) \qquad X\,(\%) = \frac{(Biomass)_i - (Biomass)_t}{(Biomass)_i} \times 100$$

$$Eqn.\,2.2) \qquad S\,(\%) = \frac{(P)_t}{(Biomass)_i - (Biomass)_t}$$

$$Eqn.\,2.3) \qquad Y\,(\%) = \frac{(P)_t}{(Biomass)_i}\ x\ 100$$

where: $(Biomass)_i$ and $(Biomass)_t$ indicate the initial molar concentration and molar concentration at time t of the biomass, respectively. $(P)_t$ is the molar concentration of the obtained products at time t.

For each product, in the case of PEC tests, the faradic efficiency (FE) was calculated through Equation 2.4:

$$Eqn.\,2.4) \qquad FE_i\,(\%) = \frac{(P)_t}{\frac{Q}{z\,F}}\ x\ 100$$

where:

- i is the product
- Q is the circulated charge (Coulomb)
- z are the electrons exchanged during the partial oxidation
- F is the Faraday constant of 96485 (Coulomb/mol)

Photoelectrochemical characterizations

The photoelectrochemical characterizations were carried out using a UV–vis Xenon lamp (power 450 W), whose light was sent to a monochromator in order to allow the irradiation of the sample surface by a selected wavelength through the quartz window of the cell. The electrode potential was controlled by a potentiostat and the measured current was sent to a two phase lock-in amplifier

to isolate the photocurrent from the overall current circulating in the cell. A mechanical chopper was used to stop the irradiation at a known frequency (namely 13 Hz). For the photoelectrochemical measurements. A Pt wire was used as counter electrode, and a silver/silver chloride (Ag/AgCl/sat. KCl) was employed as reference electrode (0 V vs Ag/AgCl = 0.197 V vs SHE).

Photocurrent transients were carried out within a three-electrode setup. A Pt wire was used as the counter electrode, while an Ag/AgCl/saturated KCl setup was the reference electrode. Current transients were recorded using monochromatic irradiation at different constant potentials. The photocurrent (I_{ph}) was quantified by manually stopping the irradiation while maintaining the applied potentials steady.

EIS measurements were carried employing a potentiostat featuring an Impedance Analyzer connected to the cell setup. The impedance spectra were obtained in a frequency range of 10 kHz to 0.1 Hz at 25 °C, using an AC amplitude of 10 mV. Before each measurement, the cell underwent a stabilization period of at least 15 minutes under irradiation. Subsequently, data analysis and fitting of the equivalent circuit were performed utilizing Power Suite and ZSimpleWin software.

3. A facile way to synthesize noble metal free TiO_2 based catalysts for glycerol photoreforming

In this published work [219], heterogeneous photocatalytic solar/UV light reforming of glycerol in aqueous media was performed with Pt-photodeposited and noble metal-free modified commercial TiO_2 (Aeroxide P25) photocatalysts prepared through ball milling, a very simple and cheap coupled catalysts preparation method (Figure 3.1). The photoactivity of the heterostructured samples obtained by coupling different amounts of Cu_2O or 3% CuO with TiO_2 was compared with that of Pt-TiO_2 (P25). During each run glycerol conversion, and 1,3-dihydroxyacetone (DHA) and glyceraldehyde (GA) formed in the liquid phase and H_2, and CO_2 formed in the gas phase, were measured. The results were confronted to verify the effectiveness of Cu_2O in replacing Pt. Using noble metal-free photocatalysts, 33% glycerol conversion, 10.3% and 5.4% selectivity towards DHA and GA, respectively, a CO_2 and H_2 concentration of 0.16 mM and 1.01 mM (corresponding to 0.17 mmol h^{-1} g^{-1}), respectively, were obtained. Ex situ photoelectrochemical characterization confirmed the formation of a heterostructure between TiO_2 and copper oxide and the effectiveness of Cu_2O towards H_2 formation.

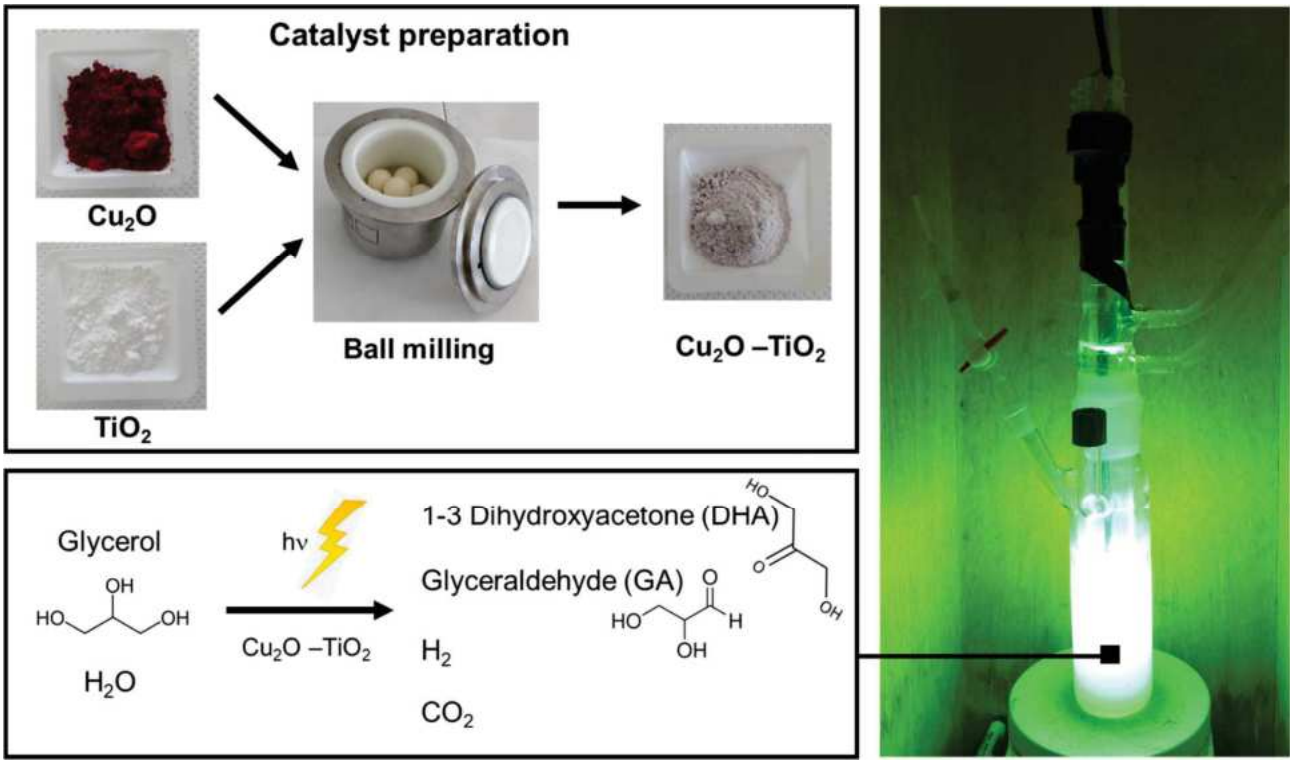

Figure 3.1. Schematic illustration of catalyst preparation and photocatalytic reactions.

3.1. Introduction

In this work, the valorization of glycerol, a biomass derivative obtained in large quantities as a waste product of the biodiesel production industry [3,224] was studied in a batch heterogeneous photocatalytic system. Notably, glycerol, compared to other biomass components, has gained great attention due to its ease of hydrogen formation [225]. Additionally, glycerol oxidation yields valuable compounds like 1-3 dihydroxyacetone (DHA) and glyceraldehyde (GA) [219], fundamental in industries such as cosmetics, pharmaceuticals, fine chemicals [53,135,219], and food production [226]. The price of DHA is ~US $150 per kg, whereas the prices of crude and refined glycerol are much lower (US $0.11 and US $0.66 per kg, respectively), making catalytic production of DHA from glycerol an economically attractive method [219,227].

Consequently, the production of DHA and GA from glycerol [227–229] represents an economically attractive option [51,52,55,134]. Traditional methods of producing DHA and GA from glycerol involve thermo-catalysis under harsh conditions, needing costly noble-metal catalysts (e.g., Pt, Au, Pd), and external oxidants like O_2 or H_2O_2 [228,230,231]. To minimize energy consumption, light-based approaches like photocatalysis (PC) have emerged, offering a sustainable pathway to oxidize organic compounds, generate valuable chemicals, and promote cathodic H_2 production

Regarding the photocatalysts studied for glycerol reforming, TiO_2 has aroused great interest as an anodic site for the oxidation of the substrate [232]. As cathodic site, responsible for H_2 evolution, a noble metal like platinum is often used [233–235] and today few cheap alternatives with activities comparable to noble metals are present in literature [236–240]. Mandari et al. synthesized CuO and $Cu_3(PO_4)_2$ clusters on the surface of titania particles as promising photo-catalyst for the production of high quantities of H_2 from glycerol-water solutions [241]. Gultom et al. obtained an H_2 production rate up to14800 μmol $g^{-1}h^{-1}$ using Ni-doped ZnO-ZnS in 50% ethanol-water mixture [242]. The use of Cu_2O is particularly useful because it presents different advantages such as low toxicity, cost, and band gap (2.0-2.2 eV) in addition to a conduction band energy suitable for H^+ reduction [243]. Notably, its coupling with TiO_2 is advantageous for H_2 production when a direct Z-scheme is formed [244] due to its redox ability [245]. In a direct Z-scheme system, two semiconductors are coupled displaying different reduction and oxidation potentials of the CB and VB. Under irradiation, the photogenerated electrons migrate from the CB of the semiconductor with the less negative edge potential to the VB of the semiconductor having the less positive potential [244]. In this way, electrons and holes are spatially separated on the semiconductor with a higher reduction potential and oxidation potential, respectively. In particular, by coupling TiO_2 with Cu_2O, the TiO_2 electrons recombine with

the Cu_2O holes making available more reducing electrons (those of Cu_2O) and more oxidizing holes (those of TiO_2).

The major drawback of Cu_2O is the instability of Cu^+ in the presence of humidity and light; one possible approach to improve its stability is to slow down the charge recombination by coupling it with other semiconductors [246–249]. Different papers explored the photocatalytic activity of Cu_xO-TiO_2 systems for photoreforming reactions in the presence of different sacrificial agents [246,248,250–257]. In some of them, glycerol was used as hole scavenger but, generally, only the H_2 production was quantified and the formation of the products of its partial oxidation was not considered. CuO/TiO_2 (10% w/w) samples obtained by physical mixing displayed the same activity as 1.5%Pt/TiO_2 towards the H_2 production from glycerol aqueous solutions under UV light irradiation [256]. Cyclic voltammetry analyses and Electron Paramagnetic Resonance measurements revealed the existence of Cu^{2+} and Cu species.

This study reports the results of anaerobic heterogeneous photocatalytic solar/UV light glycerol reforming in aqueous solution, using commercial TiO_2 loaded with platinum and/or coupled with copper oxide in order to verify the efficacy of Cu_2O in replacing Pt for the formation of H_2. The coupled samples were obtained by a simple and inexpensive ball grinding approach that allowed for the easy preparation of large quantities of catalyst, e.g., they can be used in pilot plant scale reactors [258]. The metal species amount was chosen by considering literature data [259–262].

In each experiment, the amount of hydrogen and CO_2 formed in the gas phase and that of DHA and GA in the liquid phase deriving from glycerol partial oxidation were monitored [263].

3.2. Experimental section

Samples preparation

P25 (TiO_2 P25 Degussa), $PtCl_4$ (BDH Chemicals) Cu_2O (Riedel-de Haën), CuO (Sigma Aldrich), glycerol (Sigma Aldrich), 1,3- dihydroxyacetone (Sigma Aldrich), glyceraldehyde (Sigma Aldrich), ammonium biborate tetrahydrate (ABE, $(NH_4)_2B4O_7 \cdot 4H_2O$; Sigma Aldrich), propylene carbonate (Sigma Aldrich), were used as received.

The photocatalysts were prepared in a simple way. 3% wt CuO, and 2% – 4% wt Cu_2O were obtained by mixing commercial CuO or Cu_2O with commercial TiO_2 P25 by a Retsch Ball Mills, type PM100, equipped with a chrome steel jar coated with zirconium oxide and filled with 6 zirconium oxide balls. For each preparation the solid components were mixed 2 hours, at 150 rpm, reversing the sense of the rotation after 1 hour and 10 minutes of pause. 0.5% wt of Pt was loaded on P25, Cu_2O and 3%Cu_2O TiO_2 by a photo deposition method as follows: 400 mL of H_2O, 2 g of photocatalyst, 50 mL

of ethanol, and 0.02 g of $PtCl_4$ were added to a 500 mL photoreactor. Nitrogen was bubbled for 30 minutes under dark to remove the oxygen and during the irradiation of the dispersion (about 7 h with UV light) which allowed the photo-deposition of Pt. Subsequently the dispersion was evaporated at approx. 353 K to obtain the solid photocatalysts.

Samples characterization

XRD, Raman, DRS, SSA, and SEM analyses were performed; further details are provided in the experimental section (Section 2).

Low-magnification TEM images were recorded by a Jeol JEM 1400 Plus microscope equipped with a LaB6 filament-source operating at 120 kV and GATAN Orius SC600 CCD camera. The sample was prepared by drop-casting 30 μL (1 drop) of the dispersion prepared by adding 5 milligrams of the catalyst into 1 ml water–ethanol 2:1 v/v mixture onto the carbon-coated copper grids.

The H_2-TPR (Temperature programmed reduction) measurements were carried out in a conventional flow apparatus with a TCD detector, using at heating rate of 10 °C/ min and a gas mixture of 5 vol% H_2 in Ar.

The photoluminescence (PL) spectra were determined using a JobinYvon instrument (Horiba) using an excitation k of 300 nm.

For the photoelectrochemical measurements P25, 3%CuO-P25 and 3%Cu_2O-P25 photocatalysts were drop casted on carbon paper support (Toray 40% wet Proofed-E-Tek) and immersed in 0.1 M ammonium pentaborate (ABE) aqueous solution (pH ~ 9) in a three-electrode configuration cell. A Pt wire was used as counter electrode, and a silver/silver chloride (Ag/AgCl/sat. KCl) was employed as reference electrode (0 V vs Ag/AgCl = 0.197 V vs SHE).

The EPR spectra for the investigated photocatalysts were collected at room temperature under dark or upon continuous in situ photoexcitation by UV light (maximum wavelength 365 nm; Bluepoint LED, Hönle UV Technology). An EMX EPR spectrometer purchased from Bruker was used for this purpose. The latter operates in X-band at 100 kHz field modulation in the standard TE102 (ER 4102 ST) rectangular cavity using EPR tubes made in quartz with thin walls (Bruker).

Photocatalytic tests

The photocatalytic activity of the used catalysts was studied in a 250 mL cylinder-shaped Pyrex reactor by using a 125 W medium pressure Hg lamp (main emission peak at ca. 365 nm) or a 150 W halogen lamp (simulating the solar spectrum) as irradiation sources. The catalysts were added to the glycerol solution and Helium was gurgled in the dispersion under stirring in the dark for the time

necessary for the substrate to reach saturation of the surface of the catalysts (0.5 h), then the reactor was closed, and the lamp switched on. The runs were carried out at ca. 303 K by circulating water in the reactor jacket with an initial glycerol concentration of 2 mM and 0.3 g/L of catalyst (determined by light absorption tests [264]). The tests were performed twice, and the results obtained differed by ca. 2%.

HPLC and GC were used to monitor the concentration of species in the reaction mixture and the gas phase, respectively. Further details are provided in the experimental section (Section 2).

3.3. Results and discussion

Figure 3.2 shows X-ray diffraction patterns of TiO_2 P25 (referred to simply as P25 in the following), 2% Cu_2O P25, 3% Cu_2O P25, 4% Cu_2O P25, 3% (Pt Cu_2O) P25, Pt-(3%Cu_2O P25) and 3% CuO P25. In the sample 3% (Pt Cu_2O) P25 the platinum was added by the photodeposition method described in the experimental section only to commercial Cu_2O and then mixed to P25 through balls milling, while in the sample Pt-(3%Cu_2O P25) it was added using the same method to 3% Cu_2O P25 previously prepared through balls milling.

Figure 3.2 a) and b) show, respectively, X-ray diffraction patterns within 2h range 20°–50° and 50°–90°, where the peaks relative to the two phases of TiO_2 anatase (A) and rutile (R), characteristic of the commercial P25, have been identified [265]. A close inspection of the $2\theta = 25.3°$ peak of anatase (Figure 3.2c) reveals a slight shift to lower angles for the sample Pt-(3%Cu_2O P25). For TiO_2 samples doped with metal species having an ionic radius similar to that of the Ti^{4+}, the shift was attributed to the reticular deformation resulting from the insertion of the metal ion in a substitutional position [266,267]. In our case, this shift can be due to the interaction of Pt with Cu^+ in accordance with Wang and Wang who observed some degree of photocorrosion of Cu_2O in the presence of Pt [268].

Magnifications of 2θ range between 35° and 40° are shown for all the samples in Figure 3.2d. Figure 3.2e shows X-ray diffraction patterns of P25 and 3% CuO P25. While P25 pattern shows peaks related to A and R TiO_2 phases, a small peak related to crystalline CuO can be identified in the 3% CuO P25 pattern, despite the low concentration of CuO in the mixture [269]. A similar behavior can be seen in Figure 3.2f where a small peak related to Cu_2O can be identified [270].

In Figure 3.3, the Raman spectra of modified samples and pure Cu_2O and CuO are reported. The characteristic bands of anatase at 144 cm^{-1}, 196 cm^{-1}, 397 cm^{-1}, 513 cm^{-1}, and 639 cm^{-1} are indicated [271]. No signals related to Cu_2O, CuO or Pt can be observed, due to their low amount and good dispersion on TiO_2 surface. The enlargement of main anatase band at 144 cm^{-1}, see inset, reveals a

little shift towards higher wave numbers for the samples 3% Cu_2O P25 and Pt-(3% Cu_2O P25) attributable to the interaction between the two oxides.

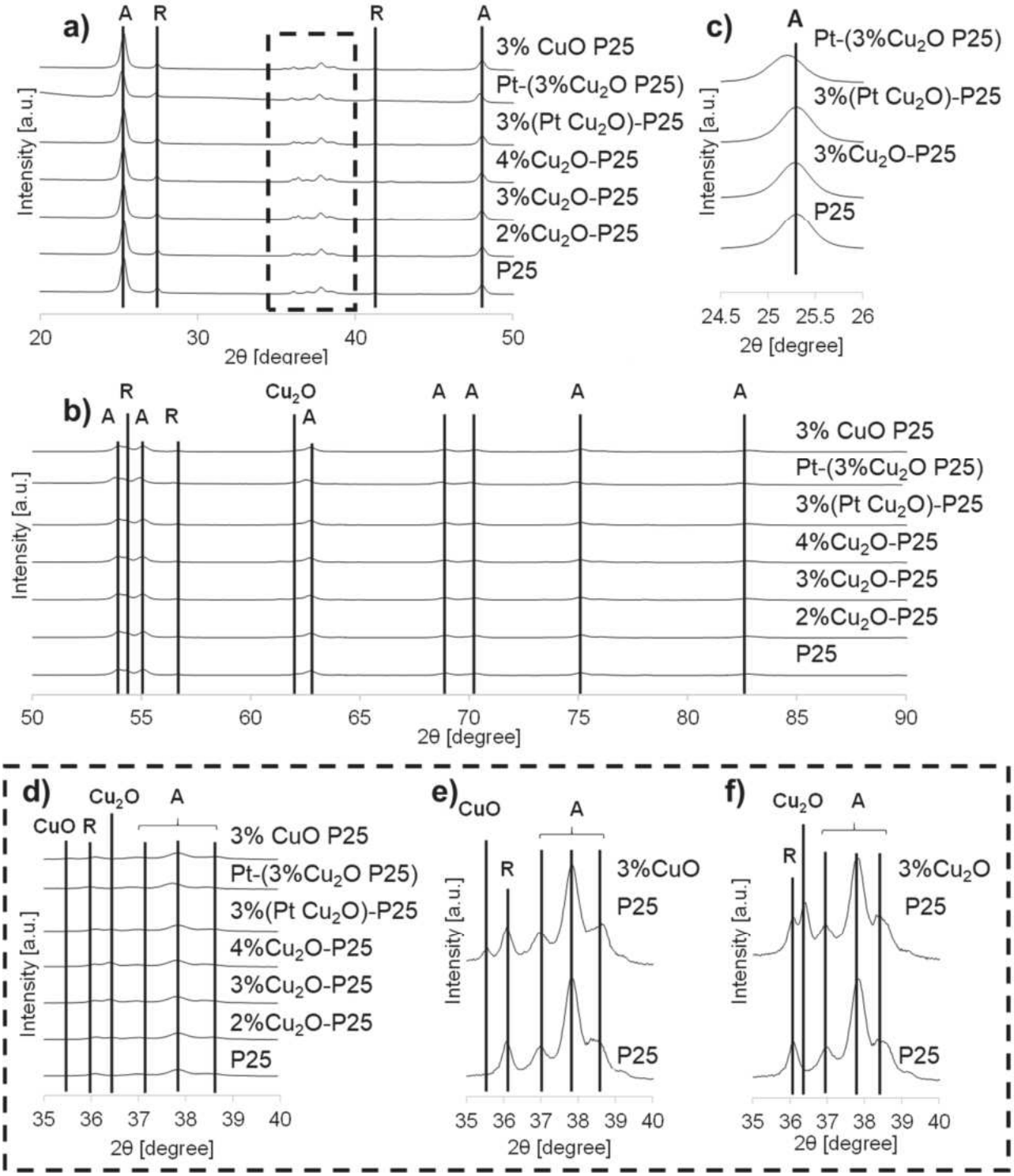

Figure 3.2. X-ray diffraction patterns of P25, 2% Cu_2O P25, 3% Cu_2O P25, 4% Cu_2O P25, 3% (Pt Cu_2O) P25, Pt-(3%Cu_2O P25) and 3% CuO P25 within 2h range of a) 20°-50°, b) 50°-90° and d) 35°-40°. Magnifications of P25, 3% Cu_2O P25, 3% (Pt Cu_2O) P25 and Pt-(3%Cu_2O P25) within 2h range of 24.5°-26° is shown in c), while P25 and 3% CuO P25 or 3% Cu_2O P25 within 2h range of 35°-40° are shown respectively in e) and f). The peaks A and R are related respectively to the anatase and rutile phase of TiO_2, CuO and Cu_2O to the respective copper oxide.

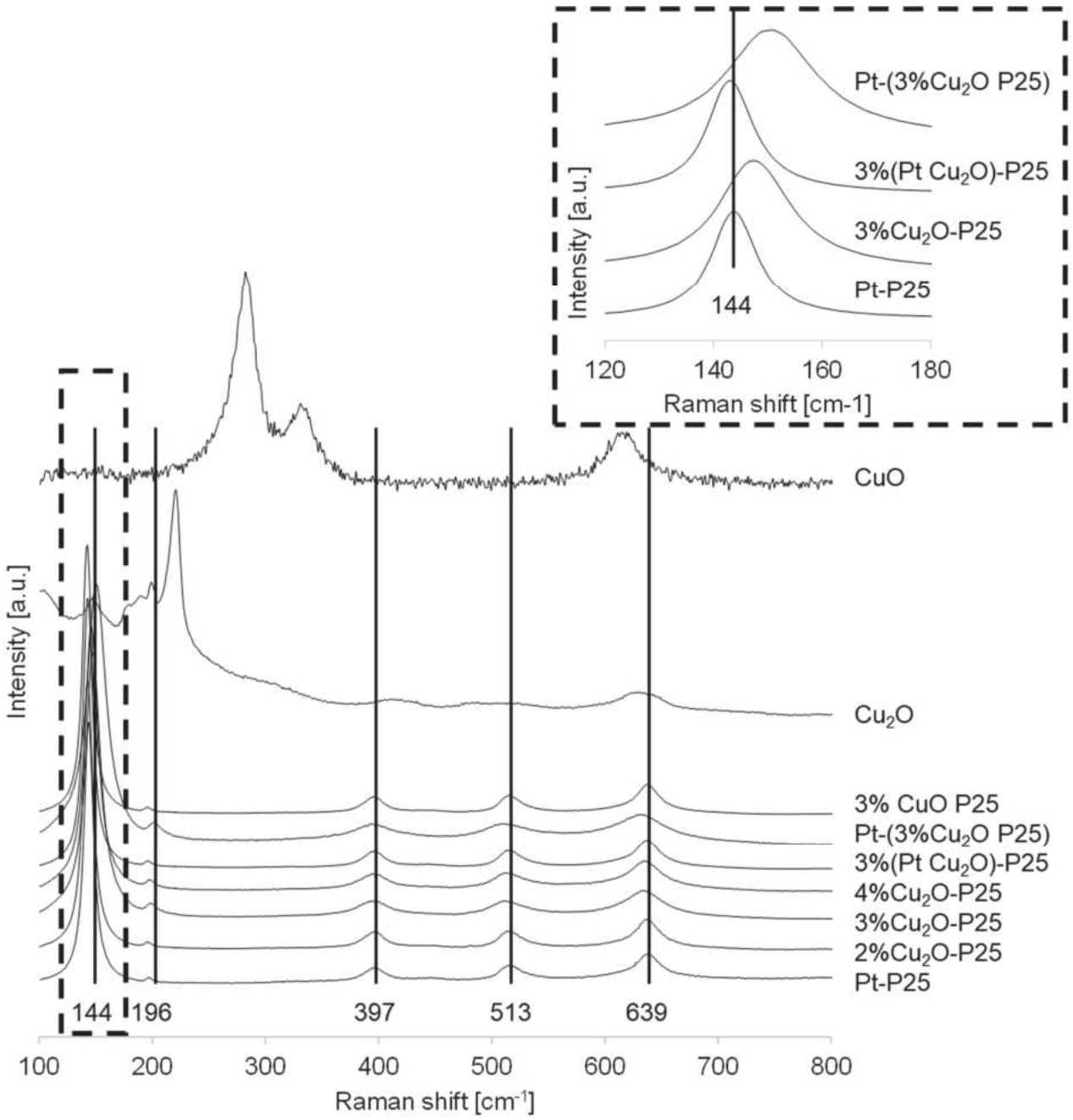

Figure 3.3. Raman spectra of tested samples and pure CuO and Cu_2O. Enlargement of main anatase band at 144 cm^{-1} is shown in the inset.

Figure 3.4 shows the diffuse reflectance spectra of all of the investigated powders. The commercial P25 shows an onset in absorption at ca. 360 nm corresponding to the typical band-gap of anatase, since rutile is in smaller quantities than anatase.

In the samples 2%-4% Cu_2O P25 can be noticed a small shift in the absorption to higher wavelengths, < 610 nm, and the shift is higher for 3% Cu_2O P25 and 4% Cu_2O P25. In the samples containing Pt a decrease in the reflectance can be noticed without any change in the absorption edges.

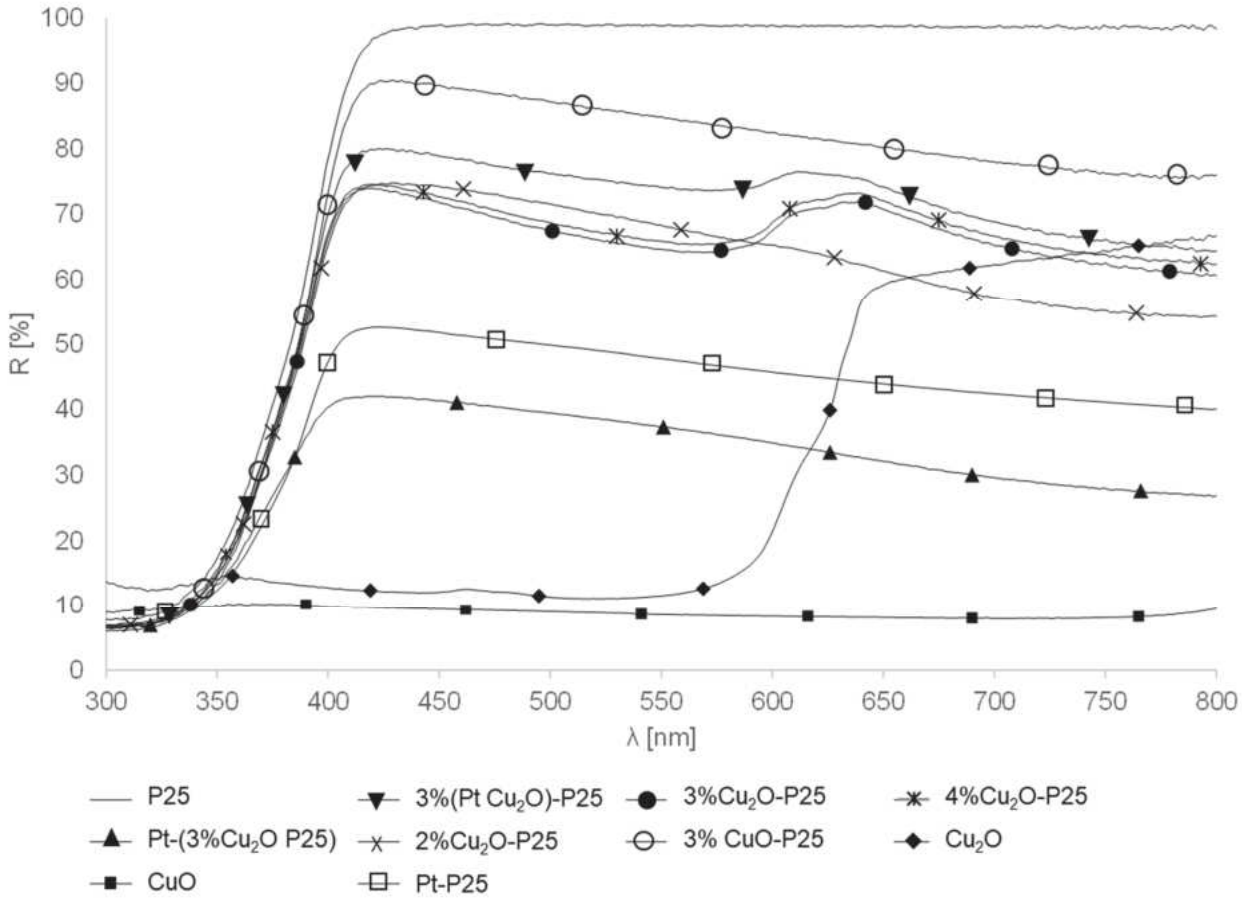

Figure 3.4. DRS spectra of the various samples

From the reflectance data the band gap values (E_g) were calculated by drawing the tangent lines to the graph of the modified Kubelka-Munk function, $[F(R'_\infty)h\nu]^{1/2}$, versus the energy of the exciting light. The obtained values are reported in Table 3.1. Commercial P25 displays a band-gap value of 3.14 eV typical of the anatase–rutile mixture; the deposition of Pt does not modify the value but increases the absorption in the visible region (Figure 3.4). The band gap of commercial Cu_2O is 1.99 eV, in accordance with the literature [272,273] whilst it was not possible to measure the value for CuO due to the high absorption over all the measured wavelengths range (Figure 3.4). The composites samples containing Cu_2O present two absorption edges corresponding to the two oxides (at ca. 3.10 eV for TiO_2 and ca. 2.00 eV for Cu_2O) that confirm the formation of a heterostructure [264,274]. In

samples with the presence also of Pt or CuO, it is possible to calculate only the band bap corresponding to TiO_2 in accordance with the reflectance spectra reported in Figure 3.4.

Table 3.1. Band-gap (E_g) and Specific Surface Area (S.S.A.) values of the different samples

Sample	**E_g (eV)**	**S.S.A. ($m^2\ g^{-1}$)**
P25	3.14	50
Pt-P25	3.12	48
Cu_2O	1.99	1
2% Cu_2O P25	3.08 2.02	51
3% Cu_2O P25	3.10 2.00	48
4% Cu_2O P25	3.09 2.00	48
Pt-(3% Cu_2O P25)	3.20	48
3% (Pt Cu_2O) P25	3.06	47

Figures 3.5a-c show the SEM image of Pt-P25 (Figure 3.5a), in which Pt was deposited on the as received commercial catalyst, and the composite samples obtained by ball milling (Figure 3.5b and c). All the samples are formed by aggregates of irregular spherical small particles, lower than 500 nm, confirming the high surface area of the powders. No substantial variations are observed when comparing Figures 3.5a and b indicating that the ball milling treatment did not induce any aggregation of particles, probably due to the mild experimental conditions (rotation speed = 150 rpm). Furthermore, the Cu_2O particles are not distinguishable, confirming their high degree of dispersion within the TiO_2 mass.

By the EDX analysis, the presence of Cu and Pt was verified, and their quantities are very similar to the nominal values, confirming the effectiveness of both balls milling and the photodeposition. Measurements carried out at different points gave approximately the same values highlighting the homogeneous distribution of the foreign species in the host material. Also, TEM images revealed a high homogeneity of the 3%Cu_2O P25 sample (Figure 3.5d) due to the low amount of Cu_2O with respect to TiO_2. HRTEM analyses performed in similar samples confirmed the formation of a heterojunction between TiO_2 and Cu_2O [240].

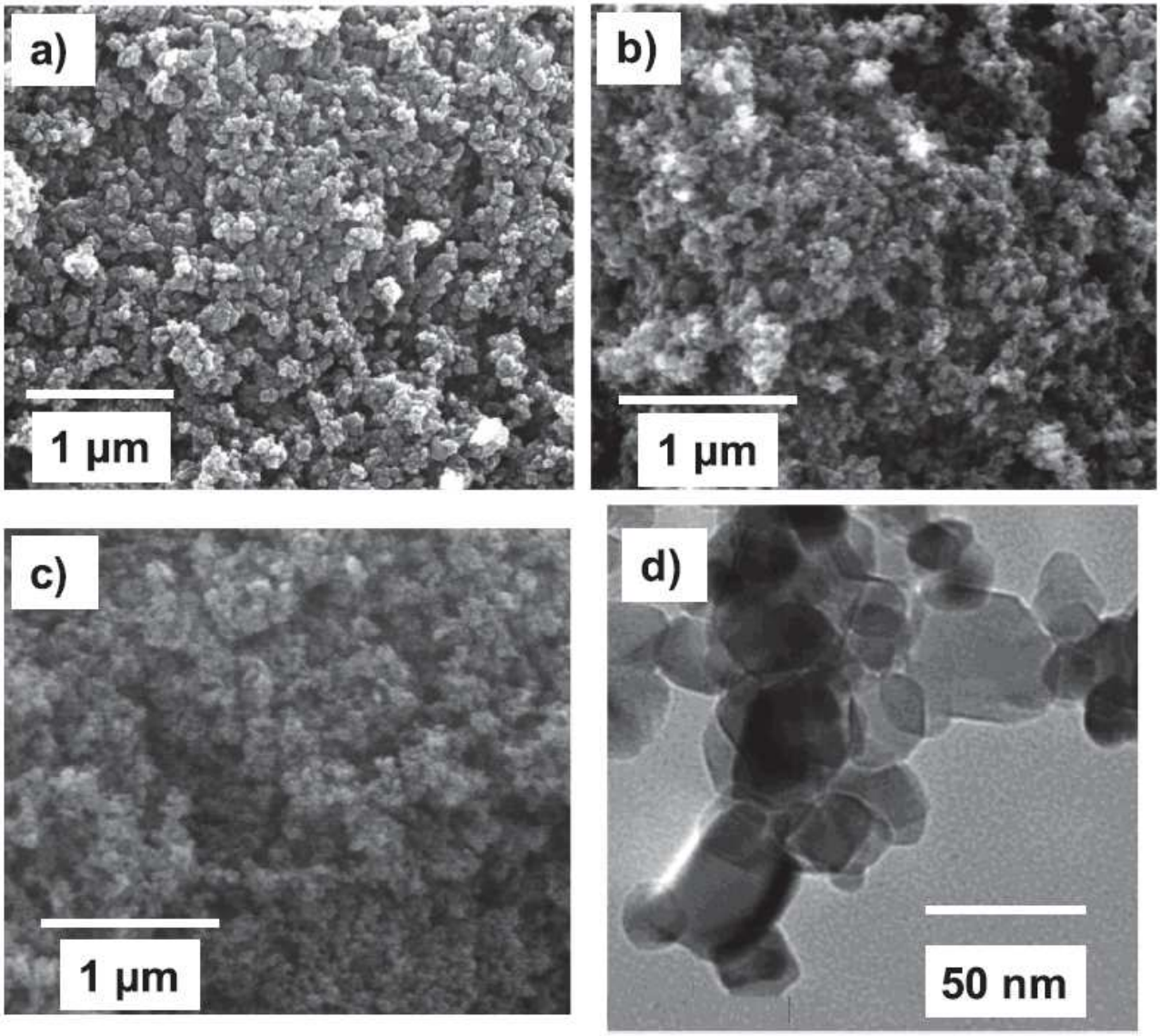

Figure 3.5. SEM images of a) Pt-P25 (without ball milling treatment), b) 3% Cu_2O P25, c) Pt-(3%Cu_2O P25). d) TEM image of the sample 3% Cu_2O P25.

To evaluate the reducibility of copper species, H_2-TPR profiles of bare TiO_2 and 3%Cu_2O P25 samples were collected in the 30–550 °C temperature range (Figure 3.6). In accordance with the literature, the profile obtained for bare TiO_2 does not show any H_2 consumption and reduction peaks in the investigated temperature range, the reduction of TiO_2 P25 indeed starts at a temperature higher than 600 °C [210,275].

The 3%Cu_2O TiO_2 sample shows, instead, a reduction peak displaying a maximum in the range 190–210 °C and a shoulder at lower temperature (around 180–190 °C). According to the literature [276] the two peaks here observed can be attributed to the reduction of Cu^+ to metallic copper occurring in a single step, the shoulder at lower temperature can be attributed to the smaller Cu_2O particles that

are more readily reduced due to their high dispersion on the support with respect to the bigger ones [277].

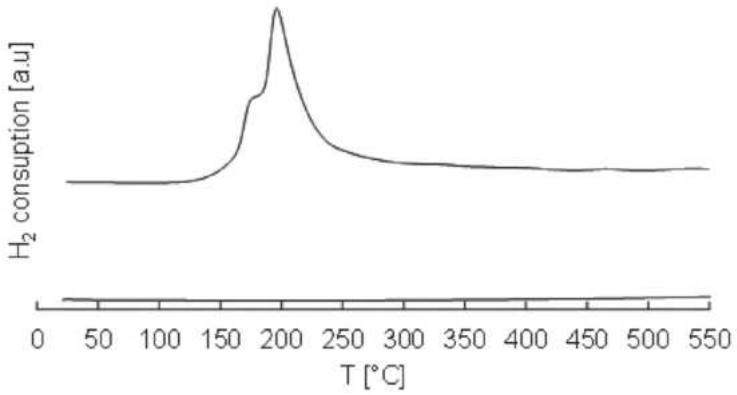

Figure 3.6. TPR profile of bare P25 and 3%Cu_2O P25 samples.

In order to have information on the effect of copper species on the electronic transitions, photoluminescence studies have been performed. PL spectra (Figure 3.7) revealed a decrease in the intensity in the presence of metal species with respect to bare TiO_2 that can be attributed to a lower recombination rate of the photoproduced charges [254,278].

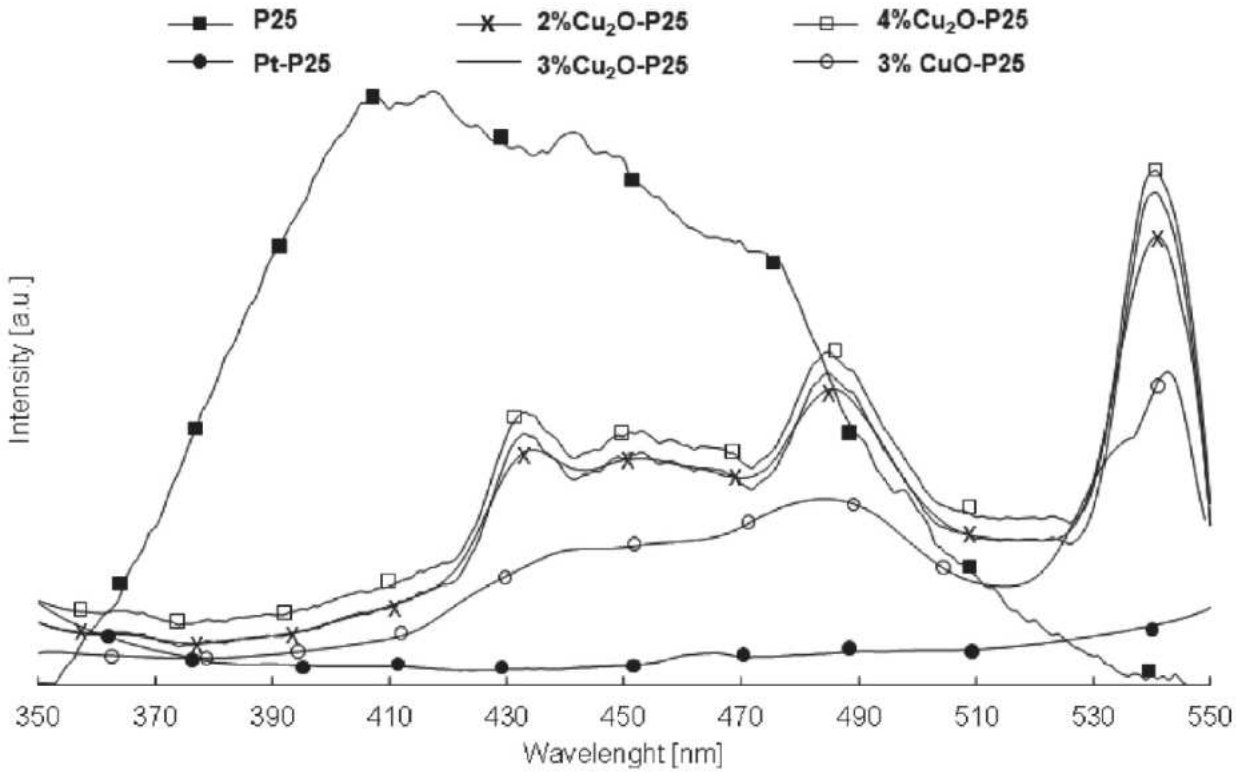

Figure 3.7. Photoluminescence spectra of various samples

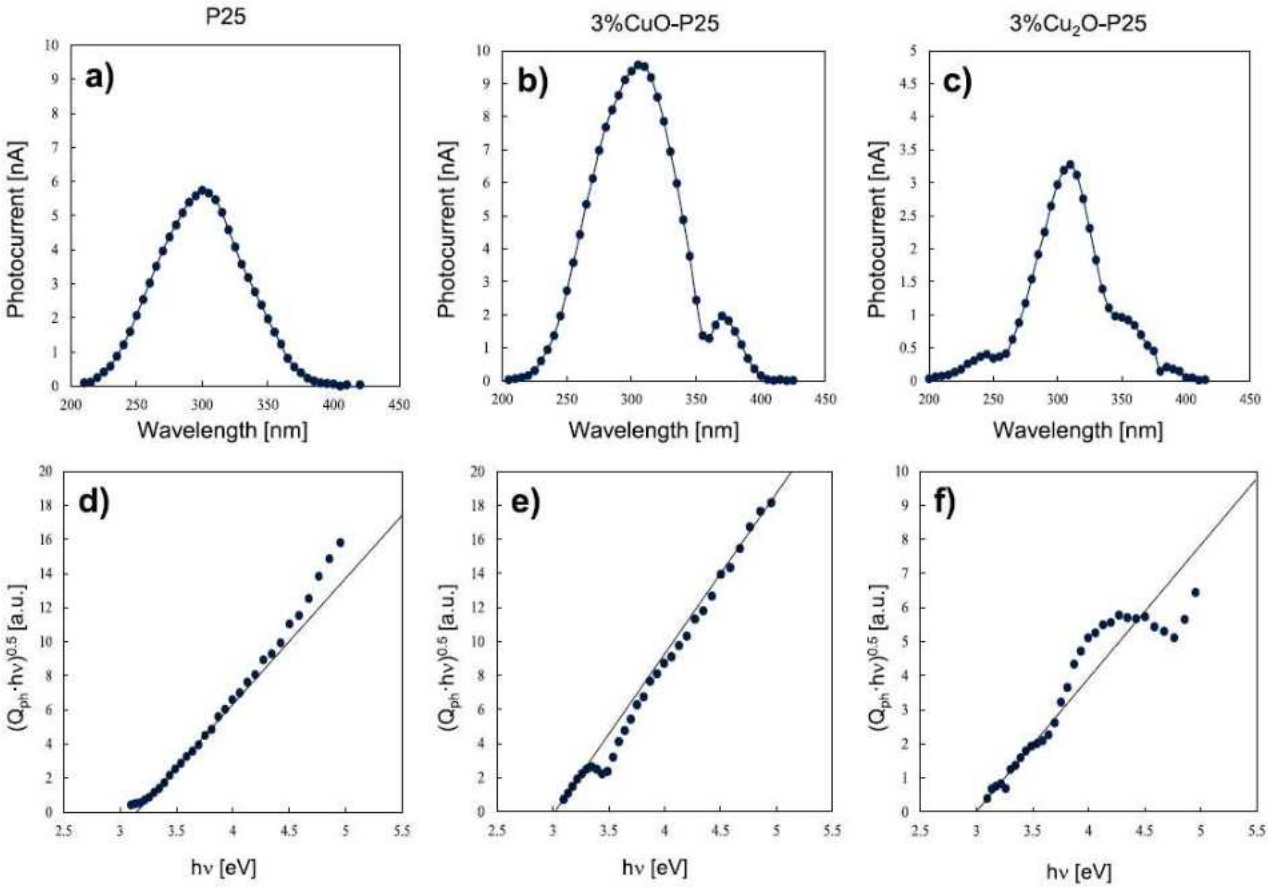

Figure 3.8. Photocurrent spectra for a) P25, b) 3%CuO-P25, c) 3%Cu_2O-P25, recorded in ABE 0.1 M solution (pH ~ 8) at UE ~ 0 V vs Ag/AgCl. d) e) and f) show the respective $(Q_{ph} \cdot h\nu)^{0.5}$ vs hν plots.

P25 exhibits various emission features: the peak at ca. 400 nm is due to the band-to-band emission, the signals in the range 410– 480 nm are attributed to a non-radiative recombination of the excited electrons towards defect levels [254,279]. The Pt loading reduces the intensities of all of the TiO_2 bands due to the electron transfer from TiO_2 to Pt [279]; the presence of Cu species also causes a shift of the peaks towards lower energies enhancing the absorption in the visible range. The band at ca. 440 nm is related to band-to-band emission of Cu_2O.

Photoelectrochemical measurements were carried out with the aim to study the influence of copper oxide addition on the electronic properties of the photocatalysts. The photocurrent spectra recorded in 0.1 M ABE at the open circuit potential (UE ~ 0 V vs Ag/AgCl) are reported in Figure 3.8. Notably, for 3%Cu_2O P25 and 3% CuO P25, in the wavelength range between 350 nm and 400 nm a second photocurrent maximum is present indicating the presence of two electronic transitions. Under the hypothesis of nondirect optical transitions, the optical band gap (E_g) values of the investigated catalysts can be determined according to the following Equation 3.1:

Eqn. 3.1) $$\left(Q_{ph} \cdot h\nu\right)^{0.5} \propto \left(h\nu - E_g\right)$$

where hν is the photon energy and Q_{ph} is the photocurrent yield. The latter is defined as the measured photocurrent corrected for the efficiency of the lamp monochromator system, which in turn is proportional to the light absorption coefficient for hν values near the band gap. As disclosed in Figures 3.8d – f the optical band gaps of all the photocatalysts are estimated by extrapolating to zero the $(Q_{ph} \cdot h\nu)^{0.5}$ vs hν plots. For P25 E_g of 3.15 eV was determined, while for 3%Cu_2O P25 and 3%CuO P25 a slightly lower band gap of 3.0 eV was estimated that can be attributed to the presence of copper oxide particles. Indeed, photocurrent at photon energy lower than the band gap of P25 is explained by optical transitions inside the Cu_2O and CuO whose band gaps are lower than that reported for TiO_2 polymorphs [250] in agreement with the experimental findings obtained by DRS.

Figure 3.9 shows the effect of light irradiation on the Open Circuit Potential (OCP) measured for P25, 3%Cu_2O P25 and 3%CuO P25 in the same solution. Soon after irradiation OCP shifts towards the negative direction for P25, as expected for n-type semiconductor.

The n-type semiconductor behaviour is also confirmed by the transient current recorded by manually stopping irradiation on the sample (see Figure 3.9d), showing the presence of an anodic photocurrent. Similar results were found for 3%CuO P25 suggesting that the presence of Cu(II) oxide does not influence the n-type character of P25 (see Figure 3.9). Conversely, a less negative photopotential is measured for 3%Cu_2O P25 that can be explained by the opposite effect of light irradiation on n-type P25 (negative shift) and p-type Cu_2O (positive shift) (see Figure 3.9c and f). Indeed, irradiation enhances the concentration of minority charge carriers, i.e.: holes in TiO_2 and electrons in Cu_2O. The holes are transferred from TiO_2 to Cu_2O by the electric field due to the built-in potential at the interface between the two oxides, while electrons are transferred from Cu_2O to TiO_2, reducing the measured photopotential. The formation of this kind of heterostructure is also confirmed by the transient photocurrent of Figure 3.9f showing a cathodic photocurrent spike followed by a stationary anodic photocurrent for 3%Cu_2O P25 sample. After irradiation electrons of Cu_2O conduction bands give a cathodic photocurrent but the built-in potential in the interfacial region drives electrons toward current collector, while holes are driven toward the oxide/electrolyte interface generating an anodic photocurrent. Moreover, these experimental results confirm that TiO_2/Cu_2O and TiO_2/CuO junctions are stable in aqueous solution.

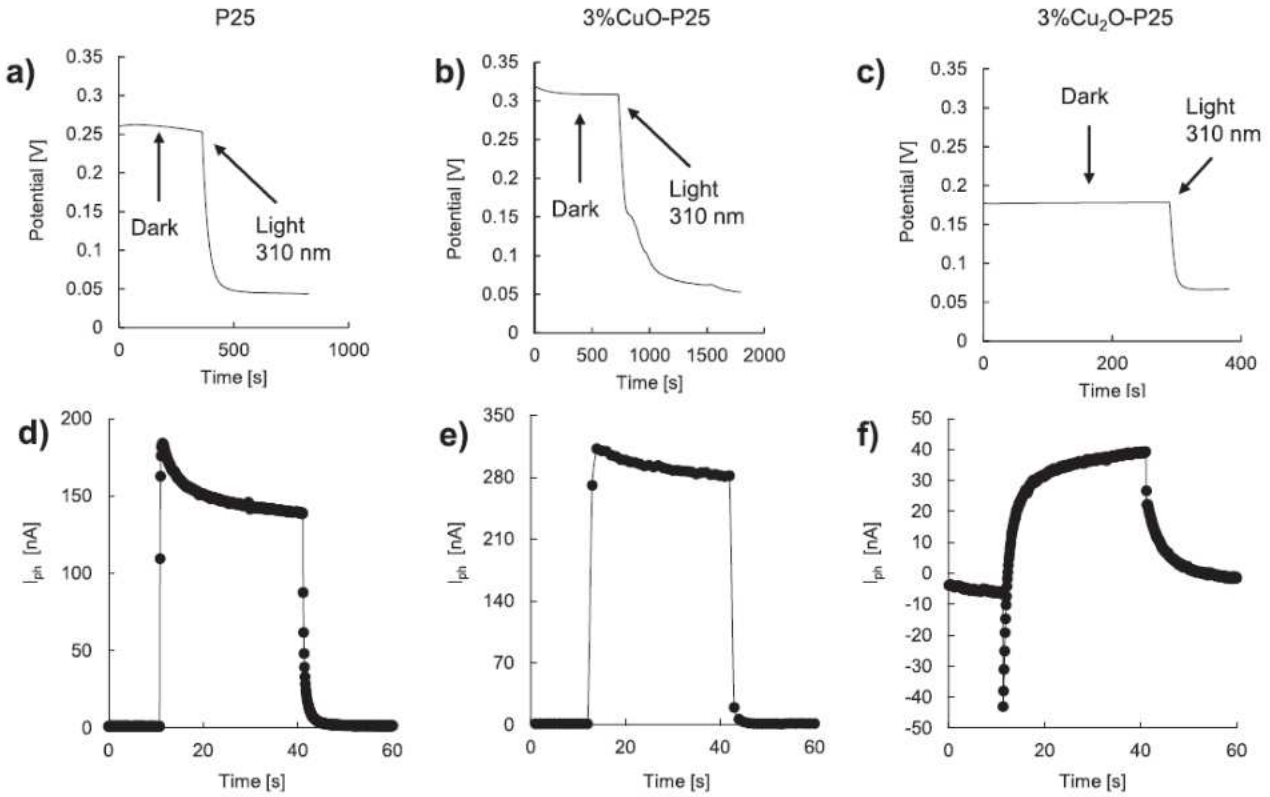

Figure 3.9. Photopotential recorded under dark and at 310 nm for a) P25, b) 3%CuO-P25, c) 3%Cu_2O-P25, recorded in ABE 0.1 M solution (pH ~ 8) . d) e) and f) show the respective current–time transients recorded at dark potential and 310 nm at UE ~ 0 V vs Ag/AgCl.

In Table 3.2 the results of the photocatalytic runs are reported in terms of conversion of glycerol, amount of CO_2 and H_2 and selectivity towards the main oxidation products. All the runs were carried out at pH ~ 7 (the natural pH obtained by adding the catalysts to the glycerol aqueous solution). As far as the Pt-P25 is concerned, the natural pH (pH = 3.5) was adjusted to 7 by a solution of NaOH.

The main glycerol partial oxidation products identified in the aqueous phase were 1,3-dihydroxyacetone and glyceraldehyde whilst CO_2 and H_2 were measured in the gas phase.

In the presence of bare P25 no hydrogen formation was observed, then two different strategies have been used: the photodeposition of Pt, as it is the most active metal towards H_2 formation, and the coupling with Cu_2O, with the aim to replace the noble metal with a less expensive and dangerous species. Pt-P25 was effective in the oxidation of glycerol with a conversion of 40.6% after 5 h of irradiation and DHA selectivity of 11.4%, and no GA was formed in the liquid phase. The maximum H_2 amount was 0.99 mM with an average production rate of 0.17 mmol h^{-1} g^{-1}. By considering the coupled systems, first the effect of the weight ratio between Cu_2O and P25 was studied. All the samples showed both a good oxidant activity and H_2 formation capability demonstrating that Cu_2O

is an excellent substitute for Pt. By increasing the amount of Cu_2O from 2 to 4%, the activity first increased and then decreased, being 3% Cu_2O P25 the best sample. In the presence of this photocatalyst, approximately, the same amounts of CO_2 and H_2 as those obtained with Pt-P25 were produced with a glycerol conversion of ca. 33%. In the presence of Cu_2O also GA was formed due probably to the different surface properties with respect to pristine P25. With the aim to increase the catalysts performance and investigate the role of cuprous oxide, other samples were studied. By coupling P25 with 3%Pt-Cu_2O a decrease in the photoactivity with respect to 3% Cu_2O P25 was observed probably due to the Cu^+ photocorrosion under irradiation when in close contact with Pt [268].

Table 3.2. Results obtained after 5 h of UV irradiation. χ = glycerol conversion, S = selectivity. DHA = 1,3-dihydroxyacetone, GA = glyceraldehyde. * indicates test carried out without glycerol

Sample	χ (%)	S_{DHA} (%)	S_{GA} (%)	CO_2 (mM)	H_2 (mM)	H_2 (mmol h^{-1} g^{-1})
Pt-P25	40.6	11.4	-	0.15	0.99	0.17
2% Cu_2O P25	22.3	9.55	13.5	0.08	0.35	0.06
3% Cu_2O P25	32.9	10.3	5.4	0.16	1.01	0.17
4% Cu_2O P25	21.3	9.94	11.2	0.08	0.45	0.07
3% (Pt Cu_2O) P25	27.5	8.23	7.9	0.10	0.58	0.09
Pt-(3% Cu_2O P25)	35.2	9.19	7.9	0.19	1.10	0.18
3% CuO P25	11.5	16.1	11.2	0.05	0.33	0.05
3% Cu_2O P25*	-	-	-	-	0.04	0.007

In the presence of the sample obtained after photodeposition of Pt onto the 3% Cu_2O P25 composite, the same photoactivity of this latter was obtained confirming that Pt Cu_2O plays the same role as Pt. On the contrary, by coupling CuO with P25 (3% CuO P25), a significant decrease in activity was obtained compared to 3% Cu_2O P25. This finding is ascribable to the position of the edge of the conduction band of CuO which, being less negative than that of TiO_2, is energetically less favourable than that of Cu_2O towards the production of H_2.

The conduction band edge of CuO is, in fact, very near to the H^+/H_2 reduction potential [280,281]. On the contrary, the conduction band edge of Cu_2O is more negative than that of TiO_2 so that the photogenerated electrons are more effective to reduce H^+ to H_2 [248,252,282].

Figure 3.10a shows the concentration vs time of glycerol and its products for the run carried out in the presence of the sample 3% Cu_2O P25. During the reaction time glycerol decreased and CO_2 increased, while DHA, GA and H_2 reached asymptotic values.

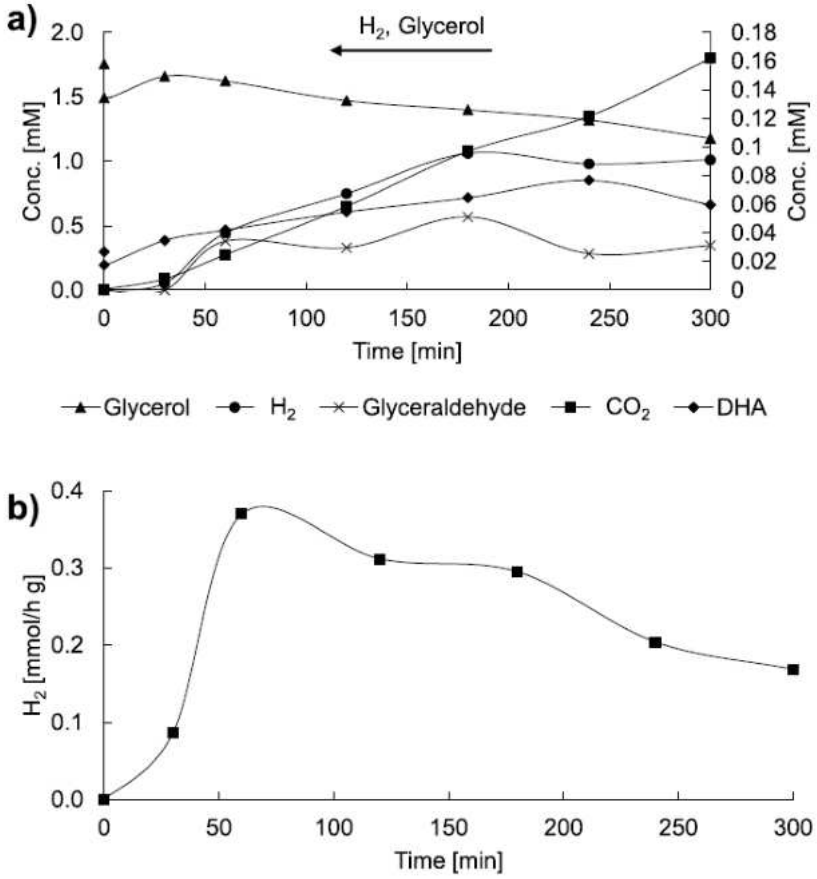

Figure 3.10. a) concentration vs time and b) H_2 production versus reaction time with the samples 3% Cu_2O P25.

In Figure 3.10b plot of H_2 production versus reaction time shows a peak of 0.37 mmol h^{-1} g^{-1} after one hour and a decrease to 0.17 mmol h^{-1} g^{-1} after five hours of reaction time because of the asymptotic H_2 concentration and the increasing reaction time. This can be probably due to the contemporary formation of little amount of O_2 deriving from water splitting. The competition of oxygen with H^+ for electrons and the occurrence of the back reaction between H_2 and O_2 decrease the H_2 evolution rate [283]. To verify the stability of the 3% Cu_2O P25 photocatalyst, it was recovered from the reaction mixture at the end of the run and reused. A good photostability was observed, but a decrease of ca. 10% in the H_2 formation was noticed, ascribable to reduction of a little percentage of Cu^+ into metallic copper [284]. It is reported that when copper was originally present as CuO, photogenerated electrons reduced a fraction of Cu^{2+} to Cu^+ [253], successively also a further reduction of some Cu^+ ions to Cu^0 is possible, whilst when Cu^+ is initial present, in a reducing environment it

can form metallic copper. It has been observed that the presence of little amounts of metallic copper present on the surface deriving from the reduction of Cu^+, can have a beneficial effect by further improving the charges separation [254,285].

A run was performed with the 3% Cu_2O P25 sample in pure water. A low quantity of H_2 was obtained by water splitting, confirming the positive effect of a sacrificial agent on the production of H_2 with the further advantage of using the holes for the formation of valuable compounds deriving from the partial oxidation of glycerol. No hydrogen was obtained by using Pt P25 under the same experimental conditions.

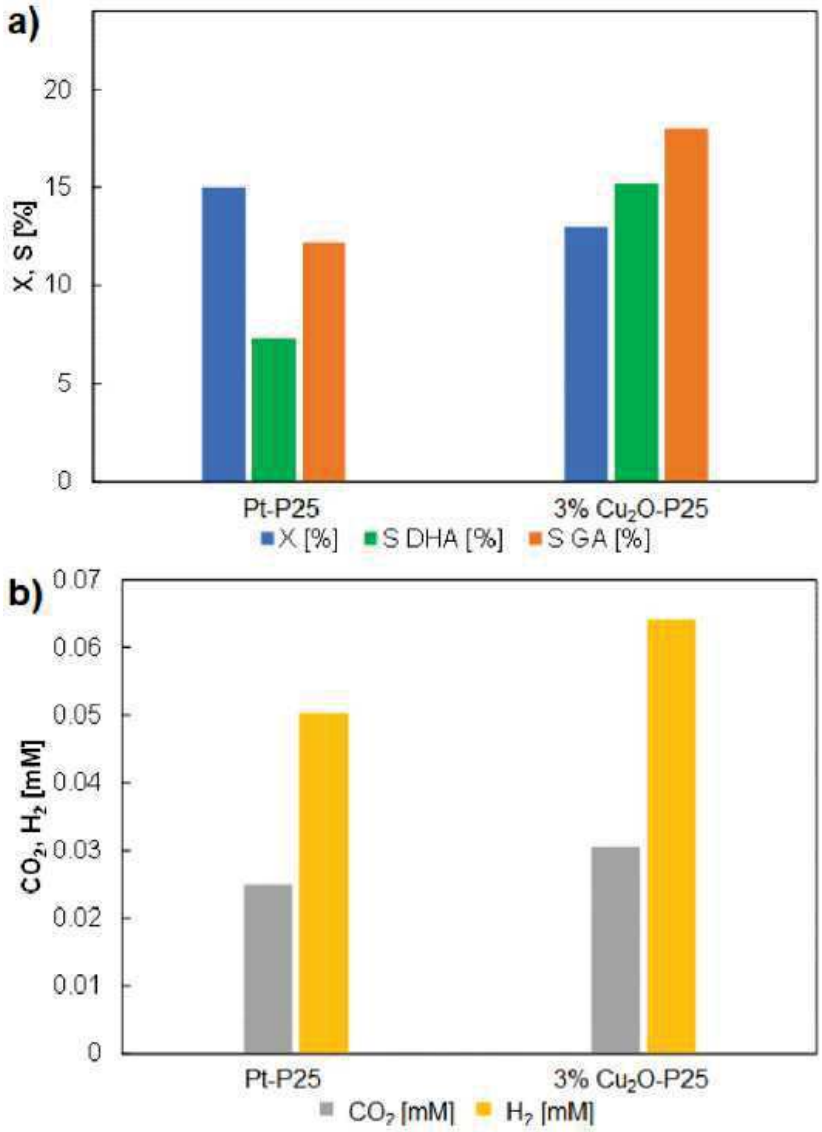

Figure 3.11. Values of a) conversion (X), selectivity towards 1–3 dihydroxyacetone (S_{DHA}), selectivity towards glyceraldehyde (S_{GA}) and b) CO_2 and H_2 concentrations during runs carried out in the presence of Pt-P25 and 3% Cu_2O-P25 under simulated solar light irradiation (150 W halogen lamp).

The photoactivity of the Pt P25 and 3% Cu_2O P25 samples was compared also under simulated solar light irradiation (Figure 3.11). Even in this case cuprous oxide had a beneficial effect both towards the partial oxidation compounds and H_2 formation. Notably, in the presence of Cu_2O, even if the glycerol conversion was slightly lower under solar irradiation, the selectivity values and the quantities of CO_2 and hydrogen formed were higher than those obtained with Pt. This finding is interesting in the view of utilization of these catalysts in a pilot plant reactor under direct solar light irradiation.
By coupling Cu_2O with TiO_2 a p-n heterojunction is generally formed. Under UV light irradiation both oxides are excited and, by considering the bands edge position (Figure 3.12) [248,249,252], electrons are transferred from the conduction band of Cu_2O to that of TiO_2 and holes from the valence band of TiO_2 to that of Cu_2O, enhancing the charges separation and increasing their lifetime (Figure 3.12 blue path). For this system also the formation of a direct Z-scheme has been reported [252,286,287] (Figure 3.12 green path). After irradiation, the TiO_2 conduction band's electrons recombine with the Cu_2O valence band's holes and electrons with high reduction ability and holes with high oxidation power are available. The negative potential value of the Cu_2O conduction band edge could explain the high activity of Cu_2O P25 samples with respect both to Pt-P25 and CuO P25. Indeed, the CB edge of CuO is not favourable for proton reduction. Moreover, the Z-scheme mechanism avoids the photocorrosion of Cu_2O [245].

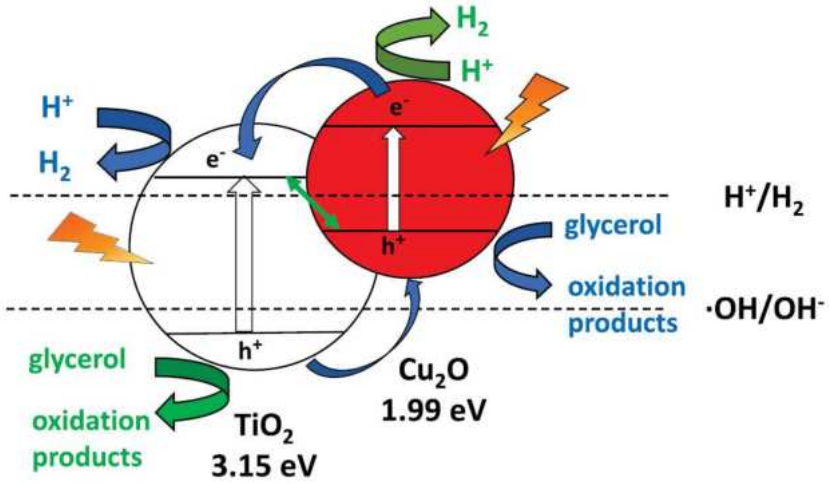

Figure 3.12. Energetic levels and possible charges transfer mechanism.

In Table 3.3 a comparison between the performance of some Cu_xO/TiO_2 (considering all the Cu species) systems towards H_2 production from glycerol aqueous solution is reported. In many cases the samples were prepared by method more complicated than ball milling and only the amount of H_2 was followed. In our case, although the photocatalysts are not very active, the identification and

quantification of valuable coproducts was accomplished. The aim was to explore the possibility to prepare high amount of catalyst by a facile and inexpensive method to be used in a continuous pilot scale reactor under natural solar light irradiation for the photoreforming of biomass derivatives.

Table 3.3. Comparison of the performance of some Cu_xO/TiO_2 systems towards H_2 formation from glycerol aqueous solutions.

Catalyst	**Preparation method**	**Light source**	**Glycerol (mM)**	**H_2 ($\mu mol\ g^{-1}h^{-1}$)**	**By-products**	**Ref.**
10% w/w CuO/TiO_2 (P25)	Physical mixture	Medium pressure 125 W-Hg lamp	10% v/v glycerol/H_2O	17600	Not identified	[256]
0.08% mol Cu–Pt/TiO_2 (P25)	Wet impregnation	300 W Xe lamp	10% v/v glycerol/H_2O	8750	Not identified	[288]
1.0 wt.% CuO_x/TiO_2 (P25)	Equilibrium deposition filtration (EDF) method	Xe arc lamp	1 M glycerol /H_2O	900	Acetone, acetaldehyde, formaldeyde not quantified	[250]
10 wt% Cu_2O/TiO_2 (P25)	Impregnation followed by a green microwave assisted method	400 W metal halide lamp	5% v/v glycerol/H_2O	196	Not identified	[254]
10 wt% Cu/TiO_2 (P25)	Impregnation followed by calcination at 300 °C on air or H_2	300 W Xe lamp	10% v/v glycerol/H_2O	Air-calcined: 2400 H_2-calcined: 5780	Not identified	[253]
3% w/w CuO/TiO_2 NTs	Wet impregnation method	Sun light	20% v/v glycerol/H_2O	12000 at 22 °C 65000 at 90 °C	Not identified	[289]
2.5%molar fraction Cu_2O/TiO_2 (P25)	Ethanol reduction method and calcination	500 W Xe arc lamp	10% v/v glycerol/H_2O	2000	Not identified	[290]
3 wt% Cu_2O/TiO_2 (P25)	Ball milling	Medium pressure 125 W-Hg lamp	2 mM glycerol /H_2O	170	S_{DHA} = 10.3 S_{GA} = 5.4	This work
3 wt% Cu_2O/TiO_2 (P25)	Ball milling	150 W halogen lamp	2 mM glycerol /H_2O	11	S_{DHA} = 15.2 S_{GA} = 18	This work

3.4. Conclusions

This work presents a facile way to prepare noble metal free photocatalysts for anaerobic heterogeneous solar/UV light reforming of glycerol in aqueous media using commercial TiO_2. Different amount of Cu_2O or 3% CuO were loaded on commercial TiO_2 using ball milling and runs were carried out monitoring the glycerol conversion and the amount of formed of 1,3-dihydroxyacetone and glyceraldehyde in the liquid phase, and that of H_2 and CO_2 in the gas phase. The results were compared with those of runs carried out using TiO_2 loaded with platinum and/or coupled with CuO with the aim to verify the effectiveness of Cu_2O in replacing Pt.

3%wt Cu_2O – TiO_2 showed the best results, with glycerol conversion of ~ 33%, selectivity of 10.3% and 5.4% for DHA and GA respectively, CO_2 concentration of 0.16 mM, H_2 of 1.01 mM, corresponding to 0.17 mmol h^{-1} g^{-1}. These values are comparable with the ones obtained using Pt – TiO_2 except for GA, where Pt – TiO_2 showed no selectivity.

Raman, Photoluminescence, and UV–Vis spectroscopies, TPR analysis, X-ray diffraction, Specific Surface Area measurements, TEM and SEM coupled with EDX observations, photopontential and transient photocurrent measurements indicated the formation of a heterostructure between TiO_2 and copper oxide and the effectiveness of ball milling method in the preparation of noble metal free modified TiO_2 photocatalysts.

4. Pt–TiO_2 catalysts for glycerol photoreforming: comparison of anatase, brookite and rutile polymorphs

In this published work [220], we compared the H_2 production from glycerol photoreforming for different TiO_2 polymorphs, highlighting an increase of activity in the order Pt-rutile < Pt-P25 ~ Pt-anatase < Pt-brookite with a different distribution of the reaction intermediates. We show that the highest ability to adsorb water and the different distribution of Pt active sites in brookite can positively influence its photoactivity (Figure 4.1).

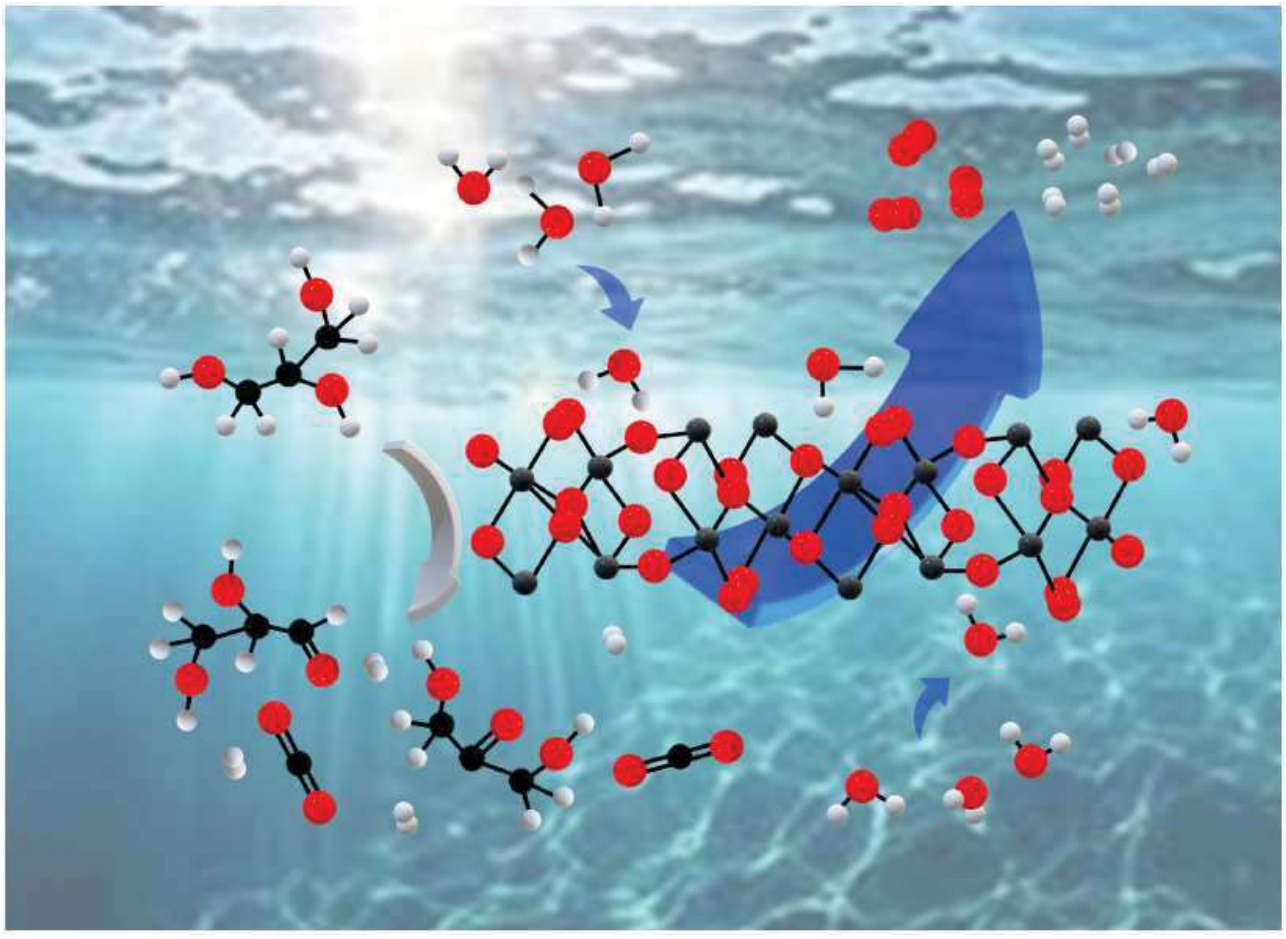

Figure 4.1. Schematic illustration of the photocatalytic reactions.

4.1. Introduction

TiO_2 displays different polymorphs and the three most used as photocatalysts are anatase, brookite, and rutile [291,292]. Generally, the polymorphs have different surface, chemical, and electronic properties that determine the photocatalytic activity [291,293,294], although also the specific substrate catalyst interaction must always be considered [295,296]. Moreover, previous works

demonstrated that the activity of the same TiO_2 phase is extremely variable depending on the particle sizes, specific surface area, porosity, exposed crystal facets, surface hydroxylation degree and amount of hydroxyl radicals produced under irradiation [297–299]. In fact, in some specific cases, rutile and brookite are reported to be more active than anatase towards H_2 production [17,300] and the binary or ternary mixtures are generally more active than the single phases because of the favored spatial separation of the photo-generated charges in the coupled systems [301,302]. Moreover, brookite and rutile are generally less active than anatase in pollutant degradation reactions but are effective in partial oxidation reactions [292,303].

In this work the activity of anatase, rutile and brookite TiO_2 polymorphs, functionalized with Pt as co-catalyst, has been compared towards the photoreforming of glycerol [219,304,305], used as model biomass compound, under both UV and simulated solar light irradiation. The worldwide used commercial TiO_2 P25 was used for the sake of comparison. FT-IR spectroscopy was employed to assess the water adsorption properties and to probe, by CO adsorption, the Pt active sites to correlate the photocatalytic activity with the catalyst surface properties.

4.2. Experimental section

Samples preparation

Home prepared Pt-TiO_2 samples displaying different phase where prepared and compared for the photoreformig of glucose. Commercial TiO_2 P25 was used as reference.

Titanium tetrachloride (Fluka 98%) and titanium(IV) oxysulfate (Sigma-Aldrich ≥29% Ti,(as TiO_2) were used as received as TiO_2 precursors whilst $PtCl_4$ (Sigma-Aldrich 96%) as Pt source.

TiO_2 anatase was prepared by adding 40 g of $TiOSO_4$ to 180 mL of distilled water and stirring the resulting mixture for ca. 2 h at room temperature until a clear solution was formed. The latter was transferred in a closed bottle and treated for 48 h at 373 K in an oven. The resulting precipitate was washed twice with water to eliminate the sulphate ions, dried at 323 K and calcined for 3 h at 873 K.

TiO_2 brookite was obtained by introducing 210 mL of demineralized water, 80 mL of HCl and 5 mL of $TiCl_4$ into a Pyrex bottle that was closed and aged in an oven for 48 h at 373 K. A precipitate containing a mixture of brookite and rutile was obtained. Pure brookite was separated from rutile by peptization with water and dried under vacuum at 323 K.

TiO_2 rutile was synthesized by adding, under stirring at room temperature, 20 mL of $TiCl_4$ to 100 ml of distilled water. The obtained solution was heated in an oven at 373 K for 48 h in a closed bottle. The solid was recovered by drying in a rotary evaporator at 323 K. Pt (0.5% wt) was loaded on TiO_2 by a photodeposition method.

Samples characterization

XRD, SSA, DRS, and SEM analyses were performed; further details are provided in the experimental section (Section 2).

Raman spectra were acquired by means of BWTek-i-micro Raman Plus System using a 532 nm laser. The spectra were collected in the 125-1000 cm^{-1} Raman shift range and every measure was the average of two repetitions.

Fourier-transform infrared spectroscopy measurements (FT-IR) were performed using a Bruker INVENIO-R spectrometer (resolution: 2 cm-1; detector: DTGS), averaging 128 scans. For the in situ experiments, an aliquot of each type of TiO_2 nanoparticles was pressed in self-supporting pellets ("optical density" of ca. 10 $mg \cdot cm^{-2}$) and placed in quartz cells equipped with KBr windows designed to carry out spectroscopic measurements in controlled atmosphere. Before CO adsorption, the TiO_2 samples were activated with the following procedure:

(i) outgassing at 673 K for 30 min;

(ii) contacting twice with 10 mbar of O_2 for 10 min at the same temperature;

(iii) cooling to 423 K in O_2, then outgassing for 10 min;

(iv) contacting with 15 mbar of H_2 at 423 K for 10 min; and

(v) Cooling from 423 K to room temperature under outgassing.

Photocatalytic activity evaluation

Glycerol, glyceraldehyde and 1,3-dihydroxyacetone were purchased by Sigma Aldrich and used as received. The photocatalytic runs were carried out in a cylindrical Pyrex reactor containing 150 mL of an aqueous glycerol (2mM) dispersion in anaerobic conditions. Both a 125 W medium pressure Hg lamp (main emission peak at 365 nm) and a 150 W halogen lamp (simulating the solar spectrum) were used as irradiation sources. Helium was bubbled in the suspension for 0.5 h under dark, then the reactor was sealed, and the lamp switched on. Water was circulated in the reactor jacket to keep the temperature of the suspension at about 303 K. To analyze the reaction mixture composition, aliquots were withdrawn at fixed times, filtered through 0.2 μm PTFE membranes and analysed by a Thermo Scientific Dionex UltiMate 3000 HPLC equipped with a Diode Array detector. A REZEK ROA Organic acid H^+ column, crossed by an aqueous 2.5 $\cdot 10^{-3}$ M H_2SO_4 solution at a flow rate of 0.6 $mL \cdot min^{-1}$, was used to separate the different compounds. An HP 6890 Series GC System equipped with a Supelco GC 60/80 CarboxenTM-1000 packed column and a thermal conductivity detector was used to analyze CO_2 and H_2 accumulated in the reactor headspace.

The Equations 2.1 – 2.2. were used for the determination of X and S, where P is the molar concentration of the obtained product (DHA or GA).

4.3. Results and discussion

The X-ray diffraction patterns of the synthesized materials (Figure 4.2a) show the main characteristic peaks of anatase (2θ = 25.21, 38.01, 48.01, 54.51), rutile (2θ = 27.51, 36.51, 411, 54.11, 56.51) and brookite (2θ = 25.341, 25.691, 30.811), confirming the presence of the three pure TiO_2 phases in the home-made samples and the coexistence of anatase and rutile in P25. The presence of the photodeposited Pt was not noticed due to its low amount. The peaks of Pt-P25 and Pt-anatase are more intense and narrower than those of Pt-brookite and Pt-rutile, indicating a greater crystallinity and a larger crystallite size (Table 4.1) in accordance with the higher temperature at which they were prepared. Raman spectra (Figure 4.2b) confirm the XRD results and, in particular, the purity of Pt-brookite. In fact, while the main XRD peaks of brookite and anatase are practically coincident, the Raman bands of brookite are distinct from those of anatase [306].

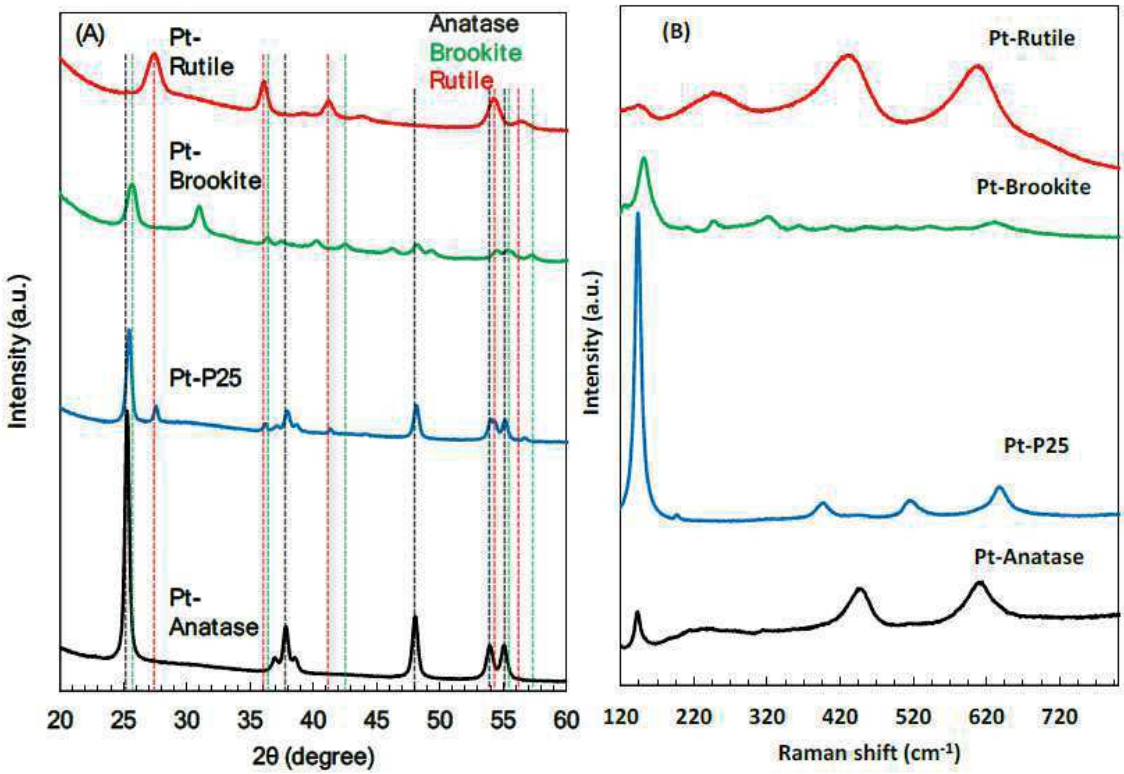

Figure 4.2. a) XRD patterns and b) Raman spectra of the different samples. Anatase: JCPDS Card No 21-1272, 2θ: 25.2° 37.3° 47.6° 53.5° 55.1° 62.2°. Rutile: JCPDS Card no. 21-1276, 2θ: 27.0° 35.6° 40.8° 54.0° 53.9° 56.1°1 and 61.0°. Brookite: JCPDS card no. 29-1360, 2θ: 25.3° 25.7° 36.2° 42.3° 55.2° 57.2°

The specific surface area (SSA) of Pt-anatase is very similar to that of Pt-P25, being 48 $m^2 g^{-1}$ and 50 $m^2 g^{-1}$, respectively, while Pt-brookite and Pt-rutile display higher values (Table 4.1). However, the higher specific surface area values of Rutile and Brookite, and consequently the particle size, do not appear to be directly related to the photoactivity. In fact, Rutile is the least active sample, while Brookite is the most active despite having very similar surface areas.

Table 4.1. TiO_2 phase (A = Anatase, R = Rutile, B = Brookite), crystallite size (ϕ), specific surface area (SSA) and band-gap (E_g) for the different samples

Sample	**Crystalline phase**	**SSA ($m^2 g^{-1}$)**	**ϕ (nm)**	**E_g (eV)**
Pt-P25	A, R	50	27 (A), 31 (R)	3.10
Pt-anatase	A	48	22	3.26
Pt-brookite	B	83	7	3.34
Pt-rutile	R	85	4	3.02

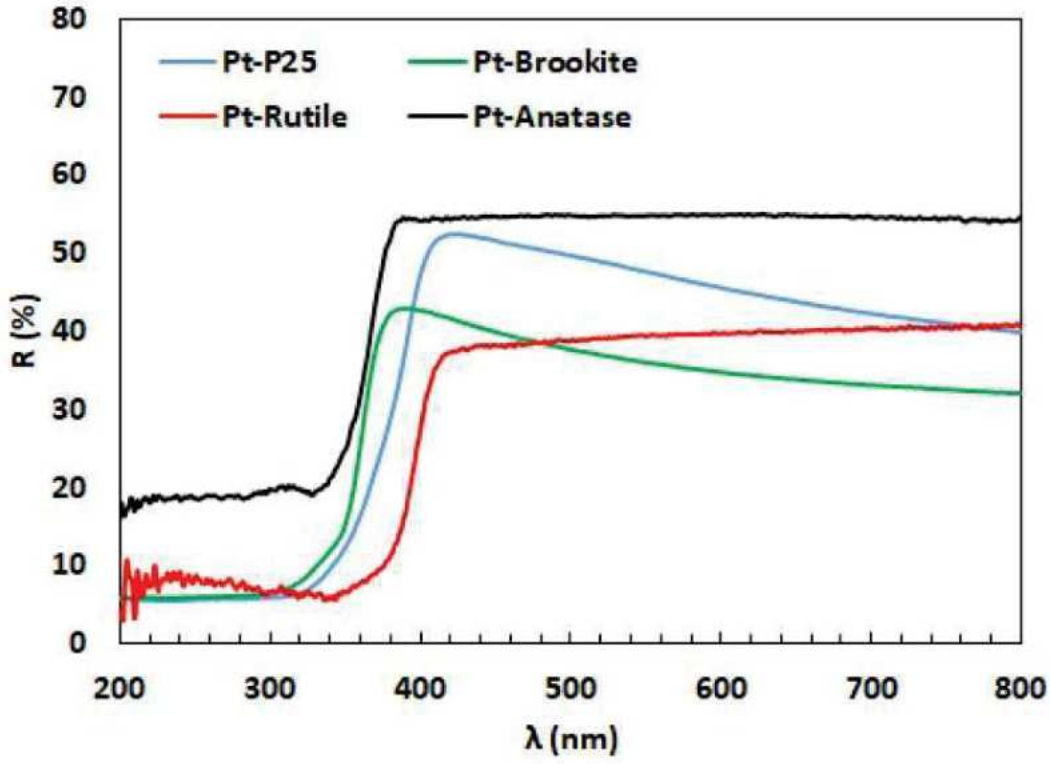

Figure 4.3. Diffuse reflectance UV-Vis spectra of the different samples

The diffuse reflectance UV-Vis spectra of the different TiO_2 samples are reported in Figure 4.3. As visible in Table 4.1, rutile shows the smallest band gap values, while the transition is shifted to higher

energies for anatase and brookite, as expected from literature results [307,308]. The commercial P25 exhibits an onset in the absorption in the UV region (λ ~ E 360 nm) typical of the anatase/rutile mixture. The presence of platinum does not change the band gap transition but only increases the visible light absorption [17].

SEM images (Figure 4.4) reveal that the photocatalysts are formed of aggregates of irregular spherical particles with dimensions in the nanometric scale. Pt particles are not distinguishable due to their small amount and uniform distribution on the TiO_2 surface.

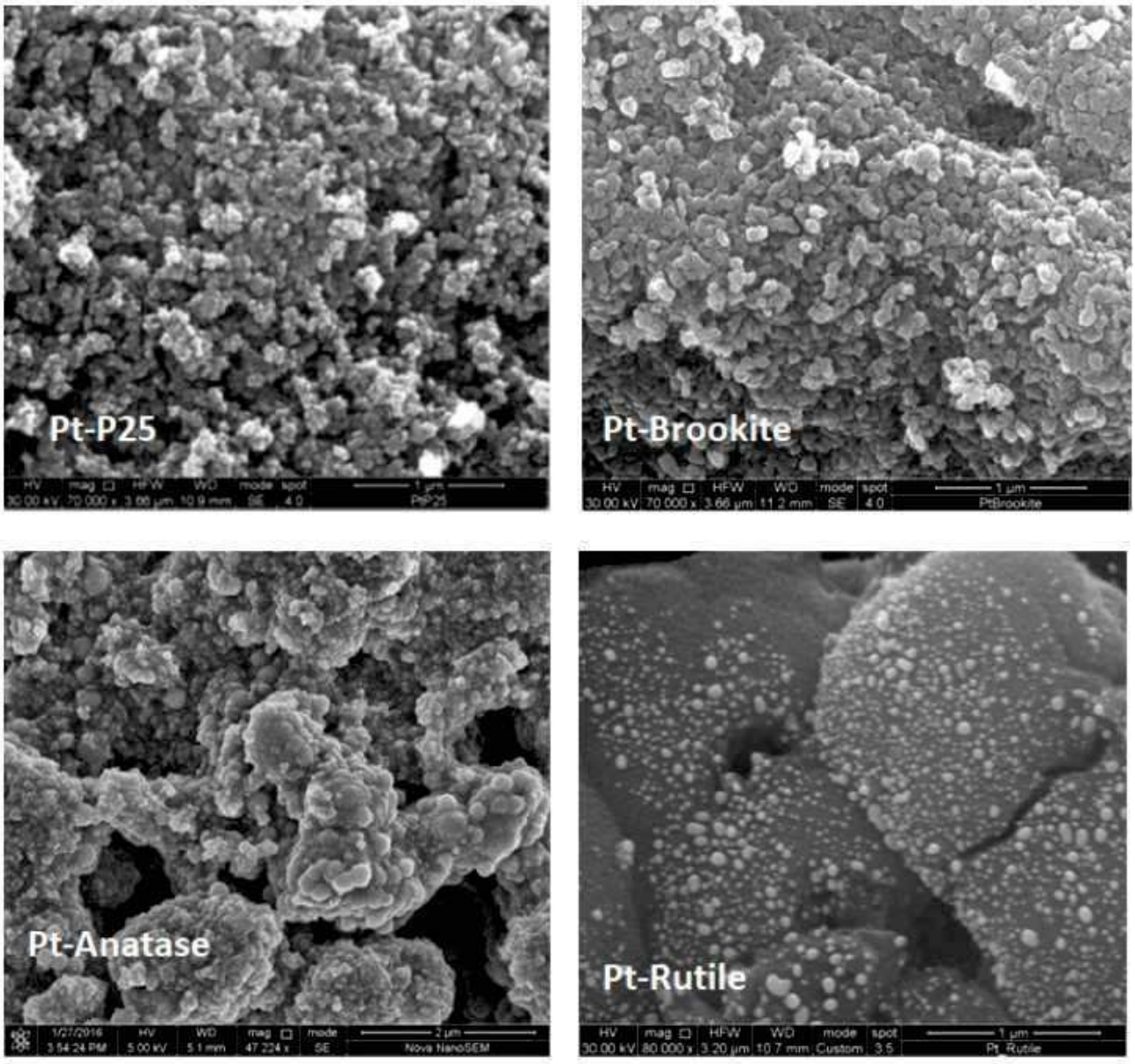

Figure 4.4. SEM images of the different samples.

In Table 4.2 the results related to the photoreforming of glycerol after 4 h of irradiation under both UV and solar light irradiation are presented in terms of glycerol conversion, selectivity towards the main reaction intermediates (1,3-dihydroxyacetone and glyceraldehyde) and concentration of CO_2 and H_2 in the gas phase accumulated in the headspace of the reactor. All photocatalysts give rise to the same partial oxidation compounds, indicating a similar reaction pathway. However, we can observe a different degree of conversion, selectivity towards the intermediates and H_2 production. Under UV irradiation in the presence of Pt-P25, glycerol reaches a conversion of 23% with a selectivity of 6.4% and 9.8% towards DHA and GA, respectively, and a H_2 concentration of 3.0 mM. Among the home prepared catalysts, Pt-anatase and especially Pt-rutile display a lower glycerol conversion and H_2 formation.

Pt-brookite shows almost the same activity as P25 regarding the partial oxidation of glycerol (23% conversion vs 26%) but was more active towards the H_2 production being the quantity obtained 3.1 times greater. Also, under simulated solar light irradiation Pt-brookite is more performant that Pt-P25.

Table 4.2. Photocatalytic results obtained after 4 h of UV or simulated solar light irradiation. X = glycerol conversion, S = selectivity. DHA = 1, 3-dihydroxyacetone, GA = glyceraldehyde

Sample	X (%)	S_{DHA} (%)	S_{GA} (%)	CO_2 (mM)	H_2 (mM)	H_2/CO_2
UV irradiation						
Pt-P25	23	6.4	9.8	0.09	3.0	33.3
Pt-Anatase	14	14.4	22.5	0.11	3.0	27.3
Pt-Brookite	26	6.8	8.1	0.23	9.3	40.4
Pt-Rutile	13	10.6	21.6	0.06	1.2	20
Simulated solar light irradiation						
Pt-P25	20	8.8	11.0	0.10	3.1	31
Pt-Brookite	21	9.1	10.0	0.18	5.4	30

The effect of varying the glycerol initial concentration is reported in Table 4.3. The results for Pt-Brookite reported in Table 4.3 show that by increasing glycerol concentration the conversion decreased and, consequently, the selectivity increased. Moreover, the amount of glycerol converted increased together with the amount of H_2 and CO_2. The higher H_2 amount can be due both the higher amount of reacted glycerol and to the greater number of H_2O molecules broken due to the greater number of available electrons. In fact, the increased quantity of holes used to convert more glycerol corresponds to a greater number of electrons available for the reduction of H^+ ions.

Table 4.3. Photocatalytic results for Pt-Brookite obtained after 4 h of UV light irradiation at two different glycerol concentrations. X = glycerol conversion, S = selectivity. DHA = 1,3-dihydroxyacetone, GA = glyceraldehyde.

Glycerol (mM)	**X (%)**	**S_{DHA} (%)**	**S_{GA} (%)**	**CO_2 (mM)**	**H_2 (mM)**	**H_2/CO_2**	**Glycerol converted (mmol)**
2	26	6.80	8.10	0.23	9.3	40.4	0.095
5	19.3	8.48	14.5	0.39	12.3	31.5	0.14

In Table 4.4, the literature results obtained by using different TiO_2-based samples are compared. Home prepared Brookite with 0.5% of photodeposited Pt revealed good photocatalytic performances producing amount of both H_2 and high value added products in many cases higher than those reported in literature even under simulated solar irradiation.

Table 4.4. Performance comparison of different TiO_2-based samples (DHA = dihydroxyacetone; GA = glyceraldehyde; GlA = glycolaldehyde, HAA = Hydroxyacetaldehyde; FA = formic acid)

Catalyst	**Conditions**	**X (%)**	**S (%)**	**H_2**	**CO_2**	**Ref.**
Pt-Brookite	2 mM glycerol concentration 4h UV irradiation (125 W) 25 °C	26	DHA 6.8 GA 8.1	9300 μmol L^{-1}	230 μmol L^{-1}	This work
Pt-Brookite	4h simulated solar light irradiation (150 W) 25 °C	21	DHA 9.1 GA 10.0	5400 μmol L^{-1}	180 μmol L^{-1}	This work
Pt-TiO_2-Nb_2O_5	5 wt% glycerol concentration 4h UV irradiation			4710 μmol L^{-1}	241 μmol L^{-1}	[309]
NiO/TiO_2	2.28 M glycerol concentration 8h 500 W high-pressure Hg lamp 50 °C			1230 μmol L^{-1}		[305]
Pt-TiO_2	1 M glycerol concentration simulated solar light irradiation (300 W Xe-lamp) 30 °C		GA 34 GlA 66	10000 μmol g^{-1} h^{-1}		[3]

Cu_2O/ TiO_2	2 mM glycerol concentration 5h UV irradiation (125 W) 25 °C	33	DHA 10.0 GA 5.4	1010 µmol L^{-1}	170 µmol L^{-1}	[219]
Pt-Rutile	20 mM glycerol concentration 8h Xe-lamp (300 W) 80 °C	12	HAA 93.2 GA 2.6	2453 µmol	1720 µmol L^{-1}	[310]
TiO_2	10 mM 6.5 h six 15W UV Neon 25 °C	35	DHA 6.5 GA 10 FA 3.1			[311]
Pt-N-TiO_2	10% vol glycerol concentration 5h simulated solar light irradiation (250 W)			3017 µmol		[312]

As documented, during a photoreforming process, the H_2 comes from both water splitting and sacrificial agent (glycerol in our case) dehydrogenation (Scheme 4.1) [130,313–315].

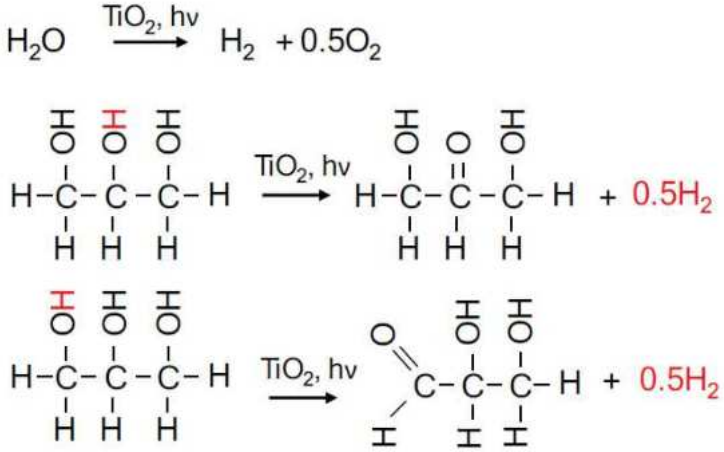

Scheme 4.1. Main products from photocatalytic glycerol reforming

To identify the hydrogen source, in literature D_2O was used instead of H_2O, obtaining a significantly lower rate of hydrogen evolution [305,309]. The results indicate that water should be a main source for hydrogen, and glycerol also could contribute to the hydrogen production. Moreover, by starting from formic acid as sacrificial agent, due to its direct decomposition to CO_2 and H_2 ($HCOOH \rightarrow CO_2 + H_2$), it was found that the H_2 amount was higher than that corresponding to the total mineralization of formic acid [283]. This finding suggested that the produced H_2 derived from both formic acid and water splitting. The different photoactivity of the catalysts is due to some specific features of each

polymorph as crystallinity, hydroxylation degree, exposed facets, hydrophilicity, capacity to form peroxo species. Chong et al. [310] found that glycerol was selectively converted to hydroxyacetaldehyde (HAA) in aqueous solution on facet tuned TiO_2-based catalysts. Rutile exposing high percentage of {110} facets resulted in over 90% selectivity to HAA, while anatase with {001} or {101} facets gave only 16% and 49% selectivity to HAA, respectively. Moreover, the EPR spin trap technique demonstrated that peroxo species are the main reactive oxygen species on rutile, while OH radicals are the prevailing active species on anatase. In our case, hydroxyl radicals are not the main active species involved in the glycerol degradation as demonstrated by adding tert-butanol as scavenger (see Figure 4.5).

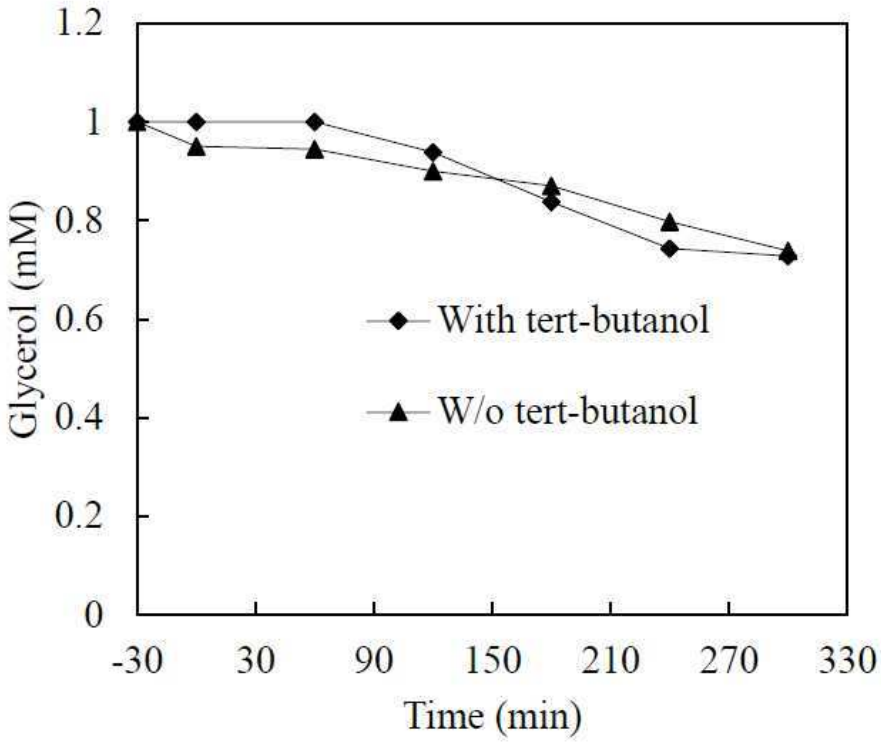

Figure 4.5. Photocatalytic degradation of glycerol with Pt-Brookite in the presence of tert-butanol as ·OH scavenger.

Evaluating the H_2/CO_2 ratio we can note that the highest value is obtained with Brookite (Table 4.2). Moreover, by comparing Pt-brookite and Pt-P25 a higher mineralization degree was found for the first photocatalyst. This finding suggests a greater contribution in the H_2 production of the water splitting with respect to glycerol reforming under UV irradiation in the presence of Brookite. In fact, as the mineralization of glycerol gives rise to H_2O and CO_2, the higher H_2/CO_2 ratio can be due to a more significant contribution of water splitting. Under solar light irradiation, instead, virtually the same ratio was obtained with Pt-P25 and Pt-brookite. This is an indirect confirmation that the water

splitting requires more energy than photoreforming, i.e. H_2 production from a sacrificial agent is an up-hill process, but the energy change is smaller than for H_2O splitting [313,316].

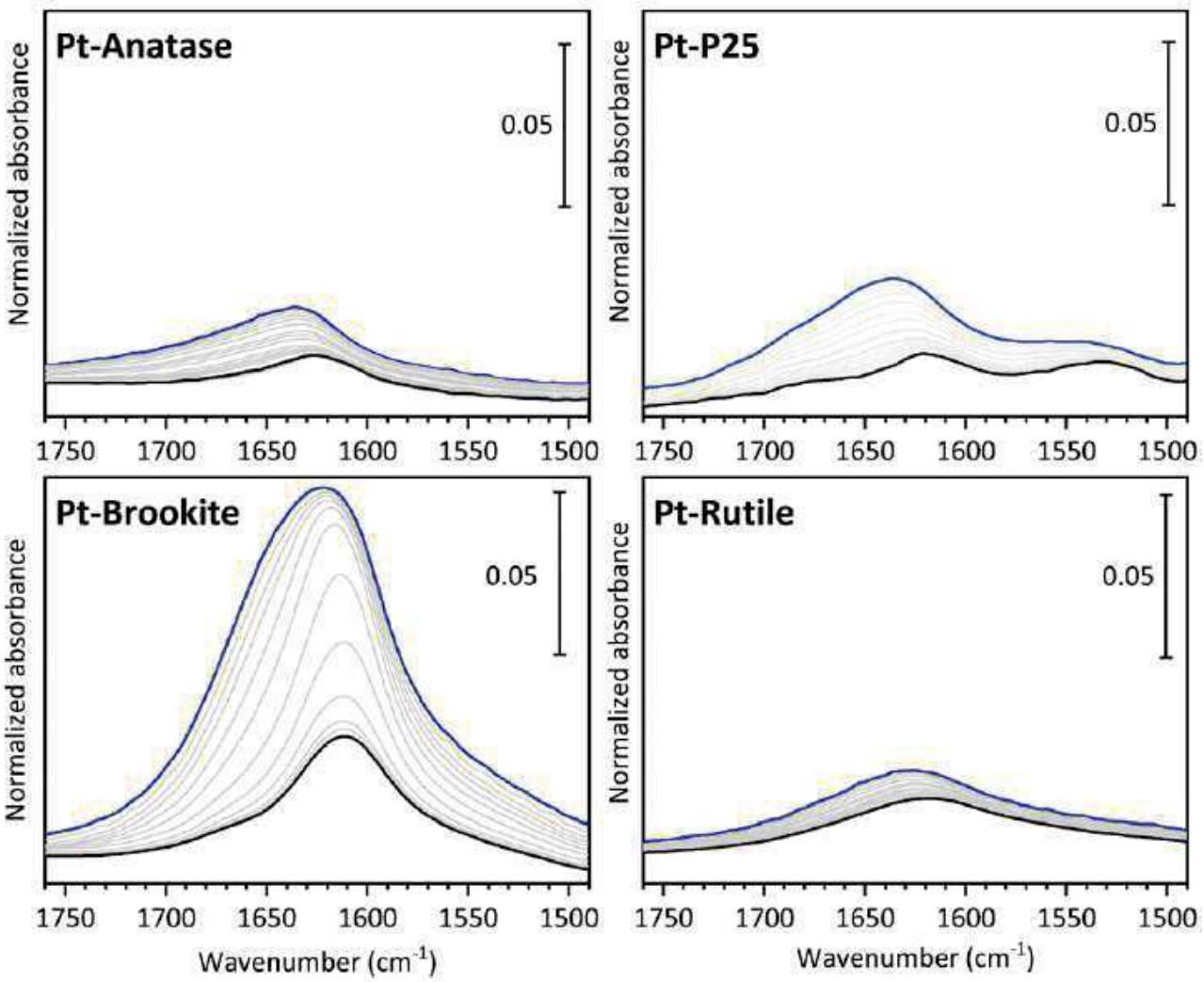

Figure 4.6. FT-IR spectra of the different materials in contact with H_2O at 15 mbar (blue curve) and progressive decreasing of the water coverage till outgassing for 15 minutes at beam temperature (black curve).

To understand which can be the impact of the catalyst surface properties on the observed photocatalytic activity, we performed an in situ FT-IR study. As first step, we performed a systematic investigation of the adsorption of molecular water by dosing controlled pressures of water on the different samples. Figure 4.6 reports the spectral region typical of the water bending mode which is particularly suitable to compare the amount of H_2O adsorbed by the different polymorphs. We can note that at maximum water coverage (blue curves in Figure 4.6) for all the materials the position of the $\delta(H_2O)$ band is significantly blue shifted with respect to the bending mode of water in gas phase which lies at 1595 cm^{-1} [317]. This behaviour is associated with H_2O molecules acting as H-bond donors [318,319] and it is particularly evident for Pt-anatase and Pt-P25, both showing a maximum

at ca. 1635 cm^{-1}, while is more limited for Pt-rutile (maximum at 1627 cm^{-1}) and for Pt-brookite (maximum at 1622 cm^{-1}). Upon water outgassing, the bands red shift owing to the fading out of the water–water interactions moving from multilayers of adsorbed H_2O to the monolayer. The final band position after 15 minutes of outgassing is 1625 cm^{-1} for Pt-anatase, 1621 cm^{-1} for Pt-P25, 1618 cm^{-1} for Pt-rutile and 1611 cm^{-1} for Pt-brookite. Concerning the intensity of the bands, we can see that the $\delta(H_2O)$ signals follow the order Pt-brookite >> Pt-P25 ~ Pt-anatase > Pt-rutile, highlighting a remarkably higher hydrophilicity for the brookite-based sample.

These findings are in agreement with previous results obtained by contact angle measurements on TiO_2 films, which revealed that the brookite films were the most hydrophilic ones. In particular, the measured contact angles values were 251, 231 and 101 for brookite, anatase and rutile, respectively [320].

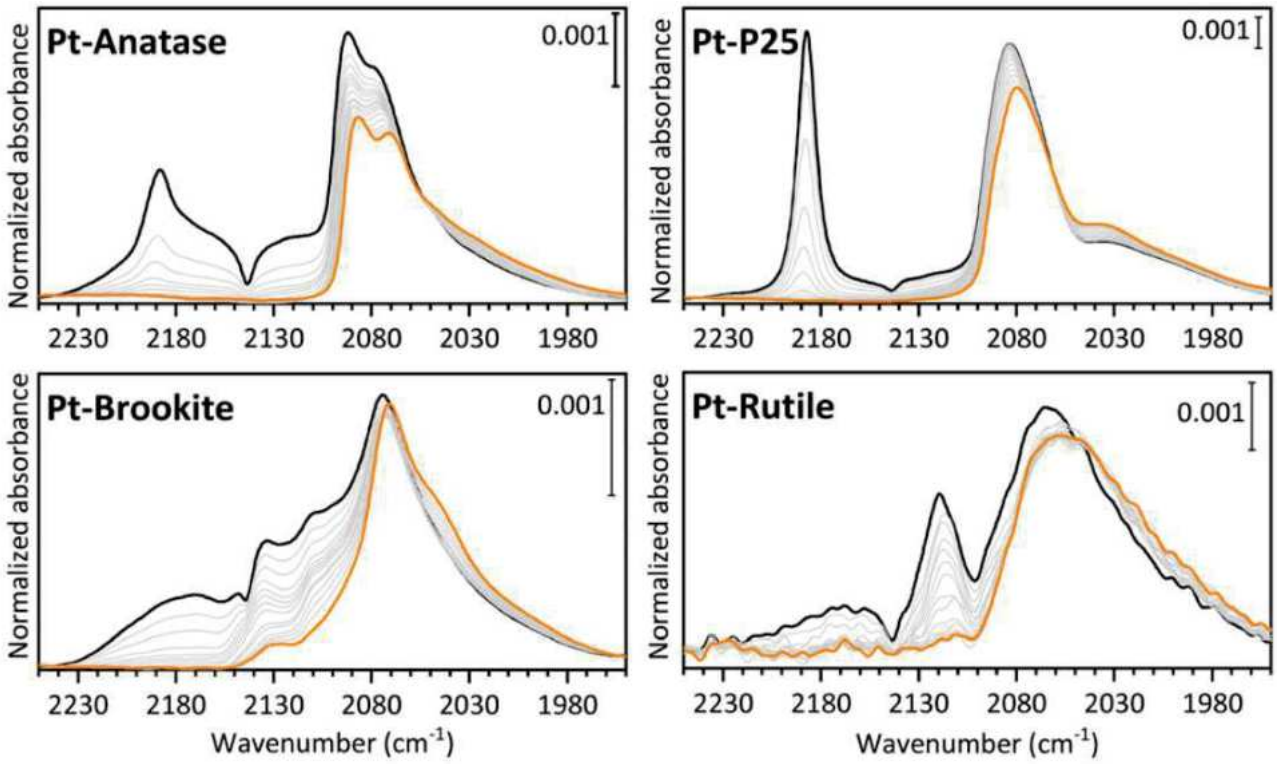

Figure 4.7. FT-IR spectra of the different materials, after activation at 673 K and reduction at 423 K, in contact with CO at 40 mbar (black curve) and progressive decreasing of the CO coverage till outgassing for 15 minutes at beam temperature (orange curve).

To investigate the properties of the surface active sites in the different samples, we employed carbon monoxide, which is a versatile probe molecule, able to interact with both Ti and Pt centers. Before performing CO adsorption experiments, the surface of the materials must be ‘‘cleaned’’ from organic contaminants coming from the synthesis and adsorbed water molecules by outgassing at 673 K. The

samples were then treated in H_2 at 423 K to reduce the Pt nanoparticles, mimicking the reducing conditions present during the photocatalytic reactions. Upon CO adsorption, we can observe in all samples a band around 2180 cm^{-1} (Figure 4.7), which can be ascribed to the interaction of CO with Ti^{4+} cations. This spectral feature is particularly sharp in Pt-P25, owing to the high regularity of the anatase {101} facets in this sample which is characterized by an excellent crystallinity [321].
These signals are in general quite weak owing to the low binding energy of CO on Ti^{4+} cations, which results in a low CO coverage of TiO_2 surfaces for room temperature adsorption [322].
Moving to the spectral features related to the interaction between CO and Pt sites, we can note the presence of a group of bands between 2135 and 2100 cm^{-1}. The signal at ca. 2130 cm^{-1} has been ascribed to Pt^{2+}–CO species, while the bands closer to 2100 cm^{-1} are associated to carbonyls on $Pt^{\delta+}$ sites with decreasing positive charge [323]. These sites are more abundant in Pt-rutile and Pt-brookite. In previous studies these signals were associated to a significant metal-support interaction [324] and to a peculiar photocatalytic activity [325]. Furthermore, below 2100 cm^{-1} we can find the most intense bands due to the formation of linear carbonyls on metallic Pt [326]. In particular, the band at ca. 2080 cm^{-1}, which is dominant in Pt-P25 and Pt-anatase, is ascribed to CO linearly adsorbed at terrace sites. Conversely, Pt-rutile and Pt-brookite show the most intense peak at lower wavenumbers, suggesting the presence of a higher fraction of edge and step sites. Indeed, it has been shown that a decrease in the coordination of the Pt^0 sites results in a red shift of the corresponding ν(CO) signal [327].Therefore, we can also assign the tail located at ca. 2030 cm^{-1} to carbonyls on corners/kinks [326]. Finally, we can note that the main peak associated to metallic Pt sites is particularly narrow in the case of Pt-brookite, highlighting a lower heterogeneity in the nanoparticle surface structure.

4.4. Conclusion

In summary our results show that the H_2 production from glycerol photoreforming and the intermediate products distribution are strongly dependent on the nature of the TiO_2 support. Brookite was the most active sample for H_2 production, and its amount decreases in the order Pt-brookite > Pt-P25 ~ Pt-anatase > Pt-rutile. This trend follows the hydrophilicity order of the different polymorphs since the measured intensity of the adsorbed water bending mode is Pt-brookite >> Pt-P25 ~ Pt-anatase > Pt-rutile. Employing IR spectroscopy of adsorbed CO we identified a different metal-support interaction for the investigated polymorphs, highlighting a lower concentration of $Pt^{\delta+}$ centers for Pt-P25 and Pt-anatase. Moreover, the probe molecule showed a different distribution of low coordinated Pt^0 sites in the samples. We can thus conclude that the observed higher activity of the Pt-

brookite sample can be ascribed to its ability to adsorb water, which is a key reactant to form hydrogen, and to the presence of a well-defined distribution of Pt^0 sites, preferentially located on edges and steps.

5. Photocatalytic and photoelectrocatalytic H_2 evolution combined with valuable furfural production

In this published work [16] the photocatalytic (PC) and photoelectrocatalytic (PEC) reforming of furfuryl alcohol (FuA) under environmentally friendly conditions was investigated (Figure 5.1). Both H_2 evolution and partial oxidation to furfuraldehyde were followed. For the first time, TiO_2-based photocatalysts were studied and the photocatalytic activity of home-prepared photocatalysts was compared with that of commercial ones under both UVA and simulated solar irradiation. PEC tests were performed by using home-prepared TiO_2 nanotubes (TiO_2 NTs) as photoanode and Pt-free Ni foam as cathode to improve the Hydrogen Evolution Reaction (HER). Both the partial FuA oxidation reaction rate and H_2 evolution rate were normalized for the lamp specific power to account for the different photon flux and the rates were higher for the PEC process. PEC is a promising strategy for the valorization of biomasses with simultaneous H_2 production despite the cost of the bias.

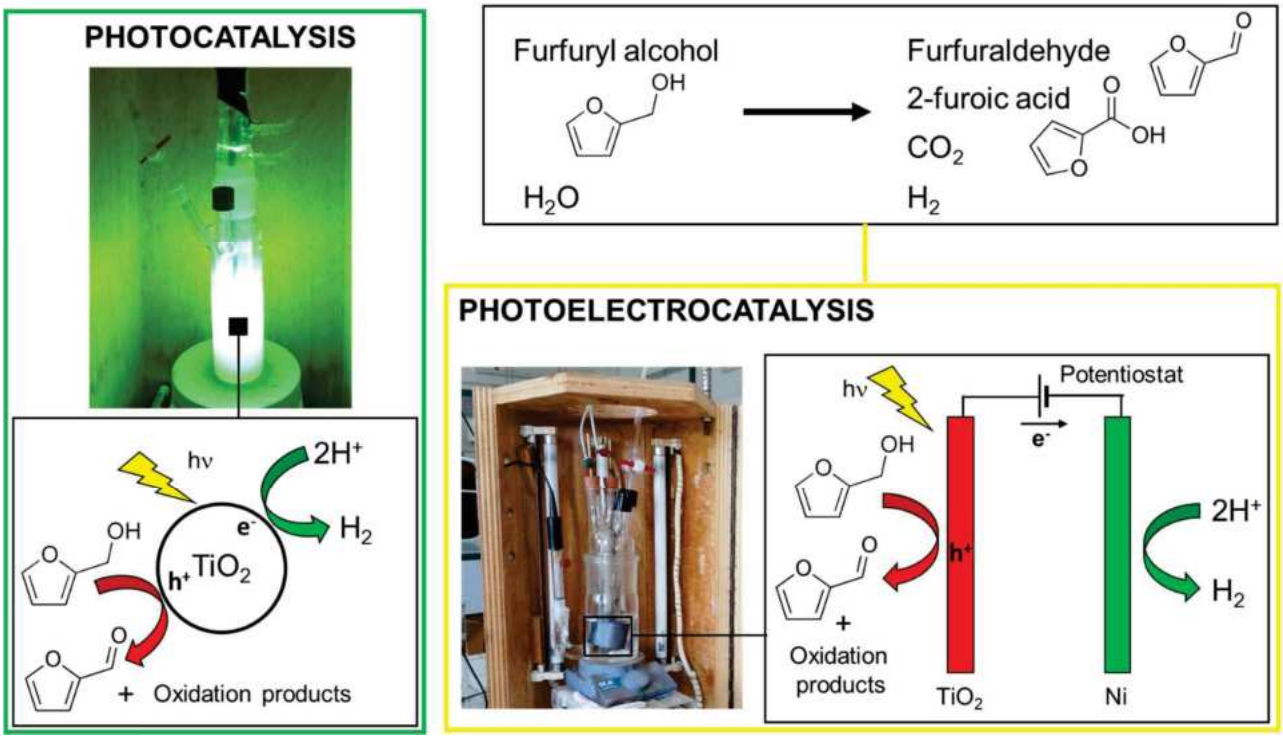

Figure 5.1. Schematic illustration of photocatalytic and photoelectrocatalytic reactions.

5.1. Introduction

As mentioned above, the reforming of renewable biomass into fuels and high value chemicals is an ideal and sustainable alternative to the use of fossil resources [3,54–56,328,329], for instance furfuryl alcohol (FuA) can be upgraded to furaldehyde, one of the top value-added chemicals from biomass

according to the U.S. Department of Energy [52], and/or 2-furoic acid to produce pharmaceutical intermediates [144,330–332].

A survey of the published literature on partial oxidation of FuA and simultaneous hydrogen production reveals that it can be achieved by both photocatalytic and electrochemical processes. Li et al. [333] fabricated a heterostructure of $LaVO_4$/CN for efficient photocatalytic H_2 evolution, 0.287 mmol g^{-1} h^{-1}, coupled with a furfural production of 0.95 mmol g^{-1} h^{-1}, while Wang et al. [334] prepared $H_{1.4}Ti_{1.65}O_4 \cdot H_2O$ nanosheet as a photocatalyst for the oxidation of FuA, obtaining FuA conversion of 54 % and furfural selectivity of 99% after 6 h of irradiation. In both cases, the authors did not mention if the catalyst can be recovered after the process and re-used for subsequent runs.

Conversely, Fang et al. [332] investigated the possibility of carrying out partial oxidation of FuA by an electrochemical process. Their investigation revealed that the reaction can be successfully performed using an anode constituted by CuO nanorods in the applied potential range of 1.35 – 1.39 V versus the RHE. Under these experimental conditions, a Cu(III) intermediate is released into the electrolyte that selectively oxidizes FuA to furfural. However, despite the very high selectivity and faradic efficiency, the drawback of this process is that a copper oxide sacrificial anode is necessary and that copper ions can be competitive at the cathode since they have a more positive standard potential compared to water reduction, thus decreasing the faradic efficiency for H_2 production.

This work aims to optimize an integrated PEC process for partial oxidation of furfuryl alcohol to furfuraldehyde in an aqueous solution with the contemporary H_2 evolution under environmentally friendly conditions exploiting the advantages and limits of photocatalysis, and evaluating the potential of photoelectrochemical method.

As regards heterogeneous photocatalysis, we tried to boost the photocatalytic properties of semiconductors containing different TiO_2 polyforms. Although titanium dioxide is the most widely used photocatalyst in various applications in the photocatalytic field, in the literature there are no reports on its use in this reaction. There are only a few papers on the use of some complex catalysts alternative to TiO_2 [144,331,335] often used in the presence of organic solvents. Many studies, instead, investigated the reverse reaction, i.e. the hydrogenation of furfural to furfuryl alcohol, with H_2 consumption [336–340]. In particular, in this work, the photocatalytic activity of TiO_2-based photocatalysts prepared in the laboratory was compared with that of commercial samples.

Photocatalytic runs were carried out under both UVA and simulated solar light irradiation. The influence of the presence of some metal species (Pt, Cu, W, Nb) and pH on the photocatalytic activity and product selectivity were investigated to improve the performance of bare TiO_2. Heterogeneous photocatalysis, under ambient conditions and in the presence of sunlight irradiation, represents one

of the cleanest ways to obtain H_2. Moreover, the use of biomass derived products as sacrificial agents allows to increase hydrogen production (reducing the e^-/h^+ recombination and decreasing the energy of the process) and to contemporaneously obtain value added products [248,283,341].

Photoelectrocatalytic tests were carried out using home-prepared TiO_2 nanotubes as photoanode and Ni foam as cathode.

Surface, morphological, and bulk characterizations of catalysts were carried out through the acquisition of X-ray diffraction (XRD) patterns, Raman spectra, UV−vis reflectance spectra, specific surface area (S.S.A.) determinations, scanning electron microscopy (SEM) and EDX analyses.

5.2. Experimental section

Samples preparation

Various TiO_2-based catalysts containing different crystalline phases have been prepared under different experimental conditions, in order to obtain different polymorphic forms of TiO_2. Titanium tetrachloride ($TiCl_4$ Sigma-Aldrich 98%), titanium(IV) isopropoxide (TTIP, Aldrich ≥ 97%), ethanol (Sigma-Aldrich), HCl (Sigma-Aldrich 37%), Pluronic P127 (Sigma-Aldrich), $PtCl_4$ (BDH Chemicals), CuCl (Sigma-Aldrich), $NbCl_5$ (Sigma-Aldrich) and WCl_6 (Sigma-Aldrich) were used as received for the synthesis of different TiO_2 based photocatalysts. Pt and in some cases W, Nb and Cu have been sometimes added to TiO_2 to improve its performance. In particular, Pt was chosen because it demonstrated excellent activity for H_2 formation from aqueous solution [262,342], Cu was effective in replacing Pt in reduction reactions as in the CO_2 valorization [343] and photoreforming processes [251,252,284] whilst W, Nb improve the charges separation efficiency and enhance the selectivity in partial oxidation reactions [295,344,345].

Commercial Anatase BDH and Aeroxide P25 TiO_2 were used in order to compare them with home prepared photocatalysts and were referred in this article as BDH and P25.

The brookite was obtained by thermal hydrolysis of $TiCl_4$ in aqueous solution of HCl, specifically 10 ml of $TiCl_4$ were slowly added to a solution containing 420 ml of water and 160 ml of concentrated HCl. Then the solution was transferred into a Pyrex glass bottle and heated to 373 K for 48h, thus obtaining a precipitate containing a mixture of brookite and rutile. The brookite was separated by peptization by adding water at different times and removing the supernatant in which the brookite was selectively dispersed. HP-B was the code used for this sample. Brookite samples containing Cu (code Cu-HP-B, B= Brookite) or Nb (code Nb-HP-B, B= Brookite) in different weight percentages were obtained by adding a certain quantity of CuCl or $NbCl_5$ to the solution of $TiCl_4$ in HCl before being transferred to the oven.

Another TiO_2 photocatalyst was synthesized by adding 29 ml of TTIP to a solution containing 230 ml of ethanol, 27 ml of H_2O, 4 ml of HCl and 5.5 g of Pluronic F127 (Poloxamer 407). A white suspension was obtained which was kept for 24 hours at 313 K to evaporate the solvent. The final solid was dried 24 hours at 383 K and subsequently calcined 24 hours at 773 K. This sample was named as HP-AR (A=Anatase, R=Rutile). For the preparation of the photocatalyst with 1 wt% of W an adequate amount of WCl_6 was added to the ethanolic solution before adding TTIP. The code W-HP-AR identifies this sample.

The pure rutile was prepared by adding 10 ml of $TiCl_4$ to 50 ml of distilled water under stirring at room temperature, the solution obtained was placed in a closed Pyrex bottle and then inside an oven at 373 K for 48h, the final solid was recovered by vacuum drying at 323 K. HP-R was the code used for this sample.

TiO_2 samples were loaded with 0.5 wt% Pt by the photodeposition method using $PtCl_4$. In a 500 ml Pyrex photoreactor, 200 ml of H_2O, 50 ml of ethanol, 1 g of TiO_2 and the right amount of $PtCl_4$ were added. N_2 was bubbled for 30 minutes in the dark to de-aerate the solution and for about 8 h under irradiation to allow metallic Pt deposition. The powders were recovered by evaporating the solution at 323 K. When Pt was present the code was accordingly modified inserting the symbol of the metal.

According to previous work [346], TiO_2 nanotubes (TiO_2 Nts) used in photoelectrocatalytic tests were prepared through anodizing process. Titanium foils (Sigma Aldrich, purity > 99.7%) with 0.127 mm thickness were properly cut and etched in a mixture of hydrofluoric acid (Sigma Aldrich, purity 39.5%), nitric acid (Sigma Aldrich, purity 69.0%) and deionized water with a volume ratio of 1:1:3 respectively for 15 seconds, then ultrasonically cleaned in acetone and ethanol for 5 minutes each and rinsed with deionized water. Samples were used after being dried in air. TiO_2 Nts were formed in an ethylene glycol (Aldrich, 99.8% anhydrous) solution containing 0.25 wt% NH_4F (Sigma Aldrich) and 0.75 wt% deionized water. Anodizing was conducted in a two-electrode configuration using aluminum foil as cathode and potential was kept constant during anodizing at 45 V for 10 minutes. Soon after the anodizing process, a thermal treatment was performed in order to induce crystallization in the TiO_2 Nts. The layers were heated up to 450°C under air exposure and kept for 3 hours at high temperature and left cooling in the furnace. Such a low annealing time was chosen to try to have a thin and not very blocking thermal oxide between bare titanium and tubes. Ni foam was used as cathode in the PEC runs as received.

Samples characterization

XRD, Raman spectra, DRS, SSA, and SEM analyses were performed; further details are provided in the experimental section (Section 2).

Tests

The photocatalytic activity was determined in a 250 mL Pyrex cylindrical reactor illuminated by a 125 W UV lamp axially immersed within the photoreactor. N_2 was bubbled into the 150 mL aqueous suspensions for ca. 0.5 h under dark to de-aerate the solution, then the reactor was sealed, and the lamp switched on. The best photocatalysts were tested also under 50 W halogen lamp simulating the solar light irradiation. The initial furfuryl alcohol (FuA) concentration was 1 mM.

The amount of the used photocatalyst was different as for every powder the quantity sufficient to absorb the 90 % of the photons emitted by the lamp was determined. It varied in the range 0.3-0.8 $g \cdot L^{-1}$ depending on the sample used (0.3 g L^{-1} for P25, 0.8 g L^{-1} for BDH and 0.6 g L^{-1} for all of the other samples) [17].

Photoelectrocatalytic tests were carried out in a 450 mL undivided glass three electrodes cell using Ni foam as cathode, TiO_2 Nts as anode and an Ag/AgCl as reference electrodes. 0.1 M FuA solution was illuminated externally by six UVA fluorescent lamps with a maximum wavelength of 365 nm (8 W) and N_2 was bubbled into 150 mL aqueous solution for ca. 0.5 h in order to de-aerate the solution. A CH Instrument 630B Series potentiostat was used to control the cell potential.

For photoelectrocatalytic tests 0.5 M Na_2SO_4 was used as electrolyte (pH ~ 7) and the applied potential was 0.5 V vs Ag/AgCl.

The selectivity of the oxidation reaction and the faradic efficiency of both anodic and cathodic processes were studied. Determination of FuA and reaction intermediates concentration was performed by using HPLC, gaseous species accumulated in the reactor headspace were analyzed by GC. Further details are provided in the experimental section (Section 2).

FuA conversion and selectivity and yield towards the formed products were calculated with the formulas in Equations. 2.1 – 2.3, respectively:

For each product, in the case of PEC tests, the faradic efficiency was calculated through Equation 2.4, with z, the electrons exchanged during the partial oxidation, is 2 for furfural and 4 for 2-furoic acid

5.3. Results and discussions

Samples characterization

Selected diffractograms of some of the photocatalysts used are reported in Figure 5.2. The XRD patterns confirmed the presence of the different crystalline phases of TiO_2 in the samples [265]. The

indications of the characteristic peaks of the three main polymorphs of TiO_2: A = Anatase, B = Brookite, R = Rutile are shown. The peaks at 2θ = 25.5°, 38.0°, 48.0°, 54.5° are characteristic of anatase, those at 2θ = 27.5°, 36.5°, 41°, 54.1°, 56.5° of rutile and those at 2θ = 25.34°, 25.69°, 30.81° of brookite. Commercial samples BDH and P25 consist of pure anatase and a mixture of anatase and rutile respectively, while those prepared in the laboratory present the different phases of TiO_2: brookite (B), rutile (R) and an anatase-rutile (AR) mixture. The photodeposition of platinum or the addition of small amounts of Cu or Nb did not cause changes in the diffractograms due to their low quantity.

The peaks of commercial photocatalysts are more intense than those of the prepared ones, indicating a greater crystallinity of the former due to the higher temperature at which they were prepared. Nevertheless, photocatalysts displaying a low crystallinity present, generally, a low oxidant power and this feature is beneficial in the partial oxidation reactions as previously demonstrated [347–349]. Consequently, home prepared low crystalline powders deserve to be prepared and tested.

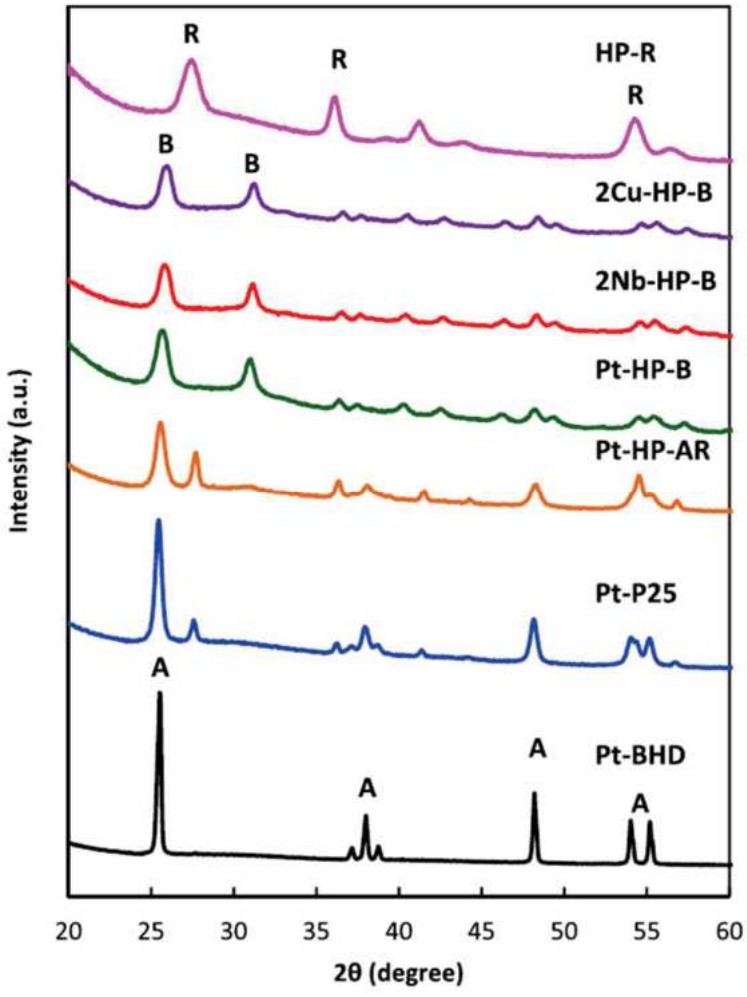

Figure 5.2. XRD patterns of used samples for photocatalytic tests

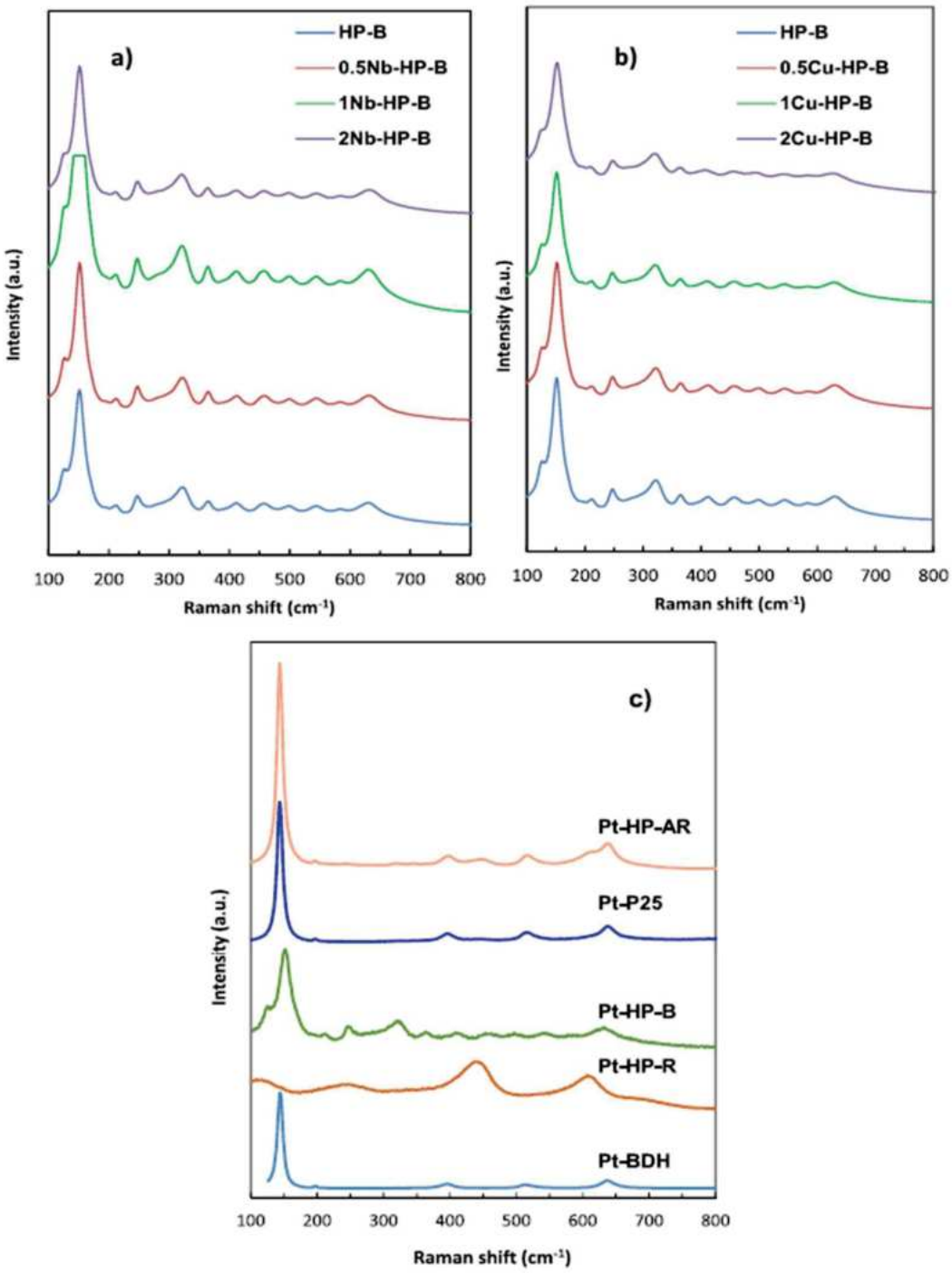

Figure 5.3. Raman spectra of pure brookite doped with different quantities of Nb a) and Cu b), some catalysts containing Pt c).

In Figure 5.3 a and b the Raman spectra of pure brookite are compared with those of brookite containing different percentages of Nb and Cu. Due to their small quantity and their high degree of dispersion in the TiO_2 matrix, the doping species did not make changes in the characteristic bands of brookite. In Figure 5.3 c the Raman spectra of some of the samples used are shown. Anatase shows

characteristic bands at 144, 196, 397, 513 and 639 cm^{-1}, rutile at 447 and 612 cm^{-1} and brookite at approx. 153, 323, 366, 413, 459, 500, 545, 584 and 633 cm^{-1}. Also in this case, the addition of Pt did not change the spectra of the different types of TiO_2.

Figures 5.4 a – c show the reflectance spectra of the catalysts. For the bare BDH sample (Figure 5.4 a) we note the typical shape of the anatase TiO_2 with an absorption edge at around 360 nm due to the transition of the photoexcited electrons from the valence band to the conduction band edge. Samples consisting of an anatase-rutile mixture (P25 and HP-AR) show a slight shift towards higher wavelengths due to the smaller band-gap of rutile compared to that of anatase. In all samples, the addition of Pt increases the absorption of light in the visible region without affecting the band-gap. The addition of tungsten (Pt-W-HP-AR) moves the absorption even more towards greater wavelengths.

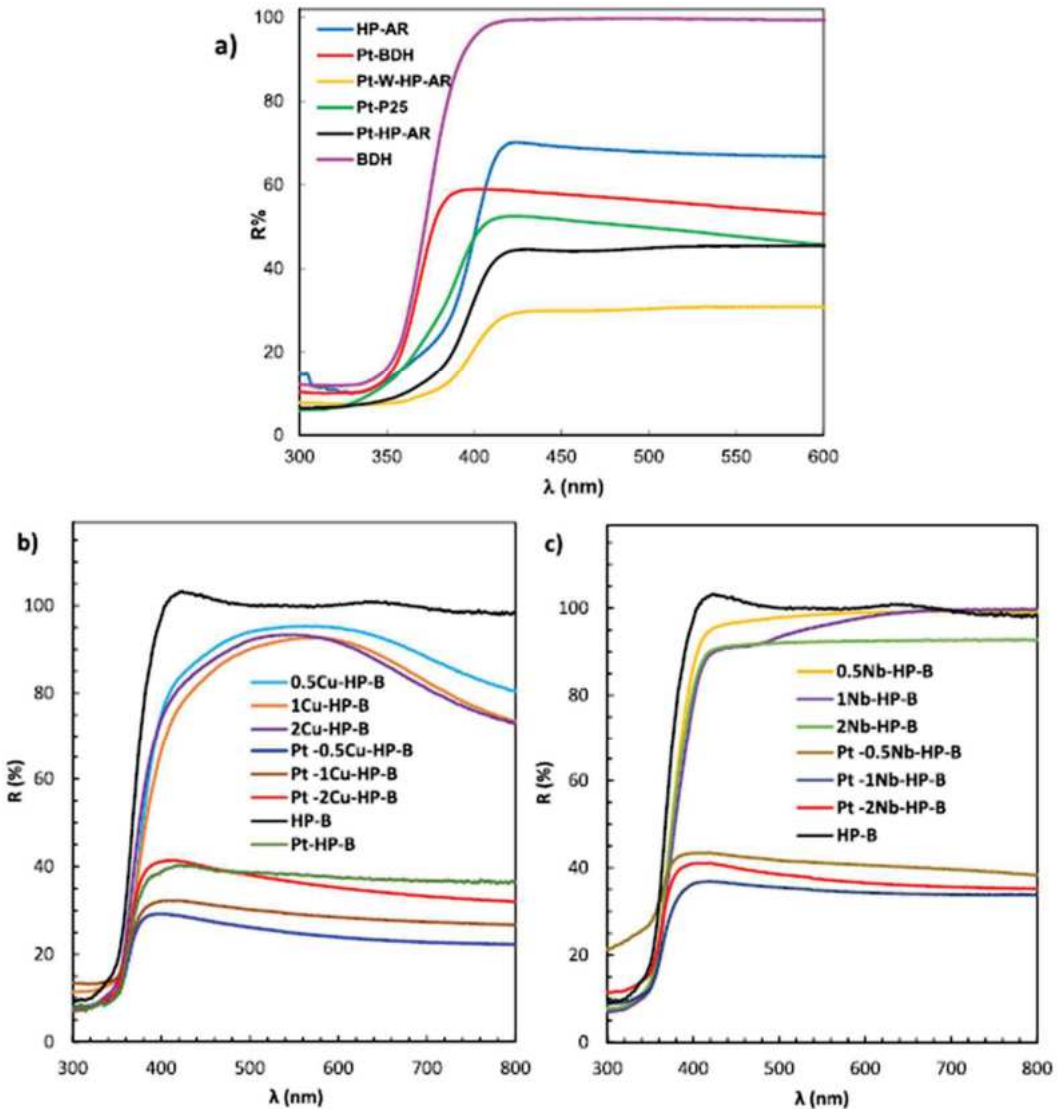

Figure 5.4. DRS spectra of the different photocatalysts

In the presence of Cu, Figure 5.4 b, the typical form associated with the presence of Cu species can be seen, and the increase in absorption between 400 and 600 nm which can be attributed to the d-d transition that occurs in Cu^{2+} ions [350]. No variation can be noticed, however, following the addition of Nb.

Table 5.1 Phase composition, band-gap (Eg), specific surface areas (S.S.A.) of the prepared samples. A = Anatase, R = Rutile; B = Brookite.

Sample	Phase	E_g (eV)	S.S.A. (m^2g^{-1})
P25	A, R	3.18	50
Pt-P25	A, R	3.10	50
BDH	A	3.20	10
Pt-BDH	A	3.26	10
HP-AR	A, R	2.92	73
W- HP-AR	A, R	2.96	79
Pt- HP-AR	A, R	2.98	78
Pt-W-HP-AR	A, R	3.10	67
Pt-HP-R	R	2.98	85
Pt-W-R	R	3.00	65
HP-B	B	3.26	100
1Cu- HP-B	B	3.18	92
Pt- HP-B	B	3.30	98
Pt-0.5Cu-HP-B	B	3.30	96
Pt-1Cu-HP-B	B	3.29	92
Pt-2Cu-HP-B	B	3.32	86
Pt-0.5Nb-HP-B	B	3.30	76
Pt-1Nb- HP-B	B	3.30	90
Pt-2Nb- HP-B	B	3.33	72

The band gap values, calculated using the modified Kubelka Munck function are shown in Table 5.1. The TiO_2-based photocatalysts are all active under UV-visible light irradiation having band gap values ranging from 3.30 at 2.92 eV.

Pure TiO_2 showed band gap values typical of the different TiO_2 polymorphs, which are little influenced by the photodeposition of Pt and by the addition of metal species.

The S.S.A. of the used samples (Table 5.1) ranges between 10 and 100 $m^2\ g^{-1}$ and the lowest values were found for the commercial powders. Generally, no significant variations, with respect to the corresponding naked TiO_2, were noticed after the Pt photodeposition whilst a little decrease was, sometimes, observed after the introduction of the other metal species. Then the different photoactivity of the various photocatalyst cannot be strictly related to the S.S.A. values.

SEM images (Figure 5.5 a – e) revealed that the different photocatalysts are constituted of aggregates of irregular spherical small particles which dimensions ranging between 100 and 500 nm. The particles sizes of home-made samples are smaller than those of commercial ones, due the lower synthesis temperature.

The addition of Pt or metal species did non influence the shape and the dimensions of the particles due to their low amount with respect TiO_2. EDX analyses (not reported for the sake of brevity) confirmed the presence of foreign species in quantities corresponding to the nominal ones.

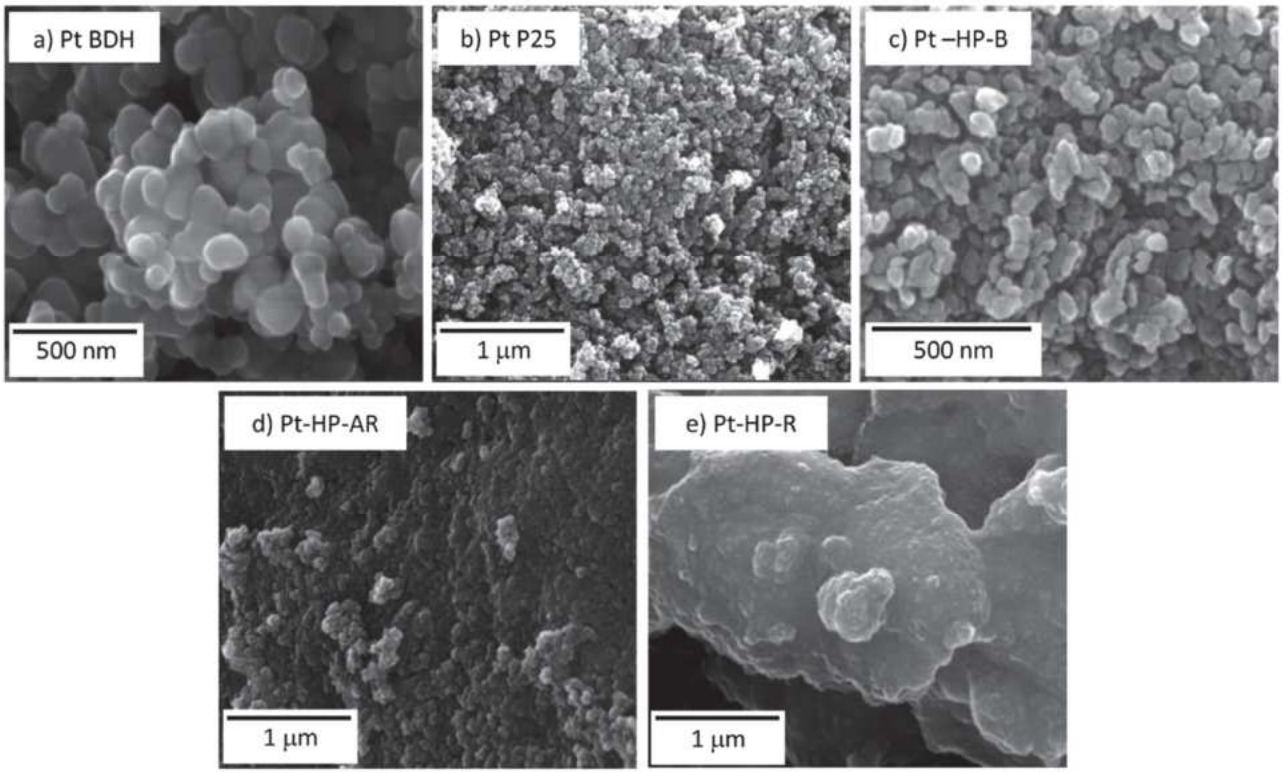

Figure 5.5. SEM micrographs of a – e) Pt loaded commercial TiO_2 BDH and P25 samples and some Pt-loaded home-prepared samples used in the photocatalytic runs

Photocatalytic process

In Figure 5.6 is reported a sketch of the photocatalytic oxidation of furfuryl alcohol. The initial steps could be the interaction of h^+ or hydroxyl radicals with the substrate producing furfural that is successively oxidized to 2-furoic acid. The over-oxidation products of these compounds are mainly aliphatic species (not identified), CO_2 and H_2O.

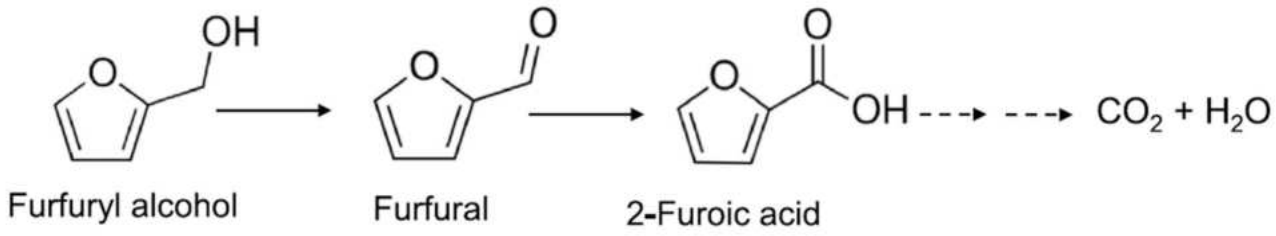

Figure 5.6. Scheme of the oxidation of furfuryl alcohol.

Table 5.2 shows the results of the photocatalytic tests performed with the UV lamp and the open reactor in terms of alcohol conversion and selectivity towards furfural, which was the main identified reaction product. In fact, only traces of 2-furoic acid and some peaks related to unknown intermediates were found in the reaction mixture. The activity of commercial samples P25 (anatase-rutile mixture) and BDH (anatase) was investigated at different pHs in order to identify the best operating conditions and compared with that of laboratory-prepared catalysts.

Table 5.2: Results of photocatalytic tests in aqueous solution obtained after 5 hours of UV irradiation with open reactor.

Sample	**pH**	**Conversion (%)**	**Sel. furfural (%)**	**Yield. furfural (%)**
P25	2	92.4	0.91	0.84
P25	6.7	49.6	3.91	1.94
P25	10	68.8	1.77	1.22
BDH	5.5	68.0	1.75	1.19
BDH	10	70.5	4.14	2.92
HP-AR	10	79.5	4.27	3.39
W-HP-AR	10	44.5	12.10	5.36
Pt-HP-AR	10	70.7	8.51	6.01

Tests were carried out at the “natural” pH of the solution (6.7) and at both acidic (pH = 2 for HCl) and alkaline (pH = 10 for NaOH) conditions. The alcohol conversion in the presence of P25 showed

the following trend: pH = 2 > pH = 10 > pH = 6.7 and the selectivity decreased as the conversion increased. A higher conversion derives from a greater oxidizing power of the catalyst which indistinctly oxidizes both the furfuryl alcohol and the formed furfural with a consequent low selectivity. The increased activity at pH 2 and 10 can be attributed to the formation of ·Cl and ·OH radicals, respectively [125]. It is not easy to correlate the photoactivity to the variation of the pH of the solution due to the occurrence of different phenomena related both to the organic substrate and the surface of the catalyst [125]. In our system, being the pK_a of FuA 9.55, the different activity cannot be directly linked to a different distribution of its protonated and deprotonated forms.

By using the BDH sample at natural pH and pH = 10, almost the same conversion was obtained (approx. 70%) while the selectivity was greater at pH = 10 (ca. 4 instead of 1.7).

In order to tentatively explain these different selectivity values, also the degradation of furfural in the presence of BDH was carried out at pH= 5 and 10 (Figure 5.7) and not significant differences of the concentration versus time were found. Instead, by comparing the values of the concentration after 2 h of adsorption in the dark (Figure 5.8), a slightly higher absorption value was noticed at pH 5 that could justify the lower selectivity, even if the behavior in the dark is not always strictly correlated to that under irradiation.

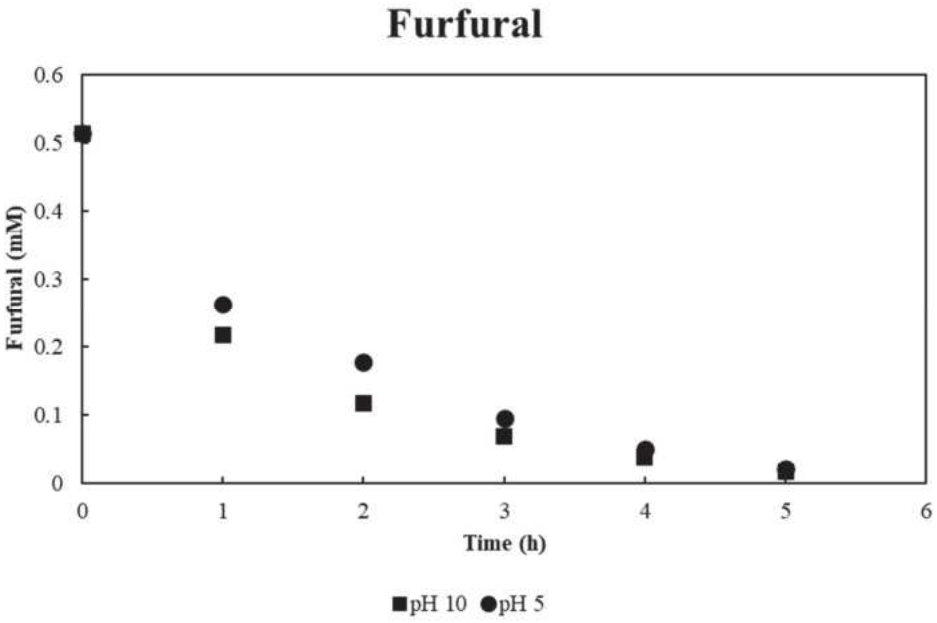

Figure 5.7: Concentrations of furfural versus time in the presence of BDH for initial pH's of 5 and 10.

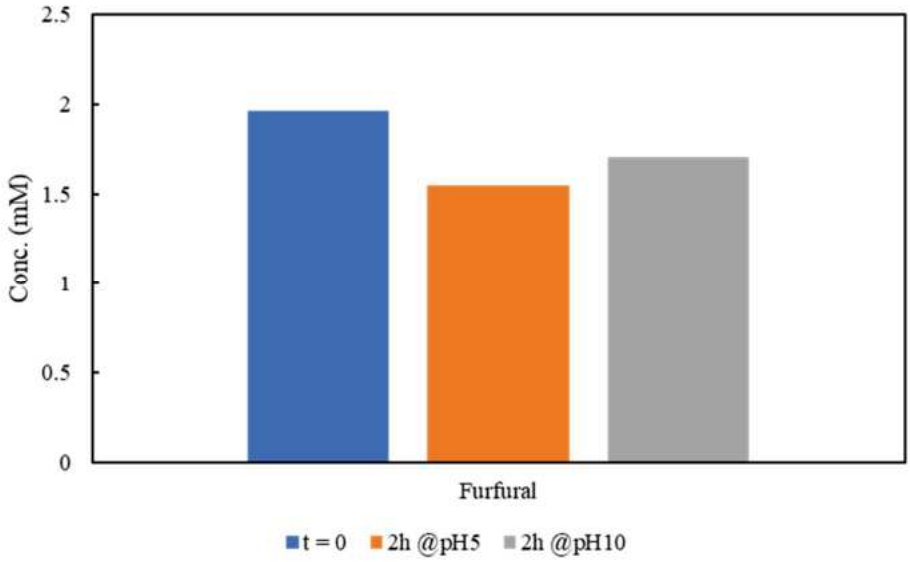

Figure 5.8. Initial concentration of furfural (t=0) and after 2 h of adsorption in the dark in the presence of BDH at pH= 5 and pH=10.

With the HP-AR sample at pH = 10 a conversion of 79% was obtained with a selectivity of ca. 4%. The prepared sample turned out to be more active than the commercial ones with an aldehyde yield of 4.4%. In order to improve the efficiency of the process, the HP-AR sample was modified by doping with W or photodeposition of Pt. After the introduction of W, a significant decrease in conversion up to 44% and an increase in selectivity at 12% (corresponding to a yield of about 5%) were observed while in the presence of Pt a conversion of 71% and a selectivity of 8.5% (yield 6%) were obtained. In all cases, the selectivity to acid was negligible (<1%). Since in the open reactor the best results were obtained with the Pt-HP-AR sample, home-prepared TiO_2-based samples on which Pt was photodeposited were used under anaerobic conditions in order to produce H_2 simultaneously with the furfuryl aldehyde.

Photocatalytic tests were carried out in the closed reactor also at varying pH (Table 5.3). With the commercial catalyst Pt-BDH at the highest pH value a fairly high conversion (approx. 55%) was obtained with the greatest selectivity to furfural between the commercial samples and an intermediate amount of hydrogen. With the Pt-HP-AR photocatalyst instead at pH 4 the conversion reached only 25% with a selectivity to furfural of ca. 16 % (yield 3.9 %) and a concentration of H_2 equal to 0.026 mM, while at pH 10 a conversion of 67%, a selectivity of 6% (yield in aldehyde 4%) and a hydrogen amount equal to 0.49 mM were measured. By taking this into account, the other tests were carried out at pH = 10. Under the same conditions (pH 10, presence of Pt) the sample prepared in the laboratory (Pt-HP-AR) was more active than the commercial P25 (Pt-P25) in terms of both conversion, selectivity and production of hydrogen. In this case the different photoactivity cannot be

attributed to different crystalline phases of TiO_2 since both samples consist of an anatase-rutile mixture, but rather to intrinsic properties of the two catalysts (degree of hydroxylation, surface acid-base properties, crystallinity, etc.) [17,206,351,352] deriving from the different preparation conditions. To try to improve efficiency, different catalysts based on the various polymorphic forms of TiO_2 were used, bare and variously modified, to shift the absorption in the visible region and to increase its photoactivity. With the pure HP-AR sample no hydrogen is obtained, confirming the essential role of Pt [17]. Doping with W, although it is reported in the literature as one of the elements that introduced into TiO_2 increases its photoactivity, in this case had no beneficial effect either alone or when contemporary present with Pt [283]. Since rutile and brookite prepared in laboratory showed good photocatalytic activity towards the production of H_2 in solutions containing glucose [17,353], these polymorphs were tested for our reaction. In this case the rutile with Pt gave good results in terms of conversion and selectivity but no hydrogen was obtained; the addition of W also made it possible to obtain a fair amount of H_2 and CO_2, indicating the latter a higher degree of mineralization than that obtained with the other samples. From the point of view of furfural production with this photocatalyst the highest yield value (approx. 5.8%) was obtained with a conversion of 37%. Pure brookite showed moderate activity (conversion 28% and selectivity to aldehyde approx. 9%), the addition of Pt not only allowed the production of H_2 but also increased conversion and selectivity, reaching a yield greater than 5%.

By doping brookite with small amount of Cu, the oxidizing properties were enhanced (higher conversion and lower selectivity compared to the Pt-HP-B sample) and hydrogen was also produced without the presence of a noble metal such as Pt. The simultaneous presence of Pt and Cu or Nb allowed to obtain more hydrogen and to increase conversion and yield due both to the enhanced transfer charge process and surface properties of the modified powders [354,355]. In our system, the modified HP-B proved to be effective both for the partial oxidation of furfuryl alcohol and to produce hydrogen. As far as 2-furoic acid is concerned, low selectivity and yield values were obtained with all the catalysts. The best results were observed with the HP-AR, HP-B and Pt-2Nb-HP-B samples.

In anaerobic conditions the most active catalyst for the production of hydrogen was Pt-HP-AR while for the production of aldehyde the best results were obtained with the Pt-2Cu-B sample, highlighting that different catalysts feature are involved in the oxidation and reduction processes.

The results obtained at the same FuA conversion degree (25%) with the most efficient samples are reported in Figure 5.9. At this conversion the sample Pt-1Cu-HP-B was the most active photocatalyst being the selectivity towards furfural after 1.5 h of irradiation ca. 30%. Nevertheless, for longer reaction times, due to the high oxidant power of this sample, both FuA and furfural were converted

with a consequently decrease of the selectivity at 5 h (Table 5.1). The contemporary presence of Pt and W showed a beneficial effect both on the FuA conversion and furfural selectivity. The highest selectivity towards 2-furoic acid was ca. 10% with the sample Pt-HP-R.

Table 5.3: Results of photocatalytic tests in aqueous solution obtained after 5 hours of UV irradiation with closed reactor.

Sample	**pH**	**Conversion (%)**	**Sel. furfural (%)**	**H_2 (mM)**	**CO_2 (mM)**	**Yield. furfural (%)**
Pt-BDH	2	68.4	1.34	0.203	0.068	0.91
Pt-BDH	6.1	84.3	1.57	0.00	0.000	1.32
Pt-BDH	10	55.9	4.78	0.069	0.009	2.67
Pt-P25	10	62.5	4.48	0.153	0 000	2.79
HP-AR	10	35.0	7.33	0.000	0.000	2.56
W-HP-AR	10	25.0	7.38	0.000	0.000	1.84
Pt-HP-AR	10	67.3	6.15	**0.490**	0.016	4.14
Pt-HP-AR	4.1	25.0	15.5	0.026	0.022	3.87
Pt-W-HP-AR	10	52.0	4.98	0.055	0.014	2.59
Pt-HP-R	10	35.1	11.9	0.000	0.019	4.19
Pt-W-HP-R	10	37.0	15.6	0.036	**0.033**	5.77
HP-B	10	28.0	9.35	0.000	0.015	2.61
Pt-HP-B	10	44.0	12.3	0.119	0.028	5.41
Cu-HP-B	10	54.0	7.4	0.057	0.013	3.99
Pt-0.5Cu-HP-B	10	60.5	12.0	0.166	0.016	7.30
Pt-1Cu-HP-B	10	73.0	10.2	0.078	0.015	7.50
Pt-2Cu-HP-B	10	70.5	10.8	0.143	0.075	7.60
Pt-0.5Nb-HP-B	10	78.7	9.58	0.123	0.025	7.50
Pt-1Nb-HP-B	10	68.0	9.83	0.252	0.027	6.70
Pt-2Nb-HP-B	10	85.9	8.13	0.183	0.035	7.00

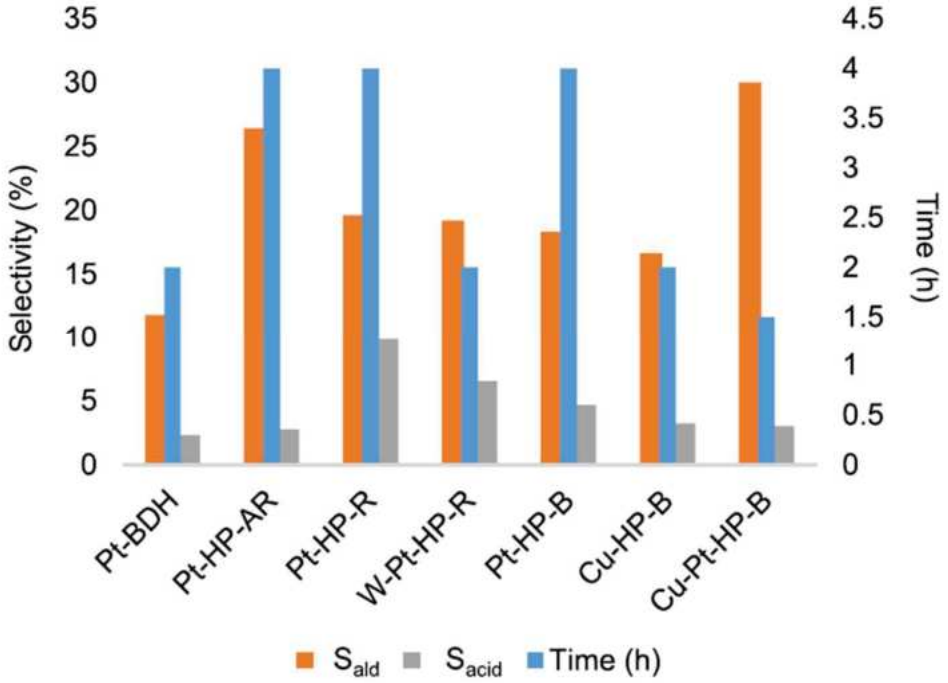

Figure 5.9. Results obtained with the different samples at 25 % FuA conversion. Time necessary to reach 25 % conversion, selectivity to furfuraldehyde (S_{ald}) and furoic acid (S_{acid}) at 25 % FuA conversion. (pH = 10). Initial FuA concentration 1 mM, runs were executed in a closed reactor under UV light in a nitrogen atmosphere.

Chronoamperometry analysis, i.e.: current transient under monochromatic light by manually stopping irradiation on the sample, has been performed for the catalysts providing the highest FuA conversion (Pt-2Nb-HP-B), the highest H_2 production rate (Pt-HP-AR) and, for comparison, for HP-B and HP-AR (see Figure 5.10). HP-AR without and with Pt, do not show evidence of recombination phenomena. Indeed, photocurrent raises reaching an almost stationary value soon after irradiation. Conversely in the case of HP-B the photocurrent raises slowly probably due to a low mobility of photogenerated carriers. This leads to charge trapping phenomena and consequent inversion of band bending explaining why at high wavelength a cathodic photocurrent is measured. The Nb doping enhances the concentration of charge carriers and thus photoconductivity of the catalyst reducing or even canceling the recombination phenomena.

In Figure 5.11 the results of the photocatalytic test under simulated solar light irradiation are showed. Also, in this case the best results were obtained in the presence of modified TiO_2 brookite samples confirming the high activity of this polymorph both in the partial oxidation of alcohol and in the H_2 formation [17,300].

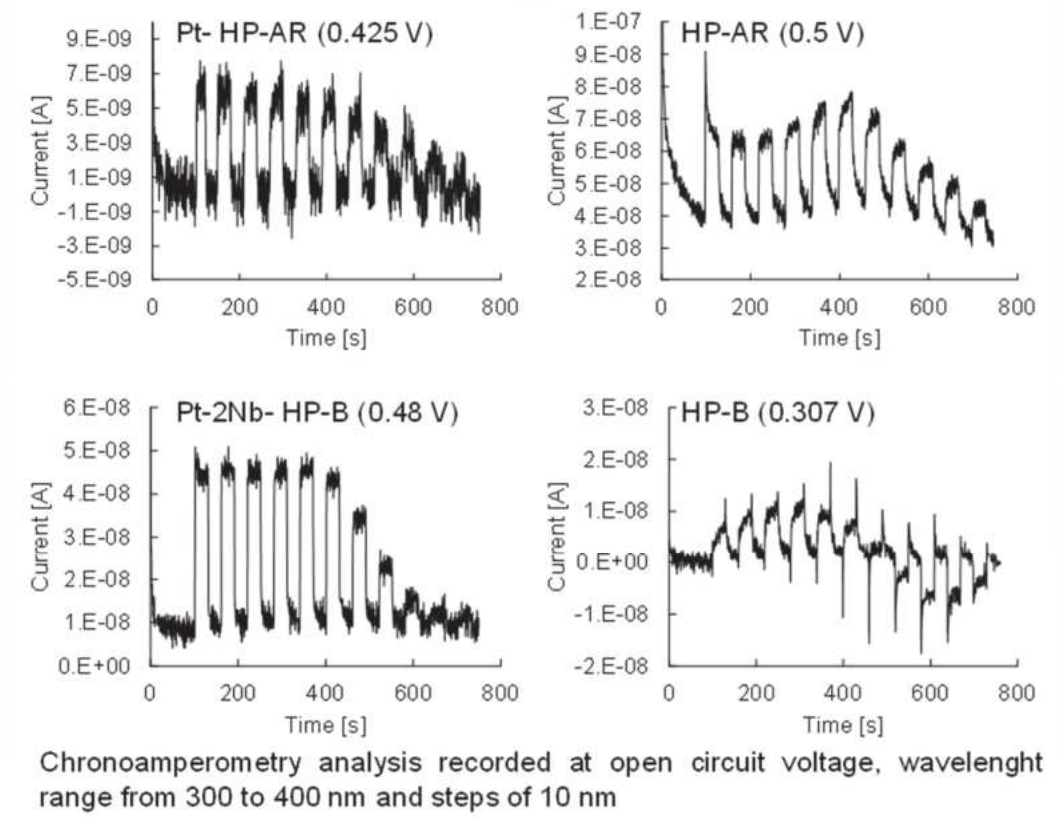

Figure 5.10. Chronoamperometry analysis of Pt-2Nb- HP-B, Pt- HP-AR, HP-B and HP-AR recorded at Open Circuit Voltage, wavelength from 300 to 400 nm and steps of 10 nm.

The low selectivity values towards furfural and 2-furoic acid and the formation of small CO_2 amount (indicating a low mineralization degree) indicate the formation of different not identified intermediates, in accordance with HPLC analyses.

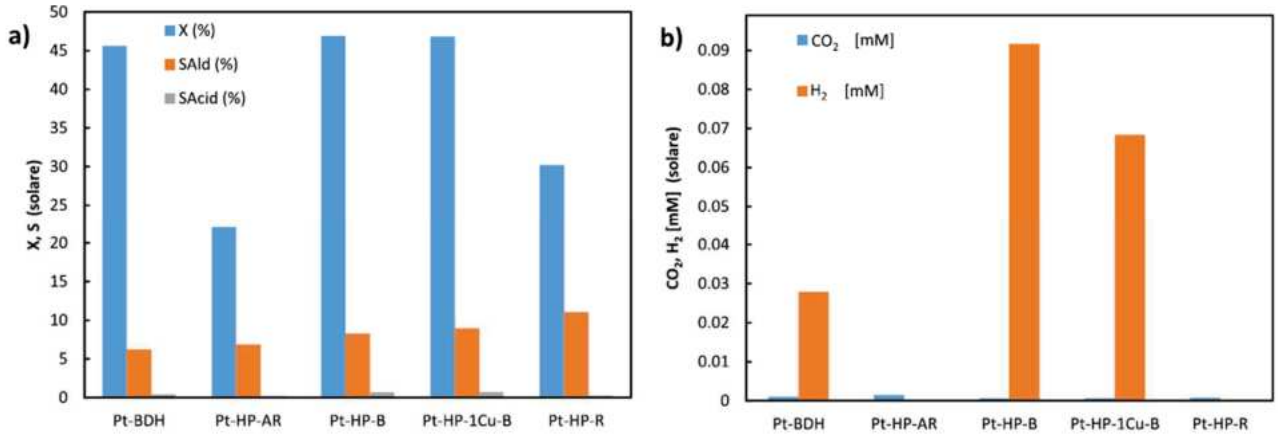

Figure 5.11. Conversion and selectivity a), and CO_2 and H_2 concentration b), after 5 h of simulated solar light irradiation. Initial FuA concentration 1 mM, pH = 10.

Photoelectrocatalytic process

Photoelectrocatalytic processes were carried out using cheap and high durable TiO_2 nanotubes as photoanode and Ni foam as cathode. Large array of TiO_2 NTs were grown by anodizing commercially pure titanium in ammonium fluoride ethylene glycol solution as described in detail in the experimental section (see Figure 5.12). After annealing at 450°C the nanotubes show the Raman bands of anatase (see Figure 5.13).

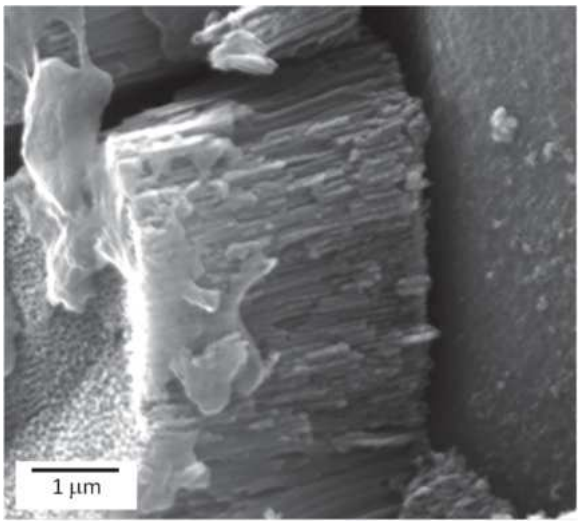

Figure 5.12. SEM pictures of TiO_2 Nts photoanode used for photoelectrocatalytic tests

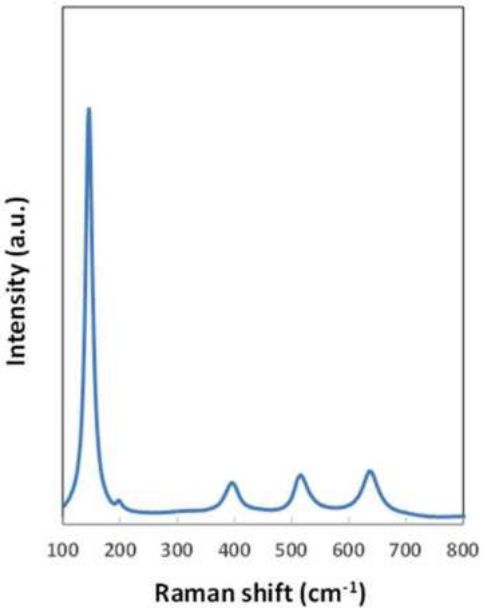

Figure 5.13. Raman spectrum of TiO_2 nts photoanode used for photoelectrocatalytic tests

Photoelectrochemical experiments were carried out in a three electrode cell (see Figure 5.14) containing 0.5 M Na_2SO_4 aqueous solution. Light irradiation allows the formation of electron - hole

pairs, that are efficiently separated inside the space charge region of the semiconductor due to the potential difference at the metal/electrode/electrolyte interface, in turn generated by applying a cell bias. Holes produced in the valence band of TiO_2 are strongly oxidants and thus can oxidize both water and FA in the electrolytic solution. Electrons can easily reach the cathode through the external circuit since they are collected by the Ti beneath the TiO_2 layer. Table 5.4 summarizes all the experimental details related to the operating conditions and obtained results.

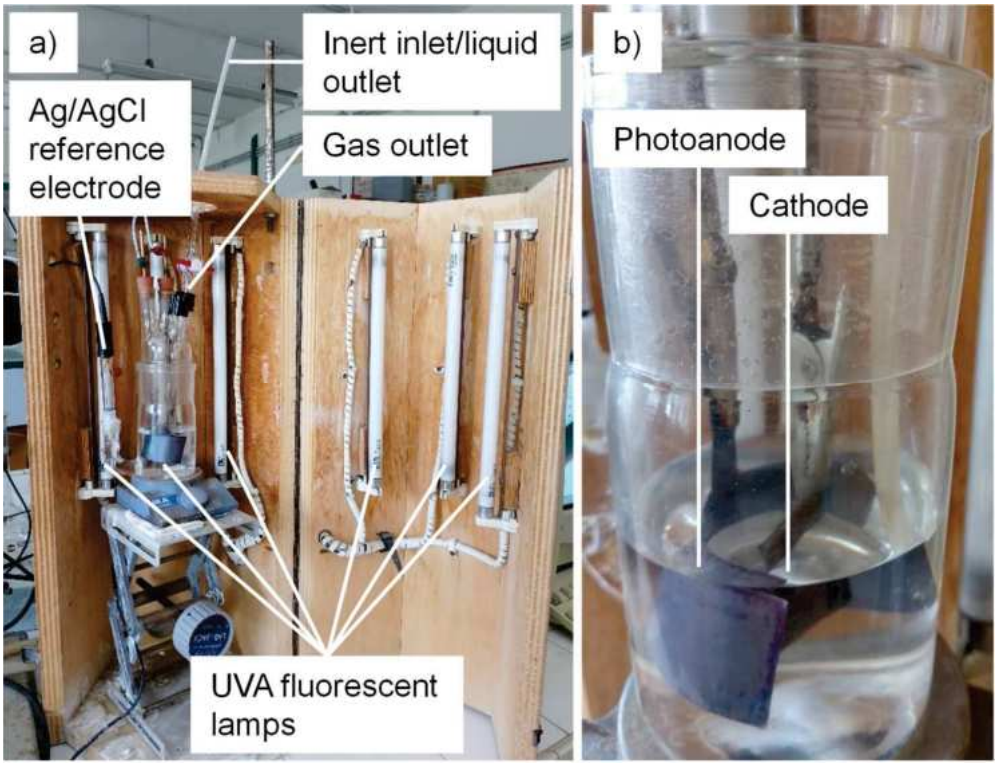

Figure 5.14: Pictures of a) PEC system overview and b) magnification of photoanode and cathode

Table 5.4: Results of photoelettrocatalytic (PEC) tests in aqueous solution obtained after 5 hours, FuA initial concentration 100 mM, photoanode TiO_2 NTs, I_{ph}: photocurrent, applied potential 0.5 (V vs Ag/AgCl), X: FA conversion, S_{ald}: selectivity towards furfural, S_{acid}: selectivity towards 2-furoic acid, FE Faradic efficiency.

Cathode	**I_{ph} (mA)**	**Cell Voltage (V)**	**X (%)**	**S_{ald} (%)**	**FE_{ald} (%)**	**S_{acid} (%)**	**FE_{acid} (%)**	**CO_2 (mM)**	**H_2 (mM)**	**FE_{H2} (%)**
Ni foam	2.3	1.28	6.4	0.42	1.92	0	0	0.041	0.484	61

The FA oxidation has a very poor selectivity toward the aldehyde as suggested by the data of Table 5.4. Indeed, HPLC analysis of the solution as a function of reaction time reveals the presence of not identified peaks thus suggesting the formation of products arising from FuA oxidation other than furaldehyde and 2-furoic acid. Moreover, we have also to take into account that FuA oxidation

competes with oxygen evolution. Figure 5.14 shows the cyclic voltammetry recorded in 0.5 M Na_2SO_4 solution without and with the addition of 0.1 M FuA using a Pt mesh as working electrode. As expected, by scanning the potential toward the anodic direction a current starts to circulate at 1.1 V vs Ag/AgCl due to the onset of oxygen evolution reaction, as it can be better appreciated in the inset of Figure 5.15, whose standard equilibrium potential at pH 7 is 0.6 V vs (Ag/AgCl). However, when FA is present in the electrolyte a current plateau appears in the cyclic voltammetry at ~ 1.5 V, that can be due to FuA adsorption on Pt mesh then stripped as furfural and/or 2-furoic acid at potential more positive than ~ 1.7 V (see inset).

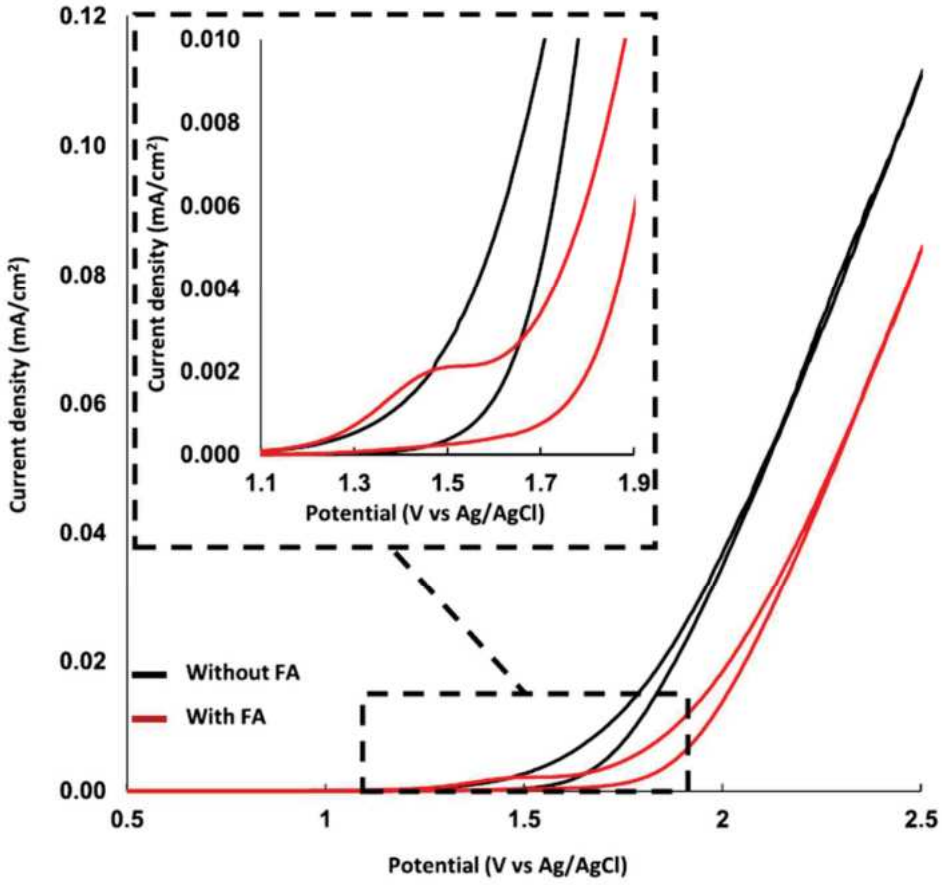

Figure 5.15. Cyclic voltammetry executed in Na_2SO_4, with and without 100 mM FA, red and black lines respectively.

Comparison of the current – potential transient without and with the addiction of FuA clearly proves that oxygen evolution is competitive with respect to FuA oxidation, thus explaining the low values of selectivity assessed for the photocatalytic process (max ~ 16% after 5 hours of irradiation) as well as for the photoelectrocatalytic process. Notably, oxidation of water produces oxygen that can diffuse toward the cathode, where its reduction will in turn compete with H_2 evolution thus reducing the

hydrogen production rate during the photocatalytic process and the faradic efficiency during the photoelectrocatalytic process.

In Table 5.5 the best results obtained by photocatalytic and photoelectrocatalytic processes are compared. Both the partial FuA oxidation reaction rate and H_2 evolution rate, normalized for the lamp specific power to account for the different photon flux, are higher for PEC process. Notably, the employed materials both at the anode (TiO_2 NTs) and at the cathode (Ni foam) are Pt free and, since they are chemically and physically stable during the runs, they can be used for many tests without losing their activity. Therefore, PEC is a promising strategy for the valorization of biomasses with simultaneous H_2 production in spite the cost of the bias.

Table 5.5: Comparison after 5h of reaction of the highest HER and furfural rate formation, photon flux, their ratio for photocatalytic tests (PC) and photoelectrocatalytic (PEC) tests and power supplied for PEC.

Test	PC	PC	PEC
Sample	Pt-HP-AR	Pt-2Cu-HP-B	TiO_2 NTs/Ni foam
HER rate (mol)	$49 \cdot 10^{-6}$		$68.5 \cdot 10^{-6}$
Furfuraldehyde production rate (mol)		$12 \cdot 10^{-6}$	$18.9 \cdot 10^{-6}$
Photon flux (Einst)	0.135	0.135	0.00486
QE HER ((mol)/(Einst))	$3.63 \cdot 10^{-4}$		$1.41 \cdot 10^{-2}$
QE Furfural ((mol)/(Einst))		$8.85 \cdot 10^{-5}$	$3.89 \cdot 10^{-3}$
Power supplied (mW)	-	-	0.051

5.4. Conclusions

At the best of our knowledge, for the first time the reforming of furfuryl alcohol in aqueous solution was carried out by means of heterogeneous photocatalysis under green experimental conditions by using TiO_2 based photocatalysts. Although the conversion values and the H_2 production were not high, we proved the effectiveness of our system even under visible light irradiation and the results are interesting in the view of the utilization of reactors working in continuous and in the presence of a selective membrane with the aim of recovering the formed valuable intermediates by preventing its further oxidation, by considering also the high degradation rate of furfural.

The presence of Pt and metal species resulted essential to produce both furfural and H_2.

The structural features of the photocatalysts, the modification of the surface due to different pH conditions (responsible for different adsorption), and the types of sites present on the different

samples influenced the conversion of the substrate and the selectivity towards the partial oxidation products and allowed to enhance the performance of the process. The best results were obtained at pH=10 and by using home prepared TiO_2 brookite containing both Pt and Cu or Nb.

Interesting results were obtained by the photoelectrocatalytic reforming of aqueous solutions containing FuA carried out using TiO_2 NTs as photoanode and Ni foam as cathode. In this case, although the applied bias represents an additional cost for the process, higher H_2 and furfural production rates were obtained with respect to PC although the absence of Pt. Moreover, the electrodes are chemically and physically stable in the employed experimental conditions, thus they can be reused for other runs.

6. Effect of pH and applied bias on H_2 and HVA products through photoelectrocatalytic glycerol oxidation

This published study [221] explores how pH and applied bias influence the generation of H_2 and high-value-added products resulting from glycerol photooxidation, specifically targeting 1,3-dihydroxyacetone (DHA) and glyceraldehyde (GA), within a photoelectrochemical cell. TiO_2 NTs with a length of 760 nm were utilized as the photoanode, while Ni foam served as the cathode. The experiments were carried out under acidic, neutral, and alkaline pH conditions, with applied biases ranging from 0.1 to 1 V vs. Ag/AgCl reference electrode.

The findings demonstrated that the highest faradaic efficiency towards high-value-added products, namely DHA and GA, was achieved at pH 7 with an applied bias of 0.5 V vs. Ag/AgCl, and this efficiency remained stable at higher bias values. Notably, at pH levels of 2 and 7, both glycerol mineralization into CO_2 and H_2, and glycerol photooxidation into DHA and GA were more pronounced. Conversely, at higher pH, the faradaic efficiency towards DHA, GA, and CO_2 decreased, while the photocurrent increased. This observed trend suggests a heightened water splitting effect at higher pH, leading to a reduction in faradaic efficiency towards H_2 due to subsequent reactions with O_2 in the gas phase.

6.1. Introduction

In this work, the effect of pH and applied bias on hydrogen production by glycerol photoreforming and water splitting was studied to enhance both the hydrogen evolution rate and the FE towards DHA and GA. Special attention was paid to the development of a photoelectrochemical cell employing both PGM-free cathode and photoanode to point towards low-cost alternative materials compared to the noble metal-based catalysts and to overcome possible poisoning effects due to the presence of organic species. As supplied commercial Ni foam was used as cathode. The photoanode was prepared by anodizing Ti foils in a fluoride containing electrolyte to induce the growth of large arrays of well aligned TiO_2 nanotubes in the attempt to widen the active surface of the electrode. Photoelectrochemical tests were carried out to assess the formation of a n-type semiconducting material, while electrochemical impedance measurements allowed to study the behavior of the photoanode/electrolyte interface under irradiation. The concentration of H_2 in the gas phase was monitored by gas chromatography (GC), while high performance liquid chromatography (HPLC) was used to determine the concentration of DHA and GA in the liquid phase.

6.2. Experimental section

TiO_2 NTs were grown on Ti foil (purity > 99.7 % and 0.127 mm thickness, Sigma Aldrich). Ti foil was cut and etched in a solution containing hydrofluoric acid (Sigma Aldrich, 39.5 %), nitric acid (Sigma Aldrich, 69 %), and deionized water in 1:1:3 volume ratios for 15 seconds. Then, it was cleaned in acetone and ethanol through ultrasonic treatment for 5 minutes each and rinsed with deionized water before being dried in air. The TiO_2 nanotubes were formed in an ethylene glycol (Sigma Aldrich, 99.8 % anhydrous) solution containing 0.25 %wt NH_4F (Sigma Aldrich, ≥ 98 %) and 0.75 %wt deionized water. The anodization of 25 cm^2 of immersed surface was performed using a two-electrode configuration with aluminum foil as the cathode and maintaining a constant potential of 45 V for 10 minutes. Post-anodizing, annealing at 450°C for 3 hours under air exposure was carried out to induce crystallization in the TiO_2 nanotubes. The cathode employed in the process was 6 cm^2 of commercial Ni foam (Goodfellow).

XRD, SEM, and Raman spectra were performed. Photocurrent transients were carried out by using TiO_2 NTs as the working electrode. The electrolyte consisted of a 0.5 M Na_2SO_4 aqueous solution. Current transients were recorded with applied potentials steady, ranging from 0.5 V to -0.5 V vs Ag/AgCl. EIS measurements were carried out in 0.5 M Na_2SO_4 aqueous solution employing a Parstat 2263 potentiostat. Further details are provided in the experimental section (Section 2).

Photoelectrocatalytic experiments were carried out in a 450 ml undivided glass cell by using three electrodes. The setup used Ni foam as the counter electrode and an Ag/AgCl electrode as the reference. The solution underwent external illumination from six UVA fluorescent lamps emitting light at a maximum wavelength of 365 nm (8 W). Before each test, Helium was bubbled through a 150 ml aqueous solution for approximately 30 minutes. The control over the cell potential was maintained by using a CH Instrument 630B Series potentiostat. A 0.5 M Na_2SO_4 solution was used as the electrolyte (pH ~ 7), the glycerol starting concentration was 0.1 M, and an applied potential up to 1 V vs Ag/AgCl was employed. To study the effect of the pH, H_2SO_4 was added dropwise, or a KOH solution was used as the electrolyte. The quantification of glycerol and the concentration of reaction intermediates was performed by HPLC. The analysis of gaseous species accumulated in the reactor headspace was carried out by using GC. Further details are provided in the experimental section (Section 2). The FE towards the products was calculated using Equation 2.4, where z, the electrons exchanged, equal to 2 for H_2, DHA, and GA and 14/3 for CO_2 according to the anodic and cathodic semi-reactions in Equations 6.1 – 6.3.

$Eqn.\,6.1)$ $\qquad Photoanode: C_3H_8O_3 + 2h^+ \rightarrow C_3H_6O_3 + 2H^+$

$Eqn.\,6.2)$ $$Photoanode: C_3H_8O_3 + 3H_2O + 14h^+ \rightarrow 3CO_2 + 14H^+$$

$Eqn.\,6.3)$ $$Cathode: 2H^+ + 2e^- \rightarrow H_2$$

where $C_3H_6O_3$ is DHA or GA.

6.3. Results and discussion

Figure 6.1a shows the SEM image of TiO_2 NTs after the anodization and annealing steps. The micrograph distinctly exhibits the successful growth of a large array of TiO_2 NTs, showing an average length of 760 nm approximately, in line with previous results [356]. The XRD pattern presented in Figure 6.1b shows distinct peaks corresponding to bare titanium [265], whereas the Raman spectra depicted in Figure 6.1c exhibits distinctive peaks corresponding to anatase at 144 cm^{-1}, 196 cm^{-1}, 397 cm^{-1}, 513 cm^{-1}, and 639 cm^{-1} [271]. According to previous findings, the annealing process involves two concurrent phenomena. Firstly, the amorphous TiO_2 within the nanotubes transforms into anatase, while the underlying layer at the interface between titanium and the nanotubes to rutile. This formation of rutile promotes a strong adhesion between the nanotubes and the metallic substrates. When the system is subjected to a thermal treatment at 450°C in an air environment for 3 hours, it results in a 140 nm thick rutile layer. Furthermore, the nanotube wall primarily consists of anatase crystals with a cylindrical morphology, extending several hundred nanometers along the nanotube axis [357].

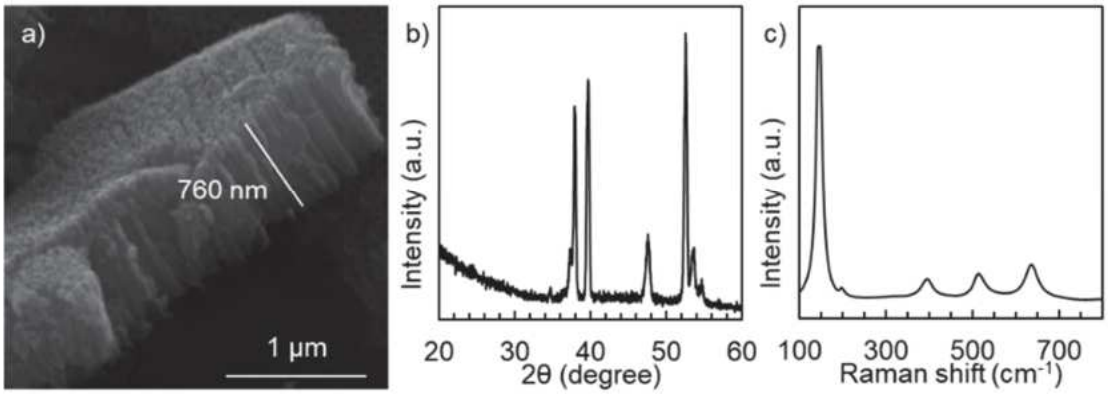

Figure 6.1. a) SEM picture, b) XRD pattern, and c) Raman spectra of TiO_2 NTs

Photocurrent transients reported in Figure 6.2 show an anodic photocurrent, confirming the n-type semiconductor characteristics of the oxide. At approximately -0.5 V vs Ag/AgCl the photocurrent

registered was close to zero, this value, as an estimate for the flat band potential, is in line with others documented in the literature [155].

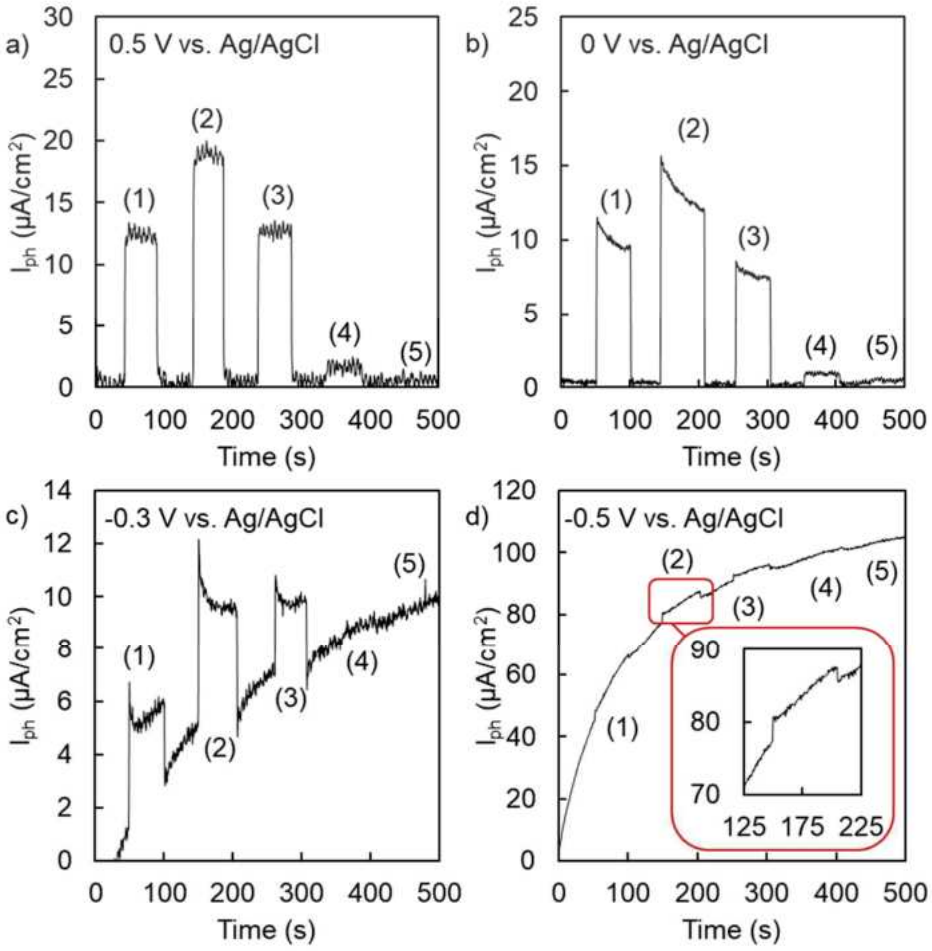

Figure 6.2. photocurrent transient executed at pH 7 and a) 0.5 V, b) 0 V, c) -0.3 V, and d) -0.5 V vs. Ag/AgCl using monochromatic light at various wavelength: (1) 300 nm, (2) 330 nm, (3) 350 nm, (4) 380 nm and (5) 400 nm.

Figure 6.3 shows the EIS spectra obtained in a 0.5 M Na_2SO_4 solution at 0.5 V vs. Ag/AgCl. The setup involved employed TiO_2 NTs as the working electrode, Ni foam as the counter electrode and an Ag/AgCl reference electrode. The EIS spectra were carried out both in the absence and in the presence of 0.1 M glycerol, with and without UV irradiation. All the spectra were fitted by using the equivalent circuit in Figure 6.3. This circuit includes elements representing different parameters: R_s represents solution resistance, R_{CT} the charge transfer resistance, and $Q_{SC,el}$ the capacitance of TiO_2. The charge transfer resistance is related to the exchange current density that takes into account the kinetic constants (i.e., rate constants, k) of the oxidation reactions, in agreement with the specific reaction mechanism. The best fitting parameters are reported in Table 6.1.

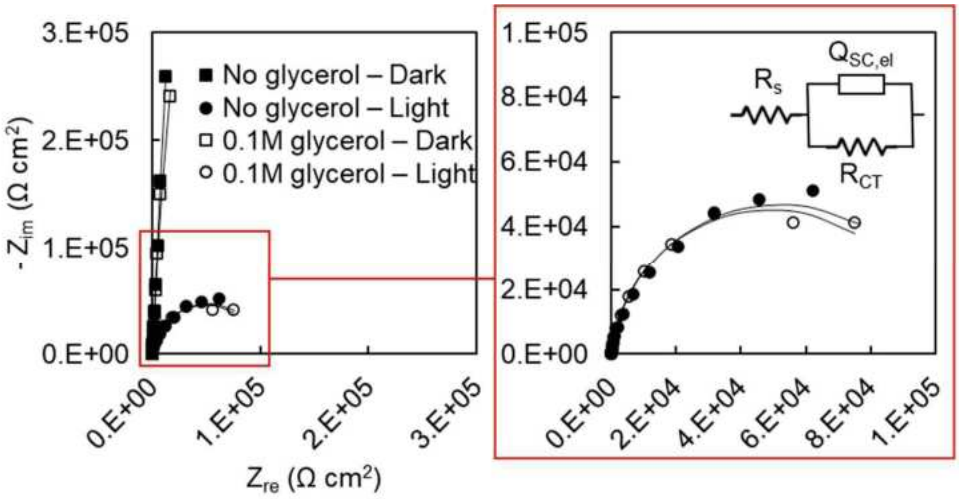

Figure 6.3. EIS spectra carried out at pH 7 and 0.5 V vs Ag/AgCl without and in the presence of glycerol and irradiation.

Table 6.1. Best fitting parameters of EIS spectra carried out at pH 7 and 0.5 V vs Ag/AgCl without and in the presence of glycerol and irradiation.

		No glycerol Dark	**No glycerol Light**	**0.1 M Glycerol Dark**	**0.1 M Glycerol Light**
R_s	(Ω cm^2)	96	86	73	73
R_{CT}	(Ω cm^2)	$4.4 \cdot 10^6$	$1.1 \cdot 10^5$	$4.0 \cdot 10^6$	$9.8 \cdot 10^4$
$Q_{sc,el}$	(S s^n cm^{-2})	$6.0 \cdot 10^{-6}$	$7.8 \cdot 10^{-6}$	$6.4 \cdot 10^{-6}$	$8.3 \cdot 10^{-6}$
n	(adm)	0.974	0.945	0.975	0.946

The influence of light irradiation on the electrode/electrolyte interface is notably evident except for R_s which shows a minor impact from both the irradiation and the presence of glycerol. Under dark conditions, the recorded R_{CT} is notably high. Additionally, the optimal fitting exponent 'n' for $Q_{sc,el}$ approximates 1, consistent with the expected behavior of an almost perfect n-type semiconductor. During post-irradiation, a substantial reduction in R_{CT} occurs, closely linked to the amplified concentration of photocarriers and in agreement with the increased capacitance. However, during illumination, lower R_{CT} are recorded in a 0.1 M glycerol-containing solution compared to estimates in a glycerol-free solution. This confirms that, from a kinetic point of view, the overall reaction is less demanding under irradiation in the glycerol-containing solution.

Photoelectrocatalytic results are detailed in Table 6.2. Generally, under constant pH conditions, an increase in the applied bias results in an increase of the cell potential. Notably, at fixed applied bias, the cell potential increases as the pH increases. The same trends are observed for the photocurrent and thus for the reaction rates. This is consistent with the increased driving force, i.e., cell potential, caused by an increase of the applied bias, and a more favorable kinetic for OER at higher pH values.

Table 6.2: Photoelectrocatalytic results varying pH and applied bias.

pH	Applied bias (V vs. Ag/AgCl)	Cell potential (V)	Photocurrent (mA)	FE DHA (%)	FE GA (%)	FE CO_2 (%)	FE H_2 (%)
2	0.5	0.90	2.3	8.4	6.2	26	85
7	0.1	1.00	3.0	15.0	6.4	13	100
7	0.2	1.12	3.5	6.8	11.7	11	91
7	0.3	1.26	4.1	6.7	11.8	8	100
7	0.4	1.34	4.0	6.5	13.8	9	100
7	0.5	1.35	4.0	7.4	16.9	12	84
7	1.0	1.85	5.4	9.5	15.2	6	85
14	0.1	1.20	4.7	1.1	0	0	96
14	0.3	1.39	4.8	1.7	0	0	51
14	0.5	1.57	5.0	3.8	0	0	41

The partial oxidation products, specifically DHA and GA, show different FEs depending on the pH of the reaction mixture. Significantly, the highest FE for DHA and GA was obtained at pH 7 with an applied bias of 0.1 V and 0.5 V vs Ag/AgCl respectively. Moreover, at higher pH, the DHA production is reduced, and it drops to 0 for GA. This may be due to the increased OER at higher pH values, thanks to its favorable kinetic, which in turn hinders the production of HVA products derived by glycerol photooxidation.

CO_2 production, indicative of glycerol mineralization, is strongly affected by the pH of the reaction mixture rather than the cell potential. Notably, FE towards CO_2 stands at 26 % at pH 2, approximately 10 % at pH 7, and drops to 0 at pH 14. This trend aligns with the hypothesis that the applied bias mainly serves to minimize recombination between photoinduced holes and electrons, rather than affecting their potential. Conversely, the pH influences the redox potential of species within the reaction mixture as well as the kinetic toward the OER, affecting the glycerol mineralization to CO_2 and H_2.

The FE towards H_2 diminishes as both the pH and the applied bias increase. This observation aligns with findings in the literature and is likely linked to higher O_2 production, which interacts with the generated H_2, thereby reducing its FE [358,359]. A higher bias as well as a higher pH favours the kinetic of oxygen evolution. Indeed, this reaction is kinetically sluggish and thus more sensitive to the electric field at across the space charge region of the semiconductor (namely TiO_2). The electric field in turn raises by raising the potential with respect to the flat band potential. Since O_2 can diffuse to the cathode its reduction becomes competitive with respect to H_2 evolution thus explain the experimental findings.

6.4. Conclusions

This study investigates the influence of pH and applied bias for H_2 production and HVA products from glycerol photooxidation in a photoelectrochemical cell. TiO_2 NTs measuring 760 nm length over 24 cm^2 as the surface area were used as the photoanode and PGM-free Ni foam of 6 cm^2 as the cathode.

Photoelectrocatalytic tests were carried out across acidic, neutral, and basic pH, employing applied bias ranging from 0.1 and 1 V vs Ag/AgCl. The results show the highest FE towards HVA products, i.e., DHA and GA at pH 7 and applied bias of 0.5 V and 0.1 V vs. Ag/AgCl respectively, remaining stable at higher applied bias. The highest glycerol photoreforming level was obtained at lower pH. Conversely, at higher pH, both the glycerol photooxidation and photoreforming, i.e., FE towards DHA, GA, and CO_2, decreased, and I_{ph} increased. This suggests that water splitting is more pronounced at higher pH, resulting in a lower FE towards H_2 because of the subsequent reaction with the O_2 in the gas phase.

As a final remark, it is important to stress that these results are encouraging considering the high chemical and physical stability of the employed PGM-free electrodes, offering interesting perspectives for future developments in targeted applications (i.e., H_2 production and/or HVA products) and opens up new routes for sustainable technologies.

7. Enhancing H_2 production rate in PGM-free photoelectrochemical cells by glycerol photo-oxidation

In this published study [155], the photo-oxidation of glycerol was carried out by using TiO_2 NTs photoanodes and Ni foam as the cathode for the Hydrogen Evolution Reaction (Figure 7.1). The photoanodes were prepared by anodizing Ti foils and titanium felt and then annealed under air exposure. They were tested in acidic aqueous solution without and with the addition of glycerol. When glycerol was present, the hydrogen production rate increased and allowed the simultaneous production of high value added partial oxidation compounds, i.e. 1,3-dihydroxyacetone (DHA), and glyceraldehyde (GA). The highest H_2 evolution and partial oxidation compounds production rates were obtained by using home prepared TiO_2 nanotubes (TiO_2 NTs) synthesized on Ti fiber felt as the photoanode with an irradiated area of 90 cm^2. These photoanodes were found to be highly stable both from a mechanical and a chemical point of view, so they can be reused after a simple cleaning step.

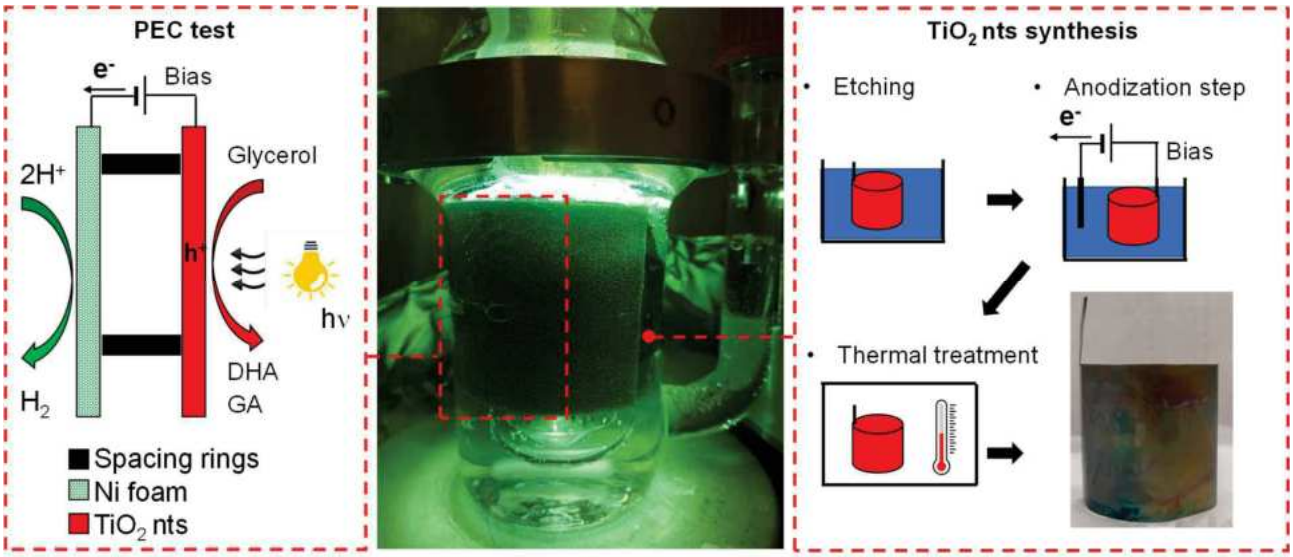

Figure 7.1. Schematic illustration of photoanode preparation and photoelectrocatalytic reactions.

7.1. Introduction

In this work, hydrogen production by glycerol photo-reforming and water splitting on TiO_2 nanotubes photoanode was studied with a specific focus on electrode surface engineering to enhance the hydrogen evolution rate and evaluate the faradic efficiency (FE) towards DHA and GA production. The photoanode was prepared by anodizing Ti foil or Ti felts with a high specific surface area further enhanced by TiO_2 NTs. PGM-free cathodes were used as a low-cost alternative compared to the noble metal-based catalysts and they were able to overcome possible poisoning effects due to the presence

of organic species [360]. In previous similar works, Cetinkaya et al. [361] studied the PEC oxidation of glycerol by using different TiO_2 geometries, obtaining glycerol conversions up to 37% and selectivity toward DHA and GA of 6% and 13% respectively after 3 h of reaction using TiO_2 NTs, and applying 1.5 V vs Ag/AgCl. Luo et al. [228] achieved high-selective PEC oxidation of glycerol to DHA by using a Bi_2O_3/TiO_2 photoanode, obtaining a glycerol conversion rate of up to 228 mmol m^{-2} h^{-1} at 1.0 V vs RHE and selectivity towards DHA up to 75.4% with a faradaic efficiency (FE) of 62.2%.

7.2. Experimental

Electrodes preparation

Previous studies [191,208,346] showed that TiO_2 NTs photoanodes can be prepared by anodizing processes. Titanium foils (Sigma Aldrich, purity > 99.7%) with 0.127 mm thickness or Titanium fiber felt (Fuel cell store) with: 0.2-0.3 mm thickness were properly cut and etched, 15 or 5 seconds, respectively, in a mixture of hydrofluoric acid (Sigma Aldrich, purity 39.5%), nitric acid (Sigma Aldrich, purity 69.0%) and deionized water with a volume ratio of 1:1:3. Then, they were cleaned by sonication in acetone and ethanol for 5 minutes each, rinsed with deionized water, and dried in air. TiO_2 NTs were formed in ethylene glycol (Aldrich, 99.8% anhydrous) solution containing 0.25 wt% NH_4F (Sigma Aldrich) and 0.75 wt% deionized water. The anodizing process was carried out in a two-electrode cell configuration, by using aluminum foil as the cathode. The potential was kept constant during anodizing at 45 V for 5, 10, or 20 minutes. After that, a thermal treatment was performed to induce the crystallization of the TiO_2 NTs. In particular, to optimize the synthesis procedure, the layers were heated in air to 450°C for 3 hours or 550°C for 12 hours respectively, and left to cool inside the oven. A relatively low annealing time was chosen to have a thin and not very blocking thermally induced titanium oxide layer between the bare titanium and the nanotubes.
Commercial Ni foam (Goodfellow) was used as the cathode.

Characterization

Thermodynamics and kinetics of the partial oxidation of glycerol were studied through cyclic voltammetry in 0.5 M Na_2SO_4 (Sigma-Aldrich, ≥ 99%) aqueous solution without and with 0.1 M glycerol (Sigma-Aldrich, ≥ 99.5%) concentrations. The pH was adjusted to 2 by adding H_2SO_4 (Sigma-Aldrich, 97%) dropwise. Cyclic voltammetry was recorded between 0 and 2 V vs Ag/AgCl, by using a three-electrode cell configuration with Pt mesh as the working and counter electrode and

Ag/AgCl/3.5 M KCl as the reference one. The scan rate was 5 mV/s and a Parstat 2263 potentiostat was used.

SEM, XRD, Raman spectra were performed; further details are provided in the experimental section (Section 2).

For the photoelectrochemical measurements, TiO_2 NTs on Ti felt photoanode was used as the working electrode in a three-electrode configuration cell, a Pt wire was used as the counter electrode, and a silver/silver chloride (Ag/AgCl/sat. KCl) was employed as the reference electrode. 0.5 M Na_2SO_4 aqueous solution was used as the electrolyte, and the pH was adjusted to 2 by adding H_2SO_4 dropwise [219]. EIS measurements were carried out using a Parstat 2263 potentiostat.

Photoelectrocatalytic tests

Photoelectrocatalytic tests were carried out by using TiO_2 NTs as photoanode, Ni foam as cathode, and Na_2SO_4 as the electrolyte. The pH was 2 (adjusted with H_2SO_4) and the applied potential between the photoanode and cathode was 1 V. The glycerol initial concentration was in the range of 0 – 0.5 M.

The reaction was carried out in the undivided glass cells shown in Figure 7.2 with a two electrodes configuration. As far as the irradiation is concerned, a Hg medium-pressure lamp with a maximum near-UV wavelength of 365 nm (125 W) was used. The photoanodes and the cathode with 24 cm^2 (irradiated) and 8 cm^2 surface, respectively were used to determine the TiO_2 NTs on Ti foil performances by varying the synthesis conditions, i.e., anodization time and thermal treatment. After this optimization, the best sample was tested by scaling up the photoanodes and the cathode surface up to 90 cm^2 (irradiated) and 180 cm^2, respectively. Moreover, improvements were obtained by using Titanium fiber felt as support instead of Titanium foil and increasing the glycerol initial concentration. A Parstat 2263 (PAR) equipped with the facilities for Electrochemical Impedance Spectroscopy (EIS) was used to control the cell potential and to collect kinetic data of both anodic and cathodic processes. Before each run, Helium was bubbled under stirring in the dark for 30 minutes in the glycerol aqueous solution, both to remove oxygen from the system and to saturate the electrode's surface by the substrate, then the reactor was closed, and the lamp switched on. Runs were carried out for 5 hours at room temperature by circulating water in the reactor cooling jacket.

The photoanode was reused after sonication with acetone and water for 5 minutes each to remove any residues of glycerol, while Ni foam was cleaned by sonication for 5 minutes in 1 M HCl.

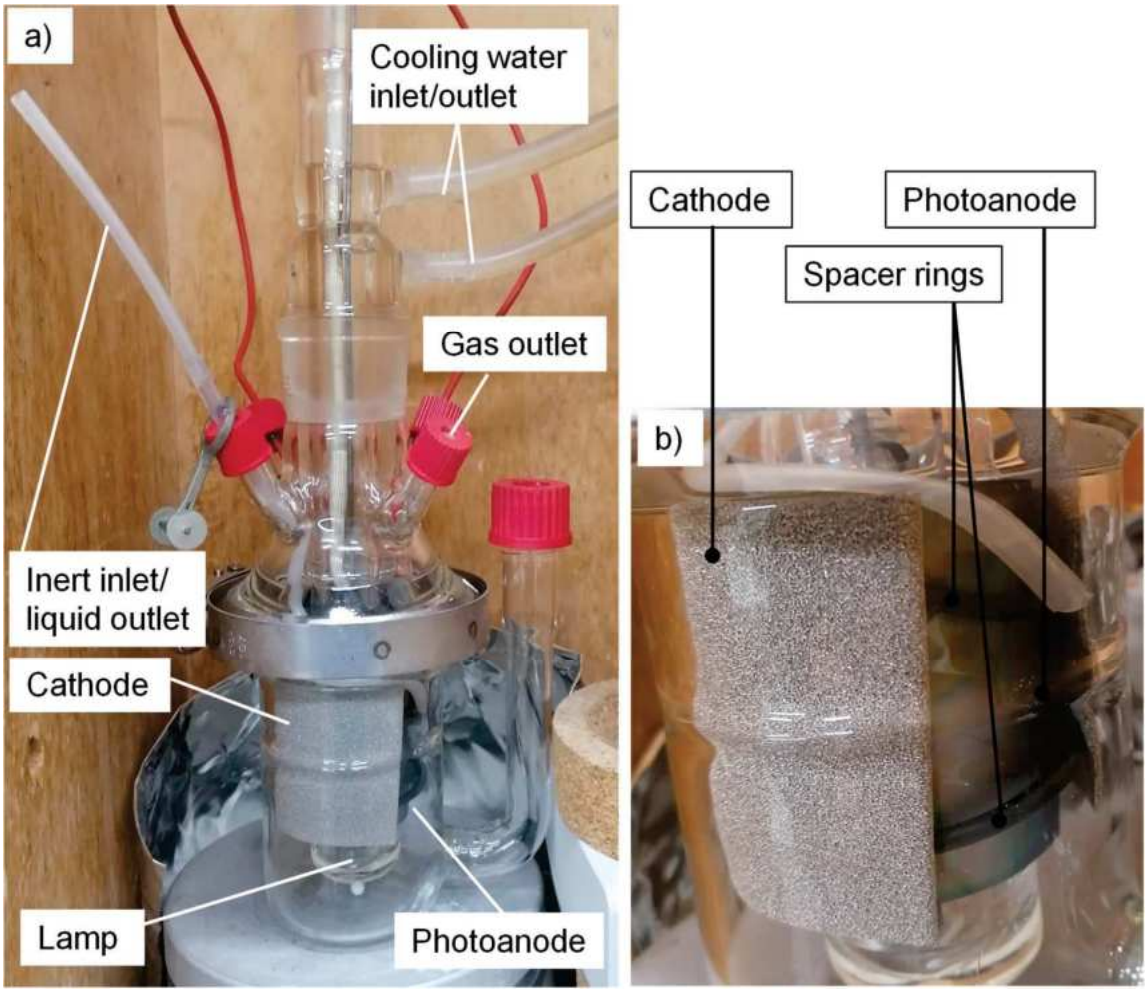

Figure 7.2. Pictures of a) PEC system with a photoanode irradiated area of 90 cm^2 and b) magnification of photoanode and cathode layout.

Analytical techniques

The identification and quantification of glycerol and reaction intermediates were performed by using HPLC. Gaseous species accumulated in the reactor headspace were analyzed by GC.

For DHA, GA, and CO_2, the faradaic efficiency was calculated through Equation 2.4, where z, the electrons exchanged, equal to 2 for H_2, DHA, and GA and 14/3 for CO_2 according to the anodic and cathodic semi-reactions in Equations 6.1 – 6.3.

7.3. Results and discussion

A preliminary electrochemical investigation was carried out to obtain information about the kinetic of glycerol oxidation in aqueous solution. Figure 7.3a shows the cyclic voltammetry recorded in glycerol-free and glycerol-containing 0.5 M Na_2SO_4 solution at pH 2 by using a Pt mesh as the working electrode. The Faradaic current, attributed to the glycerol oxidation, starts to circulate by

increasing the potential toward the positive direction (see inset of Figure 7.3a). Indeed, in glycerol-free solution the onset potential for the circulation of a Faradaic current (due to OER) is higher, suggesting that glycerol oxidation is kinetically favorable.

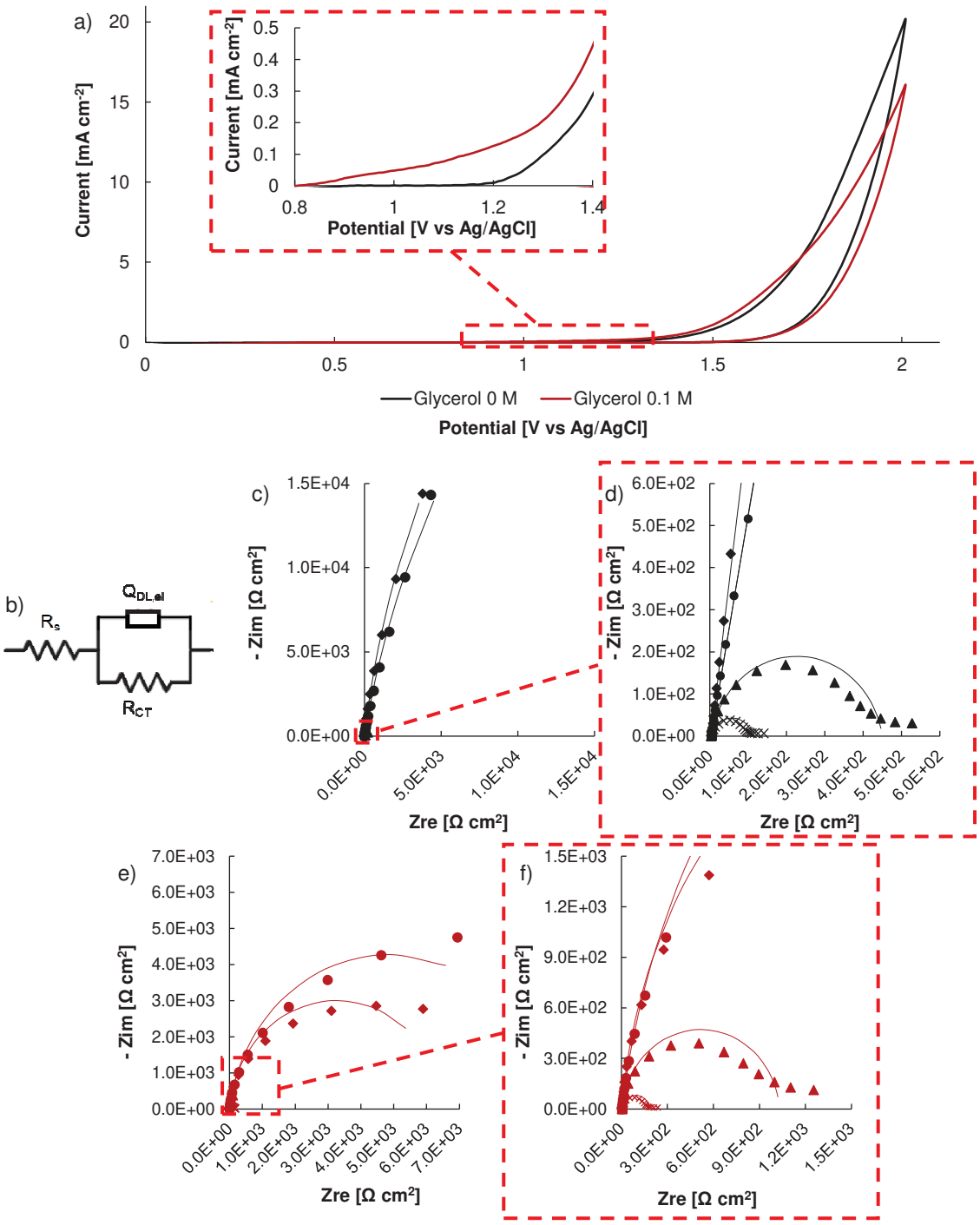

Figure 7.3. Cyclic voltammetry using Pt as the counter and the working electrode, recorded at 5 mV/s without and with 0.1 M glycerol in 0.5 M Na_2SO_4 and pH 2, black and red lines respectively. EIS spectra recorded without, and 0.1 M glycerol are reported in c) - d) and e) – f) respectively. Spectra recorded at (●) 0.9, (♦) 1.1, (▲) 1.3, and (x) 1.5 V vs Ag/AgCl were fitted using the equivalent circuit shown in b).

This finding is also supported by the EIS spectra recorded in 0.5 M Na_2SO_4 at pH 2 without (Figure 7.3c and d) and with the addition of glycerol (Figure 7.3e and f).

In Table 7.1 are reported the parameters of the equivalent circuit in Figure 7.3b, related to the EIS spectra shown in Figure 7.3c-f. R_s is the solution resistance, R_{ct} is the charge transfer resistance, and $Q_{DL,el}$ accounts for the double-layer capacitance.

R_s and $Q_{DL,el}$ are practically the same as the potential varies and are not affected by the presence of glycerol. A very high charge transfer resistance (in the order of 10^5 W cm^2) was estimated at the equilibrium potential for oxygen evolution (i.e. ~ 0.9 V vs Ag/AgCl) and at an even higher potential (1.1 V vs Ag/AgCl) in the absence of glycerol (Table 7.1a). Conversely, when glycerol is present in the electrolytic solution, at the lowest potential values, its oxidation allows lower charge transfer resistance. On the contrary, at higher potentials, in the presence of glycerol and its partial oxidation products, higher charge transfer resistance and lower current density occur, probably due to their strong adsorption on the Pt surface (see Figure 7.3a).

Table 7.1 a). Fitting parameters of EIS spectra recorded in 0.5 M Na_2SO_4 at pH 2 using Pt mesh as the counter and the working electrode recorded at various potentials without glycerol.

Applied potential (V vs Ag/AgCl)	**R_s (Ω cm^2)**	**R_{ct} (Ω cm^2)**	**$Q_{DL,el}$ (S s^n cm^{-2})**	**n**	**χ square (adm)**
0.9	3.99	$1.06 \cdot 10^5$	$9.95 \cdot 10^{-5}$	0.887	$7.23 \cdot 10^{-4}$
1.1	4.2	$1.11 \cdot 10^5$	$1.05 \cdot 10^{-4}$	0.921	$1.43 \cdot 10^{-3}$
1.3	4.1	446	$1.4 \cdot 10^{-4}$	0.898	$4.52 \cdot 10^{-3}$
1.5	3.89	101	$1.94 \cdot 10^{-4}$	0.853	$8.53 \cdot 10^{-3}$

Table 7.1 b). Fitting parameters of EIS spectra recorded in 0.5 M Na_2SO_4 at pH 2 using Pt mesh as the counter and the working electrode recorded at various potentials with 0.1 M glycerol.

Applied potential (V vs Ag/AgCl)	**R_s (Ω cm^2)**	**R_{ct} (Ω cm^2)**	**$Q_{DL,el}$ (S s^n cm^{-2})**	**n**	**χ square (adm)**
0.9	4.13	9740	$1.04 \cdot 10^{-4}$	0.918	0.0259
1.1	3.97	6505	$1.03 \cdot 10^{-4}$	0.949	0.0284
1.3	3.96	1028	$1.07 \cdot 10^{-4}$	0.945	0.0316
1.5	3.93	180	$1.2 \cdot 10^{-4}$	0.9225	0.0364

Photoanode preparation

Figure 7.4 shows the SEM images of TiO_2 NTs after anodizing and thermal treatment. The micrographs clearly show the successful formation of a large array of TiO_2 NTs (Figures. 7.4a, b) with an average length range of ~ 350 nm – ~ 1.22 mm when the anodization time increases from 5 to 20 minutes, respectively. These results agree with previous studies on flat titanium sheets [346]. Conversely, NTs length is not affected by the time and temperature of thermal treatment (i.e. 3 h at 450°C (Figures 6.4 c,d) and 12 h at 550°C (Figure 6.4 e) or the use of Ti felt instead of Ti foil (Figures 6.4 f and 6.4 g respectively).

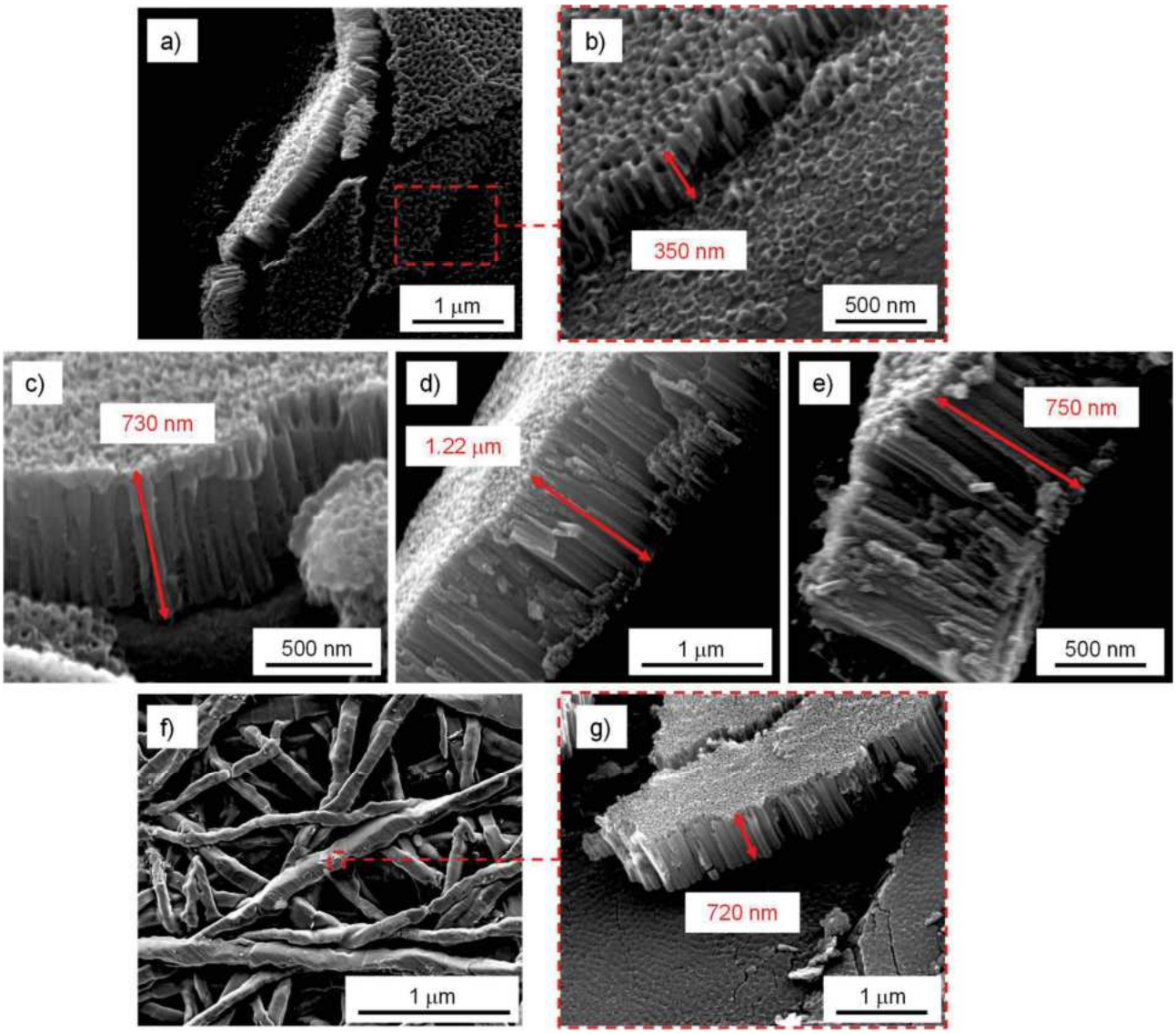

Figure 7.4. SEM pictures of TiO_2 NTs synthesized at different conditions. a), b) anodization step (AS) 5 minutes at 45 V, thermal treatment (TT) of 3 hours at 450°C on Ti foil. c) AS 10 minutes at 45 V, TT of 3 hours at 450°C on Ti foil. d) AS 20 minutes at 45 V, TT of 3 hours at 450°C on Ti foil. e) AS 20 minutes at 45 V, TT of 12 hours at 550°C on Ti foil. f), g) AS 10 minutes at 45 V, TT of 3 hours at 450°C on Ti felt.

XRD patterns in Figure 7.5 show peaks related to TiO_2 anatase and rutile phases and bare titanium [265]. As shown in Figure 7.5a, a more evident peak of the rutile phase is present when the thermal treatment was carried out at a higher temperature and longer time in agreement with previous results reported in the literature [362]. According to previous works, due to the annealing treatment following the anodizing process, two phenomena occur simultaneously. Amorphous TiO_2 of the nanotubes becomes anatase, while at the titanium/nanotube interface, a thermal oxidation process occurs involving the not anodized substrate to form rutile. The latter allows also a strong adhesion between the NTs and the metallic substrates. A thermal treatment at 450°C under air exposure for 3h induces the formation of 140 nm thick rutile layer. Moreover, the tube wall mainly consists of anatase crystals with a cylindrical shape that can be several hundred nanometers long in the direction of the nanotube axis [356,357].

No evident TiO_2 peaks were detected for NTs synthesized on Ti felt, only a small peak at ~ 40° related to Ti is present, probably due to the different orientations of the nanotubes along the Ti felt fibers.

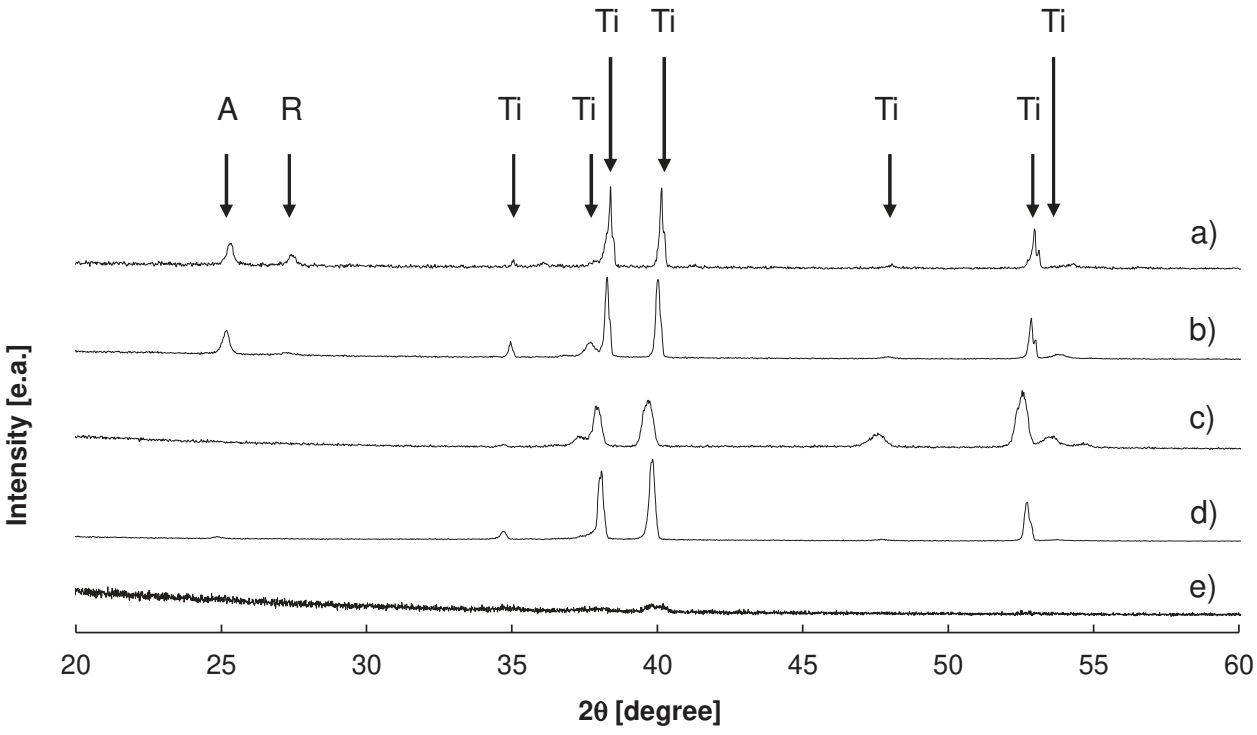

Figure 7.5. XRD patterns of TiO_2 photoanodes synthesized at different conditions: a) anodization step (AS) 10 minutes at 45 V, thermal treatment (TT) of 12 hours at 550°C on Ti foil, b) AS 20 minutes at 45V TT of 3 h at 450°C on Ti foil, c) AS 10 minutes at 45V TT of 3 h at 450°C on Ti foil, d) AS 5 minutes at 45V TT of 3 h at 450°C on Ti foil and e) AS 10 minutes at 45V TT of 3 h at 450°C on Ti felt.

Raman spectra in Figure 7.6 show characteristic bands of anatase at 144 cm^{-1}, 196 cm^{-1}, 397 cm^{-1}, 513 cm^{-1}, and 639 cm^{-11} and rutile at 447^{-1} and 612 cm^{-1} [271]. As confirmed by XRD patterns in

Figure 7.5 rutile phase appears by increasing temperature and time of the thermal treatment [16], while no differences were observed using Ti felt as substrate. A slight shift in the peak at ca. 144 cm^{-1} can be noticed for some of the samples ascribable to the presence of oxygen vacancies in the TiO_2 structure [363].

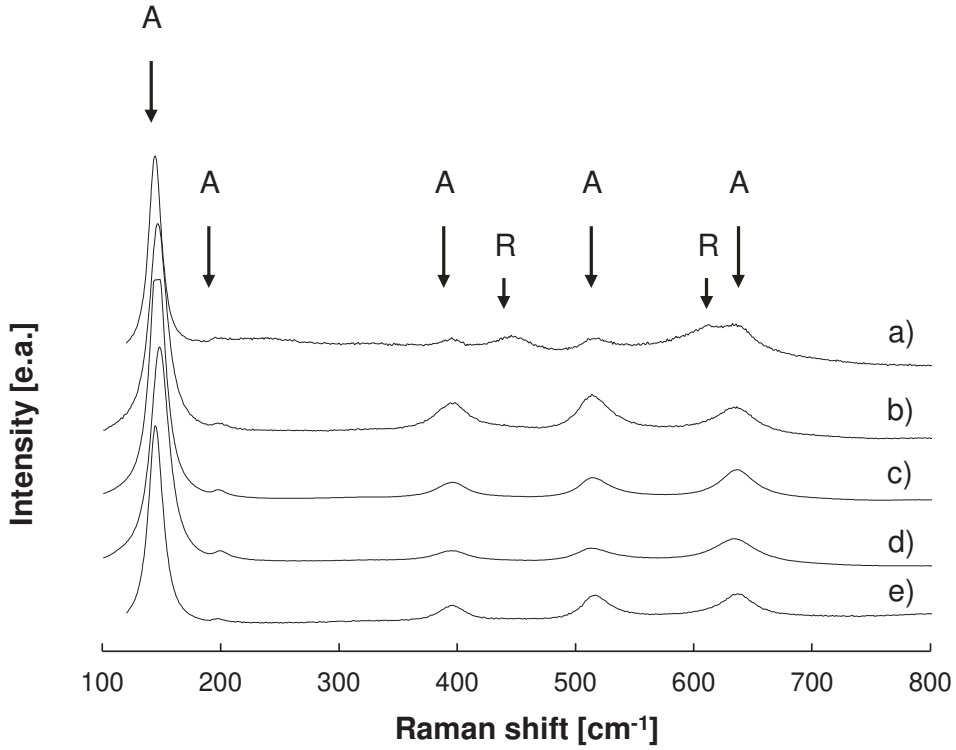

Figure 7.6. Raman spectra of TiO_2 photoanodes synthesized at different conditions: a) anodization step (AS) 10 minutes at 45 V, thermal treatment (TT) of 12 hours at 550°C on Ti foil, b) AS 5 minutes at 45V TT of 3 h at 450°C on Ti foil, c) AS 10 minutes at 45V TT of 3 h at 450°C on Ti foil, d) AS 20 minutes at 45V TT of 3 h at 450°C on Ti foil and e) AS 10 minutes at 45V TT of 3 h at 450°C on Ti felt.

Photoelectrochemical measurements were carried out to study the electronic properties of the photocatalysts. The photocurrent spectrum (i.e. photocurrent vs wavelength curve) recorded in 0.5 M Na_2SO_4 at pH 2 at 0.5 V vs Ag/AgCl reported in Figure 7.7a shows a maximum photocurrent value at ca. 320 nm. By assuming non-direct optical transitions, it is possible to estimate an optical band gap value, E_g, by extrapolating to zero $(Q_{ph} \cdot h\nu)^{0.5}$ vs $h\nu$ plot (see Fig. 7.7b. E_g is 3.05 eV, lower than that reported for anatase (i.e. 3.2 eV, [346,364]). This finding can be due to optical transitions related to the presence of allowed localized states inside the gap. Indeed, thermal treatment induces the formation of a sub-stoichiometric oxide TiO_{2-x} with oxygen vacancies responsible for the previously mentioned localized states. Current transients were recorded under monochromatic irradiation (l = 320 nm) at several constant potentials. The photocurrent was measured by manually stopping the

irradiation at applied potential varying from 1 to -0.75 V vs Ag/AgCl (see Figure 7.7c). An anodic photocurrent was measured confirming the n-type semiconductor behavior of the oxide, and the photocurrent was zero at ~ -0.75 V vs Ag/AgCl, that can be therefore assumed as an estimate of the flat band potential, V_{fb}. This value is more cathodic if compared to other results reported in the literature [364] in agreement with a high concentration of oxygen vacancies whose presence generates an empty allowed localized state close to the conduction band edge [365].

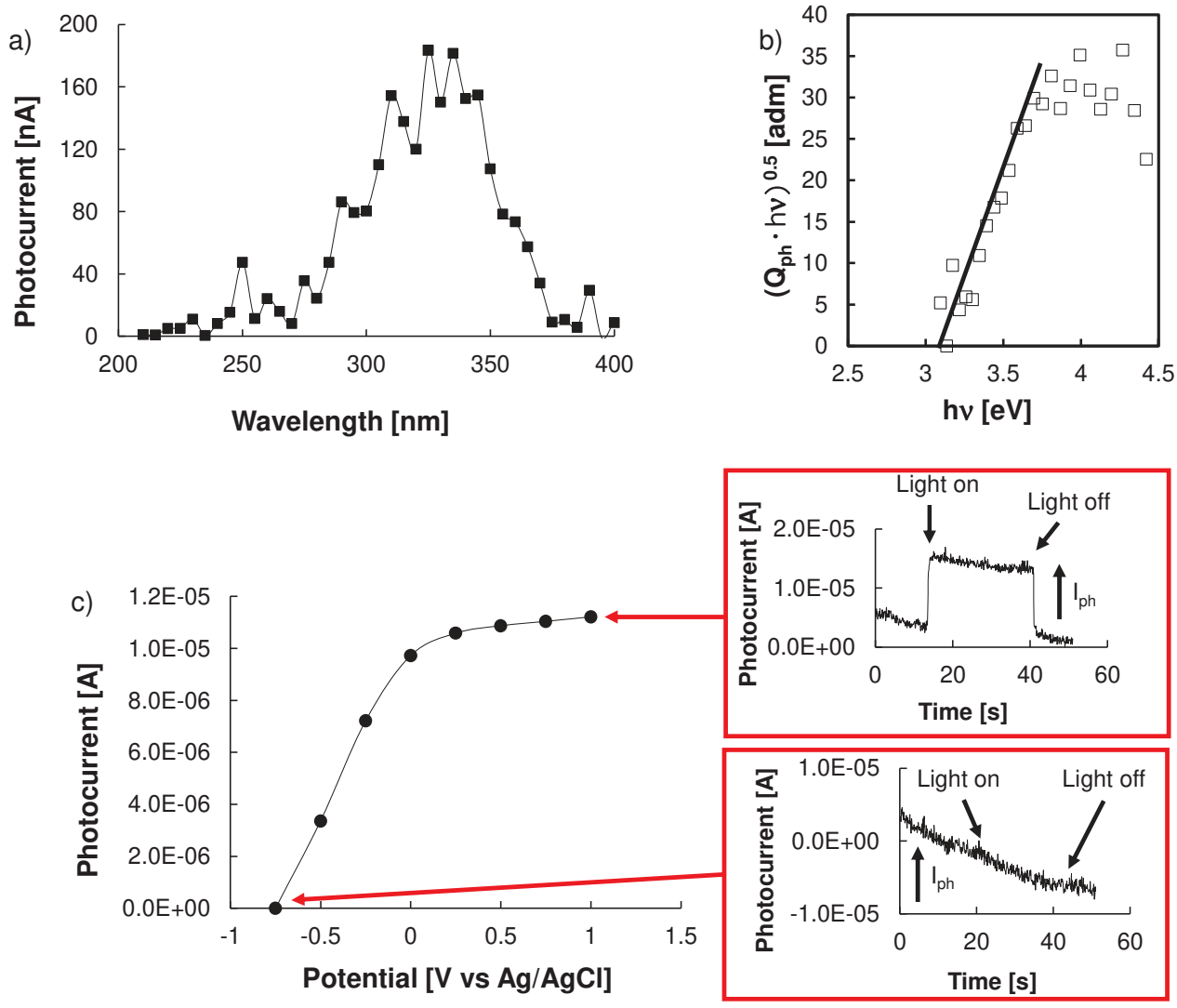

Figure 7.7. a) Photocurrent spectra of TiO_2 NTs on Ti felt recorded in 0.5 M Na_2SO_4 at pH 2 and applied potential of 0.5 V vs Ag/AgCl, the respective $(Q_{ph} \cdot h\nu)^{0.5}$ vs hν plot is shown in b). Current transient under monochromatic light recorded at 320 nm and applied potential from 1 to -0.75 V vs Ag/AgCl with a step of 0.25 V are reported in c), respective photocurrent vs time plots recorded at 1 and -0.75 V vs Ag/AgCl are reported in the inset.

Photoelectrochemical tests

Several TiO_2 NTs photoanodes were prepared by changing the anodizing time (and consequently the NTs length) and the thermal treatment temperature. Their activity was evaluated in aqueous solutions

without and with the addition of glycerol. The analysis of the reaction mixture composition and the gaseous stream produced at the anode provided information about the obtained products with specific interest to those derived by glycerol oxidation. Among them, it was possible to identify DHA, GA, and CO_2 corresponding to the following half-cell reactions in Equations 6.1 and 6.2:

Table 7.2 summarizes the results obtained by using a photoanode irradiated surface of 24 cm^2. As it can be noticed, in the same experimental conditions, the addition of glycerol enhances the measured photocurrent by ~ 30%, thus suggesting that glycerol photo-oxidation occurs in parallel with oxygen evolution. Notably, the enhanced photocurrent due to glycerol oxidation resulted in a higher H_2 production.

As suggested by the data of Table 7.2, the optimum NTs performance in terms of measured photocurrent corresponds to the anodizing time of 10 min at 45 V and thermal treatment of 3 h at 450°C. On the other hand, maintaining the same anodization conditions, the raising of time and temperature of the thermal treatment does not improve the photoanode performance. It is also interesting to mention that the amounts of DHA and GA produced during the overall process in 5 h are not strongly dependent on the NTs features.

Table 7.2: results of the tests executed using TiO_2 NTs on Ti foil varying the photoanode synthesis conditions, photoanodes irradiated surface was 24 cm^2. TT = thermal treatment step, I_{ph} = photocurrent, FE = Faradaic efficiency, DHA = 1,3-dihydroxyacetone, GA = glyceraldehyde. The reaction time of each test was 5 h.

Anodizing conditions	10 min at 45 V	10 min at 45 V	5 min at 45 V	20 min at 45 V	10 min at 45 V
TT	3 h at 450°C	3 h at 450°C	3 h at 450°C	3 h at 450°C	12 h at 550°C
Glycerol concentration (M)	0	0.1	0.1	0.1	0.1
I_{ph} (mA)	9.44	12.3	3.88	11.1	7.78
DHA (mmol)		$3.54 \cdot 10^{-2}$	$3.3 \cdot 10^{-2}$	$3.5 \cdot 10^{-2}$	$3.16 \cdot 10^{-2}$
FE DHA (%)		3.09	9.16	2.37	2.18
GA (mmol)		$3.62 \cdot 10^{-2}$	$3.5 \cdot 10^{-2}$	$3.9 \cdot 10^{-2}$	$3.08 \cdot 10^{-2}$
FE GA (%)		11.7	9.68	3.81	4.26
CO_2 (mmol)		$5.65 \cdot 10^{-3}$	$2.3 \cdot 10^{-5}$	$3.3 \cdot 10^{-3}$	$3.7 \cdot 10^{-3}$
FE CO_2 (%)		3.47	0.045	2.09	3.59
H_2 (mmol)	0.88	1.15	0.362	1.03	0.726

After this preliminary screening, larger photoanodes (the irradiated area has been increased from 24 cm^2 to 90 cm^2) were synthesized (10 min at 45 V and thermal treatment of 3 h at 450°C) to better collect the light irradiation on both Ti foil and Ti felt. The cathode surface was also increased from 8 cm^2 to 180 cm^2 to allow a better distribution of the current lines and to reduce the cathodic current density and thus the corresponding necessary overvoltage. The measured photocurrent increased by ~ 4.3 times with Ti foil and by ~ 6.5 times with Ti felt (see Table 7.3). In the attempt to enhance the glycerol mass transfer inside the NTs of Ti fiber felt, the initial glycerol concentration was increased up to 0.5 M, resulting in I_{ph} up to 82.8 mA (Table 7.3), while further increasing of the biomass concentration did not provide I_{ph} enhancement. The maximum H_2 amount was 7.72 mmol after 5h of reaction.

Based on the experiments carried out using Ti felt as photoanode and an initial glycerol concentration of 0.1 M, after 5 hours of irradiation glycerol conversion is ~ 13.6%, with a selectivity of 6.7% towards DHA and 19.8% towards GA. Since this is a photoelectrochemical process, we expect that the longer is the polarization the higher will be the conversion.

Table 7.3: results of the tests executed using TiO_2 NTs on Ti foil and Ti felt, obtained through an anodization step of 10 min at 45 V and a thermal treatment step of 3 h at 450°C. Photoanodes irradiated surface was 90 cm^2, I_{ph} = photocurrent, FE = Faradaic efficiency, DHA = 1,3-dihydroxyacetone, GA = glyceraldehyde. The reaction time of each test was 5 h.

Substrate	Ti foil	Ti foil	Ti felt	Ti felt	Ti felt
Initial glycerol (M)	0	0.1	0	0.1	0.5
I_{ph} (mA)	41.7	53.3	50.0	80.5	82.8
DHA (mmol)		0.184		0.218	0.36
FE DHA (%)		3.12		2.74	3.39
GA (mmol)		0.518		0.605	0.493
FE GA (%)		10.4		8.07	6.39
CO_2 (mmol)		$7.62 \cdot 10^{-2}$		0.141	0.15
FE CO_2 (%)		10.7		13.2	13.6
H_2 (mmol)	3.89	4.97	4.66	7.51	7.72

Table 7.4 summarizes the DHA, GDA, and H_2 production rate, normalized for incident photonic flux as well as the faradaic efficiency to allow a comparison with the previous results reported in the literature. The H_2 production rate normalized for both the incident photon flux and the photoanode area is one order of magnitude greater than that reported in other works.

Table 6.4. H_2, DHA, and GA production rate related to incident photon flux and photoanode found in this work and comparison with data found in the literature.

Ref.	[366]	[367]	[228]	This work
Photoanode	$BiVO_4$	$NiO_x(OH)_y$/W:$BiVO_4$	Bi_2O_3/TiO_2	TiO_2
Cathode	Pt		Pt	Ni foam
Electrolyte	Glycerol 2 M 0.1 M $Na_2B_4O_7$ pH 9.4	Glycerol 0.1 M 0.5M KBi pH=9.3	Glycerol 0.1 M 0.5 M Na_2SO_4 pH=2	Glycerol 0.1 M 0.5 M Na_2SO_4 pH=2
Applied bias	0.7 V vs RHE	1.2 V vs. RHE	2 V	1 V
Photoanode area (cm^2)	4	-	7	90
Light source ($mW\ cm^{-2}$)	100	100	100	10
DHA production rate ($mmol\ h^{-1}\ mW^{-1}$)	$4.2 \cdot 10^{-2}$	$13.8 \cdot 10^{-2}$	$17.2 \cdot 10^{-2}$	$4.84 \cdot 10^{-2}$
GA production rate ($mmol\ h^{-1}\ mW^{-1}$)	n.a.	0 (0.1 in 0.5 M Na_2SO_4 electrolyte)	0.28	0.134
H_2 production rate ($mmol\ h^{-1}\ mW^{-1}$)	0.0833	0.40	0.155	1.67

In an attempt to explain the obtained results, the energetic sketch of the TiO_2 NTs-electrolyte interface was built (see Figure 7.8). The location of characteristic energy levels of the junction (Fermi level, E_F, conduction, and valence band edges) was carried out by considering the flat band potential derived

from the photocurrent vs potential plot at 320nm (Figure 7.7c). Indeed, it is possible to locate semiconductor Fermi level, E_F, by knowing the flat band potential, V_{FB}, according to Equation 7.1 [368].

$$E_F = -|e|V_{fb} + |e|V_{ref} \qquad Eqn.\,7.1)$$

where V_{ref} is the potential of the reference electrode used in the photoelectrochemical measurements. After the location of the conduction band edge of oxide around 0.2 eV above E_F (in agreement with the semiconductor behavior of TiO_2 NTs), the valence band edge was determined by considering the estimated band gap mentioned above.

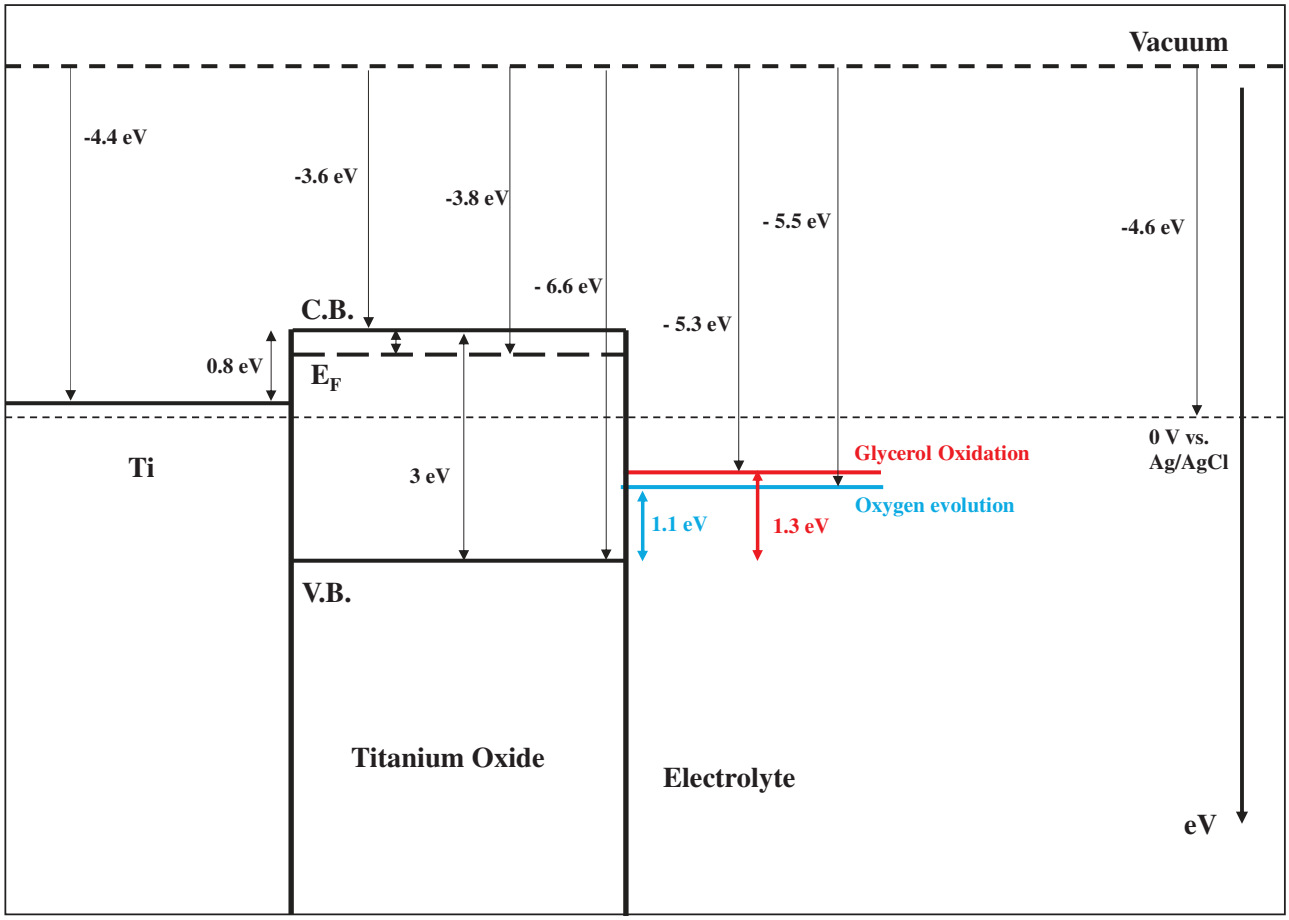

Figure 7.8. Sketch of the energetic levels of the metal/oxide/electrolyte interface.

The high oxidizing capacity of the formed holes at the metal oxide electrolyte interface can be attributed to the distance between the valence band edge and the redox potential for glycerol and water oxidation, of 1.3 eV and 1.1 eV respectively (see Figure 7.8). This can allow both water photo

splitting and biomass photo reforming. Moreover, despite the low selectivity toward DHA and GA, the production rate of these high-value-added products is comparable to those reported in [228], where the formation of a Bi_2O_3/TiO_2 heterojunction allows to reduce the potential of the photogenerated holes and thus to reduce OER and glycerol mineralization to CO_2 (see Equation. 6.2). These photoanodes are very stable both from a chemical and a mechanical point of view. Indeed, they were used for at least 10 runs (each run lasted 5 h) without suffering any damage or poisoning effect thanks to the mechanical properties of the titanium support and to the absence of Pt and/or Pt group metals which are very sensitive to the presence of CO species. Moreover, no appreciable changes were detected in their morphology, structure, and composition according to SEM, Raman, XRD analyses and measured photocurrent after the experiments (Figure 7.9).

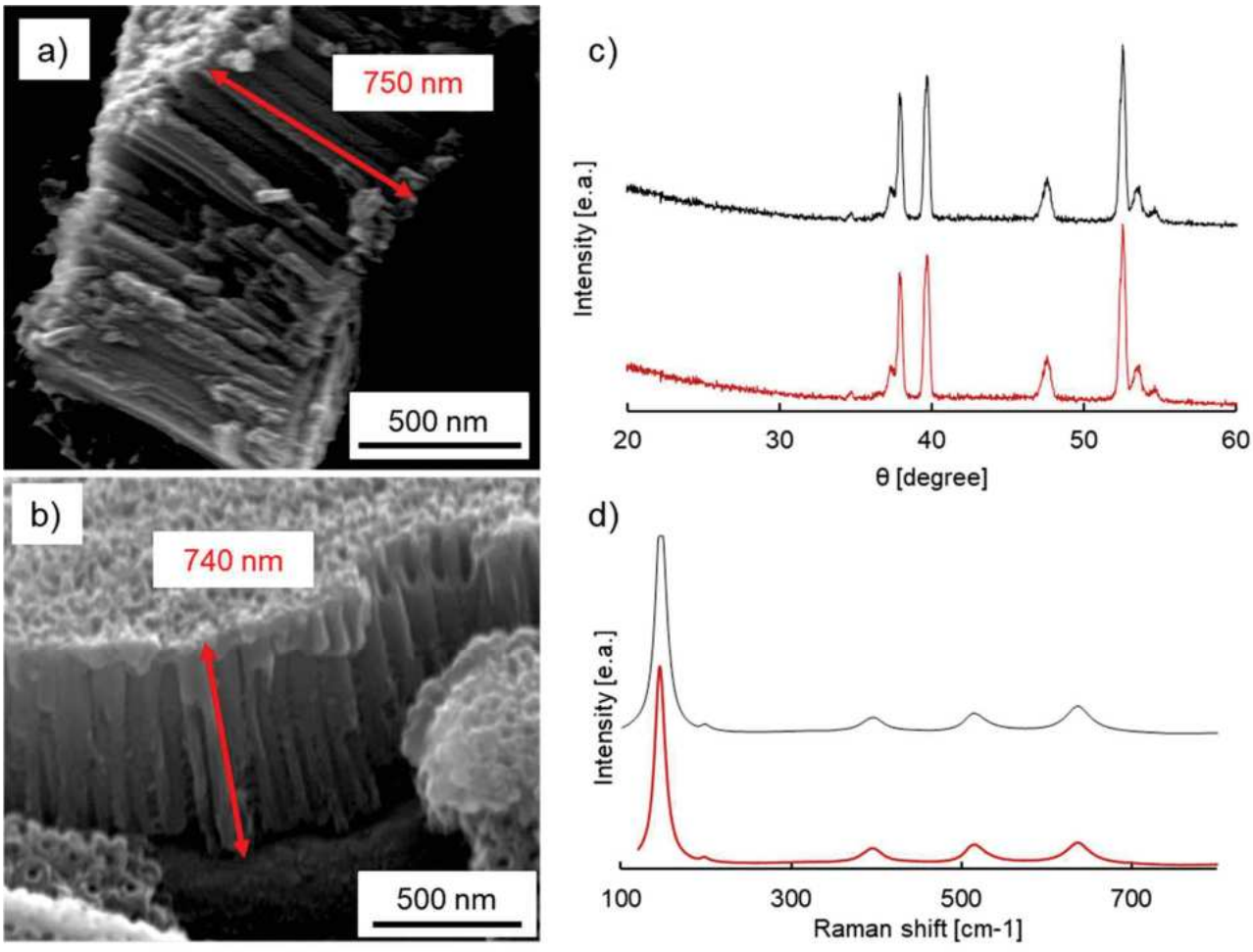

Figure 7.9. SEM images of TiO_2 nts synthesized through an anodization step of 10 minutes at 45 V and thermal treatment of 3 hours at 450°C on Ti foil before and after irradiation are reported in a) and b) respectively. XRD patterns and Raman spectra for the same sample before (black line) and after irradiation (red line) are reported in c) and d) respectively. Photocurrents measured during the first and the second run were 53.2 mA and 53.4 mA respectively.

Figure 7.10 shows EIS spectra recorded in 0.5 M Na_2SO_4 at pH 2 by applying 1 V between the anode and cathode, using TiO_2 NTs as the working electrode and Ni foam as the counter electrode. Figures 7.10a and b show EIS spectra recorded using TiO_2 NTs sample on Ti foil, glycerol concentration of 0.1 M with and without UV irradiation, respectively. Figures 7.10 c and d show EIS spectra recorded using TiO_2 NTs sample on Ti felt with and without UV irradiation, respectively, and glycerol concentrations of 0.1 M, 0.5 M, and without glycerol. All spectra were fitted using the equivalent circuit shown in Figure 7.10e, where R_s is the solution resistance, R_{ct} is the charge transfer resistance, $Q_{SC,\,el}$ accounts for the capacitance of the n-type SC TiO_2, and C_{Brug} is the TiO_2 capacitance calculated by the Brug formula in Equation 7.2 [369].

$$C_{Brug} = Q_{SC,el}^{(1/n)} \left(\frac{R_s\, R_{ct}}{R_s + R_{ct}}\right)^{\frac{(1-n)}{n}} \qquad Eqn.\,7.2)$$

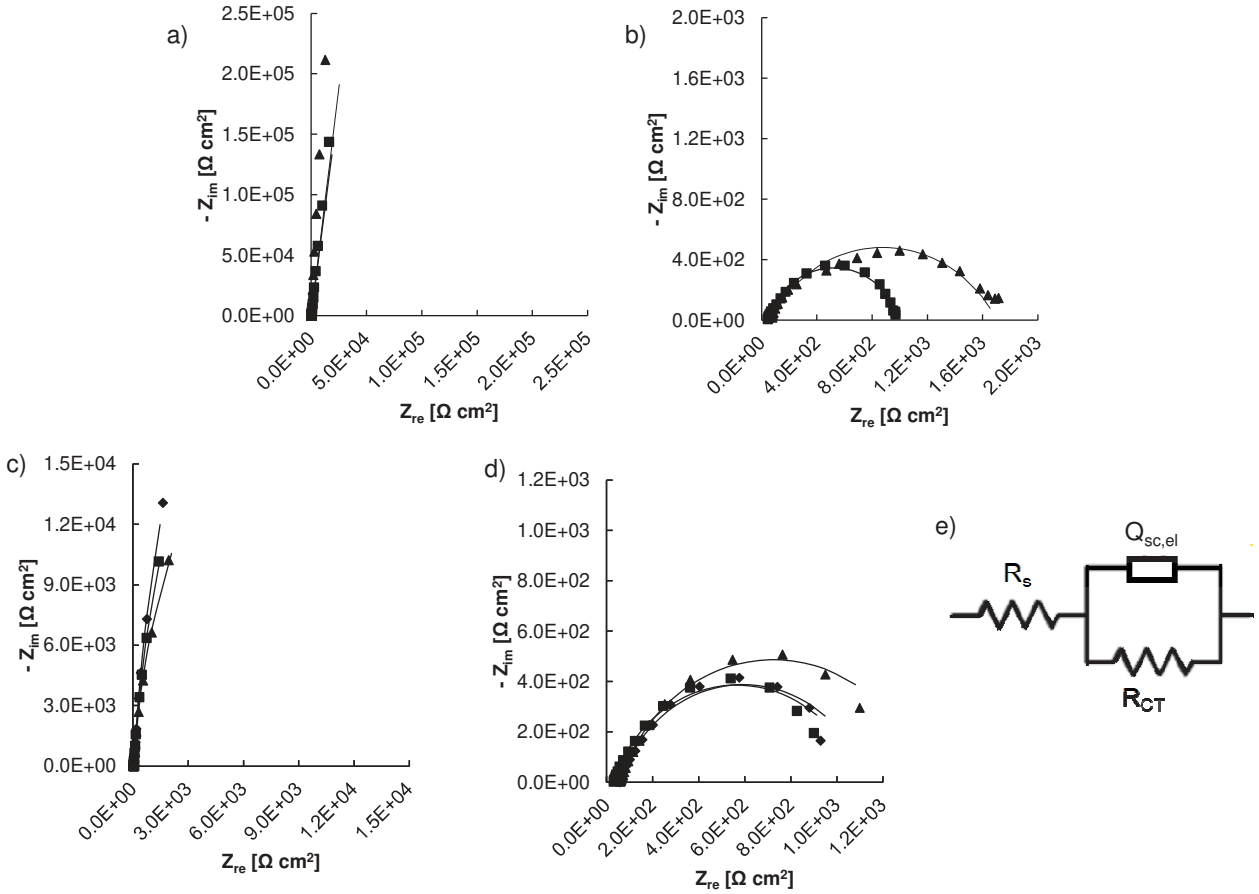

Figure 7.10. EIS spectra performed in 0.5M Na_2SO_4 electrolyte at pH 2 using TiO_2 NTs on Ti foil or Ti felt and Ni foam as the counter electrode. a) and b) show EIS spectra recorded using TiO_2 nts on Ti foil without and with UV irradiation, respectively, and glycerol concentration of (■) 0.1 M, and (▲) without glycerol. c) and d) show EIS spectra recorded using TiO_2 NTs on Ti felt without and with UV irradiation, respectively, and glycerol concentration of (■) 0.1 M, (♦) 0.5 M, and (▲) without glycerol. All spectra were fitted using the model shown in e).

The parameters obtained by a best-fitting procedure are reported in Table 7.5.

Table 7.5: Fitting parameters of EIS spectra recorded using TiO_2 photoanodes and Ni foam as the cathode. TiO_2 NTs were obtained through an anodization step of 10 min at 45 V and a thermal treatment step of 3 h at 450°C. EIS spectra were recorded in 0.5 M Na_2SO_4 at pH 2 by applying 1 V between the anode and cathode, results were obtained with and without UVA irradiation.

Photoanode	R_s (Ω cm^2)	R_{ct} (Ω cm^2)	$Q_{SC,\,el}$ (mS s^n cm^{-2})	n	C_{Brug} (mF cm^{-2})	χ square (adm)
TiO_2 NTs on Ti foil Glycerol 0 M Dark	83	$5.1\cdot10^5$	8.0	0.916	4.09	$1.88\cdot10^{-2}$
TiO_2 NTs on Ti foil Glycerol 0 M Light	58	1644	46.0	0.674	2.62	$6.92\cdot10^{-3}$
TiO_2 NTs on Ti foil Glycerol 0.1 M Dark	49	$6.49\cdot10^6$	11.4	0.911	5.48	$1.04\cdot10^{-2}$
TiO_2 NTs on Ti foil Glycerol 0.1 M Light	43	970	90.3	0.779	18.7	$2.64\cdot10^{-3}$
TiO_2 NTs on Ti felt Glycerol 0 M Dark	71	$7.86\cdot10^4$	140	0.966	119	$1.41\cdot10^{-3}$
TiO_2 NTs on Ti felt Glycerol 0 M Light	61	1326	500	0.8068	216	$1.78\cdot10^{-3}$
TiO_2 NTs on Ti felt Glycerol 0.1 M Dark	33	$1.48\cdot10^5$	150	0.957	118	$1.13\cdot10^{-2}$
TiO_2 NTs on Ti felt Glycerol 0.1 M Light	31	1070	480	0.796	163	$2.02\cdot10^{-2}$
TiO_2 NTs on Ti felt Glycerol 0.5 M Dark	61.2	$1.86\cdot10^5$	130	0.967	110	$3.3\cdot10^{-2}$
TiO_2 NTs on Ti felt Glycerol 0.5 M Light	58.4	1074	460	0.796	182	$2.85\cdot10^{-2}$

It is evident that light irradiation significantly affects the behavior of the electrode/electrolyte interface. Indeed, the charge transfer resistance (R_{ct}) measured in the dark for all the investigated photoanodes is very high and the best fitting exponent n for the $Q_{sc, el}$ is close to 1, as expected for an almost ideal n-type semiconductor, which results to be blocking toward the electronic current. Notably, the capacitance calculated by the Brug formula shown in Table 7.5 depends on the kind of photoanode and since the TiO_2 layers were grown by the same anodizing process and were subjected to the same thermal treatment, the different capacitance can be attributed to a different specific surface. Therefore, the real active surface of TiO_2 NTs grown on Ti felt is higher than that of the TiO_2 NTs grown on the foil. This is still true even after light irradiation in agreement with the higher photocurrent measured by using the felt.

Soon after irradiation, a significant reduction of R_{ct} occurs strictly linked to the enhanced photocarrier concentration and in agreement with the higher capacitance. However, under illumination, lower R_{ct} and higher photocurrent were measured in 0.1 M glycerol-containing solution than that estimated in glycerol-free solution, indicating that the overall reaction is less demanding from a kinetic point of view.

7.4. Conclusions

Photoelectrochemical H_2 production in PGM-free cells by water and glycerol photo-oxidation was studied using TiO_2 NTs on Ti foil as photoanode and Ni foam as cathode with working areas ranging from 24 to 90 cm^2 and from 6 to 180 cm^2, respectively.

Photoelectrocatalytic tests carried out in acidic aqueous solutions revealed that the presence of glycerol allowed an enhancement of the measured photocurrent resulting in a higher H_2 production rate and in the formation of high-value added oxidation products (i.e. DHA and GA). The best results were obtained with TiO_2 NTs ~ 730 nm long annealed for 3 h at 450°C. Consequently, photoanodes with a higher surface were prepared under the same conditions for better collecting light irradiation.

Further improvements were obtained by using high specific surface Ti fiber felt as substrate and increasing initial glycerol concentration up to 0.5 M. A H_2 production rate of 1.67 mmol h^{-1} mW^{-1} was obtained resulting significantly higher with respect to previous results reported in the literature. Moreover, DHA and GA were also produced by the photo-oxidation of glycerol even if with a faradaic efficiency lower with respect to the value reported for functionalized TiO_2 electrodes.

The obtained results are encouraging if it is also considered that both photoanode and cathode can be used for a not limited number of runs, due to their high mechanical and chemical stability and reproducibility in the reaction conditions.

8. Bandgap Engineering of TiO_2 for Enhanced Selectivity in Photoelectrochemical Glycerol Oxidation

This published work [222] was conducted in collaboration with Prof. Dr. Patrik Schmuki, Chair of Surface Science and Corrosion, Department of Material Science and Engineering during my time abroad at Friedrich Alexander University in Erlangen, Germany.

The application of photoelectrochemical cells to the partial oxidation of biomass represents a promising avenue as a sustainable process for obtaining valuable products. However, achieving both efficient conversion rates and high selectivity of desired products remains a great challenge. In this study, we investigate the photoelectrochemical oxidation of glycerol to produce dihydroxyacetone (DHA) and glyceraldehyde (GA) using TiO_2 nanotubes (NTs) as the photoanode. Notably, considering its commercial applications, DHA production was the primary goal of our work. We use nitrogen doping to modify the TiO_2 NTs, resulting in enhanced visible light photoactivity in N-doped NTs. These N-doped NTs exhibit a high selectivity toward DHA and shows a remarkable faradaic efficiency when irradiated with light at a wavelength of 450 nm i.e., light that excites N-related states in the band gap of TiO_2. The N-doped material also exhibits remarkable stability over prolonged reaction periods. The superior performance of N-doped NTs can be attributed to the band-engineering effects induced by nitrogen doping. Specifically, N-doping leads to an upward shift of the valence band, thereby adjusting the exit energy levels of photogenerated holes that results in a high selectivity towards glycerol conversion to DHA and GA.

8.1. Introduction

As mentioned above, despite TiO_2 has been established as the most widely used photoanode, its use in PEC glycerol is limited as the generated holes exiting the electrode leave a high surface energy level that is sufficient to form hydroxyl radicals (·OH). Their strong oxidation power typically leads to a complete mineralization of glycerol to CO_2 or H_2O, thus strongly reducing the FE toward high value-added products such as DHA and GA.

Therefore, in this study, we focus on improving the selectivity and FE of PEC oxidation of glycerol by tuning the band structure of TiO_2 towards a milder oxidation condition. To achieve this goal, we subject TiO_2 nanotubes to nitrogen doping treatment, resulting in N-doped NTs. We then investigate the conversion of glycerol to DHA and GA using both undoped and doped TiO_2 photoanodes under UV (365 nm) and visible light (450 nm) irradiation. Our results show that nitrogen doping, as expected [370,371], induces an upward shift in the valence band and narrows the band gap. This allows the use of lower energy light sources and most importantly it reduces the oxidation power of

photogenerated h^+, and as a result, it leads to a significantly improved selectivity towards DHA production and a higher FE for glycerol oxidation.

8.2. Experimental

Synthesis

TiO_2 photoelectrodes were synthesized using Ti foils (99.6% purity, 0.125 mm thick, ADVENT) as substrates. Ti foil was first cleaned by ultrasonication in acetone, ethanol, and deionized water for 15 min each, followed by drying with a stream of N_2. The synthesis of 1 cm^2 anodic nanotube layers took place in a two-electrode configuration, employing Ti foil as the anode and Pt foil as the cathode. The anodization process occurred at room temperature, applying a voltage of 60 V for 15 minutes in an electrolyte solution composed of ethylene glycol (Roth, ≥ 99%), 0.15 M NH_4F (Roth, ≥ 98%), and 3 vol% deionized water. Soon after the anodization step, the samples were rinsed with ethanol and then dried using a N_2 stream.

The as-formed oxide layers were subsequently subjected to annealing in air inside a tubular furnace at 450°C for 1 h.

For nitrogen doping, the samples underwent a treatment process inside a tube furnace. This treatment involved exposing the samples to an NH_3 flow (200 cm^3/min, 99.8% purity, Air Liquide) within a quartz glass tube at a temperature of 450°C for a duration of 1 hour.

Characterization

Field-emission Scanning Electron Microscopy (SEM), carried out with a Hitachi S-4800 instrument was employed to investigate the surface morphology of TiO_2 NTs.

To analyze the crystal structure of the TiO_2 layers, X-ray diffraction (XRD) was performed using an X‘pert Philips MPD instrument equipped with a Panalytical X‘celerator detector. This analysis utilized graphite-monochromatized Cu Kα radiation with a wavelength of 1.5406 Å. Additionally, the chemical composition was studied using X-ray Photoelectron Spectroscopy (XPS, PHI 5600).

For diffusive reflectance spectral analysis of the samples, a fiber-based UV-VIS-IR spectrophotometer (Avantes, ULS2048) equipped with an integrating sphere (AvaSphere-30) and powered by an AvaLight-DH-S-BAL balanced power light source was utilized. A $BaSO_4$ standard whiteboard served as the reference material.

Photoelectrochemical measurements

Photoelectrochemical measurements, specifically incident photon-to-current conversion efficiency (IPCE), was conducted within a three-electrode cell configuration with the TiO_2 sample as the working electrode, a Pt foil as the counter electrode, and an Ag/AgCl (3 M KCl) reference electrode. A bias of 0.5 V vs. Ag/AgCl was applied. The electrolyte employed was an air-saturated water solution with 0.1 M Na_2SO_4 (Roth, ≥ 99%, anhydrous) and 0.1 M glycerol (Roth, ≥ 99.7%). As the light source, an Oriel 6365 150 W Xenon lamp equipped with an Oriel Cornerstone 7400 1/8 m monochromator was utilized, covering a wavelength range of 300–600 nm. The light intensity at a wavelength of 350 nm was 230 μW cm^2. The corresponding band gaps were determined by replotting the IPCE spectra, considering an indirect transition.

Electrochemical Impedance Spectroscopy (EIS), photocurrent transients, Mott-Schottky (M-S) plots, and cyclic voltammetry were conducted within a three-electrode cell configuration in 0.1 M Na_2SO_4 using a Zahner IM6 electrochemical workstation from Zahner Elektrik in Kronach.

The impedance spectra were recorded both with and without the presence of 0.1 M glycerol in the range 10 kHz - 0.1 Hz at room temperature. A potential of 0.5 V (vs. Ag/AgCl) with an AC amplitude of 10 mV was applied to the working electrode. During the measurement, the photoanode was continuously irradiated with a light source of 365 nm or 450 nm wavelengths.

Photocurrent transients were carried out with and without the presence of 0.1 M glycerol by manually stopping the irradiation. A light source of 365 nm or 450 nm wavelengths was used, and the applied potential was 0.5 V (vs. Ag/AgCl).

Mott-Schottky analysis was conducted under dark conditions by varying the applied potential from 0.6 V to -1 V vs. Ag/AgCl with a sinusoidal modulation of the applied potential of 10 mV amplitude and a frequency of 1 kHz.

Photoelectrocatalytic glycerol oxidation

Photoelectrocatalytic tests were carried out employing TiO_2 NTs as photoanode, Pt foil as cathode, Ag/AgCl as the reference electrode, and 0.1 M Na_2SO_4 as the electrolyte. A 0.5 V vs. Ag/AgCl voltage was applied, the initial glycerol concentration was 0.1 M, and the reaction volume was 30 ml.

The reaction was carried out in an undivided quartz cell with a three-electrode configuration. As the light source, an LED of 365 nm (65 mW cm^{-1}) or 450 nm (30 mW cm^{-1}) wavelength was used. A Zahner IM6 electrochemical workstation from Zahner Elektrik in Kronach was used to control the cell potential.

Before each experiment, Argon was bubbled in the absence of light for 30 minutes in the glycerol aqueous solution. This step served the purpose of both removing oxygen from the system and

saturating the electrode's surface with the substrate. Runs were carried out for 4 hours at room temperature.

In each experiment, 0.5 ml of the solution was taken every hour. After analysis, the sampled portion was returned to maintain the original reaction volume. After analyzing the sample aliquot, the cell underwent a 15-minute purge with Argon before being resealed.

The identification and quantification of glycerol and reaction intermediates were performed by using a Shimadzu Prominence Modular HPLC equipped with a REZEK ROA Organic acid H^+ column.

The Faradic Efficiency of (FE) dihydroxyacetone (DHA) and glyceraldehyde (GA) was calculated through Equation 2.4, considering the oxidation reaction in Equation 6.1, where z are the electrons exchanged, that are equivalent to the number of holes, equal to 2 for both DHA and GA

Experimental determination of electronic band structures

The positioning of the characteristic energy levels, including the Fermi level (E_F), conduction and valence band edges, was determined by considering the V_{FB} obtained from the M-S plot. In fact, the E_F of the semiconductor can be determined from the V_{FB} as described by Equation 7.1:

Following the determination of the conduction band edge of the oxide, which was found to be approximately 0.2 eV above E_F (in accordance with the semiconductor behavior of TiO_2 NTs) [155], the valence band edge was determined by considering the previously mentioned estimated band gap.

Thermodynamic calculation of standard equilibrium potential

The equilibrium potentials of H^+/H_2, $O_2/\cdot O_2^-$, H_2O/O_2, H_2O/H_2O_2, and $H_2O/\cdot OH$ were determined from the literature [372,373], whilst in DHA and GA case they were calculated by using Equations 8.1a-b, obtaining the values of 0.44 and 0.58 V vs Ag/AgCl respectively. In all cases, the equilibrium potentials were corrected considering the pH of the solution of 7.

$$Eqn\ 8.1a) \qquad E = -\frac{\Delta G}{nF} + 2.3\,\frac{RT}{F}\,pH\ (V\ vs\ SHE)$$

$$Eqn\ 8.1b) \qquad E = -\frac{G_{DHA/GA} - G_{Glycerol}}{nF} + 0.059 \cdot pH - 0.205\ (V\ vs\ SHE)$$

where:

- ΔG is the Gibbs free energy of the oxidation reaction to produce DHA or GA (Equation 6.1)
- R is the universal ideal gas constant: R = 8.31 J K^{-1} mol^{-1},

- T is the room temperature (298 K),
- G_{DHA}, G_{GA} and $G_{Glycerol}$ are the Gibbs energy formation of -428.18 (Joback method), -387, and -478.6 [374] kJ/mol respectively.

8.3. Results and discussion

Figure 8.1 shows the SEM images of the bare NTs and Figure 8.1a shows the SEM image of the N-doped NTs. Both bare NTs and N-doped NTs show a self-organized structure with tubes averaging 8 μm in length and approximately 60 nm in diameter. I.e. No noticeable variation in morphology is observed after N-doping. Additionally, the XRD patterns of both bare NTs and N-doped NTs (Figure 8.2) show the characteristic diffraction peaks at $2\theta = 25.3°$ and 48.1°, indicating the presence of the anatase phase.[191,356]. These results show that N-doping has a minimal effect on the morphology and crystal structure of TiO_2 NTs.

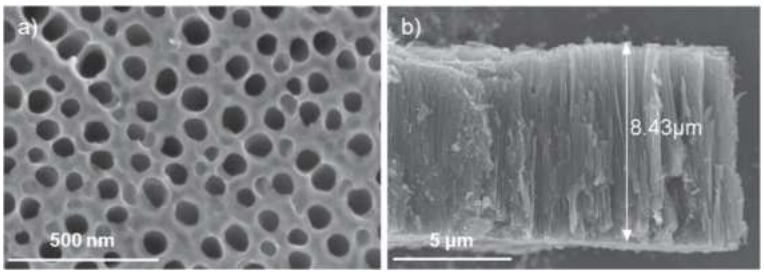

Figure 8.1. SEM pictures of a) top view and b) cross-section of bare TiO_2 NTs.

To characterize the effect of N-doping, we investigated the photoelectrochemical behavior and light reflectance properties. Figure 8.2c shows the incident photon-to-current conversion efficiency (IPCE) spectra for the TiO_2 NTs before and after N-doping measured in 0.1 M Na_2SO_4 at 0.5 V (vs Ag/AgCl). In both cases, a maximum IPCE value of 50% is observed under UV illumination at a wavelength of approximately 330 nm. In the visible light region, N-doped NTs leads to a tail photoresponse up to 400-450 nm, well in line with the literature [370,375]. If the data is plotted according to an indirect optical transition (inset of Figure 8.2c), a band gap (E_g) of 3.15 eV can be determined for the bare NTs, which is typical for anatase TiO_2 [208]. After N-doping, the E_g was determined to be 2.35 eV, which is generally attributed to the shift of the valence band (VB) to a lower energy level by N-doping [376]. Mott-Schottky (M-S) measurements were then conducted to determine the flat band potential (V_{FB}), and the results are depicted in Figure 8.3 for both the TiO_2 NTs before and after N-doping. In both cases, a value of -0.7 V vs. Ag/AgCl was obtained, aligning with findings in the literature [155,377,378].

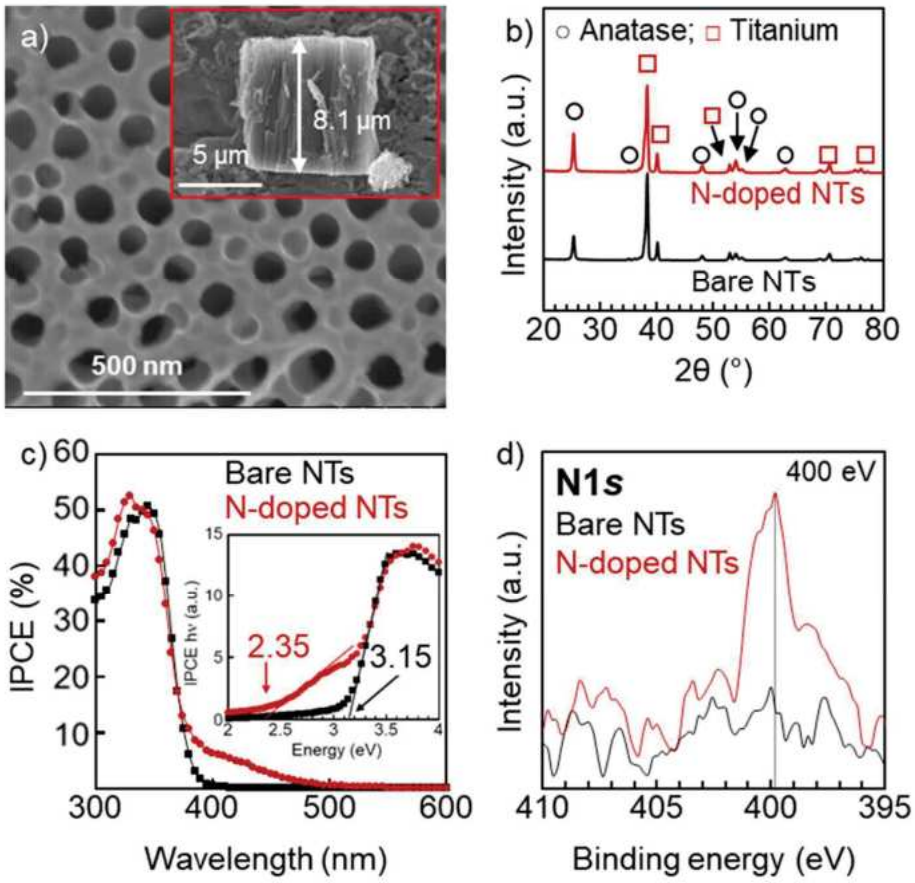

Figure 8.2. a) SEM pictures of N-doped NTs. b) XRD patterns, c) IPCE spectra with the respective evaluation of the band gap in the inset, and d) XPS spectra in the N 1s region of TiO_2 NTs before and after N-doping.

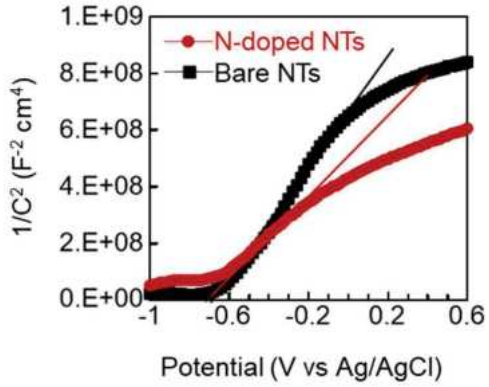

Figure 8.3. M-S plots of TiO_2 NTs recorded at 1 kHz.

UV-vis spectra (Figure 8.4) further confirm the visible light adsorption of N-doped NTs.

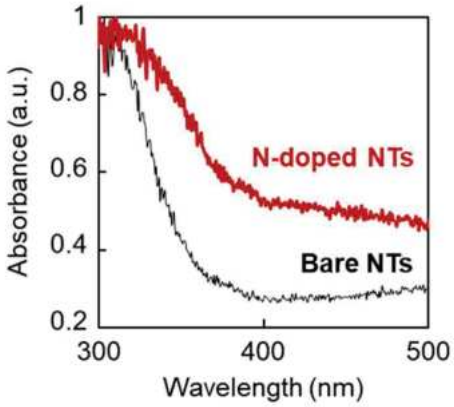

Figure 8.4. UV-Vis spectra of TiO_2 NTs recorded before and after N-doping.

XPS analysis is also performed to investigate the chemical composition of the bare and N-doped NTs, the spectra are shown in Figure 8.2d and Figure 8.5. For both bare and N-doped NTs, the Ti 2*p* spectra show the Ti-doublet at 458.7 eV and 464.5 eV, and the O 1*s* XPS spectra show one peak at 530 eV, which are attributed to the Ti-O bond. I.e. N-doping doesn't affect the chemical state of Ti and O in TiO_2. In the N 1*s* XPS spectra (Figure 8.2d), a distinct peak at 399.8 eV appears in the N-doped NTs, which is in line with the literature [379], can be attributed to the incorporation of N atoms into the TiO_2 lattice, forming an O–Ti–N structural feature. This observation suggests that N atoms are doped by substituting oxygen atoms in the lattice, rather than chemisorbed nitrogen species on the surface of the TiO_2 NTs. In addition, an N doping amount of 0.7 at% is determined by XPS.

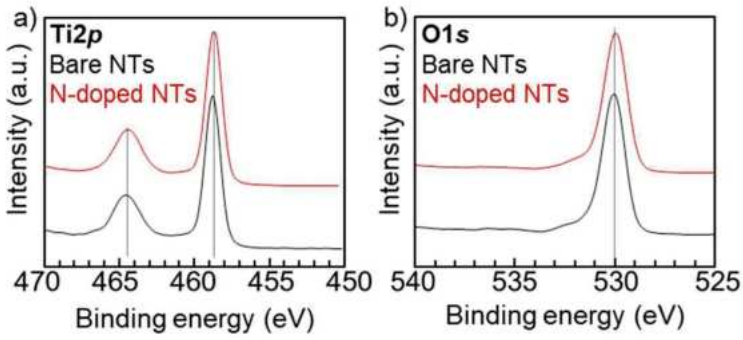

Figure 8.5. XPS spectra in the a) Ti2*p* and b) O1*s* region of TiO_2 NTs before and after N-doping.

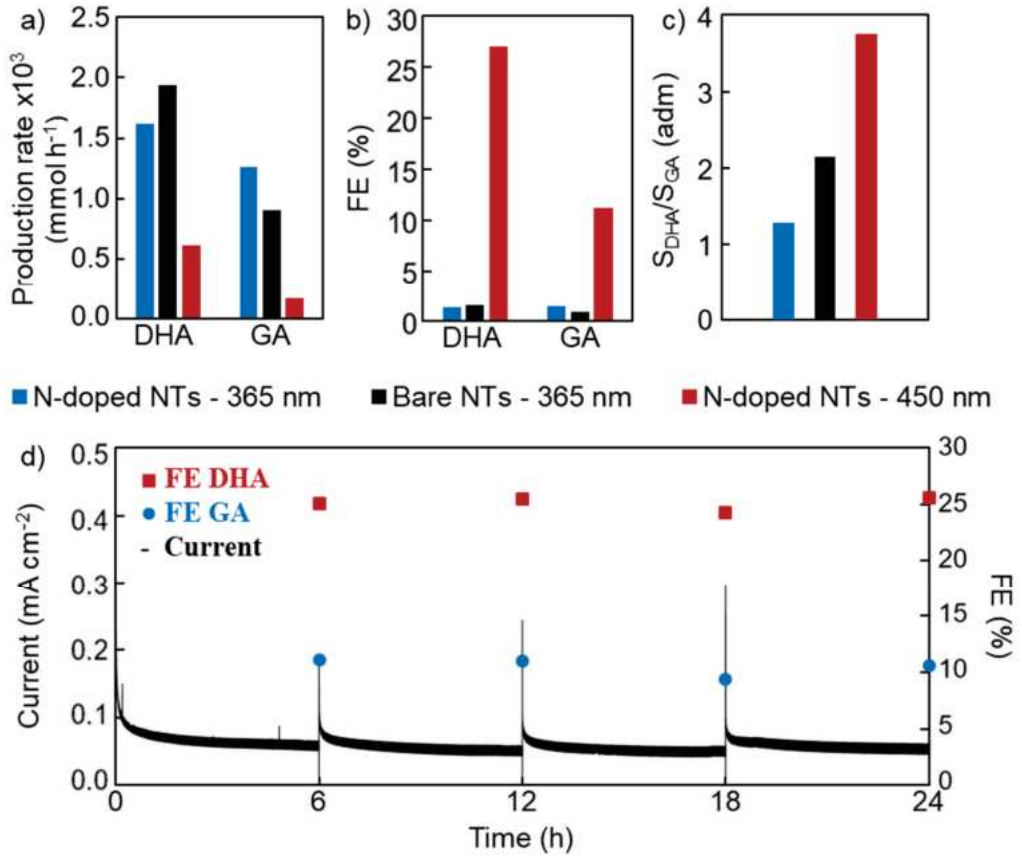

Figure 8.6. a) production rate and b) FE of DHA and GA after 4 hours of irradiation with 365 nm or 450 nm LED by using TiO_2 NTs before and after N-doping. The final DHA/GA ratio is reported in c). d) stability test carried out by irradiating the N-doped NTs with 450 nm LED.

The photoelectrochemical behavior of TiO_2 photoanodes was investigated in a glycerol electrolyte under irradiation at wavelengths of either 365 nm or 450 nm, focusing on the selectivity towards the glycerol oxidation products DHA and GA. Figure 8.6a and Figures 8.7-8.9 illustrate the DHA and GA production rates over bare NTs and N-doped NTs at a constant potential of 0.5 V vs Ag/AgCl in a 0.1 M Na_2SO_4 electrolyte with 0.1 M glycerol over 4 h. The oxidation products were quantitatively analyzed by high-performance liquid chromatography (HPLC). A higher production rate of DHA over GA is observed under all conditions, indicating a preferential conversion of glycerol to the target product DHA. Under 365 nm irradiation, bare NTs exhibits the highest production rate of DHA due to the intrinsic photoactivity of TiO_2 in the UV region. This is supported by the photocurrent measurements, where bare NTs display higher photocurrent than N-doped NTs under 365 nm LED illumination (Figures 8.7 – 8.8). A remarkable difference is observed under 450 nm LED irradiation for N-doped NTs. I.e. despite a decrease in photocurrent (Figures 8.8 – 8.9), the FEs for both DHA and GA increase significantly, with DHA showing a more pronounced rise, reaching up to 27% and 11%, respectively (Figure 8.6b). This observation, in contrast to the efficiencies under 365 nm

irradiation where the FEs remained below 2% (see Table 8.1), underscores a more effective charge utilization in glycerol conversion under visible light by N-doped NTs. The selectivity of DHA over GA was further evaluated by calculating the ratio of their production. Remarkably, N-doped NTs irradiated with 450 nm LED exhibit the highest selectivity for DHA among all the conditions, as evidenced by the calculated ratio of their production detailed in Table 8.1 and illustrated in Figure 8.6c. Additionally, the results of photon-to-chemical conversion efficiency (Table 8.2) show that N-doped NTs under 450 nm irradiation achieve a comparable conversion of photons to chemicals compared to UV experiments, despite the visible light utilization and exhibiting a lower measured photocurrent.

The stability of N-doped NTs was also evaluated by 24h long-term experiments under 450 nm LED illumination, and the results are shown in Figure 8.6d. N-doped NTs show a consistent photocurrent and FE towards DHA and GA, and no structural changes are observed in N-doped NTs after the test (Figure 8.10), indicating its excellent stability.

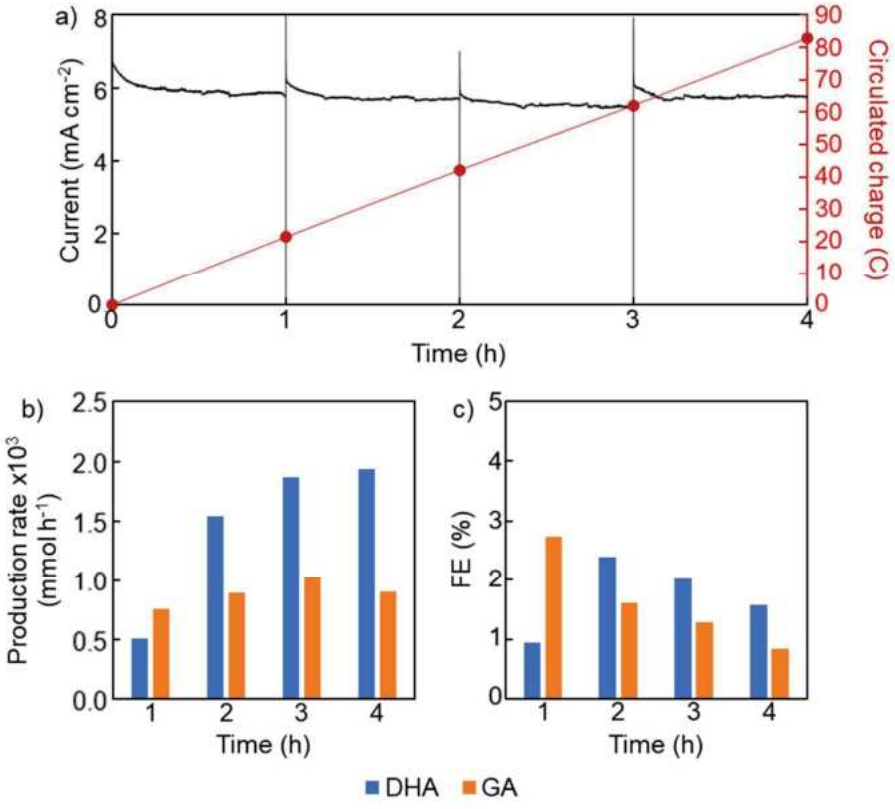

Figure 8.7. a) I_{ph} vs time plot of photoelectrochemical test executed using bare TiO_2 NTs and 365 nm LED as the light source. The production rate and the FE of DHA and GA recorded after each hour are reported in b) and c) respectively.

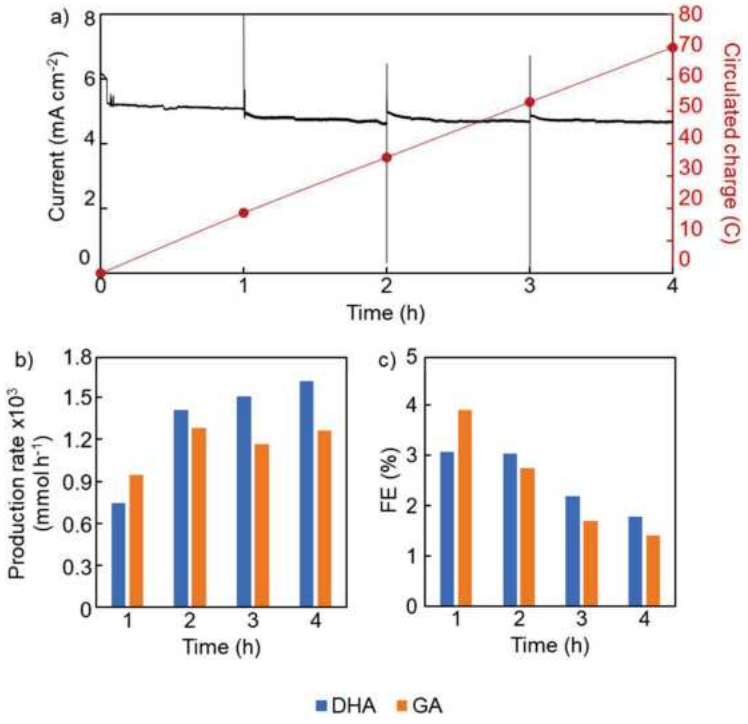

Figure 8.8. a) I_{ph} vs time plot of photoelectrochemical test executed using N-doped TiO_2 NTs sample and 365 nm LED as the light source. The production rate and the FE of DHA and GA recorded after each hour are reported in b) and c) respectively.

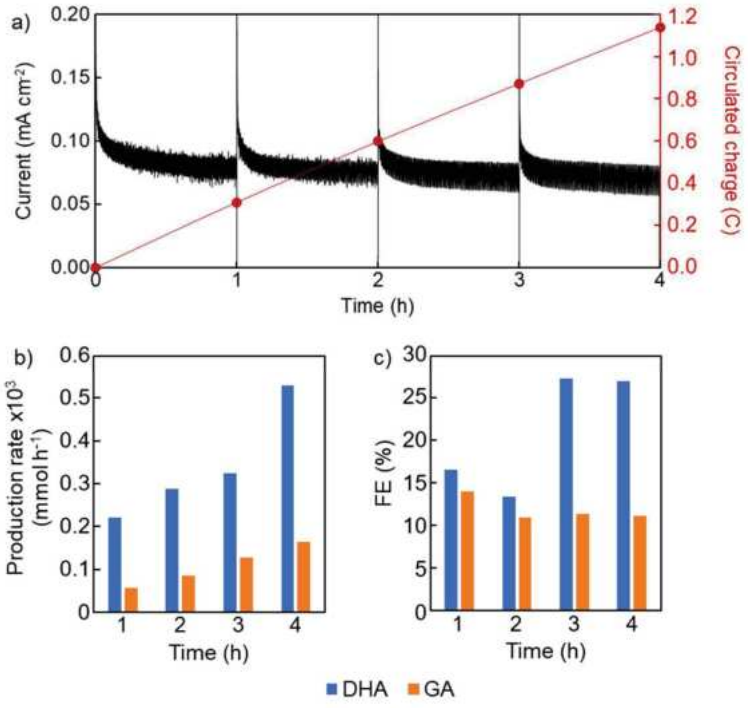

Figure 8.9. a) I_{ph} vs time plot of photoelectrochemical test executed using N-doped TiO_2 NTs sample and 450 nm LED as the light source. The production rate and the FE of DHA and GA recorded after each hour are reported in b) and c) respectively.

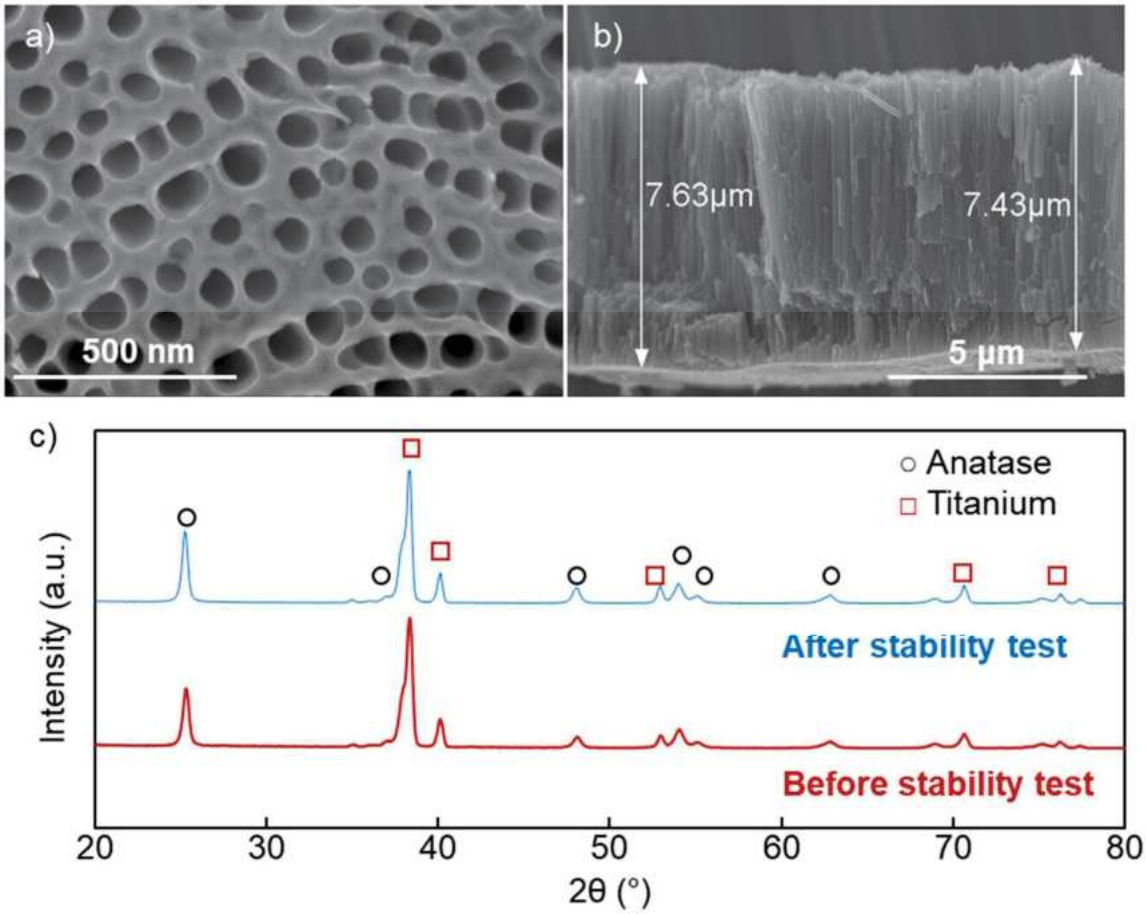

Figure 8.10. SEM pictures of a) top view and b) cross-section of N-doped TiO_2 NTs after stability test. c) XRD pattern of N-doped TiO2 NTs executed before and after the stability test.

Table 8.1. Production rate and relative amount of DHA and GA after 4 hours of irradiation with 365 nm or 450 nm LED by using TiO_2 NTs before and after N-doping.

	DHA (mmol h^{-1})	GA (mmol h^{-1})	DHA (%)	GA (%)
Bare NTs – 365 nm	1.94	0.903	68	32
N-doped NTs – 365 nm	1.62	1.26	56	44
N-doped NTs – 450 nm	0.529	0.127	79	21

Table 8.2. Photocurrent measured during the photoelectrocatalytic reactions, power density of the light sources, and DHA and GA production normalized by the irradiated area, the reaction time, and the incident photon flux, and respective FE.

	Bare NTs - 365 nm	N-Doped NTs - 365 nm	N-Doped NTs - 450 nm
I_{ph} (mA cm^{-2})	6	5	$6 \cdot 10^{-2}$
Light source (mW cm^{-2})	65	65	30
DHA (μmol h^{-1} mW^{-1})	$2.98 \cdot 10^{-2}$	$2.48 \cdot 10^{-2}$	$2.06 \cdot 10^{-2}$
GA (μmol h^{-1} mW^{-1})	$1.38 \cdot 10^{-2}$	$1.94 \cdot 10^{-2}$	$5.5 \cdot 10^{-3}$
FE DHA (%)	2.0	1.3	27
FE GA (%)	1.0	1.4	11

To obtain some further insight into the different PEC glycerol oxidation behavior of bare NTs and N-doped NTs, we performed transient photocurrent measurement and electrochemical impedance spectroscopy (EIS) under 365 nm and 450 nm LED light irradiation in both aqueous and glycerol-containing solution. The transient photocurrent results (Figures 8.11a and 8.11b) show that under 365 nm LED irradiation, both bare and N-doped NTs experience an increase in photocurrent with the addition of 0.1 M glycerol, confirming the role of glycerol as an effective hole trapping agent. However, bare NTs consistently exhibit higher photocurrents than N-doped NTs under these conditions. In contrast, under 450 nm LED light, the photocurrent behavior diverges significantly (Figures 8.11c and 8.11d). N-doped NTs exhibit a noticeable photocurrent that is further enhanced by the addition of glycerol, confirming its visible light activity. Conversely, bare NTs exhibit a negligible photocurrent that is unaffected by the addition of glycerol. This contrast highlights the superior visible light response of N-doped NTs. EIS measurements (Figures 8.11e, 8.11f, and Figure 8.12) show that light exposure significantly reduces the charge transfer resistance (R_{ct}) for all samples, highlighting the critical role of irradiation in facilitating charge generation and transfer. In the presence of glycerol, there is a further reduction in R_{ct} for both types of NTs. In particular, under 365 nm LED, bare NTs show the lowest R_{ct}, while under 450 nm they show the highest R_{ct}. Meanwhile, N-doped NTs maintain low R_{ct} values under both wavelengths, confirming their effective charge transfer properties, especially under visible light. These results illustrate that the improved PEC glycerol oxidation performance in N-doped NTs is due to the high visible light utilization and enhanced charge transfer efficiency for the N-doped material.

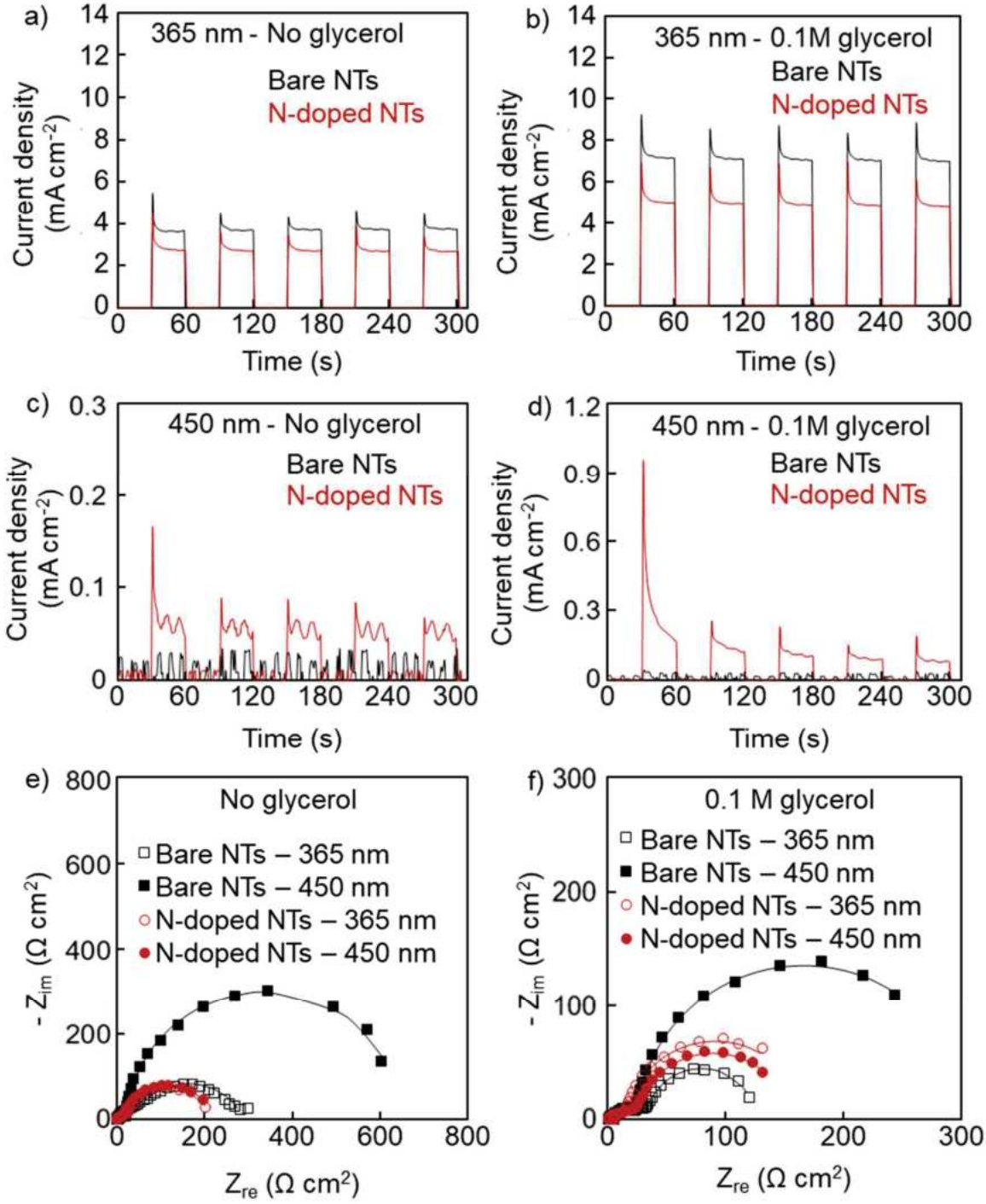

Figure 8.11. Photocurrent transients recorded without a), c) and with 0.1M glycerol b), d) by irradiating the TiO_2 NTs before and after N-doping with 365 nm or 450 nm LED. EIS spectra recorded without and with 0.1M glycerol are reported in e) and f), respectively, using TiO_2 NTs before or after N-doping and irradiating the sample with 365 nm or 450 nm LED.

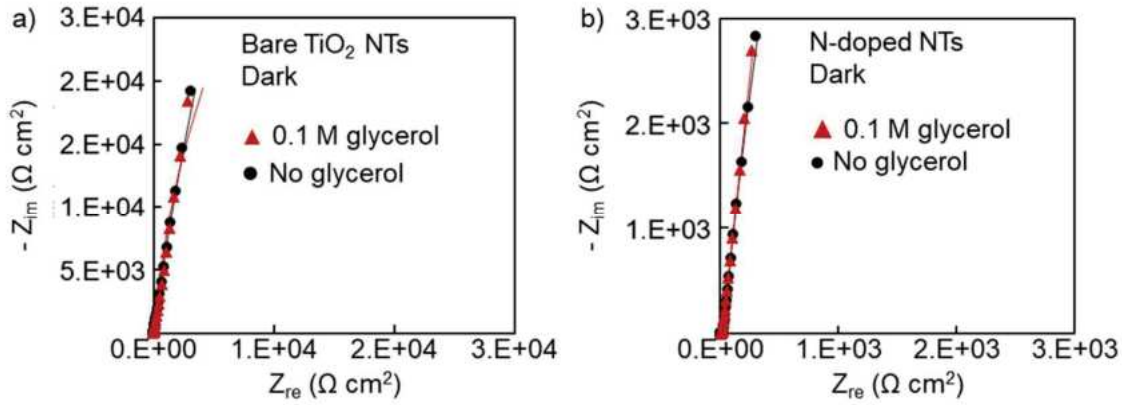

Figure 8.12. EIS of TiO_2 NTs recorded a) before and b) after N-doping without irradiation.

Based on above data, an energetic sketch was constructed and is shown in Figure 8.13 to illustrate the impact of N-doping on the band structure and the resulting photoelectrocatalytic effects. The preferential formation of DHA over GA during glycerol oxidation can be attributed to the lower oxidation potential of DHA (0.44 V vs. Ag/AgCl) compared to GA (0.58 V vs. Ag/AgCl), determined considering the Gibbs free energy found in the literature [374]. This results in a lower energy input required for the partial oxidation of glycerol to DHA, thus favoring its selective formation.

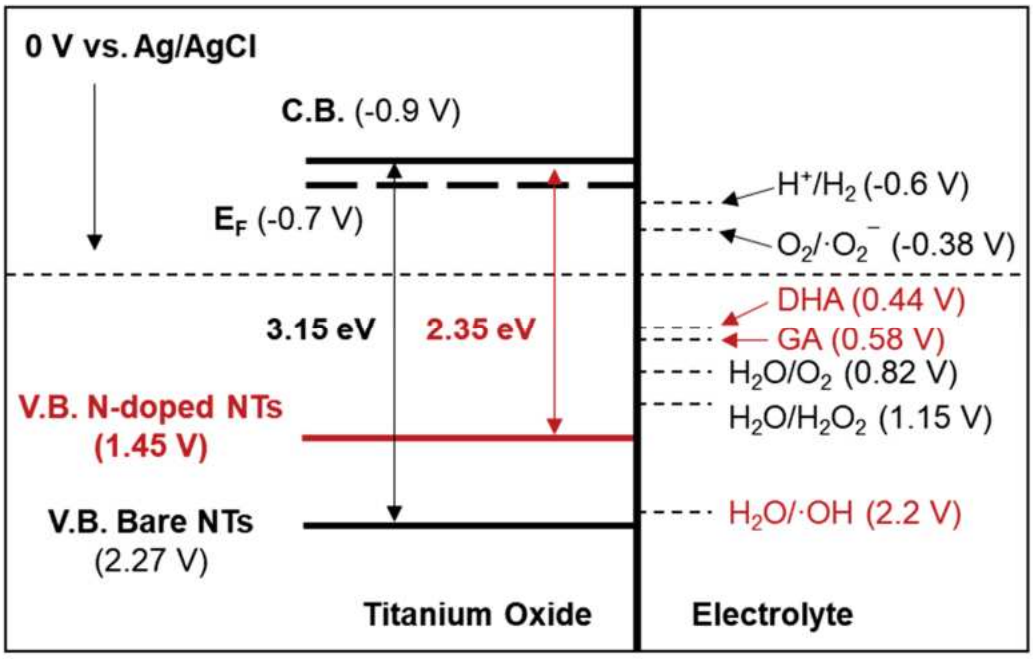

Figure 8.13. Sketch of the energetic levels of the oxide/electrolyte interface

As indicated by the band alignment, both water splitting and glycerol oxidation are energetically favorable processes for bare and N-doped NTs. However, the energy level of the VB in bare NTs is

higher than the energy required to generate ·OH, facilitating the production of these highly reactive radicals. This leads to the preferential oxidation of glycerol to smaller, more oxidized products, ultimately resulting in the complete mineralization of glycerol to CO_2 and H_2 and consequently low FE for DHA and GA. In contrast, the VB of N-doped NTs is below the energy required to generate ·OH, which suppresses the formation of these radicals, and thus shifts the glycerol oxidation pathway toward the production of partial oxidation products such as DHA and GA. Therefore, modifying the electronic band structure of TiO_2 by nitrogen doping effectively tunes the reaction pathway of glycerol oxidation and increases the selectivity of the oxidation products.

8.4. Conclusions

In this study, we investigated the efficiency of N-doped NTs for the photoelectrochemical oxidation of glycerol to produce DHA and GA. The N-doped NTs exhibit superior FE under 450 nm irradiation, with 27% for DHA and 11% for GA. They also show remarkable long-term stability. The key factor behind this performance is the significant shift in the valence band energy caused by N-doping, which effectively narrows the band gap. This adjustment allows for the harvesting of visible light and suppresses the formation of hydroxyl radicals, thereby reducing undesired complete glycerol mineralization. In summary, the results highlight the effectiveness of bandgap engineering approach to modify the selectivity of electrochemical reactions on semiconductors. This method can effectively fine-tune the performance of PEC oxidation reactions of organic compounds, thereby improving selectivity and as shown for glycerol oxidation, facilitate the production of high value-added products.

9. Photoelectrolysis of glucose and fructose containing solution in PGM-free cells for hydrogen and valuable chemicals production

This published study [223] study investigates the reforming of glucose and fructose by photoelectrolyis, employing TiO_2 NTs photoanodes for the selective oxidation of the carbohydrates and Ni foam as cathode. TiO_2 NTs with different structural features were grown on Ti felt via anodizing and annealing to promote their crystallization (Figure 9.1).

These electrodes were tested in aqueous solutions at three different pH values (i.e. 2, 7, and 12) both without and with the addition of biomass. When biomass was present, the hydrogen production rate increased, reaching faradic efficiencies (FEs) ~ 100 % in spite of the use of undivided cell, allowing the simultaneous production of valuable partial oxidation compounds, such as gluconic acid (GA) and formic acid (FA), with FEs of 24% and 55% respectively, and overall quantum yields of 5.67% and 4.36% respectively. The photoanodes used demonstrated high mechanical and chemical stability under all the tested conditions, with electrode performance remaining consistent over time, allowing the reuse of the same electrode for a not limited number of runs after a mild cleaning step.

The results demonstrated that this photoelectrocatalytic (PEC) process is promising for both biomass valorization and H_2 production.

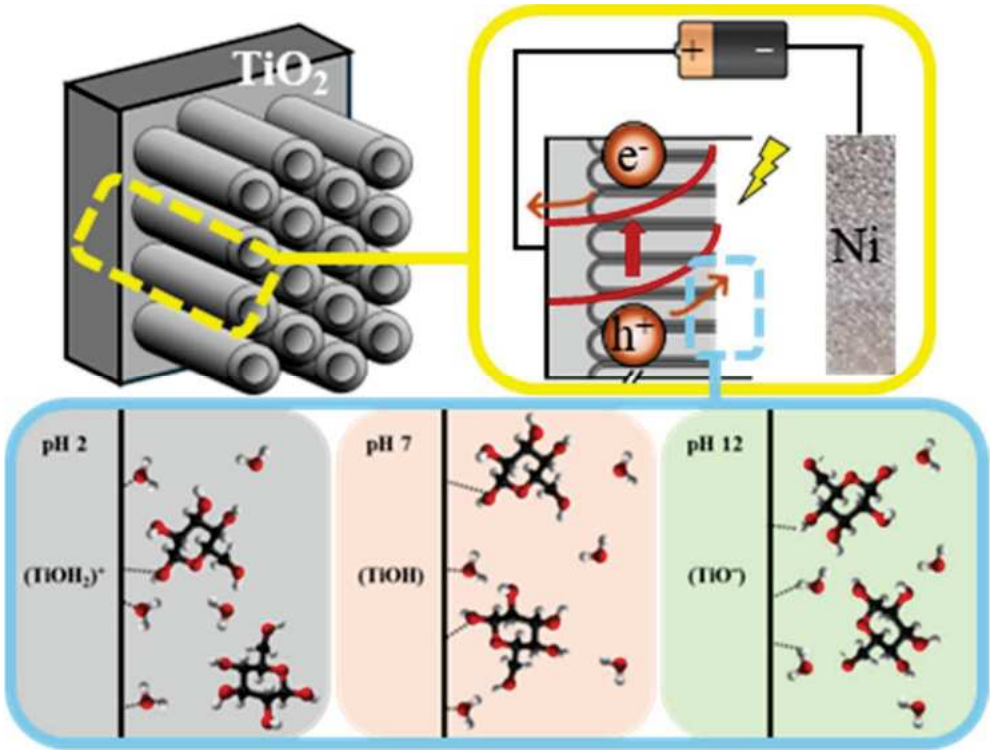

Figure 9.1. Schematic illustration of photoelectrocatalytic reactions.

9.1. Introduction

In this work, glucose and its isomer fructose have been investigated as substrates to produce HVA products. They can be produced directly from cellulose and are the most abundant and renewable biomasses on Earth [380–382]. They can serve as precursors for producing ethanol, renewable diesel, and jet fuels, along with a wide array of biobased chemicals used as industrial feedstocks for bioplastics and hydrogen production [283,383–386]. Notably, the selective oxidation of these compounds to produce gluconic and formic acids is particularly appealing due to their industrial applications as platform chemicals [387–390].

Gluconic acid (GA) and its derivatives market values are expected to reach $1.9 billion by 2028 and find extensive use in the food, pharmaceutical, and detergent industries as flavoring and chelating agents [391,392]. Moreover, formic acid (FA) serves as an energy carrier and is a crucial intermediate in chemical synthesis across industries ranging from chemical and agricultural to pharmaceutical, textile, and rubber. Its market value is expected to increase up to $4 billion in the next 10 years [393,394].

Various technologies involving high temperature and pressure conditions have been employed to produce GA and FA with low selectivity, difficult separation, pollutant emissions, and low yields, despite the use of expensive catalysts, oxidizing agents, and high energy consumption [395–401]. Therefore, there's a high demand for alternative methods for glucose and fructose conversion.

This study focuses on the anaerobic partial oxidation of glucose and fructose in an aqueous medium under mild temperature and pressure conditions to produce H_2 and high-value-added (HVA) products in photoelectrochemical cells. Platinum group metal (PGM) free TiO_2 nanotubes (NTs) photoanode with different features (tubes wall thickness and distances among parallel tubes) and Ni foam cathode were used in the attempt to realize cost effective process with high stable materials. A photoelectrochemical investigation was carried out to get a complete description of the energetics of the semiconductor/electrolyte interface. To estimate FE toward HVA and H_2, GC and HPLC analyses were carried out as function of electrolyte pH.

9.2. Experimental

Electrodes preparation

TiO_2 nanotube photoanodes were fabricated by anodization (Figure 9.2) [155,208,346].

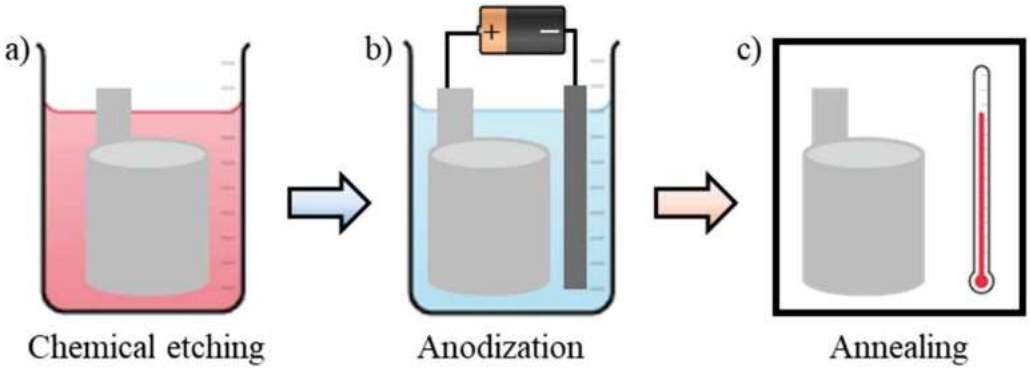

Figure 9.2. Schematic illustration of the photoanode preparation process: a) chemical etching, b) anodization, c) annealing.

Titanium fiber felt (Fuel cell store) with a thickness ranging from 0.2 to 0.3 mm was cut and etched for 2 seconds in a solution containing hydrofluoric acid (HF, Sigma Aldrich, purity 39.5%), nitric acid (Sigma Aldrich, purity 69.0%), and deionized water at a volume ratio of 1:1:3. Subsequently, they were sonicated in acetone and ethanol for 5 minutes each, followed by rinsing with deionized water and air-drying. Anodization was carried out in a two-electrode cell setup, with aluminum foil serving as the cathode in an ethylene glycol solution (EG, Aldrich, 99.8% anhydrous) containing NH_4F (Sigma Aldrich) and deionized water. TiO_2 nanotubes with different features were obtained by varying the anodization conditions, i.e., the composition of the anodization bath, time, and potential. The synthesis conditions are reported in Table 9.1.

Table 9.1. Details of the bath composition, applied potential, and duration of the anodization process for the synthesis of the two samples used in the photoelectrocatalytic tests.

Sample	EG (%wt)	NH_4F (%wt)	H_2O (%wt)	Potential (V)	Time (min)
0.75%w	99	0.25	0.75	45	10
50%w	49.5	0.5	50	30	30

Soon after the anodization step, both samples were annealed in air to 450°C for 3 hours to promote the crystallization of the TiO_2 nanotubes towards the anatase phase.
Commercial Ni foam (Goodfellow) was employed as the cathode.

Characterization

SEM, XRD, Raman spectra were performed; further details are provided in the experimental section (Section 2).

For the photoelectrochemical measurements, the TiO_2 nanotubes photoanode served as the working electrode in a three-electrode cell configuration. A 0.1 M ammonium biborate tetrahydrate (ABE, $(NH_4)_2B_4O_7 \cdot 4H_2O$; Sigma Aldrich), was employed as the electrolyte. The electrode potential was regulated by a versastat potentiostat. Further details are provided in the experimental section (Section 2).

Mott-Schottky (M-S) analysis was conducted under dark conditions by varying the applied potential from 1 V to -0.7 V vs. Ag/AgCl with a sinusoidal modulation of the applied potential of 10 mV amplitude and a frequency of 1 kHz.

Thermodynamic and kinetic aspects of the partial oxidation of glucose (Sigma-Aldrich) and fructose (Sigma-Aldrich) were investigated via cyclic voltammetry (CV) in a 0.5 M Na_2SO_4 (99% Sigma-Aldrich), both in the absence and presence of 0.1 M of biomass. Cyclic voltammetry measurements were conducted by employing a Parstat 4000 potentiostat within the voltage range of 0 to 1.9 V vs RHE, utilizing a three-electrode cell configuration with Pt mesh serving as the working and counter electrode, and Ag/AgCl/sat. KCl as the reference electrode. A scan rate of 5 mV/s was employed. For the sake of comparison, CVs were plotted using the Reverse Hydrogen Electrode (RHE) potential, as described in Equation 9.1.

$$E_{RHE}\ (V) = 0.198 + 0.059\ pH + \ E_{Ag/AgCl} \qquad Eqn.\ 9.1)$$

where $E_{Ag/AgCl}$ is the working potential.

Electrochemical Impedance Spectroscopy (EIS) measurements were conducted using a Parstat 4000 potentiostat.

Photoelectrocatalytic test

Photoelectrocatalytic experiments were conducted utilizing TiO_2 NTs as the photoanode, Ni foam as the cathode, and 0.5 M Na_2SO_4 as the electrolyte. A scheme of the experimental setup is reported in Figure 9.2. The pH was adjusted to 2 or 12 using H_2SO_4 or NaOH, respectively, and a potential of 1 V was applied between the photoanode and the cathode for three hours. Glucose or fructose concentrations were 0.1 M. The reactions took place in undivided glass cells (Figure 9.3), employing a two-electrode configuration. As the light source, a 125 W medium-pressure Hg lamp emitting mainly near-UV light at a wavelength of 365 nm was used. The power density of the emitted light of 10 mW/cm² was measured by using a radiometer. Photoanode and cathode surfaces were 90 cm^2 (irradiated) and 180 cm^2, respectively. A Parstat 4000 (PAR) potentiostat equipped with

Electrochemical Impedance Spectroscopy (EIS) capabilities was utilized to regulate cell potential and gather kinetic data for both anodic and cathodic processes.

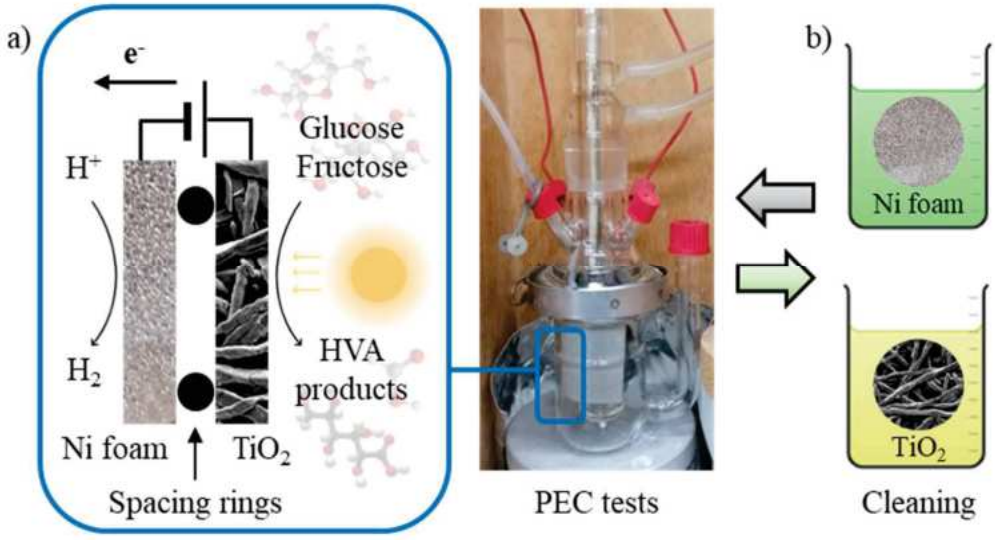

Figure 9.3. a) Image of the PEC cell used, and the corresponding schematic illustration. b) Schematic representation of the electrode cleaning process.

Before each run, Helium was bubbled under stirring in the dark for 30 minutes within the biomass aqueous solution to eliminate oxygen from the system and saturate the electrode surfaces with the substrate. Subsequently, the reactor was sealed, and the lamp was turned on. During the reaction time, water was circulated in the reactor cooling jacket to maintain the room temperature within the reaction mixture.

The photoanode was subjected to reuse after sonication with acetone and water for 5 minutes each to eliminate any glycerol residues, while Ni foam was cleaned by sonication for 5 minutes in 1 M HCl and water.

Analitycal tecniques

The detection and quantification of glucose, fructose, and reaction intermediates were conducted using HPLC. Analysis of gaseous species collected in the reactor headspace was carried out using a GC system, further details are provided in the experimental section (Section 2).

The faradic efficiency for GA, FA, CO_2, and H_2 was determined using Equation 2.4, where z are the electrons exchanged, that are equivalent to the number of holes reported in Table 9.2 considering the half-reactions in Equations 6.3 and 9.2 – 9.4.

$Eqn.\ 9.2)$ $$C_6H_{12}O_6 + H_2O + 2\,h^+ \rightarrow C_6H_{12}O_7 + 2\,H^+$$

$Eqn.\ 9.3)$ $$C_6H_{12}O_6 + 6\,H_2O + 12\,h^+ \rightarrow 6\,CH_2O_2 + 12\,H^+$$

$Eqn.\ 9.4)$ $$C_6H_{12}O_6 + 6\,H_2O + 24\,h^+ \rightarrow 6\,CO_2 + 24\,H^+$$

Table 9.2. Electrons/holes exchanged in the half cell reactions reported in the Equations 6.3 and 9.2-9.4

Compound	Chemical formula	Electrons/holes exchanged
Glucose/fructose	$C_6H_{12}O_6$	
GA	$C_6H_{12}O_7$	2
FA	CH_2O_2	2
Carbon dioxide	CO_2	4
Hydrogen	H_2	2

Quantum yield calculation

The quantum yield (η) can be defined as the ratio of circulated electrons to absorbed photons, as shown in Equation 9.5:

$Eqn.\ 9.5)$ $$\eta = \frac{circulated\ electrons\ (mols)}{absorbed\ photons\ (mols)}$$

Furthermore, the energy of the photons emitted by the light source can be calculated using the Planck equation (Equation 9.6):

$Eqn.\ 9.6)$ $$E = \frac{h\ (J \cdot s)\ c\ (m \cdot s^{-1})}{\lambda\ (m)} = 5.45 \cdot 10^{-19}\ (J)$$

where h = 6.626 10^{-34} (J s) is the Planck constant, c = 3^8 (m s^{-1}) is the speed of light, and λ = 3.65 10^{-7} (m) is the emitted light wavelength

Given the emitted light's power density (P) of 100 W/m² measured with a radiometer the mols of absorbed photons can be calculated using Equation 9.7:

$$Eqn.\ 9.7) \qquad Absorbed\ photons = \frac{P\ (J\ \cdot s^{-1}\ \cdot m^{-2})\ t\ (s)\ S\ (m^2)}{E\ (J)\ N_A\ (mol^{-1})} = \ 2.96 \cdot 10^{-2}\ (mol)$$

where t is the reaction time (3 h), S is the photoanode surface (90cm^2), and N_A is Avogadro's number (6.022 10^{23} mol^{-1}).

9.3. Results

Figure 9.4 compares the morphological features of TiO_2 NTs grown in ammonium fluoride containing ethylene glycol solution with 50% (Figures 9.4a-c) and 0.75% of water (Figures 9.4d-f), respectively, after thermal treatment at 450 °C for 3 h. The SEM micrographs distinctly reveal the achievement of a large array of TiO_2 NTs, wherein the average length is ~ 720 nm and 850 nm (inset of Figures 9.4a and d). Notably, NTs grown in 50%w show thinner sharp walls with a large space among NTs, thus allowing a better contact and refreshment of the electrolyte during the photoelectrochemical process. These findings are consistent with earlier investigations [346].

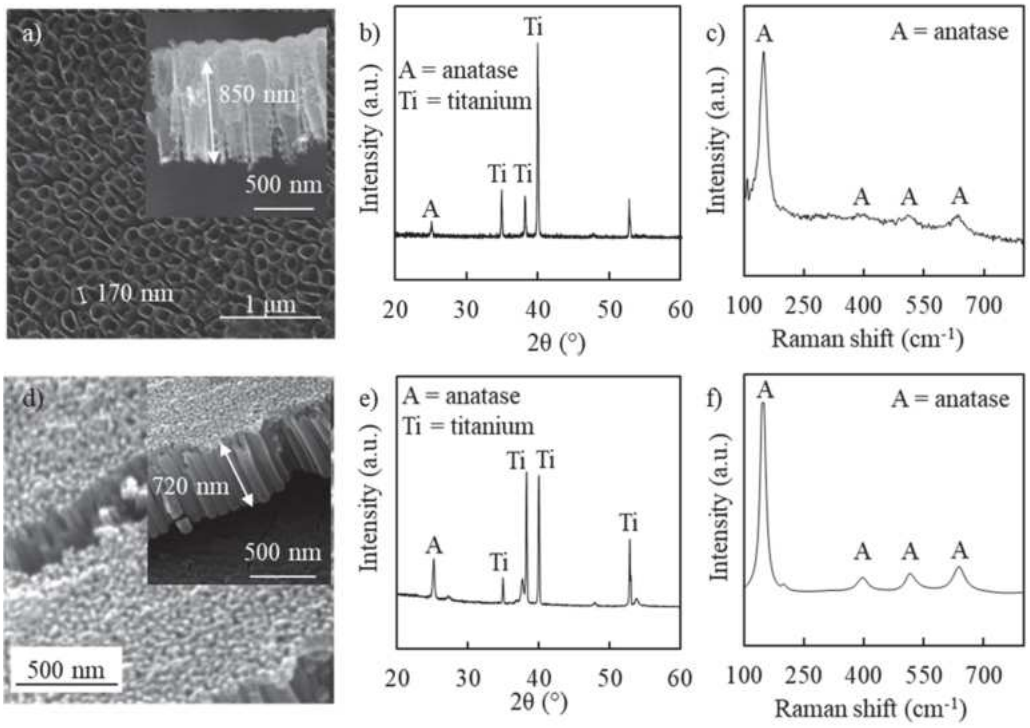

Figure 9.4. SEM pictures, XRD patterns, and Raman spectra of (a – c) 50 %w NTs sample and (d – f) 0.75%w NTs sample.

XRD pattern for annealed TiO_2 NTs, reported in Figures 9.4b and d, shows the reflections of anatase polymorph due to the crystallization of TiO_2 grown by the anodizing process, together with the reflections of titanium arising from the not anodized metal still present beneath the nanotube layers that allows an efficient electrical contact with the photoactive titania [265]. The presence of anatase is also confirmed by Raman spectroscopy. As shown in Figures 9.4c and e characteristic bands of anatase polymorph are present at 144 cm^{-1}, 196 cm^{-1}, 397 cm^{-1}, 513 cm^{-1}, and 639 cm^{-1} [271].

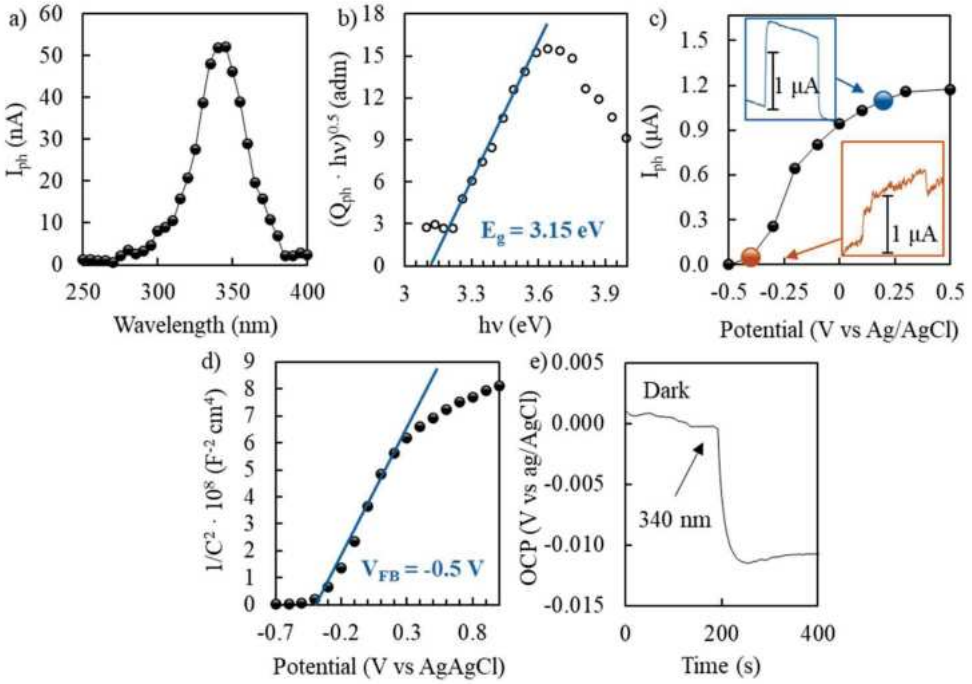

Figure 9.5. a) photocurrent spectra recorded in a 0.1 M ABE aqueous solution at 0.5 V vs Ag/AgCl, b) respective $(Q_{ph} \cdot h\nu)^{0.5}$ vs hν plot for the E_g estimation, c) photocurrent transients under monochromatic light recorded at 340 nm and applied potential from 0.5 to -0.5 V vs Ag/AgCl, d) M-S plot recorded in a 0.1 M ABE aqueous solution at 1 kHz, and e) photopotential recorded for 50%w NTs by irradiating the sample with 340 nm monochromatic light.

A photoelectrochemical investigation aimed to gain information about the electronic characteristics of the photoanodes was carried out. The photocurrent spectrum, i.e. photocurrent as a function of the monochromatic irradiating wavelength, recorded under a constant bias polarizing the Ti/TiO_2 NTs layer electrode in a 0.1 M ABE aqueous solution at 0.5 V vs Ag/AgCl, is reported in Figure 9.5a and shows that the photoresponse is high in the UV region due to the fundamental typical absorption of anatase TiO_2. Under the hypothesis of non-direct optical transitions, an estimation of the optical band gap value (E_g) was made by extrapolating to zero the $(Q_{ph} \cdot h\nu)^{0.5}$ vs hν plot (Figure 9.5b). The determined E_g is 3.15 eV, which is in line with the reported value for anatase (3.2 eV [346]). The

photocurrent transients were measured by manually interrupting monochromatic irradiation (at λ = 340 nm), while applying a constant potential ranging from 0.5 to -0.5 V vs Ag/AgCl (see Figure 9.5c). An anodic photocurrent was observed, confirming the n-type semiconductor behavior of the oxide, with the photocurrent reaching zero at approximately - 0.5 V vs Ag/AgCl. The zero photocurrent potential can be considered an estimate of the flat band potential, U_{fb}. This value agrees with that estimated by the M-S plot recorded at 1 kHz (Figure 9.5d). It is important to mention that the flat band potential of TiO_2 NTs grown in water containing solution is slightly more positive than that estimated for NTs grown on ethylene glycol solution (i.e. -0.75 V Ag/AgCl [155]). This implies that the flat band potential is shifted toward the mid gap position. Additionally, the n-type behaviour of TiO_2 NTs is also confirmed by the cathodic photopotential recorded during the irradiation of the sample, as shown in Figure 9.5e [219].

A preliminary electrochemical assessment was conducted to gather insights into the kinetics of glucose and fructose oxidation in 0.5 M Na_2SO_4 aqueous solution at different pH (i.e., 2, 7, and 12) within a potential range of 0 to 1.9 V vs. RHE. Figure 9.6 illustrates the cyclic voltammograms obtained in solutions without and with biomass, utilizing a Pt mesh as the working and the counter electrode. At pH 2 (Figure 9.6a), cyclic voltammogram reveals two oxidation peaks at 0.2, 0.7, and an oxidation current starting at 1.1 vs. RHE in presence of glucose or fructose, with higher values being measured with fructose. According to the literature [402] in the case of glucose the first peak corresponds to the oxidation of the adsorbed hydrogen produced by chemisorption of the glucose molecule, that however does not poison the surface of the electrode, while the second peak is assigned to the oxidation of strongly adsorbed intermediate produced from the glucose oxidation in the first process. Only at high potential (namely 1.6 V vs RHE), oxygen evolution occurs suggesting that both glucose and fructose oxidation is more favorable. Notably, the OER is not significantly affected by the presence of the biomass, i.e., the current recorded at higher potential is comparable with and without biomass in the electrolyte.

The cyclic voltammograms recorded at pH 7 (Figure 9.6b) show three peaks at 0.2, 0.9, and a more pronounced one at 1.4 V vs RHE only when glucose is present with the anodic current starting at 1.1 V vs RHE. According to the literature [403], the oxidation current at 0.2 V vs RHE is associated to the production of the carboxylic acids such as gluconic acid, glucuronic acid and/or glucaric acid with a higher selectivity towards the generation of gluconic acid. The reaction proceeds through a complex mechanism, in which at first step glucose is oxidized to gluconic acid, and when the potential is increased, gluconic acid generates CO species and cyclic carbonate, and both are practically completely removed from the electrode surface when they are oxidized to CO_2. According to the

cyclic voltammogram recorded in biomass free solution, OER starts at ~ 1.5 V vs RHE. No peaks are observed with fructose, although an increased faradic current indicating its oxidation is noted by comparing the cyclic voltammetry recorded without and with fructose.

At pH 12 (Figure 9.6c), the cyclic voltammograms show multiple peaks in presence of biomass, suggesting that several oxidation steps occur by increasing the applied potential involving oxidation of glucose or fructose. According to the literature [404,405] the first peak corresponds to the oxidation of the adsorbed hydrogen produced by glucose chemisorption, while peaks at 0.7 V vs RHE corresponds to the direct oxidation of glucose from the bulk. Finally, peak at 1.1 V vs RHE corresponds to the oxidation of the adsorbed species resulting from the chemisorption of glucose occurring at lower potential. At this pH, OER appears to be partially inhibited in presence of fructose since water oxidation starts only at 1.7 V vs RHE, while with glucose there is no evidence of a current due to O_2 evolution up to 1.9 V vs RHE.

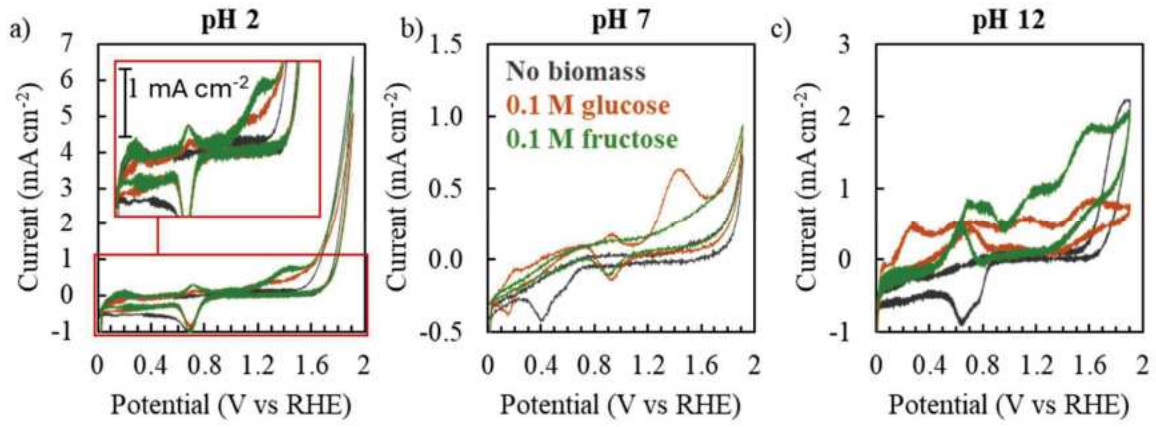

Figure 9.6. Cyclic voltammetries carried out without irradiation by using Pt mesh as the counter and the working electrode, recorded at 5 mV/s in a 0.5 M Na_2SO_4 aqueous solution at a) pH 2, b) pH 7, and c) pH 12 with and without the presence of biomass.

Figure 9.7 summarizes the results of the photoelectrochemical reforming of glucose and fructose containing solutions at different pH (namely pH 2, 7 and 12), carried out under a bias of 1 V using the TiO_2 NTs photoanodes. First of all, it is important to stress that the measured photocurrent is comparable to that measured in biomass free solution (see Figure 9.8), but with higher hydrogen evolution rate due to the Faradic efficiency of 100% or slightly lower than 100 % for glucose and fructose containing solutions, respectively, in spite the use of undivided cell. Indeed, the amount of Oxygen produced at the photoanode is significantly lower, thus limiting the competition of O_2 reduction with respect to Hydrogen Evolution Reaction (HER). Moreover, I_{ph} is higher for NTs grown in solution with a low concentration of water, probably due to the higher thickness of the tubes' wall

allowing a more efficient light absorption [191,406], but also to a more negative flat band potential with respect to NTs grown in 50%w solution. Indeed, the electric field driving the transport of photogenerated holes and electrons is directly connected to the band bending, $\Delta\Phi_{SC} = U_E - U_{FB}$ where U_E is the polarization potential [407]. Finally, for NTs grown with a low water concentration the measured photocurrent is slightly influenced by the electrolyte pH, the lowest value being measured in neutral solution. Conversely, the measured photocurrent is almost independent on the pH for TiO_2 NTs grown with a high concentration of water.

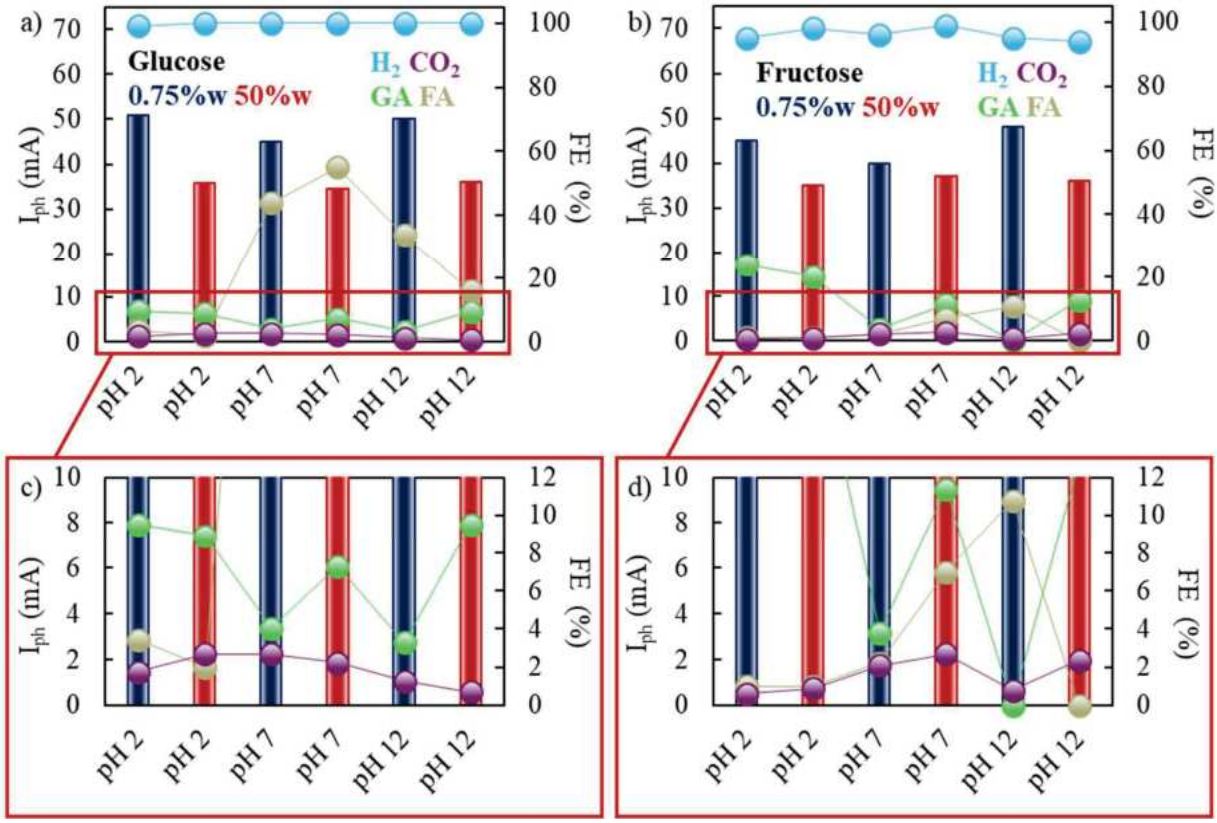

Figure 9.7. Photoelectrochemical results obtained by using a) c) glucose or b) d) fructose as the starting biomass. The blue and red bars represent the photocurrent measured using the 0.75 wt% NTs and 50 wt% NTs samples, respectively. The calculated FEs are reported in the secondary axis for H_2 (turquoise), CO_2 (purple), gluconic acid (GA, green), and formic acid (FA, brown). The reaction time of each test was 3 h.

A clear idea of the products of the photoelectrochemical reactions is provided by the plots of Figure 9.7, showing the faradic efficiencies for both the employed photoanodes as a function of the pH. For glucose, in acidic solution (pH = 2) the most abundant product is GA (FE ~ 8%) followed by FA and CO_2. This finding can be explained by CV recorded in the same solution (see Figure 9.6a) showing very low current due to glucose oxidation and an onset potential for oxygen evolution close to the third oxidation step involving glucose.

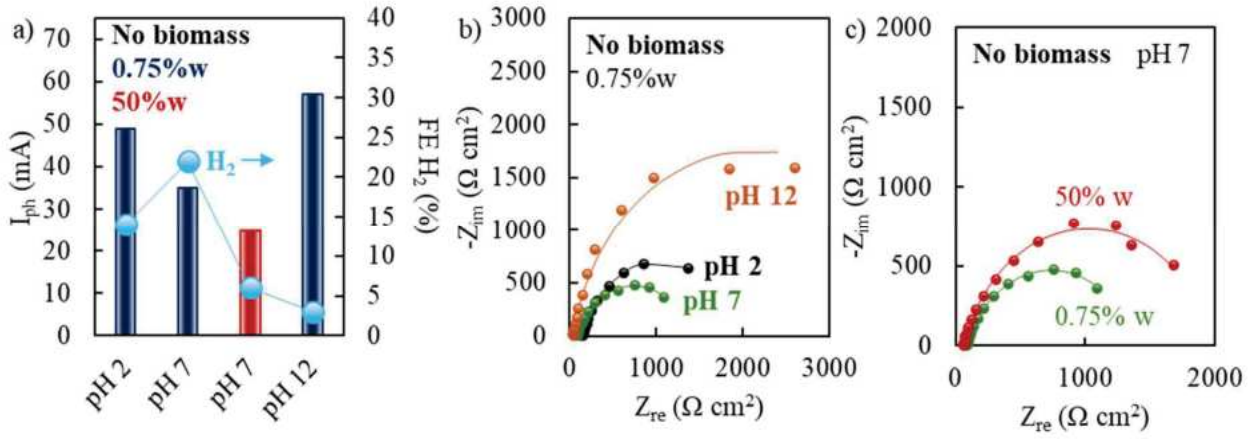

Figure 9.8. a) Photoelectrocatalytic tests and b), c) EIS recorded under irradiation without biomass

Table 9.3. Comparison with the literature of HVA and H_2 production rates normalized by photoanode area and incident photon flux.

	[156]	This work
Photoanode	Pt(SA)/def-TiO_2 NRs[(a)]	TiO_2 NTs
Cathode	Pt foil	Ni foam
Biomass	Glucose 0.01 M	Glucose 0.1 M
Electrolyte	1 M KOH	0.5 M Na_2SO_4 pH 7
Applied bias	0.6 V vs RHE	1 V (Cell potential)
Photoanode area (cm^2)	1	90
Light source (mW cm^{-2})	100	10
HVA production rate (μmol h^{-1} mW^{-1})	0.340[(b)]	0.565[(c)]
H_2 production rate (μmol h^{-1} mW^{-1})	0.356	0.933

(a) Defective TiO_2 nanorods decorated with Pt single atom

(b) Considering both gluconic and glucaric acid

(c) Considering both gluconic and formic acid

Better results were obtained in neutral solution, where partial oxidation of glucose leads to a very high faradic efficiency in FA, even if FE for GA is lower than that measured at pH 2. At this pH according to the CV of Figure 9.6b, the third glucose oxidation step occurs at potential significantly

lower than that of O_2 evolution, which is therefore significantly less favourable on a kinetic point of view. At pH 12 the most favourable reaction is partial oxidation of glucose to FA, but with lower FE than that estimated at pH 7. These results were compared with those reported in the literature by normalizing the HVA and H_2 production rates based on the photoanode area and incident photon flux. To our knowledge, only one scientific article has been published on photoelectrochemical glucose reforming to obtain HVA and H_2 [156]. As shown in Table 8.3, our system demonstrated better performances in both cases, despite the use of PGM-free materials. Additionally, no scientific articles related to the photoelectrochemical oxidation of fructose to produce HVA have been found in the literature.

Different results were obtained by photoelectrolysis of fructose containing solutions. At pH 2 the photoelectrochemical oxidation of the biomass leads to the formation of GA with FE = 24% and 20.3% for NTs grown in 0.75% water and 50% water, respectively. This finding agrees with the results of the cyclic voltammetry (see Figure 9.6a) showing a better kinetic for fructose oxidation in acidic solution. Lower faradic efficiencies for both GA and FA are estimated at higher pH, making the process less promising with respect to the photoelectrolysis of glucose.

In the photoelectrolysis experiments that yielded the highest Faradaic efficiencies (FE) towards formic acid (FA) and gluconic acid (GA) (Figure 9.7), the measured circulated charges were 125 C and 162 C, respectively. Dividing these by the Faraday constant (96485 C/mol) gives 1.29×10^{-3} mol and 1.68×10^{-3} mols of circulated electrons, respectively. The ratio of the circulated mols of electrons to absorbed photons calculate by using the Equation 9.7 yields quantum yields (η) of 4.36% and 5.67%, respectively. However, it's important to note that, although this number is higher than typical values obtained in photocatalytic processes [16], a significant portion of the light is lost due to the cell geometry and, therefore, we are currently working on improving the cell design to minimize this energy loss.

Electrochemical impedance spectra were recorded under 1 V of bias during photoelectrolysis of both glucose and fructose. Figure 9.9 shows the corresponding spectra in the Nyquist representation recorded under irradiation. For comparison we also recorded impedance spectra in biomass free solution (i.e. water photoelectrolysis) and without irradiation, that are reported in Figures 9.10b-c and 9.11, with the relative fitting parameters in Tables 9.4-9.5. All the spectra are slightly depressed semicircles, thus they can be fitted with the very simple equivalent circuit of Figure 9.9, where R_{CT} is the charge transfer resistance, Q_{SC} the capacitance of the semiconductor under irradiation, while R_{el} accounts for the electrolyte resistance. The corresponding fitting parameters are summarized in Table 9.6. At a first glance it is evident that a constant phase element is necessary to simulate the non-

ideal capacitance of TiO_2 NTs layer (see exponent n < 1). Using the Brug formula [369] it is possible to estimate the NTs capacitance, that results slightly higher for NTs grown in solution with a lower concentration of water. This is in agreement with a higher concentration of donors as suggested by the more negative flat band potential measured for these NTs [155]. The higher doping level and the consequent higher concentration of charge carriers under irradiation explain the higher photocurrent measured for these NTs with respect to those grown in 50%water. Table 9.6 also reports the charge transfer resistance for both glucose and fructose oxidation at different pH and for both NTs layers. According to Table 9.6, the charge transfer resistance ranges from 1.3 to 2.3 kΩ cm^2, with the lowest value being measured during photoelectrolysis of glucose containing solution at pH 7 by employing 0.75%w NTs. Notably, it is interesting to mention that the charge transfer resistance is inversely proportional to the overall Faradic efficiency in biomass oxidation products due to the sluggish kinetic of oxygen evolution reaction affecting the overvoltage necessary to activate the reaction. The charge transfer resistances estimated in the presence of fructose are comparable to those estimated for glucose despite the lower photocurrent in agreement with a lower overall faradic efficiency and consequent higher photocurrent wasted for O_2.

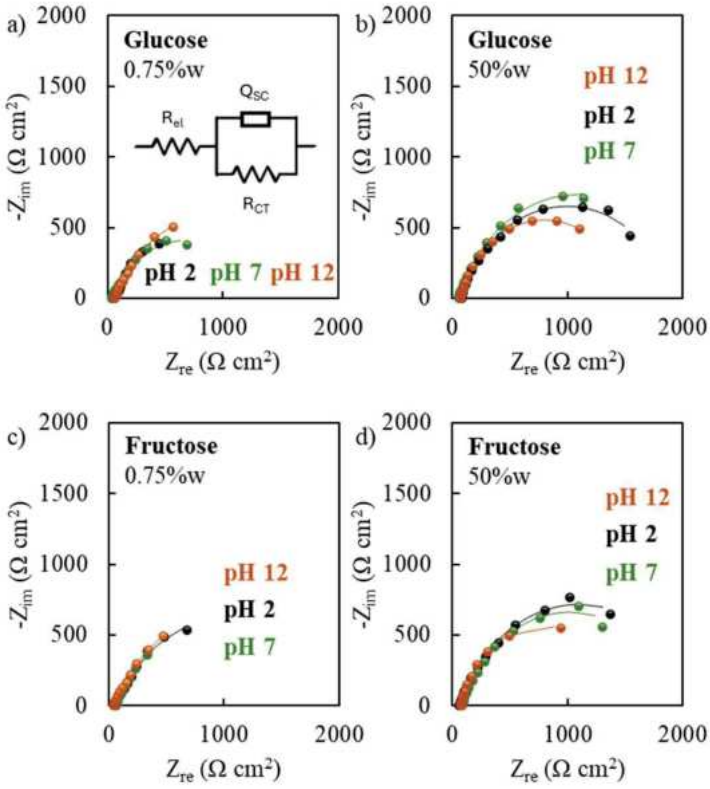

Figure 9.9. In situ EIS spectra recorded under UV irradiation (125 W medium-pressure Hg lamp) in the presence of glucose a) – b) and fructose c) – d). All the spectra were fitted by using the equivalent circuit shown in the inset of a). Impedance spectra were measured within a frequency range of 100 kHz to 0.1 Hz, applying a potential of 1 V between the photoanode and cathode, and using an AC amplitude of 10 mV.

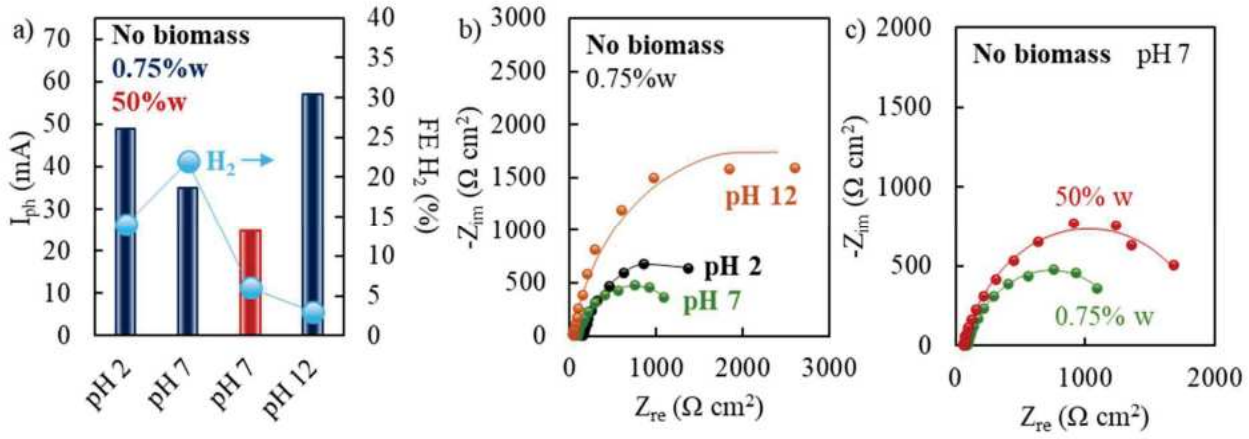

Figure 9.10. a) Photoelectrocatalytic tests and b), c) EIS recorded under irradiation without biomass

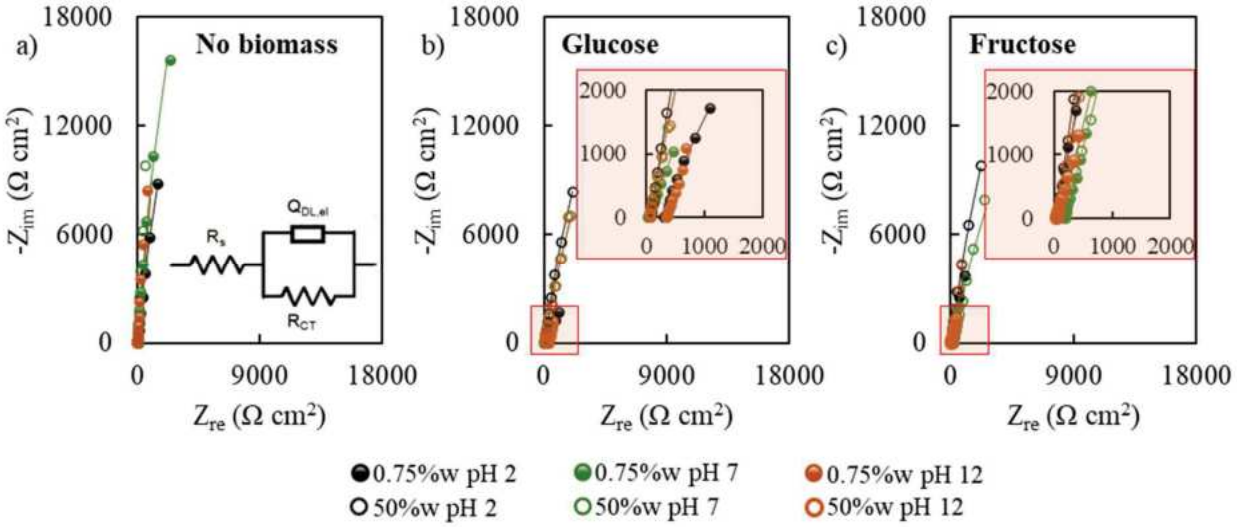

Figure 9.11. EIS recorded in dark conditions irradiation a) without biomass, and in a b) glucose or c) fructose containing solution. All the spectra were fitted by using the equivalent circuit shown in the inset of a).

Table 9.4. Fitting parameters obtained by EIS spectra recorded under irradiation without biomass

Sample	pH	R_{el} (Ω cm^2)	R_{CT} (Ω cm^2)	Q_{SC} (μS s^n cm^{-2})	n (adm)	χ square (adm)
0.75%w	2	150	$1.8 \cdot 10^3$	$3.6 \cdot 10^{-4}$	0.84	$3.2 \cdot 10^{-3}$
0.75%w	7	91	$1.3 \cdot 10^3$	$3.7 \cdot 10^{-4}$	0.80	$9.2 \cdot 10^{-4}$
50%w	7	64.7	$1.9 \cdot 10^3$	$1.9 \cdot 10^{-4}$	0.83	$3.7 \cdot 10^{-3}$
0.75%w	12	40	$4.2 \cdot 10^3$	$2.1 \cdot 10^{-4}$	0.89	$6.4 \cdot 10^{-3}$

Table 9.5. Fitting parameters obtained by EIS spectra recorded without irradiation

Sample	pH	Substrate	R_{el} (Ω cm^2)	R_{CT} (Ω cm^2)	Q_{SC} (μS s^n cm^{-2})	n (adm)	χ square (adm)
0.75%w	2	NO	74	$1.7 \cdot 10^5$	$1.7 \cdot 10^{-4}$	0.96	$4.4 \cdot 10^{-3}$
0.75%w	2	Glucose	337	$1.5 \cdot 10^4$	$5.1 \cdot 10^{-4}$	0.82	$2.9 \cdot 10^{-3}$
50%w	2	Glucose	84	$9.9 \cdot 10^4$	$1.2 \cdot 10^{-4}$	0.90	$2.7 \cdot 10^{-4}$
0.75%w	2	Fructose	66	$4.1 \cdot 10^4$	$2.6 \cdot 10^{-4}$	0.90	$9.6 \cdot 10^{-4}$
50%w	2	Fructose	65	$1.2 \cdot 10^5$	$9.9 \cdot 10^{-5}$	0.91	$5.7 \cdot 10^{-4}$
0.75%w	7	NO	39	$2.0 \cdot 10^{15}$	$1.7 \cdot 10^{-4}$	0.93	$2.6 \cdot 10^{-3}$
50%w	7	NO	69	$2.5 \cdot 10^5$	$6.2 \cdot 10^{-5}$	0.95	$4.8 \cdot 10^{-4}$
0.75%w	7	Glucose	49	$7.2 \cdot 10^{14}$	$9.0 \cdot 10^{-4}$	0.75	$2.6 \cdot 10^{-3}$
50%w	7	Glucose	53	$1.2 \cdot 10^5$	$1.4 \cdot 10^{-4}$	0.87	$5.7 \cdot 10^{-4}$
0.75%w	7	Fructose	195	$7.2 \cdot 10^{14}$	$7.1 \cdot 10^{-4}$	0.83	$6.2 \cdot 10^{-4}$
50%w	7	Fructose	108	$2.8 \cdot 10^5$	$1.9 \cdot 10^{-4}$	0.82	$3.1 \cdot 10^{-3}$
0.75%w	12	NO	42	$1.6 \cdot 10^{16}$	$1.2 \cdot 10^{-4}$	0.93	$4.5 \cdot 10^{-3}$
0.75%w	12	Glucose	349	$1.3 \cdot 10^{15}$	$8.9 \cdot 10^{-3}$	0.76	$3.3 \cdot 10^{-3}$
50%w	12	Glucose	74	$9.0 \cdot 10^4$	$1.4 \cdot 10^{-4}$	0.88	$4.4 \cdot 10^{-4}$
0.75%w	12	Fructose	38	$8.9 \cdot 10^{12}$	$7.3 \cdot 10^{-4}$	0.80	$2.3 \cdot 10^{-3}$
50%w	12	Fructose	76	5.20E+05	$2.3 \cdot 10^{-4}$	0.89	$9.3 \cdot 10^{-4}$

Table 9.6. Fitting parameters obtained by EIS spectra recorded under irradiation.

Sample	pH	Substrate	R_{el} (Ω cm^2)	R_{CT} (Ω cm^2)	Q_{SC} (μS s^n cm^{-2})	n (adm)	C_{Brug} (μF cm^{-2})	χ square (adm)
0.75%w	2	Glucose	58	$2.3 \cdot 10^3$	$1.8 \cdot 10^{-3}$	0.68	622	$5.2 \cdot 10^{-3}$
50%w	2	Glucose	79	$1.8 \cdot 10^3$	$3.5 \cdot 10^{-4}$	0.79	135	$1.2 \cdot 10^{-3}$
0.75%w	2	Fructose	59	$2.0 \cdot 10^3$	$9.6 \cdot 10^{-4}$	0.71	297	$2.1 \cdot 10^{-3}$
50%w	2	Fructose	61	$2.1 \cdot 10^3$	$3.7 \cdot 10^{-4}$	0.77	119	$1.1 \cdot 10^{-3}$
0.75%w	7	Glucose	36	$1.3 \cdot 10^3$	$1.2 \cdot 10^{-3}$	0.72	354	$4.1 \cdot 10^{-3}$
50%w	7	Glucose	55	$2.1 \cdot 10^3$	$4.6 \cdot 10^{-4}$	0.78	163	$1.4 \cdot 10^{-3}$
0.75%w	7	Fructose	63	$1.7 \cdot 10^3$	$1.5 \cdot 10^{-3}$	0.73	627	$9.7 \cdot 10^{-4}$
50%w	7	Fructose	86	$1.9 \cdot 10^3$	$5.6 \cdot 10^{-4}$	0.78	238	$1.6 \cdot 10^{-3}$
0.75%w	12	Glucose	64	$1.8 \cdot 10^3$	$1.2 \cdot 10^{-3}$	0.75	510	$1.4 \cdot 10^{-3}$
50%w	12	Glucose	74	$1.5 \cdot 10^3$	$5.7 \cdot 10^{-4}$	0.82	284	$1.1 \cdot 10^{-3}$
0.75%w	12	Fructose	41	$2.4 \cdot 10^3$	$1.2 \cdot 10^{-3}$	0.69	310	$9.8 \cdot 10^{-4}$
50%w	12	Fructose	74	$1.4 \cdot 10^3$	$5.9 \cdot 10^{-4}$	0.84	325	$8.2 \cdot 10^{-4}$

9.4. Discussion

Figure 9.12 shows the energetic of Ti/TiO_2 NTs/electrolyte interface. Conduction and valence band edges were located according to the literature [155], while their flat band potential is quoted using the relationship reported in Equation 7.1:

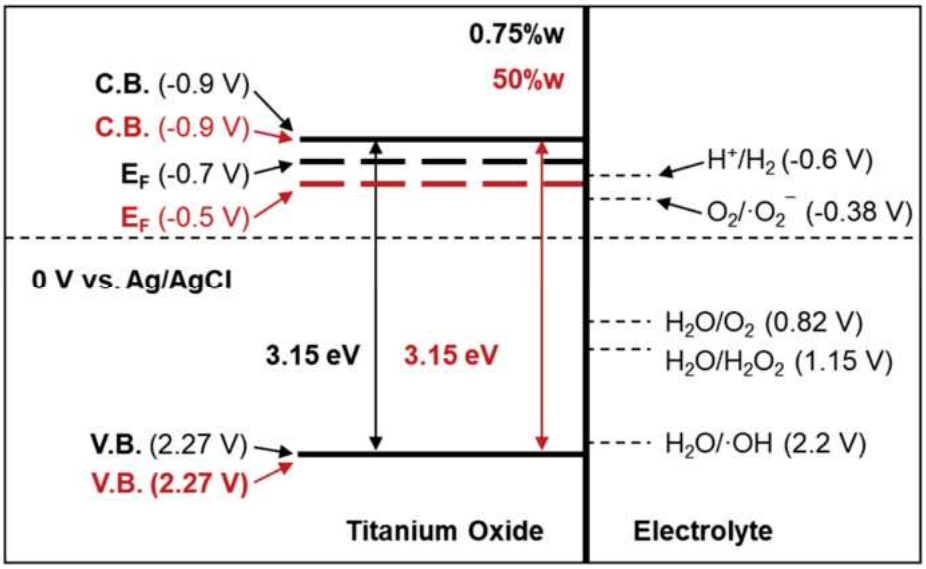

Figure 9.12. Sketch of the energetic levels of the metal/oxide/electrolyte interface for the 0.75%w NTs sample (black) and 50%w NTs sample (red).

According to this sketch, the photogenerated holes can oxidize water to produce not only oxygen and hydrogen peroxide, but also hydroxyl radicals. This information can be used to explain the reactions going on during biomass photoelectrolysis.

The results of glucose and fructose photoelectrolysis show that a proper selection of the process conditions allows to get high value added products with simultaneous hydrogen production. Carrying out the process at pH 7 in 0.1 M glucose aqueous solution allows to convert the biomass in formic acid with a good Faradic efficiency (44% and 55% for 0.75%w and 50%w NTs respectively) with part of the anodic current being also employed to produce gluconic acid. Hydrogen is produced at the cathode with a FE of 100%. Conversely, the best results starting with fructose containing solution are obtained at pH 2, where the reaction has a high selectivity toward gluconic acid whose production occurs with a Faradic efficiency of 24% and 20.3% for 0.75%w and 50%w NTs respectively.

These results suggest that glucose and fructose photoelectrochemical oxidation follows a different path. PEC oxidation of glucose to GA and FA on TiO_2 NTs photoanode starts with the generation of holes due to light absorption. The holes can oxidize water to form adsorbed •OH radicals, which in turn can oxidize the biomass (Figure 9.10). According to previous results reported in the literature

[17,156,283,408–412], a first adsorption step is necessary for biomass oxidation and, thus, the oxidation reaction rate as well as the products depend on how strong the biomass adsorption is (Figure 9.13). The adsorption of glucose on TiO_2 surface is affected by the electrolyte pH, since the excess surface charge on TiO_2 depends on the pH of the solution with respect to the pH of zero charge, that for anodic TiO_2 is around 5.8 [413]. Surface hydroxyl groups are present on TiO_2 in aqueous solution, and they are involved in superficial ionization equilibria that can be described according to the Equations 9.7 – 9.8:

$$-TiOH_2^+ \leftrightarrow -TiOH + H^+ \qquad Eqn.\ 9.7)$$

$$-TiOH \leftrightarrow -TiO^- + H^+ \qquad Eqn.\ 9.8)$$

where -TiOH represent an hydroxyl group on titanium oxide surface (i.e. titanol surface group). Thus, taking into account the pH of zero charge for titania, we expect that the surface species are $-TiOH_2^+$ in acidic solution, -TiOH in neutral solution and $-TiO^-$ in alkaline conditions.
Glucose molecule (RHCOH) can be adsorbed on the catalyst through hydrogen bond (indicated as ⋯). The adsorption reaction can be expressed by Equation 9.9:

$$-TiOH + RHCOH \leftrightarrow -TiOH \cdots OHCHR \qquad Eqn.\ 9.9)$$

As reported in ref [408], the pyranose oxygen of the cyclic form of glucose (Figure 9.14) can strongly affect the hydroxyl group at C_1 due to the shortest distance, therefore the strength of hydrogen bond between -TiOH and the hydroxyl group at C_1 is much larger than those between -TiOH and other hydroxyl groups. Thus, we could assume that a glucose molecule can be adsorbed mainly at TiO_2 surface by the hydroxyl group at C_1. As soon as irradiation generates electron-hole pairs, electrons are transported by the electric field (due to the band bending) toward the cathode through the external circuit where they allow HER. The holes in the valence band can oxidize water to produce hydroxyl radicals on the TiO_2 surface, i.e. $TiOH^{+}\cdot$. Adsorbed glucose (electron donor) is oxidized by these species at C_1, as shown in Equation 9.10:

$$-TiOH \bullet + RHCOH \leftrightarrow -TiOH_2^+ + RC \bullet OH \qquad Eqn.\ 9.10)$$

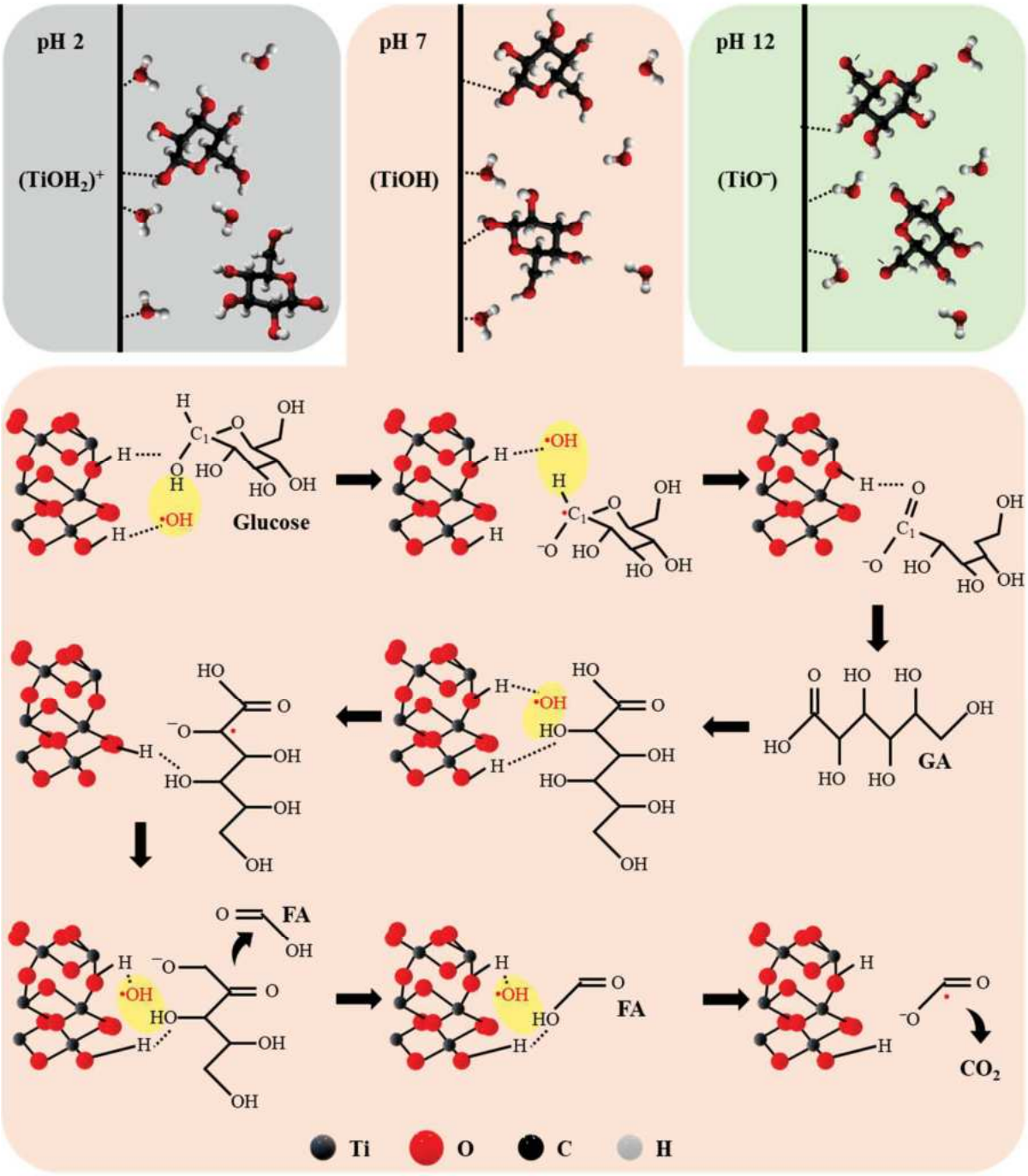

Figure 9.13. Schematic illustration of interaction between NTs surface, water and glucose at various pH and the proposed reaction mechanism at pH 7

The formed RC•OH can react further with water and the hydroxyl radicals to produce GA. Subsequently, the C_5-O bond is split by hydrolysis, and then the GA is formed through desorption from the photoanode in agreement with previous findings reported in the literature [156]. Gluconic acid would react further with hydroxyl radicals so that C_5 compounds with formic acid are formed. Since there is no evidence of C_5 compounds among the products, these compounds are presumably

converted to C_4 compounds by the further attack of radicals, followed by the formation of C_3 compounds, and so on. Finally, carbon dioxide may be the mineralization product for the photoelectrocatalytic degradation of glucose explaining the presence of only GA, FA and CO_2.

Notably, the fraction of titania where glucose is adsorbed depends on the pH due to effect on the excess charge on titania surface as well as on the possibility to find glucose in ionic form. Indeed, pKa of glucose is about 12.3 [412]. When the pH <pKa, glucose in the solution is mainly in molecular form, while in alkaline condition, it can dissociate into $RHCO^-$, which can be adsorbed on TiO_2 through hydrogen bonds. Due to the negative charge of the dissociated form, $RHCO^-$ captures holes more efficiently than the molecular form. However, with increasing pH the surface of titania is negatively charged, hence electrostatic repulsion between TiO^- and $RHCO^-$ increases slowing down the formation rate of glucose oxidation products. This explains why the highest faradic efficiency of glucose oxidation is measured at pH 7, i.e. in a neutral solution not so far from the pH of zero charge. A different behaviour is observed with fructose that shows the highest faradic efficiency in products other than oxygen at pH 2. It is likely that the adsorption of fructose on TiO_2 surface is weaker than that of glucose in agreement with DFT calculation of the adsorption energy for both sugars [411] with a negative impact on the kinetic of fructose oxidation.

9.5. Conclusions

Photoelectrochemical H_2 and HVA production in PGM-free cells via glucose and fructose photo-oxidation at various pH was investigated using TiO_2 nanotubes on Ti felt with different features as the photoanode and Ni foam as the cathode, with working areas of 90 cm^2 and 180 cm^2, respectively. Photoelectrocatalytic tests in biomass containing solutions showed that their presence enhanced the H_2 production rate up to 0.933 μmol h^{-1} mW^{-1} and ~ 100% of faradic efficiency (FE), with the formation of valuable oxidation products such as gluonic acid and formic acid up to 0.565 μmol h^{-1} mW^{-1} and FE of 25% and 55% respectively.

Notably, this study demonstrated that the PEC oxidation of glucose and fructose using TiO_2 NT photoanodes is a promising approach for producing hydrogen and high-value-added chemicals under mild conditions. The findings highlight the importance of optimizing NTs synthesis conditions and pH reaction medium to enhance PEC performance and product selectivity. Moreover, both the photoanode and cathode demonstrated high mechanical and chemical stability, allowing reusability under the reaction conditions.

10. Biomass photoelectrolysis in PGM-free continuous flow cells for the simultaneous production of hydrogen and valuable chemicals

This study explores the reforming of glycerol, glucose, and fructose, in a continuous photoelectrocatalytic cell, utilizing TiO_2 NTs photoanodes for selective oxidation and Ni foam cathode. TiO_2 NTs with varying structural characteristics were developed on Ti felt through anodizing followed by annealing to promote crystallization.

These electrodes were tested in acidic aqueous solutions (pH 2) without and with biomass addition. When biomass was present, hydrogen production occurred simultaneously with the formation of valuable partial oxidation compounds – dihydroxyacetone (DHA) and glyceraldehyde (GA) from glycerol, and gluconic acid (GluA) and formic acid (FA) from glucose or fructose – achieving FEs of 13%, 53%, 54%, and 18% respectively. The photoanodes exhibited excellent mechanical and chemical stability, maintaining performance over time, and could be reused for numerous cycles following a simple cleaning procedure.

These results highlight the potential of this photoelectrocatalytic (PEC) process for both biomass valorization and hydrogen production.

10.1. Introduction

As mentioned above, glycerol, glucose, and fructose have attracted significant interest due to their low cost and abundance [134,380–382]. Their partial oxidation can be employed to produce fuels like hydrogen, ethanol, or renewable diesel, as well as a variety of biobased HVA chemicals [135,283,383–386]. Notably, the selective oxidation of these compounds to yield dihydroxyacetone (DHA) and glyceraldehyde (GA) from glycerol, and gluconic acid (GluA) and formic acid (FA) from glucose or fructose, is particularly appealing because of their industrial applications as platform chemicals [219,387–390,414].

This study investigates the anaerobic partial oxidation of glycerol, glucose, and fructose in aqueous solutions under mild temperature and pressure conditions to produce hydrogen and HVA products using a continuous PEC cell. PGM-free TiO_2 NTs photoanode with varying features and a nickel foam cathode were employed to develop a cost-effective process using stable materials. GC and HPLC analyses were conducted to estimate the FE for HVA and H_2 production. The results were then compared with those obtained from previous studies involving PC and PEC batch systems.

10.2. Experimental

Electrodes preparation

TiO_2 nanotube photoanodes were fabricated by anodization [155,208,346]. Titanium fiber felt (Fuel cell store) with a thickness of 0.2 to 0.3 mm was cut and etched before the anodization process. The anodization was performed using a two-electrode cell setup, where aluminum foil acted as the cathode. The electrolyte was an ethylene glycol solution (EG, Aldrich, 99.8% anhydrous) containing NH_4F (Sigma Aldrich) and deionized water. By adjusting the etching and anodization parameters, TiO_2 nanotubes with different characteristics were synthesized. The specific synthesis conditions are detailed in Table 10.1. Following anodization, both samples were annealed in air at 450°C for 3 hours to induce the crystallization of TiO_2 nanotubes into the anatase phase.

Commercially available Ni foam (Goodfellow) was used as the cathode.

Table 10.1. Details of the synthesis conditions of the two samples used in the photoelectrocatalytic tests.

Sample	Etching	Anodization bath	Anodization conditions
30V	Sonication in acetone, in ethanol, and H_2O 15 min each	EG solution containing 0.15 M NH_4F and 3 vol% H_2O	5 min, 30 V
45V	2 s in HF (Sigma Aldrich, purity 39.5%):HNO_3 (Sigma Aldrich, purity 69.0%):H_2O (1:1:3v), followed by sonication and acetone and ethanol 5 min each	EG: 99 %wt NH_4F: 0.25 %wt H_2O: 0.75 %wt	10 min 45 V

Characterization

SEM and Raman spectra analyses were performed; further details are provided in the experimental section (Section 2).

For the photoelectrochemical measurements, the TiO_2 nanotubes photoanode served as the working electrode in a three-electrode cell configuration. A 0.1 M ammonium biborate tetrahydrate (ABE, $(NH_4)_2B_4O_7 \cdot 4H_2O$; Sigma Aldrich), was employed as the electrolyte. The electrode potential was regulated by a versastat potentiostat. EIS measurements were performed with a Parstat 4000 potentiostat, with an applied voltage of 1 V between the photoanode and cathode. Further details are provided in the experimental section (Section 2)

Photoelectrocatalytic test

The setup used for the photoelectrocatalytic test is represented in Figure 10.1a. The anolyte and catholyte tanks were filled with their respective solutions: 0.5 M Na_2SO_4 as the electrolyte, with the anolyte also containing 0.1 M of biomass (glycerol, glucose, or fructose). In both cases, the pH was adjusted to 2 by adding H_2SO_4 (Sigma Aldrich, 98%). The solution temperature was kept at room temperature using an RM6 LAUDA cryostat.

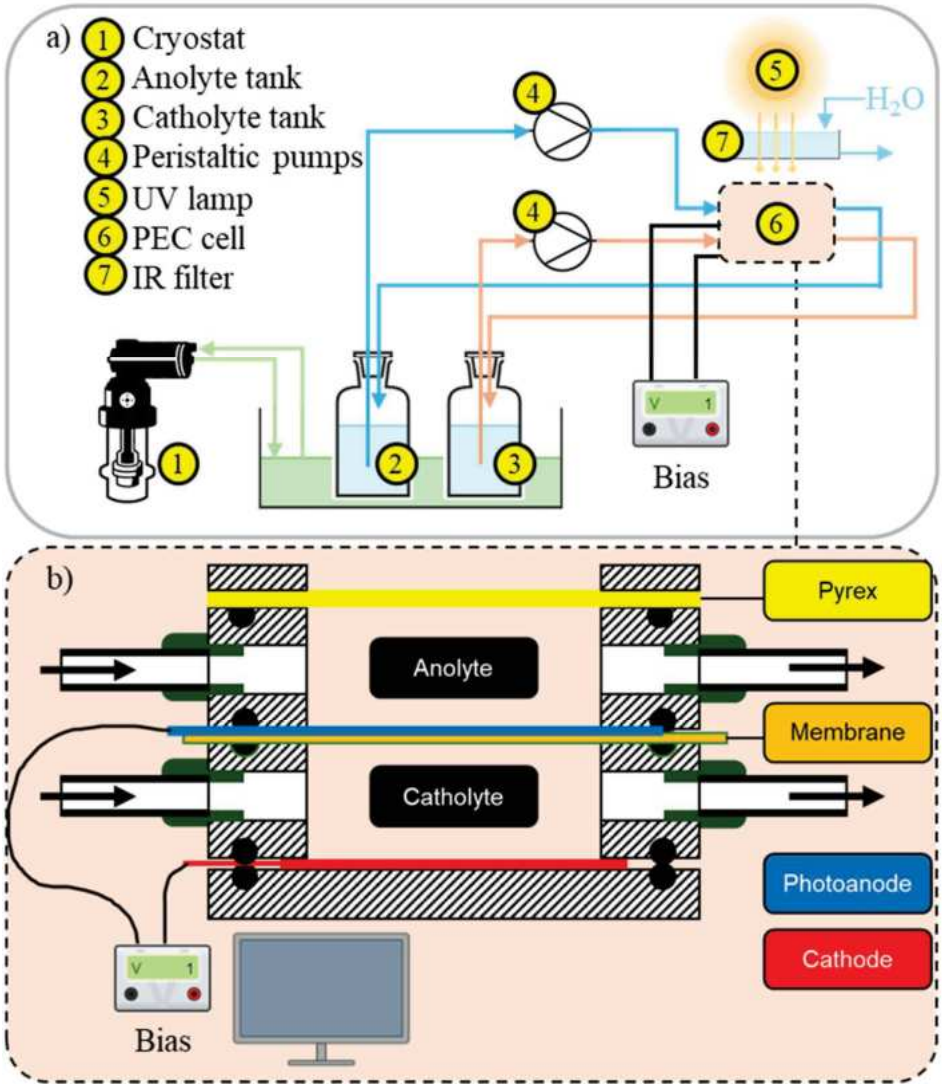

Figure 10.1. a) Image of the PEC system used. b) Schematic representation of the PEC cell.

The anolyte and catholyte were pumped to the PEC cell shown in Figure 10.1b through two peristaltic pumps at a flow rate of 100 ml min^{-1} using ¼" PTFE tubing. A 300 W lamp, emitting primarily near-UV light at 365 nm, served as the light source, with an IR filter to prevent local heating and a Pyrex window before the light reached the photoanode. The photoelectrocatalytic experiments employed

TiO_2 nanotubes as the photoanode and Ni foam as the cathode. A potential of 1 V was applied between the electrodes for three hours using a two-electrode configuration, with a Nafion 117 membrane (Fuel Cell Store) placed between the anodic and cathodic compartments. The light power density was 10 mW/cm², measured using a radiometer. The surface areas of both the photoanode and cathode were 20 cm², with the photoanode's irradiated surface being the same. A Parstat 4000 (PAR) potentiostat, equipped with Electrochemical Impedance Spectroscopy (EIS), was used to control cell potential and gather kinetic data for both anodic and cathodic reactions.

Before each experiment, the Nafion membrane was functionalized in an H_2SO_4 solution at pH 1 for 15 minutes, and helium was bubbled through the solutions in both tanks for 30 minutes to remove oxygen from the system. The reactor was then sealed, the pumps were started, and after 15 minutes of equilibration, the lamp was switched on. After each run, the photoanode was cleaned by sonicating it in acetone and water for 5 minutes each to remove any glycerol residue, while the Ni foam was cleaned by sonicating it in 1 M HCl and water for 5 minutes.

Analitycal tecniques

The detection and quantification of glycerol, glucose, fructose, and their reaction intermediates were performed using HPLC. Gaseous species collected from both tanks headspaces were analyzed using GC; further details are provided in the experimental section (Section 2).

The faradic efficiency was determined using Equation 2.4, where z are the electrons exchanged, that are equivalent to the number of holes reported in Table 10.2 considering the half-reactions in Equations 6.1 -6.3 and 9.2 – 9.4.

Table 10.2. Electrons/holes exchanged in the half cell reactions reported in Equations 6.1 -6.3 and 9.2 – 9.4

Compound	Chemical formula	Electrons/holes exchanged
Glycerol	$C_3H_8O_3$	
DHA/GA	$C_3H_6O_3$	2
Glucose/fructose	$C_6H_{12}O_6$	
GluA	$C_6H_{12}O_7$	2
FA	CH_2O_2	2
Carbon dioxide	CO_2	14/3 (glycerol) 4 (glucose/fructose)
Hydrogen	H_2	2

10.3. Results and discussion

Figure 10.2 compares the morphological characteristics of TiO_2 NTs anodized at 30V or 45V, following thermal treatment at 450 °C for 3 h. The SEM images clearly show the formation of a large array of TiO_2 NTs, with the average length of ~ 1.1 μm and 700 nm, respectively (inset of Figures 10.2a and b). Notably, the 30V NTs show thinner and sharper walls with no gaps between NTs. These findings align with previous studies [346]. Raman spectroscopy confirms the presence of the anatase phase in both samples after thermal treatment. As depicted in Figure 10.2c, characteristic anatase bands appear at 144 cm^{-1}, 196 cm^{-1}, 397 cm^{-1}, 513 cm^{-1}, and 639 cm^{-1} [271].

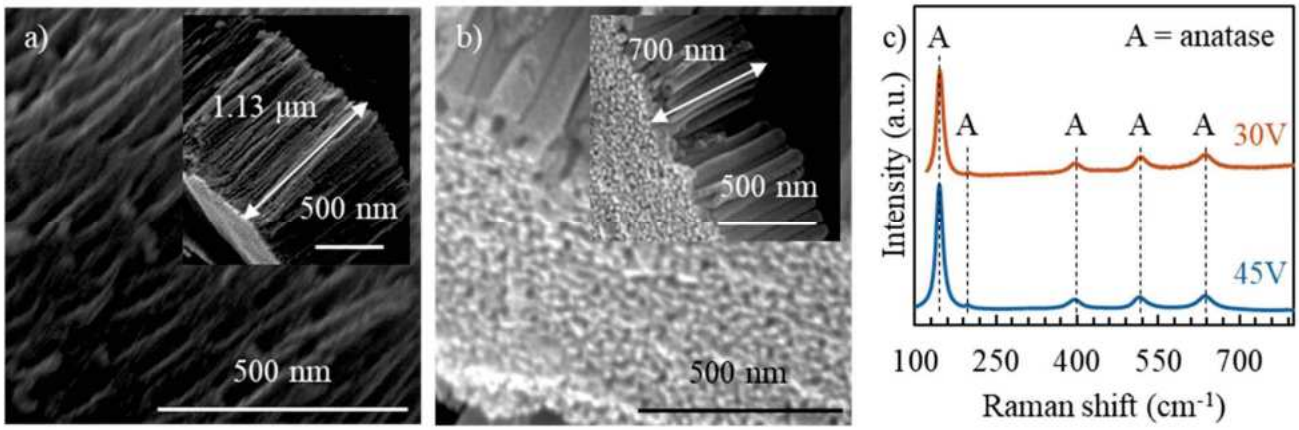

Figure 10.2. SEM pictures and Raman spectra of (a, c up) 30V NTs sample and (b, c down) 45V NTs sample.

A photoelectrochemical study, illustrated in Figure 10.3, was conducted to explore the electronic properties of photoanodes with varying characteristics. The photocurrent spectrum, which shows the photocurrent as a function of the monochromatic irradiating wavelength, was recorded under a constant bias of 0.5 V vs Ag/AgCl, with the Ti/TiO_2 NTs electrode immersed in a 0.1 M ABE aqueous solution. As depicted in Figures 10.3a and 10.3e, both samples exhibit a strong photoresponse in the UV region, corresponding to the typical absorption of anatase TiO_2. Notably, the photocurrent spectrum for the 30V sample (Figure 10.3a) shows a blue shift, with photocurrents detected at wavelengths as low as 210 nm, in contrast to the 45V sample (Figure 10.3e). Assuming indirect optical transitions, the optical band gap (E_g) was estimated by extrapolating the $(Q_{ph} \cdot h\nu)^{0.5}$ vs $h\nu$ plot to zero (Figures 10.3b and 10.3f). The calculated E_g values of 3.1 eV and 3.15 eV align with the reported value for anatase (3.2 eV [223,346]). The n-type behavior of the TiO_2 NTs is confirmed by the cathodic photopotential observed during irradiation, as shown in Figures 10.3c and 10.3f [219]. Photocurrent transients were recorded by manually stopping monochromatic irradiation at 330 nm,

while applying potentials ranging from 0.5 V to -0.7 V vs Ag/AgCl (Figures 10.3d and 10.3h). An anodic photocurrent was observed, further confirming the n-type semiconductor nature of the oxide, with the photocurrent reaching zero at around -0.7 V vs Ag/AgCl for both samples. This zero photocurrent potential is considered an estimate of the flat band potential (U_{fb}), consistent with values reported in the literature [155].

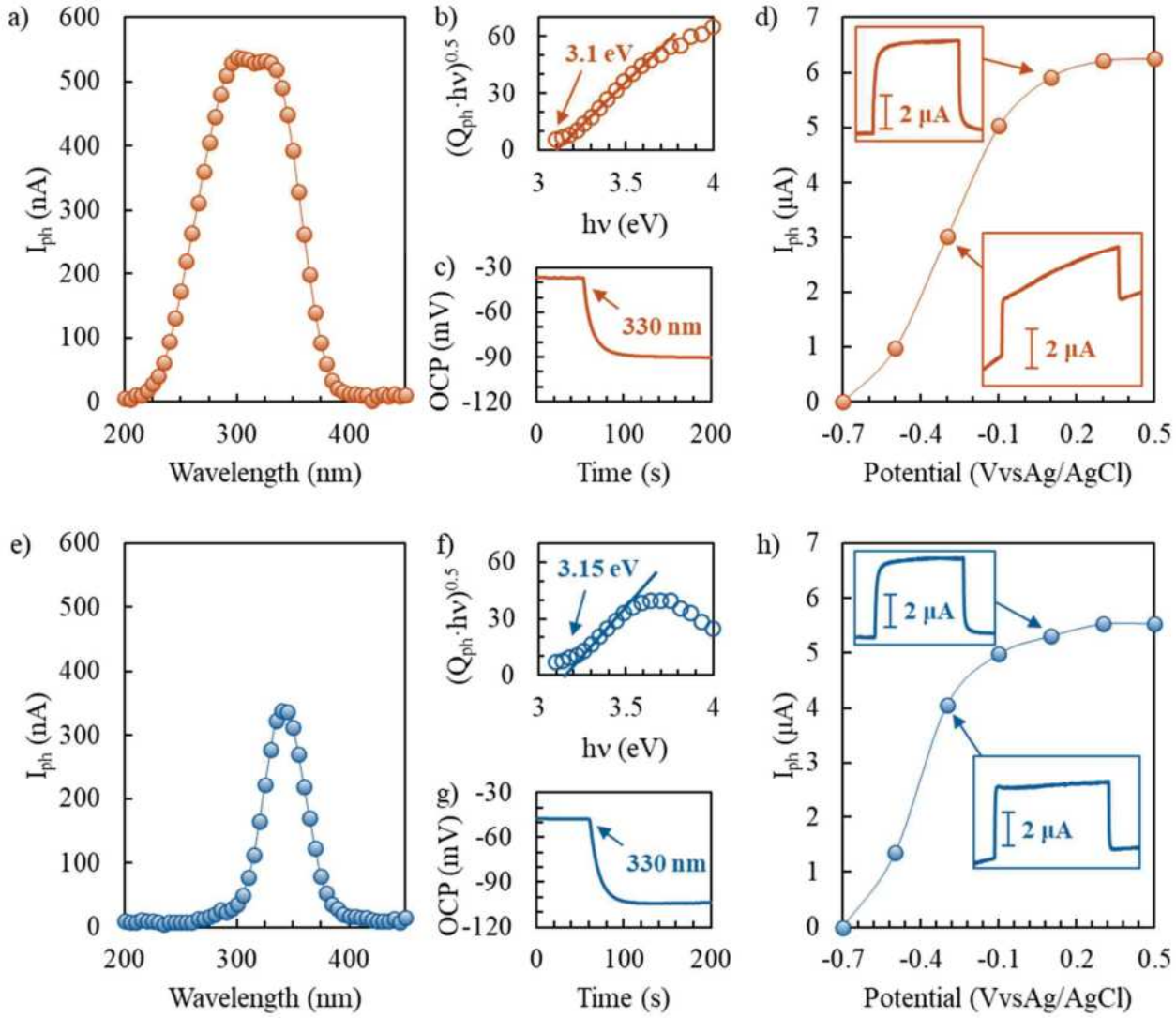

Figure 10.3. a) photocurrent spectra recorded in a 0.1 M ABE aqueous solution at 0.5 V vs Ag/AgCl, b) respective $(Q_{ph} \cdot h\nu)^{0.5}$ vs hν plot for the E_g estimation, c) photopotential recorded by irradiating the sample with 330 nm monochromatic light, d) photocurrent transients under monochromatic light recorded at 330 nm and applied potential from 0.5 to -0.7 V vs Ag/AgCl for 30V sample. The same measures carried out for the 45V sample are reported in e)-h).

Figure 10.4 presents the results of the photoelectrochemical reforming of glycerol, glucose, and fructose aqueous solutions at pH 2, with an applied bias of 1 V. As shown, the addition of biomass leads to an increase of the measured photocurrent compared to that measured in biomass-free solution,

with hydrogen production achieving FE of 100% in all cases due to the use of a divided cell. Finally, it is worth noting that among the biomasses tested, glycerol with 45V NTs produced the highest photocurrent, corresponding to a hydrogen production rate of 181 μmol h^{-1}.

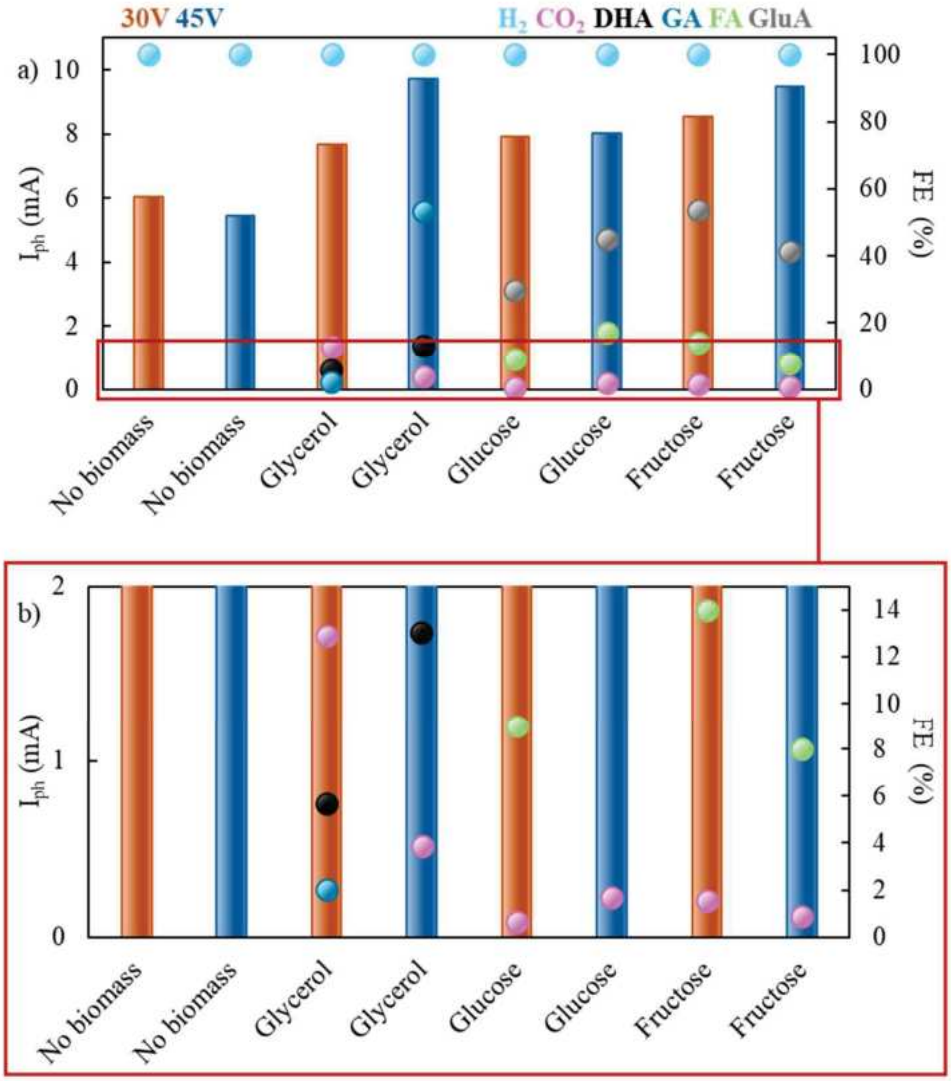

Figure 10.4. Photoelectrochemical results obtained by using glycerol, glucose, or fructose as the starting biomass. The orange and blu bars represent the photocurrent measured using the 30V and 45V NTs samples, respectively. The calculated FEs are reported in the secondary axis for H_2 (turquoise), CO_2 (purple), DHA (black), GA (dark blu), FA(gray), and GluA, green. The reaction time of each test was 3 h.

Figures 10.4a and b provide an overview of the products formed during the photoelectrochemical reactions, as evidenced by the FEs for both photoanodes. In the absence of biomass in the anolyte, i.e., only water splitting to produce H_2 and O_2 occurs, the 30V NTs exhibited a higher I_{ph}. Upon glycerol addition, a I_{ph} increase was observed, although the 45V NTs showed higher FEs for DHA (53%) and GA (13%), compared to the considerably lower values obtained with the 30V NTs (5.6% and 2%, respectively). Notably, the FE toward CO_2 was higher with the 30V NTs sample (12.9%)

compared to 45V NTs (3.9%), suggesting that glycerol can be preferentially adsorbed on 30V NTs surface promoting the glycerol mineralization to CO_2 and H_2. For glucose, the most abundant product being GluA for both samples (FE ~ 45% for 45V NTs and 29.7% for 30V NTs) followed by FA (FE ~ 17% for 45V NTs and 9% for 30V NTs), while FE for CO_2 was always < 2%. When fructose was used as the starting biomass, the 30V NTs sample exhibited the best performances in terms of FE towards GluA and FA (53.6% and 14% respectively), while the 45V NTs sample had lower values of 41.5% and 8% respectively. Additionally, in this case, the CO_2 FE remained < 2% for both samples.

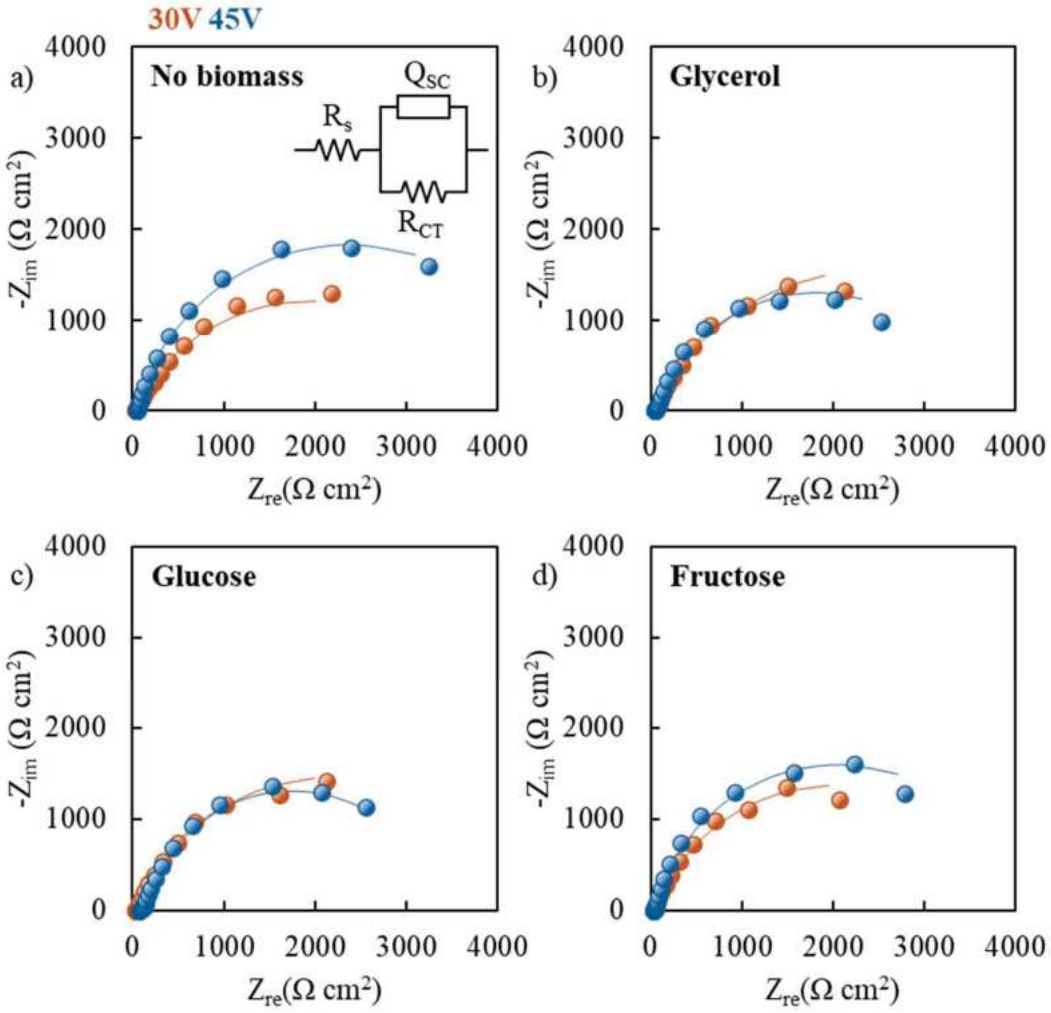

Figure 10.5. In situ EIS spectra recorded under UV irradiation a) without biomass addition, and in the presence of b) glycerol, c) glucose, or d) fructose. All the spectra were fitted by using the equivalent circuit shown in the inset of a). Impedance spectra were measured within a frequency range of 100 kHz to 0.1 Hz, applying a potential of 1 V between the photoanode and cathode, and using an AC amplitude of 10 mV.

Electrochemical impedance spectra (EIS) were carried out under a 1 V bias during photoelectrolysis of glycerol, glucose, or fructose. Figure 10.5 presents the corresponding Nyquist plots, showing spectra recorded under irradiation in biomass-free solution (Figure 10.5a), i.e. water

photoelectrolysis, and upon the addition of biomass Figures 10.5 b-d. EIS measurements carried out without irradiation are shown in Figure 10.6. In this model, R_{CT} represents the charge transfer resistance, while Q_{SC} denotes the capacitance of the semiconductor, and R_s accounts for the overall electrolyte resistance, including the anodic compartment, the membrane, and the cathodic compartment. The corresponding fitting parameters are summarized in Tables 10.3-10.4. At first glance, it is evident that upon irradiation, R_{CT} decreases, indicating enhanced charge transfer resistance, while Q_{SC} increases, reflecting a higher number of donors in the photoanode. A constant phase element (Q) is needed to account for the non-ideal capacitance (exponent n < 1). Notably, the charge transfer resistance for each biomass oxidation at pH 2 and for both NTs layers reported in Table 10.3 range from 3548 to 4706 Ω cm^2, with the lowest value measured during photoelectrolysis of glycerol by employing 45 V NTs sample.

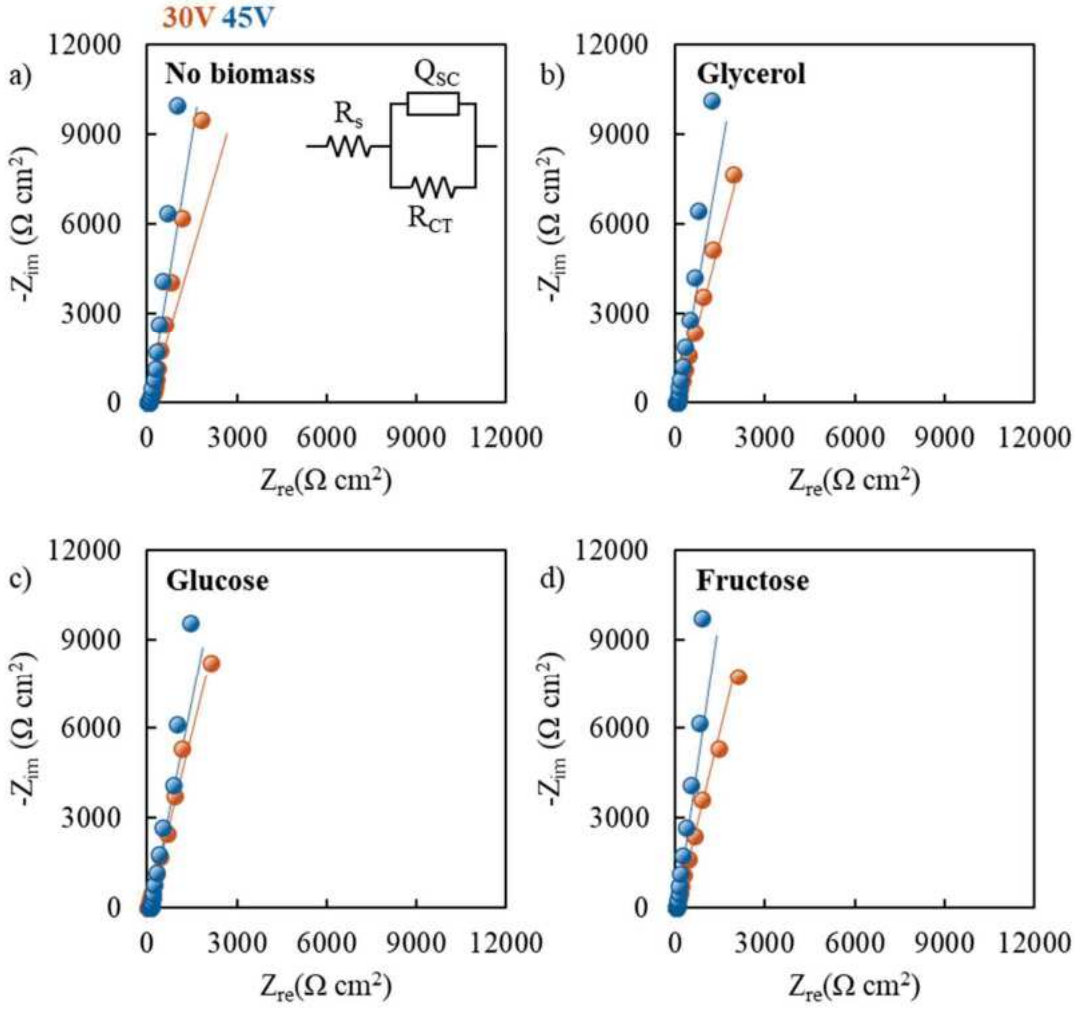

Figure 10.6. In situ EIS spectra recorded without irradiation a) without biomass addition, and in the presence of b) glycerol, c) glucose, or d) fructose. All the spectra were fitted by using the equivalent circuit shown in the inset of a). Impedance spectra were measured within a frequency range of 100 kHz to 0.1 Hz, applying a potential of 1 V between the photoanode and cathode, and using an AC amplitude of 10 mV.

Using the Brug formula (Equation 7.2) [369], the capacitance of the electrodes can be estimated. For the two NTs samples, C_{brug} values are comparable. However, overall the 30 V NTs sample shows slightly higher values, suggesting a higher concentration of charge carriers under irradiation (Table 10.4).

Table 10.3. Fitting parameters obtained by EIS spectra recorded in dark conditions.

Sample	Biomass	R_S (Ω cm^2)	R_{CT} (Ω cm^2)	Q_{SC} (S s^n cm^{-2})	n (adm)	χ square (adm)
30V	NO	33.9	$8.16\cdot10^{14}$	$1.55\cdot10^{-4}$	0.817	$3.09\cdot10^{-2}$
45V	NO	44.9	$1.07\cdot10^{20}$	$1.51\cdot10^{-4}$	0.897	$1.94\cdot10^{-2}$
30V	Glycerol	48.3	$3.14\cdot10^{10}$	$1.94\cdot10^{-4}$	0.835	$4.38\cdot10^{-3}$
45V	Glycerol	49.6	$5.02\cdot10^{19}$	$1.58\cdot10^{-4}$	0.889	$5.42\cdot10^{-3}$
30V	Glucose	38.3	$2.35\cdot10^{8}$	$1.84\cdot10^{-4}$	0.843	$2.15\cdot10^{-4}$
45V	Glucose	96.1	$2.60\cdot10^{19}$	$1.68\cdot10^{-4}$	0.872	$1.33\cdot10^{-2}$
30V	Fructose	33.8	$2.77\cdot10^{6}$	$1.89\cdot10^{-4}$	0.846	$1.84\cdot10^{-3}$
45V	Fructose	38.5	$1.43\cdot10^{18}$	$1.64\cdot10^{-4}$	0.908	$4.33\cdot10^{-3}$

Table 10.4. Fitting parameters obtained by EIS spectra recorded under UV irradiation.

Sample	Biomass	R_S (Ω cm^2)	R_{CT} (Ω cm^2)	Q_{SC} (S s^n cm^{-2})	n (adm)	χ square (adm)
30V	NO	31.8	3824	$3.47\cdot10^{-4}$	0.720	$1.85\cdot10^{-2}$
45V	NO	44.8	4662	$2.14\cdot10^{-4}$	0.850	$4.17\cdot10^{-3}$
30V	Glycerol	46.9	4706	$4.02\cdot10^{-4}$	0.741	$3.35\cdot10^{-3}$
45V	Glycerol	48.4	3548	$2.82\cdot10^{-4}$	0.807	$5.35\cdot10^{-3}$
30V	Glucose	37.9	4314	$3.73\cdot10^{-4}$	0.759	$4.07\cdot10^{-3}$
45V	Glucose	92.1	3316	$2.37\cdot10^{-4}$	0.850	$1.43\cdot10^{-2}$
30V	Fructose	33.1	4002	$3.75\cdot10^{-4}$	0.766	$4.74\cdot10^{-3}$
45V	Fructose	37.8	4038	$2.45\cdot10^{-4}$	0.853	$4.10\cdot10^{-3}$

Table 10.5. C_{Brug} values obtained by EIS spectra.

Sample	Biomass	Dark, C_D ($\mu F\ cm^{-2}$)	Light, C_L ($\mu F\ cm^{-2}$)
30V	NO	142	263
45V	NO	101	116
30V	Glycerol	411	1172
45V	Glycerol	108	137
30V	Glucose	80	99
45V	Glucose	113	152
30V	Fructose	130	203
45V	Fructose	105	118

For comparison with previous works [155,219], Table 10.6 presents the results obtained using glycerol as the starting biomass, alongside data from PGM free photocatalytic (PC) and PEC batch systems. The production rates of H_2, DHA, and GA were normalized based on the photoanode area and the incident photon flux. Additionally, the quantum efficiencies (η) for the three systems, defined as the amount of DHA and GA produced divided by the adsorbed photons were calculated using Equation 10.1.

$$Eqn.\ 10.1) \qquad \eta = \frac{DHA + GA\ (mols)}{absorbed\ photons\ (mols)}$$

Where the number of absorbed photons was calculated using Equation 9.7 and E, the energy of the photons, using Equation 9.6

As shown in Table 10.6, the continuous PEC system outperformed the other systems for H_2, DHA and GA production. Compared to the PEC batch system, the normalized production rate of HVA increased ~ 6.9 times for DHA and 10.1 times for GA, while the normalized H_2 production rate increased by ~ 65%. Notably, the highest normalized H_2 production rate was obtained with a 45V Nts sample using glycerol as the starting biomass, reaching 2.74 μmol h^{-1} mW^{-1}. A similar trend was observed for η of DHA and GA, which increased by three times with the continuous PEC system. When compared to the PC batch system, these values dramatically increase, with DHA production increasing by ~ 10^4, GA by ~ 10^5, H_2 by ~ 10^4, and η improving by ~ 10^4 when using the continuous PEC system.

Table 10.6. Comparison with the previous works, using glycerol as the starting biomass, on the quantum efficiencies (η) and production rates of HVA and H_2 normalized by photoanode area and incident photon flux.

Ref.	[219]	[155]	This work
Applied bias (V)	N.A.	1	1
Photoanode area (cm^2)	$2.50 \cdot 10^4$	90	20
Light source (mW cm^{-2})	10	10	3.3
DHA (μmol h^{-1} mW^{-1})	$7.20 \cdot 10^{-6}$	$4.84 \cdot 10^{-2}$	0.333
GA (μmol h^{-1} mW^{-1})	$3.60 \cdot 10^{-6}$	0.134	1.35
H_2 (μmol h^{-1} mW^{-1})	$4.00 \cdot 10^{-5}$	1.67	2.74
Absorbed photons (mol)	$1.37 \cdot 10^1$	$4.94 \cdot 10^{-2}$	$6.59 \cdot 10^{-3}$
Photons for GA and DHA production (mol)	$2.70 \cdot 10^{-5}$	$1.65 \cdot 10^{-3}$	$6.68 \cdot 10^{-4}$
Quantum efficiency, η (%)	$1.97 \cdot 10^{-4}$	3.33	10.1

These improved performances are attributed to the applied bias compared to the PC system, which reduces hole/electron recombination, and to enhanced mass transport, compared to the PEC batch system, which decreases biomass adsorption on the photoanode surface. This facilitates partial oxidation rather than complete mineralization of glycerol to CO_2 and H_2.

Following the same approach, a normalized GluA production rate up to 1.44 (μmol h^{-1} mW^{-1}) was achieved using the 30V NTs with fructose as the starting biomass. Additionally, an FA production rate up to $2.85 \cdot 10^{-1}$ (μmol h^{-1} mW^{-1}) and quantum efficiency up to 10.9% were obtained using 45V NTs and glucose as the starting biomass.

10.4. Conclusions

Photoelectrochemical H_2 and HVA production in continuous PEC cells through photo-oxidation of glycerol, glucose, and fructose were investigated using TiO_2 nanotubes grown with different features on Ti felt as the photoanode and Ni foam as the cathode, both with working areas of 20 cm^2. Photoelectrocatalytic tests in biomass-containing solutions showed that the presence of biomass enhanced the H_2 production rate up to 2.74 μmol h^{-1} mW^{-1}, achieving ~ 100% of faradic efficiency (FE). Valuable oxidation products were also formed, such as dihydroxyacetone and glyceraldehyde from glycerol with normalized production rates up to 0.333 and 1.35 μmol h^{-1} mW^{-1} and FEs of 13% and 53% respectively. Gluconic acid and formic acid were produced from glucose or fructose at normalized rates up to 1.44 and $2.85 \cdot 10^{-1}$ μmol h^{-1} mW^{-1} and FEs of 54% and 17% respectively.

This study demonstrated that the PEC oxidation of glycerol, glucose, and fructose using TiO_2 NT photoanodes is a promising method for producing hydrogen and high-value-added chemicals under mild conditions. The results emphasize the importance of optimizing NTs synthesis conditions and cell design to enhance PEC performance and product selectivity. Additionally, both the photoanode and cathode were PGM-free and exhibited high mechanical and chemical stability, enabling reusability under the reaction conditions.

11. Summary, conclusions and perspectives

In this PhD project, we explored the combined biomass oxidation and H_2 production using photocatalytic (PC) and photoelectrocatalytic (PEC) cells, with a focus on the use of chemically and physically stable PGM-free electrodes and improving the cell design.

We began by testing PGM-free materials - both photocatalysts and cocatalysts - for photocatalytic glycerol reforming coupled with H_2 evolution. The study focuses on the co-catalyst and the crystalline phase of the TiO_2-based photocatalysts. The presence of glycerol in the reaction mixture enhanced H_2 evolution, and we successfully replaced Pt cocatalyst on TiO_2 with Cu_2O using ball milling, forming a heterojunction with TiO_2 and enabling a Z-scheme mechanism. This led to a glycerol conversion of 33%, and selectivity values of 10.3% for dihydroxyacetone (DHA) and 5.4% for glyceraldehyde (GA), with CO_2 and H_2 concentration of 0.16 mM, of 1.01 mM (corresponding to 0.17 mmol h^{-1} g^{-1}), respectively. These results were comparable to those obtained using Pt–TiO_2 except for GA, where Pt–TiO_2 showed no selectivity. Focusing on the photocatalyst itself, our findings indicate that the H_2 production from glycerol photoreforming and the distribution of the intermediate products depend heavily on the nature of the TiO_2 support. Brookite was the most active sample for H_2 production, and its amount decreased following the order Pt-brookite > Pt-P25 ~ Pt-anatase > Pt-rutile. This trend correlated the hydrophilicity order of the different polymorphs since the measured intensity of the adsorbed water bending mode is Pt-brookite >> Pt-P25 ~ Pt-anatase > Pt-rutile. Employing IR spectroscopy of adsorbed CO revealed differences in the metal–support interaction among the investigated polymorphs, highlighting a lower concentration of $Pt^{\delta+}$ centers for Pt-P25 and Pt-anatase. Moreover, the probe molecule showed a different distribution of low coordinated Pt^0 sites in the samples. Thus, the higher activity of the Pt-brookite sample is attributed to its water adsorption capacity and the distribution of Pt^0 sites, which are preferentially located at edges and steps.

Further investigations involved the reforming of furfuryl alcohol (FuA) in aqueous solution using TiO_2 based photocatalysts in a PC cell under green experimental conditions. In this case, conversion values and H_2 production were lower than with glycerol substrate, and Pt and other metal species were essential for both FuA oxidation and H_2 production. The best results were obtained at pH 10 using home-prepared TiO_2 brookite containing Pt and Cu or Nb. Interesting results were also achieved in PEC reforming using TiO_2 NTs photoanode and Ni foam cathode in an undivided batch cell and an irradiated photoanode area of 24cm^2. In this case, although the additional cost of the applied bias, higher H_2 and furfural production rates were obtained compared to PC, despite the absence of Pt.

Encouraged by the promising PEC results, we investigated the effects of pH and applied bias on H_2 production and HVA products from glycerol photooxidation. PEC tests were carried out across acidic, neutral, and basic pH conditions with applied bias between 0.1 and 1 V vs Ag/AgCl. The results show the highest FE towards DHA and GA at pH 7 and applied bias of 0.5 V and 0.1 V vs. Ag/AgCl respectively, remaining stable at higher applied bias. Lower pH favored glycerol photoreforming, while higher pH led to a decrease of both glycerol photooxidation and photoreforming, i.e., FE towards DHA, GA, and CO_2, and an I_{ph} increase. This suggests that water splitting is more pronounced at higher pH, resulting in a lower FE towards H_2 because of the subsequent reaction with the O_2 in the gas phase.

We proceeded with our investigations by scaling up the PEC cell, still remaining in an undivided configuration. A photoanode with an irradiate area of up to 90 cm^2 was synthesized to enhance H_2 production through water and glycerol photooxidation. PEC test in acidic aqueous solutions revealed that the presence of glycerol significantly boosted the photocurrent, resulting in a higher H_2 production rate and the formation of DHA and GA. The best results were obtained with TiO_2 NTs ~730 nm long, annealed for 3 h at 450 °C, producing an H_2 rate of 1.67 mmol $h^{-1}mW^{-1}$, higher than previous results reported in the literature. Moreover, DHA and GA were also produced by the photooxidation of glycerol even if with a faradaic efficiency lower than the value reported for functionalized TiO_2 electrodes.

To improve FE towards HVA products from glycerol oxidation, we investigated N-doped NTs. Under 450 nm irradiation, the N-doped NTs exhibited superior FE - 27% for DHA and 11% for GA – due to the significant shift in the valence band energy caused by N-doping, narrowing the band gap. This adjustment allowed the visible light harvesting and suppressed the formation of hydroxyl radicals, thereby reducing undesired complete glycerol mineralization. The results highlighted the effectiveness of bandgap engineering approach to modify the selectivity of electrochemical reactions on semiconductors, although resulting in an I_{ph} reduction due the increased recombination of holes and electrons due to the N-doping treatment.

We extended our research to the PEC oxidation of glucose and fructose for H_2 and HVA production at various pH, using TiO_2 nanotubes grown on Ti felt with different features and with working areas of 90 cm^2 as the photoanode. PEC tests in biomass containing solutions showed enhanced the H_2 production rate to 0.933 μmol h^{-1} mW^{-1} and ~ 100% of FE, with HVA formation such as gluonic acid (GluA) and formic acid (FA) up to 0.565 μmol h^{-1} mW^{-1} and FE of 25% and 55% respectively. The findings confirmed the importance of optimizing NTs synthesis conditions and pH reaction medium to enhance PEC performance and product selectivity.

Based on these findings, H_2, and HVA production through photo-oxidation of glycerol, glucose, and fructose was investigated in continuous PEC cells, with divided compartments by a Nafion membrane for anolyte and catholyte, using TiO_2 nanotubes grown with different features on Ti felt as the photoanode. The presence of biomass in the reaction mixture enhanced the H_2 production rate up to 2.74 μmol h^{-1} mW^{-1}, achieving ~ 100% FE. HVA products were also formed, such as DHA and GA from glycerol with normalized production rates up to 0.33 and 1.35 μmol h^{-1} mW^{-1} and FEs of 13% and 53% respectively, or GluA and FA from glucose or fructose at normalized rates up to 1.44 and $2.85 \cdot 10^{-1}$ μmol h^{-1} mW^{-1} and FEs of 54% and 17% respectively.

Among the biomasses studied, glycerol proved to be the most promising for both HER and HVA production. Glucose and fructose also contributed to increased H_2 production compared to biomass-free solutions. In contrast, for furfuryl alcohol, the presence of biomass did not enhance HER, despite the production of HVA. This behavior can be attributed to the oxidation potential of the biomass, which depends on whether it is more favorable than water oxidation from both a thermodynamic and kinetic perspective.

In all PEC experiments, both electrodes (TiO_2 NTs photoanodes and the Ni foam cathode) exhibited remarkable chemical and physical stability, allowing for their reuse after a simple cleaning process. On the other hand, in the PC system, catalyst recovery presented a significant challenge, along with the necessity of maintaining a low biomass concentration to prevent catalyst fouling and deactivation. Future research will focus on functionalizing stable TiO_2 NTs supports to design photoanodes for specific reactions, integrating the continuous PEC setup with a membrane system that can continuously separate HVA compounds from the reaction system, and optimizing the PEC cell to enhance mass transport. The same system will also be applied to other applications, such as CO_2 reduction, environmental remediation, and biomass oxidation in wastewater from biomass processes. Future prospects will also include scaling up the electrodes and the entire system, building a pilot plant that utilizes sunlight for both process activation and power generation via a photovoltaic panel, with the final goal of further advancing the technology readiness level of this highly promising method for sustainable hydrogen production and high-value-added products.

12. PhD Scientific Output

Publications in International Journals

1. **Pecoraro, C. M**., Bellardita, M., Loddo, V., Di Franco, F., Palmisano, L., & Santamaria, M. (2023). A facile way to synthesize noble metal free TiO_2 based catalysts for glycerol photoreforming. Journal of Industrial and Engineering Chemistry, 118, 247–258. https://doi.org/10.1016/j.jiec.2022.11.010

2. **Pecoraro, C. M.**, Mino, L., Kozyr, E., Palmisano, L., Di Franco, F., Loddo, V., Santamaria, M., & Bellardita, M. (2024). Pt–TiO_2 catalysts for glycerol photoreforming: comparison of anatase, brookite and rutile polymorphs. Chemical Communications, 60(28), 3782–3785. https://doi.org/10.1039/D4CC00353E

3. **Pecoraro, C. M.**, Bellardita, M., Loddo, V., Virtù, D., Di Franco, F., & Santamaria, M. (2023). Photocatalytic and photoelectrocatalytic H_2 evolution combined with valuable furfural production. Applied Catalysis A: General, 650, 118987. https://doi.org/10.1016/j.apcata.2022.118987

4. **Pecoraro, C. M. (Corresponding author)**, Di Franco, F., Loddo, V., Bellardita, M., & Santamaria, M. (2024). Effect of pH and Applied Bias on H_2 and HVA Products Through Photoelectrocatalytic Glycerol Oxidation. Chemical Engineering Transactions, 109, 283–288. https://doi.org/10.3303/CET24109048

5. **Pecoraro, C. M.**, Di Franco, F., Bellardita, M., Loddo, V., & Santamaria, M. (2024). Enhancing H_2 production rate in PGM-free photoelectrochemical cells by glycerol photo-oxidation. International Journal of Hydrogen Energy, 49, 322–336. https://doi.org/10.1016/j.ijhydene.2023.08.011

6. Djaballah, A. M., Bellardita, M., Palmisano, L., Loddo, V., Umair, M., **Pecoraro, C. M.**, Bagtache, R., & Trari, M. (2023). Facile preparation of $CuBi_2O_4/TiO_2$ hetero-systems employed for simulated solar-light selective oxidation of 4-methoxybenzyl alcohol model compound. Molecular Catalysis, 546, 113251. https://doi.org/10.1016/j.mcat.2023.113251

7. Umair, M., **Pecoraro, C. M.**, Di Franco, F., Santamaria, M., Palmisano, L., Loddo, V., & Bellardita, M. (2024). Efficient Photocatalytic Partial Oxidation of Aromatic Alcohols by Using $ZnIn_2S_4$ under Green Conditions. ChemSusChem. https://doi.org/10.1002/cssc.202400404

8. **Pecoraro, C. M.**, Di Franco, F., Loddo, V., Bellardita, M., & Santamaria, M. (2024). Photoelectrolysis of glucose and fructose containing solution in PGM-free cells for hydrogen and valuable chemicals production. International Journal of Hydrogen Energy, 87, 1277–1287. https://doi.org/10.1016/J.IJHYDENE.2024.09.124

9. **Pecoraro, C. M.**, Wu, S., Santamaria, M., & Schmuki, P. (2024). Bandgap Engineering of TiO_2 for Enhanced Selectivity in Photoelectrochemical Glycerol Oxidation. Advanced Materials Interfaces, 2400583. https://doi.org/10.1002/ADMI.202400583

10. **Pecoraro C.M.**, Sopha H., Wu S., Kim H., Wang Y., Macak J., Santamaria M., & Schmuki P., Platinum Single Atoms on Titania Aid Dye Photodegradation Whereas Platinum Nanoparticles don't (Currently under revision)

11. Umair, M., **Pecoraro, C. M.**, Di Franco, F., Santamaria, M., Palmisano, L., Loddo, V., & Bellardita, Enhanced aqueous photocatalytic selective oxidation of HMF: comparison of the performance of different photocatalysts (Currently under revision)

Conference Contributions

1. M. Santamaria, **C. M. Pecoraro**, F. Di Franco, V. Loddo, L. Palmisano, M. Bellardita. Biomass valorization toward value-added products and hydrogen production in photoelectrochemical cells. Giornate dell'Elettrochimica Italiana - GEI 2022, September 11th – 15th 2022, Orvieto, Italy. (https://gei2022.it/)

2. M. Bellardita, **C. M. Pecoraro**, V. Loddo, D. Virtù, F. Di Franco, M. Santamaria, L. Palmisano. Photocatalytic and photoelectrocatalytic H_2 production by furfuryl alcohol reforming. XII Congresso nazionale SCI della divisione di Chimica Industriale, November 7th – 8th 2022, Catania, Italy. (https://www.chimind.it/congressi/276-xxii-congresso-nazionale-divisione-chimica-industriale-7-8-novembre-2022-catania)

3. M. Bellardita, **C. M. Pecoraro**, V. Loddo, F. Di Franco, L. Palmisano, M. Santamaria. Noble metal free Cu_2O/TiO_2 catalysts for glycerol photoreforming. XIII Congresso nazionale AICIng e II congresso Nazionale della divisione di Chimica Industriale della SCI, June 25th - 28th 2023, Politecnico di Milano, Italy. (https://www.soc.chim.it/it/node/3144)

4. **C. M. Pecoraro (Presenting Author**), F. Di Franco, M. Bellardita, V. Loddo, M. Santamaria. H_2 production and biomass valorization in PGM-free photoelectrochemical cells by glycerol photo-oxidation. 74th Annual Meeting of the International Society of Electrochemistry, September 3rd -8th 2023, Centre de congrès de Lyon, Lyon, France. (https://annual74.ise-online.org/img_conf/ISE-AM74-program_web.pdf)

5. **C. M. Pecoraro (Presenting Author)**, F. Di Franco, M. Bellardita, V. Loddo, M. Santamaria. Combined biomass valorization and H_2 production in PGM-free photoelectrochemical cells by glycerol photo-oxidation. IConBM2024, May 19th -22nd 2024, Starhotel SPLENDID HOTEL LA TORRE, Palermo, Italy. (https://www.aidic.it/iconbm2024/programma/pro.html)

6. **C. M. Pecoraro (Presenting Author)**, F. Di Franco, M. Bellardita, V. Loddo, M. Santamaria. Enhancing H_2 production rate by addition of biomasses in PGM-free batch and continuous photoelectrochemical cells. 37th Topical Meeting of the International Society of Electrochemistry, June 9th -12th 2024, Stresa Convention Centre, Stresa, Italy. (https://topical37.ise-online.org/img_conf/TM-37-PROGRAM-A5.pdf)

7. **C. M. Pecoraro (Presenting Author)**, F. Di Franco, M. Bellardita, V. Loddo, M. Santamaria. Hydrogen production and high value added products formation by glucose and fructose photoelectrochemical reforming in PGM free cells. HYCELTEC 2024, June 30th - July 03rd 2024, Complesso Monumentale Castello di Milazzo, Salita Castello, 98057 Milazzo (ME) - Italy. (https://www.hyceltec2024.it/scientific-programme/)

Other activities

1. From July 06th to 09th 2022 I followed the PhD school GRICU 2022 at Ischia (NA), Italy

2. From April 18th to October 11th, 2023, I attended six months for research purposes at Prof. Dr. Patrik Schmuki's group, Department of Materials Science and Engineering, Friedrich Alexander University, Erlangen, Germany

13. References

[1] R. Michal, S. Sfaelou, P. Lianos, Photocatalysis for Renewable Energy Production Using PhotoFuelCells, Molecules 2014, Vol. 19, Pages 19732-19750 19 (2014) 19732–19750. https://doi.org/10.3390/MOLECULES191219732.

[2] P.A. Owusu, S. Asumadu-Sarkodie, A review of renewable energy sources, sustainability issues and climate change mitigation, Http://Www.Editorialmanager.Com/Cogenteng 3 (2016). https://doi.org/10.1080/23311916.2016.1167990.

[3] V. Maslova, A. Fasolini, M. Offidani, S. Albonetti, F. Basile, Solar-driven valorization of glycerol towards production of chemicals and hydrogen, Catal Today 380 (2021) 147–155. https://doi.org/10.1016/j.cattod.2021.03.008.

[4] F. Martins, C. Felgueiras, M. Smitkova, N. Caetano, Analysis of Fossil Fuel Energy Consumption and Environmental Impacts in European Countries, Energies 2019, Vol. 12, Page 964 12 (2019) 964. https://doi.org/10.3390/EN12060964.

[5] I. Capellán-Pérez, M. Mediavilla, C. de Castro, Ó. Carpintero, L.J. Miguel, Fossil fuel depletion and socio-economic scenarios: An integrated approach, Energy 77 (2014) 641–666. https://doi.org/10.1016/J.ENERGY.2014.09.063.

[6] P. Pablo-Romero, R. Pozo-Barajas, J. Sánchez, R. García, J.L. Holechek, H.M.E. Geli, M.N. Sawalhah, R. Valdez, A Global Assessment: Can Renewable Energy Replace Fossil Fuels by 2050?, Sustainability 2022, Vol. 14, Page 4792 14 (2022) 4792. https://doi.org/10.3390/SU14084792.

[7] S. Yi, K. Raza Abbasi, K. Hussain, A. Albaker, R. Alvarado, Environmental concerns in the United States: Can renewable energy, fossil fuel energy, and natural resources depletion help?, Gondwana Research 117 (2023) 41–55. https://doi.org/10.1016/J.GR.2022.12.021.

[8] IRENA, Green hydrogen cost reduction: scaling up electrolysers to meet the 1.5°C climate goal, 2020. www.irena.org/publications.

[9] J.C. Ruth, G. Stephanopoulos, Synthetic fuels: what are they and where do they come from?, Curr Opin Biotechnol 81 (2023) 102919. https://doi.org/10.1016/J.COPBIO.2023.102919.

[10] T. Ahmad, D. Zhang, A critical review of comparative global historical energy consumption and future demand: The story told so far, Energy Reports 6 (2020) 1973–1991. https://doi.org/10.1016/J.EGYR.2020.07.020.

[11] IRENA, Making the breakthrough: Green hydrogen policies and technology costs, 2021. www.irena.org.

[12] J.D. Holladay, J. Hu, D.L. King, Y. Wang, An overview of hydrogen production technologies, Catal Today 139 (2009) 244–260. https://doi.org/10.1016/j.cattod.2008.08.039.

[13] Y. Li, D. Bahamon, M. Sinnokrot, K. Al-Ali, G. Palmisano, L.F. Vega, Computational modeling of green hydrogen generation from photocatalytic H_2S splitting: Overview and perspectives, Journal of Photochemistry and Photobiology C: Photochemistry Reviews 49 (2021) 100456. https://doi.org/10.1016/j.jphotochemrev.2021.100456.

[14] L. Zhang, C. Jia, F. Bai, W. Wang, S. An, K. Zhao, Z. Li, J. Li, H. Sun, A comprehensive review of the promising clean energy carrier: Hydrogen production, transportation, storage, and utilization (HPTSU) technologies, Fuel 355 (2024) 129455. https://doi.org/10.1016/J.FUEL.2023.129455.

[15] S.E. Hosseini, M.A. Wahid, Hydrogen from solar energy, a clean energy carrier from a sustainable source of energy, Int J Energy Res 44 (2020) 4110–4131. https://doi.org/10.1002/ER.4930.

[16] C.M. Pecoraro, M. Bellardita, V. Loddo, D. Virtù, F. Di Franco, M. Santamaria, Photocatalytic and photoelectrocatalytic H_2 evolution combined with valuable furfural production, Appl Catal A Gen 650 (2023) 118987. https://doi.org/10.1016/j.apcata.2022.118987.

[17] M. Bellardita, E.I. García-López, G. Marcì, L. Palmisano, Photocatalytic formation of H_2 and value-added chemicals in aqueous glucose (Pt)-TiO_2 suspension, Int J Hydrogen Energy 41 (2016) 5934–5947. https://doi.org/10.1016/J.IJHYDENE.2016.02.103.

[18] K. Brlec, S.R. Kavanagh, C.N. Savory, D.O. Scanlon, Understanding the Photocatalytic Activity of $La_5Ti_2AgS_5O_7$ and $La_5Ti_2CuS_5O_7$ for Green Hydrogen Production: Computational Insights, ACS Appl Energy Mater 5 (2022) 1992–2001. https://doi.org/10.1021/acsaem.1c03534.

[19] R. Kumar, R. Singh, S. Dutta, Review and Outlook of Hydrogen Production through Catalytic Processes, Energy and Fuels 38 (2024) 2601–2629. https://doi.org/10.1021/ACS.ENERGYFUELS.3C04026

[20] B.S. Zainal, P.J. Ker, H. Mohamed, H.C. Ong, I.M.R. Fattah, S.M.A. Rahman, L.D. Nghiem, T.M.I. Mahlia, Recent advancement and assessment of green hydrogen production technologies, Renewable and Sustainable Energy Reviews 189 (2024) 113941. https://doi.org/10.1016/J.RSER.2023.113941.

[21] P. Afanasev, A. Askarova, T. Alekhina, E. Popov, S. Markovic, A. Mukhametdinova, A. Cheremisin, E. Mukhina, An overview of hydrogen production methods: Focus on

hydrocarbon feedstock, Int J Hydrogen Energy 78 (2024) 805–828. https://doi.org/10.1016/J.IJHYDENE.2024.06.369.

[22] P. Saha, F.A. Akash, S.M. Shovon, M.U. Monir, M.T. Ahmed, M.F.H. Khan, S.M. Sarkar, M.K. Islam, M.M. Hasan, D.V.N. Vo, A.A. Aziz, M.J. Hossain, R. Akter, Grey, blue, and green hydrogen: A comprehensive review of production methods and prospects for zero-emission energy, Int J Green Energy 21 (2024) 1383–1397. https://doi.org/10.1080/15435075.2023.2244583.

[23] A. Di Nardo, M. Portarapillo, D. Russo, G. Luciani, G. Landi, G. Ruoppolo, A. Pezzella, A. Di Benedetto, Cyan Hydrogen Process: A New Route for Simultaneous Hydrogen Production and Carbon Valorization, ACS Omega (2023). https://doi.org/10.1021/ACSOMEGA.3C07277

[24] Y. Luo, Z. Zhang, M. Chhowalla, B. Liu, Y. Luo, Z. Zhang, B. Liu, M. Chhowalla, Recent Advances in Design of Electrocatalysts for High-Current-Density Water Splitting, Advanced Materials 34 (2022) 2108133. https://doi.org/10.1002/ADMA.202108133.

[25] H. Sun, X. Xu, H. Kim, W.C. Jung, W. Zhou, Z. Shao, Electrochemical Water Splitting: Bridging the Gaps Between Fundamental Research and Industrial Applications, Energy & Environmental Materials 6 (2023) e12441. https://doi.org/10.1002/EEM2.12441.

[26] C. Bie, L. Wang, J. Yu, Challenges for photocatalytic overall water splitting, Chem 8 (2022) 1567–1574. https://doi.org/10.1016/j.chempr.2022.04.013.

[27] Z.P. Ifkovits, J.M. Evans, M.C. Meier, K.M. Papadantonakis, N.S. Lewis, Decoupled electrochemical water-splitting systems: a review and perspective, Energy Environ Sci 14 (2021) 4740–4759. https://doi.org/10.1039/D1EE01226F.

[28] A. González-Garay, N. mac Dowell, N. Shah, A carbon neutral chemical industry powered by the sun, Discover Chemical Engineering 1 (2021) 2. https://doi.org/10.1007/s43938-021-00002-x.

[29] V.A. Panchenko, Y. V. Daus, A.A. Kovalev, I. V. Yudaev, Y. V. Litti, Prospects for the production of green hydrogen: Review of countries with high potential, Int J Hydrogen Energy 48 (2023) 4551–4571. https://doi.org/10.1016/J.IJHYDENE.2022.10.084.

[30] L. Eicke, N. De Blasio, Green hydrogen value chains in the industrial sector—Geopolitical and market implications, Energy Res Soc Sci 93 (2022) 102847. https://doi.org/10.1016/J.ERSS.2022.102847.

[31] G. Kakoulaki, I. Kougias, N. Taylor, F. Dolci, J. Moya, A. Jäger-Waldau, Green hydrogen in Europe – A regional assessment: Substituting existing production with electrolysis powered

by renewables, Energy Convers Manag 228 (2021) 113649. https://doi.org/10.1016/J.ENCONMAN.2020.113649.

[32] IRENA, Renewable Power Generation Costs in 2019, International Renewable Energy Agency (2020) 160. https://www.irena.org/-/media/Files/IRENA/Agency/Publication/2018/Jan/IRENA_2017_Power_Costs_2018.pdf (accessed July 10, 2024).

[33] Y.Z. Wang, M. Yang, Y.-M. Ding, N.-W. Li, L. Yu, Y.Z. Wang, M. Yang, Y.-M. Ding, N.-W. Li, L. Yu, Recent Advances in Complex Hollow Electrocatalysts for Water Splitting, Adv Funct Mater 32 (2022) 2108681. https://doi.org/10.1002/ADFM.202108681.

[34] W. Lei, Y. Yu, H. Zhang, Q. Jia, S. Zhang, Defect engineering of nanostructures: Insights into photoelectrochemical water splitting, Materials Today 52 (2022) 133–160. https://doi.org/10.1016/J.MATTOD.2021.10.028.

[35] L. Li, P. Wang, Q. Shao, X. Huang, Metallic nanostructures with low dimensionality for electrochemical water splitting, Chem Soc Rev 49 (2020) 3072–3106. https://doi.org/10.1039/D0CS00013B.

[36] Y. Zhou, H.J. Fan, Progress and Challenge of Amorphous Catalysts for Electrochemical Water Splitting, ACS Mater Lett 3 (2021) 136–147. https://doi.org/10.1021/ACSMATERIALSLETT.0C00502

[37] A.B.S. Semente, C.B. Madeira Rodrigues, M.A. Mariano, M.B. Gaspar, B. Šljukić, D.M.F. Santos, Prospects and challenges for the green hydrogen market, Solar-Driven Green Hydrogen Generation and Storage (2023) 381–415. https://doi.org/10.1016/B978-0-323-99580-1.00021-2.

[38] H. Ishaq, I. Dincer, C. Crawford, A review on hydrogen production and utilization: Challenges and opportunities, Int J Hydrogen Energy 47 (2022) 26238–26264. https://doi.org/10.1016/J.IJHYDENE.2021.11.149.

[39] A. Velazquez Abad, P.E. Dodds, Green hydrogen characterisation initiatives: Definitions, standards, guarantees of origin, and challenges, Energy Policy 138 (2020) 111300. https://doi.org/10.1016/J.ENPOL.2020.111300.

[40] G. Ghanashyam, H. Kyung Jeong, Flower-like molybdenum disulfide for efficient hydrogen and oxygen evolution reaction, Inorganica Chim Acta 541 (2022) 121098. https://doi.org/10.1016/J.ICA.2022.121098.

[41] L. She, G. Zhao, T. Ma, J. Chen, W. Sun, H. Pan, On the Durability of Iridium-Based Electrocatalysts toward the Oxygen Evolution Reaction under Acid Environment, Adv Funct Mater 32 (2022) 2108465. https://doi.org/10.1002/ADFM.202108465.

[42] M. Yu, E. Budiyanto, H. Tüysüz, Principles of Water Electrolysis and Recent Progress in Cobalt-, Nickel-, and Iron-Based Oxides for the Oxygen Evolution Reaction, Angewandte Chemie International Edition 61 (2022) e202103824. https://doi.org/10.1002/ANIE.202103824.

[43] X. Lin, J. Wang, Green synthesis of well dispersed TiO_2/Pt nanoparticles photocatalysts and enhanced photocatalytic activity towards hydrogen production, Int J Hydrogen Energy 44 (2019) 31853–31859. https://doi.org/10.1016/J.IJHYDENE.2019.10.062.

[44] K.A. Davis, S. Yoo, E.W. Shuler, B.D. Sherman, S. Lee, G. Leem, Photocatalytic hydrogen evolution from biomass conversion, Nano Convergence 2021 8:1 8 (2021) 1–19. https://doi.org/10.1186/S40580-021-00256-9.

[45] A. Augustin, C. Chuaicham, M. Shanmugam, B. Vellaichamy, S. Rajendran, T.K.A. Hoang, K. Sasaki, K. Sekar, Recent development of organic–inorganic hybrid photocatalysts for biomass conversion into hydrogen production, Nanoscale Adv 4 (2022) 2561–2582. https://doi.org/10.1039/D2NA00119E.

[46] M. Bellardita, L. Palmisano, V. Loddo, Boosting High Added-Value Chemicals Formation By Means Of Photoelectrocatalysis, Journal of Photocatalysis 3 (2022). https://doi.org/10.2174/2665976x03666220513153344.

[47] I.K.M. Yu, K.L. Ong, D.C.W. Tsang, M.A. Haque, T.H. Kwan, S.S. Chen, K. Uisan, S. Kulkarni, C.S.K. Lin, Chemical transformation of food and beverage waste-derived fructose to hydroxymethylfurfural as a value-added product, Catal Today 314 (2018) 70–77. https://doi.org/10.1016/J.CATTOD.2018.01.011.

[48] J. Lee, S. Jung, Y.T. Kim, H.J. Kim, K.H. Kim, Catalytic and electrocatalytic conversion of glucose into value-added chemicals, Renewable and Sustainable Energy Reviews 181 (2023) 113337. https://doi.org/10.1016/J.RSER.2023.113337.

[49] D. Aboagye, R. Djellabi, F. Medina, S. Contreras, Radical-Mediated Photocatalysis for Lignocellulosic Biomass Conversion into Value-Added Chemicals and Hydrogen: Facts, Opportunities and Challenges, Angewandte Chemie 135 (2023) e202301909. https://doi.org/10.1002/ANGE.202301909.

[50] M.K. Awasthi, T. Sar, S.C. Gowd, K. Rajendran, V. Kumar, S. Sarsaiya, Y. Li, R. Sindhu, P. Binod, Z. Zhang, A. Pandey, M.J. Taherzadeh, A comprehensive review on thermochemical,

and biochemical conversion methods of lignocellulosic biomass into valuable end product, Fuel 342 (2023) 127790. https://doi.org/10.1016/J.FUEL.2023.127790.

[51] P. Gallezot, Conversion of biomass to selected chemical products, Chem. Soc. Rev. 41 (2012) 1538–1558. https://doi.org/10.1039/C1CS15147A.

[52] T.A. Werpy, J.E. Holladay, J.F. White, Top Value Added Chemicals From Biomass: I. Results of Screening for Potential Candidates from Sugars and Synthesis Gas, Richland, WA, 2004. https://doi.org/10.2172/926125.

[53] C. Espro, E. Paone, F. Mauriello, R. Gotti, E. Uliassi, M.L. Bolognesi, D. Rodríguez-Padrón, R. Luque, Sustainable production of pharmaceutical, nutraceutical and bioactive compounds from biomass and waste, Chem Soc Rev 50 (2021) 11191–11207. https://doi.org/10.1039/D1CS00524C.

[54] K.E. Sanwald, T.F. Berto, A. Jentys, D.M. Camaioni, O.Y. Gutiérrez, J.A. Lercher, Kinetic Coupling of Water Splitting and Photoreforming on SrTiO3-Based Photocatalysts, ACS Catal 8 (2018) 2902–2913. https://doi.org/10.1021/ACSCATAL.7B03192/SUPPL_FILE/CS7B03192_SI_001.PDF.

[55] J.C. Serrano-Ruiz, R. Luque, A. Sepúlveda-Escribano, Transformations of biomass-derived platform molecules: from high added-value chemicals to fuelsvia aqueous-phase processing, Chem Soc Rev 40 (2011) 5266–5281. https://doi.org/10.1039/C1CS15131B.

[56] C.H. Christensen, J. Rass-Hansen, C.C. Marsden, E. Taarning, K. Egeblad, The Renewable Chemicals Industry, ChemSusChem 1 (2008) 283–289. https://doi.org/10.1002/CSSC.200700168.

[57] T. Lepage, M. Kammoun, Q. Schmetz, A. Richel, Biomass-to-hydrogen: A review of main routes production, processes evaluation and techno-economical assessment, Biomass Bioenergy 144 (2021) 105920. https://doi.org/10.1016/J.BIOMBIOE.2020.105920.

[58] M. Antar, D. Lyu, M. Nazari, A. Shah, X. Zhou, D.L. Smith, Biomass for a sustainable bioeconomy: An overview of world biomass production and utilization, Renewable and Sustainable Energy Reviews 139 (2021) 110691. https://doi.org/10.1016/J.RSER.2020.110691.

[59] C. Espro, E. Paone, F. Mauriello, R. Gotti, E. Uliassi, M.L. Bolognesi, D. Rodríguez-Padrón, R. Luque, Sustainable production of pharmaceutical, nutraceutical and bioactive compounds from biomass and waste, Chem Soc Rev 50 (2021) 11191–11207. https://doi.org/10.1039/D1CS00524C.

[60] J. Ma, K. Liu, X. Yang, D. Jin, Y. Li, G. Jiao, J. Zhou, R. Sun, Recent Advances and Challenges in Photoreforming of Biomass-Derived Feedstocks into Hydrogen, Biofuels, or Chemicals by Using Functional Carbon Nitride Photocatalysts, ChemSusChem 14 (2021) 4903–4922. https://doi.org/10.1002/CSSC.202101173.

[61] K. Chaudhary, K. Bhardvaj, A. Chaudhary, A qualitative assessment of hydrogen generation techniques for fuel cell applications, Fuel 358 (2024) 130090. https://doi.org/10.1016/J.FUEL.2023.130090.

[62] C. Drawer, J. Lange, M. Kaltschmitt, Metal hydrides for hydrogen storage – Identification and evaluation of stationary and transportation applications, J Energy Storage 77 (2024) 109988. https://doi.org/10.1016/J.EST.2023.109988.

[63] L. Ge, B. Zhang, W. Huang, Y. Li, L. Hou, J. Xiao, Z. Mao, X. Li, A review of hydrogen generation, storage, and applications in power system, J Energy Storage 75 (2024) 109307. https://doi.org/10.1016/J.EST.2023.109307.

[64] M. Reda, G. Pangestu, Z. Malaibari, A. Muhammad, N. Al-Rowaili, U. Zahid, Comprehensive Review on Methane Pyrolysis for Sustainable Hydrogen Production, Energy & Fuels (2024). https://doi.org/10.1021/ACS.ENERGYFUELS.4C01551.

[65] IRENA, Reaching zero with renewables : eliminating CO_2 emissions from industry and transport in line with the 1.5°C climate goal, (n.d.) 214.

[66] J.L. Aleixandre-Tudó, L. Castelló-Cogollos, J.L. Aleixandre, R. Aleixandre-Benavent, Renewable energies: Worldwide trends in research, funding and international collaboration, Renew Energy 139 (2019) 268–278. https://doi.org/10.1016/J.RENENE.2019.02.079.

[67] T. Kurbatova, T. Perederii, Global trends in renewable energy development, 2020 IEEE KhPI Week on Advanced Technology, KhPI Week 2020 - Conference Proceedings (2020) 260–263. https://doi.org/10.1109/KHPIWEEK51551.2020.9250098.

[68] Q. Hassan, S. Algburi, A.Z. Sameen, T.J. Al-Musawi, A.K. Al-Jiboory, H.M. Salman, B.M. Ali, M. Jaszczur, A comprehensive review of international renewable energy growth, Energy and Built Environment (2024). https://doi.org/10.1016/J.ENBENV.2023.12.002.

[69] M. Grahn, E. Malmgren, A.D. Korberg, M. Taljegard, J.E. Anderson, S. Brynolf, J. Hansson, I.R. Skov, T.J. Wallington, Review of electrofuel feasibility - Cost and environmental impact, Progress in Energy 4 (2022). https://doi.org/10.1088/2516-1083/ac7937.

[70] S.W. Sharshir, A. Joseph, M.M. Elsayad, A.A. Tareemi, A.W. Kandeal, M.R. Elkadeem, A review of recent advances in alkaline electrolyzer for green hydrogen production: Performance

improvement and applications, Int J Hydrogen Energy 49 (2024) 458–488. https://doi.org/10.1016/J.IJHYDENE.2023.08.107.

[71] M. Wappler, D. Unguder, X. Lu, H. Ohlmeyer, H. Teschke, W. Lueke, Building the green hydrogen market – Current state and outlook on green hydrogen demand and electrolyzer manufacturing, Int J Hydrogen Energy 47 (2022) 33551–33570. https://doi.org/10.1016/J.IJHYDENE.2022.07.253.

[72] T. Smolinka, E.T. Ojong, J. Garche, Hydrogen Production from Renewable Energies—Electrolyzer Technologies, Electrochemical Energy Storage for Renewable Sources and Grid Balancing (2015) 103–128. https://doi.org/10.1016/B978-0-444-62616-5.00008-5.

[73] M. Ni, M.K.H. Leung, D.Y.C. Leung, Technological development of hydrogen production by solid oxide electrolyzer cell (SOEC), Int J Hydrogen Energy 33 (2008) 2337–2354. https://doi.org/10.1016/J.IJHYDENE.2008.02.048.

[74] K. Zhang, X. Liang, L. Wang, K. Sun, Y. Wang, Z. Xie, Q. Wu, X. Bai, M.S. Hamdy, H. Chen, X. Zou, Status and perspectives of key materials for PEM electrolyzer, Nano Research Energy 1 (2022) e9120032. https://doi.org/10.26599/NRE.2022.9120032.

[75] D. Franzmann, H. Heinrichs, F. Lippkau, T. Addanki, C. Winkler, P. Buchenberg, T. Hamacher, M. Blesl, J. Linßen, D. Stolten, Green hydrogen cost-potentials for global trade, Int J Hydrogen Energy 48 (2023) 33062–33076. https://doi.org/10.1016/J.IJHYDENE.2023.05.012.

[76] S. Shiva Kumar, H. Lim, An overview of water electrolysis technologies for green hydrogen production, Energy Reports 8 (2022) 13793–13813. https://doi.org/10.1016/J.EGYR.2022.10.127.

[77] L. Kruitwagen, K.T. Story, J. Friedrich, L. Byers, S. Skillman, C. Hepburn, A global inventory of photovoltaic solar energy generating units, Nature 2021 598:7882 598 (2021) 604–610. https://doi.org/10.1038/s41586-021-03957-7.

[78] C.A. Schoeneberger, C.A. McMillan, P. Kurup, S. Akar, R. Margolis, E. Masanet, Solar for industrial process heat: A review of technologies, analysis approaches, and potential applications in the United States, Energy 206 (2020) 118083. https://doi.org/10.1016/J.ENERGY.2020.118083.

[79] A.M. Oliveira, R.R. Beswick, Y. Yan, A green hydrogen economy for a renewable energy society, Curr Opin Chem Eng 33 (2021) 100701. https://doi.org/10.1016/J.COCHE.2021.100701.

[80] V.A. Panchenko, Y. V. Daus, A.A. Kovalev, I. V. Yudaev, Y. V. Litti, Prospects for the production of green hydrogen: Review of countries with high potential, Int J Hydrogen Energy 48 (2023) 4551–4571. https://doi.org/10.1016/J.IJHYDENE.2022.10.084.

[81] N. Barhorst, Green Hydrogen - A Guide to Policy Makaing, 39th World Energy Engineering Conference, WEEC 2016 2 (2016) 52.

[82] B. Zhang, S.X. Zhang, R. Yao, Y.H. Wu, J.S. Qiu, Progress and prospects of hydrogen production: Opportunities and challenges, Journal of Electronic Science and Technology 19 (2021) 100080. https://doi.org/10.1016/J.JNLEST.2021.100080.

[83] A.G. Olabi, A. saleh bahri, A.A. Abdelghafar, A. Baroutaji, E.T. Sayed, A.H. Alami, H. Rezk, M.A. Abdelkareem, Large-vscale hydrogen production and storage technologies: Current status and future directions, Int J Hydrogen Energy 46 (2021) 23498–23528. https://doi.org/10.1016/J.IJHYDENE.2020.10.110.

[84] M. Younas, S. Shafique, A. Hafeez, F. Javed, F. Rehman, An Overview of Hydrogen Production: Current Status, Potential, and Challenges, Fuel 316 (2022) 123317. https://doi.org/10.1016/J.FUEL.2022.123317.

[85] A. Ajanovic, M. Sayer, R. Haas, On the future relevance of green hydrogen in Europe, Appl Energy 358 (2024) 122586. https://doi.org/10.1016/J.APENERGY.2023.122586.

[86] S.A. Grigoriev, V.N. Fateev, D.G. Bessarabov, P. Millet, Current status, research trends, and challenges in water electrolysis science and technology, Int J Hydrogen Energy 45 (2020) 26036–26058. https://doi.org/10.1016/J.IJHYDENE.2020.03.109.

[87] R. Gérardy, D.P. Debecker, J. Estager, P. Luis, J.C.M. Monbaliu, Continuous Flow Upgrading of Selected C2-C6Platform Chemicals Derived from Biomass, Chem Rev 120 (2020) 7219–7347. https://doi.org/10.1021/ACS.CHEMREV.9B00846

[88] W.M. Lewandowski, M. Ryms, W. Kosakowski, Thermal Biomass Conversion: A Review, Processes 2020, Vol. 8, Page 516 8 (2020) 516. https://doi.org/10.3390/PR8050516.

[89] F. Shen, X. Xiong, J. Fu, J. Yang, M. Qiu, X. Qi, D.C.W. Tsang, Recent advances in mechanochemical production of chemicals and carbon materials from sustainable biomass resources, Renewable and Sustainable Energy Reviews 130 (2020) 109944. https://doi.org/10.1016/J.RSER.2020.109944.

[90] J.A. Okolie, S. Nanda, A.K. Dalai, J.A. Kozinski, Chemistry and Specialty Industrial Applications of Lignocellulosic Biomass, Waste Biomass Valorization 12 (2021) 2145–2169. https://doi.org/10.1007/S12649-020-01123-0/FIGURES/6.

[91] A.A. Longati, A.M. Elias, F.F. Furlan, E.A. Miranda, R. de Campos Giordano, Techno-economic-environmental Analysis of the Production of Biosurfactants in the Context of Biorefineries, Biosurfactants and Sustainability: From Biorefineries Production to Versatile Applications (2023) 281–300. https://doi.org/10.1002/9781119854395.CH14.

[92] N. Thongchul, P. Charoensuppanimit, A. Anantpinijwatna, R. Gani, S. Assabumrungrat, Overview of biorefinery, A-Z of Biorefinery: A Comprehensive View (2022) 3–32. https://doi.org/10.1016/B978-0-12-819248-1.00020-8.

[93] R. Reshmy, T.A.P. Paulose, E. Philip, D. Thomas, A. Madhavan, R. Sirohi, P. Binod, M. Kumar Awasthi, A. Pandey, R. Sindhu, Updates on high value products from cellulosic biorefinery, Fuel 308 (2022) 122056. https://doi.org/10.1016/J.FUEL.2021.122056.

[94] N. Singh, R.R. Singhania, P.S. Nigam, C. Di Dong, A.K. Patel, M. Puri, Global status of lignocellulosic biorefinery: Challenges and perspectives, Bioresour Technol 344 (2022) 126415. https://doi.org/10.1016/J.BIORTECH.2021.126415.

[95] I. Ridjan, B.V. Mathiesen, D. Connolly, Terminology used for renewable liquid and gaseous fuels based on the conversion of electricity: a review, J Clean Prod 112 (2016) 3709–3720. https://doi.org/10.1016/J.JCLEPRO.2015.05.117.

[96] A. Nemmour, A. Inayat, I. Janajreh, C. Ghenai, Green hydrogen-based E-fuels (E-methane, E-methanol, E-ammonia) to support clean energy transition: A literature review, Int J Hydrogen Energy 48 (2023) 29011–29033. https://doi.org/10.1016/J.IJHYDENE.2023.03.240.

[97] F. Ueckerdt, C. Bauer, A. Dirnaichner, J. Everall, R. Sacchi, G. Luderer, Potential and risks of hydrogen-based e-fuels in climate change mitigation, Nature Climate Change 2021 11:5 11 (2021) 384–393. https://doi.org/10.1038/s41558-021-01032-7.

[98] M. Fasihi, O. Efimova, C. Breyer, Techno-economic assessment of CO2 direct air capture plants, J Clean Prod 224 (2019) 957–980. https://doi.org/10.1016/J.JCLEPRO.2019.03.086.

[99] M. Götz, J. Lefebvre, F. Mörs, A. McDaniel Koch, F. Graf, S. Bajohr, R. Reimert, T. Kolb, Renewable Power-to-Gas: A technological and economic review, Renew Energy 85 (2016) 1371–1390. https://doi.org/10.1016/J.RENENE.2015.07.066.

[100] S. Brynolf, M. Taljegard, M. Grahn, J. Hansson, Electrofuels for the transport sector: A review of production costs, Renewable and Sustainable Energy Reviews 81 (2018) 1887–1905. https://doi.org/10.1016/J.RSER.2017.05.288.

[101] I. Hannula, Hydrogen enhancement potential of synthetic biofuels manufacture in the European context: A techno-economic assessment, Energy 104 (2016) 199–212. https://doi.org/10.1016/J.ENERGY.2016.03.119.

[102] P. Schmidt, V. Batteiger, A. Roth, W. Weindorf, T. Raksha, Power-to-Liquids as Renewable Fuel Option for Aviation: A Review, Chemie Ingenieur Technik 90 (2018) 127–140. https://doi.org/10.1002/CITE.201700129.

[103] M. Hillestad, M. Ostadi, G.D. Alamo Serrano, E. Rytter, B. Austbø, J.G. Pharoah, O.S. Burheim, Improving carbon efficiency and profitability of the biomass to liquid process with hydrogen from renewable power, Fuel 234 (2018) 1431–1451. https://doi.org/10.1016/J.FUEL.2018.08.004.

[104] J. Ikäheimo, J. Kiviluoma, R. Weiss, H. Holttinen, Power-to-ammonia in future North European 100 % renewable power and heat system, Int J Hydrogen Energy 43 (2018) 17295–17308. https://doi.org/10.1016/J.IJHYDENE.2018.06.121.

[105] I. Hannula, Hydrogen enhancement potential of synthetic biofuels manufacture in the European context: A techno-economic assessment, Energy 104 (2016) 199–212. https://doi.org/10.1016/J.ENERGY.2016.03.119.

[106] M.S. Lester, R. Bramstoft, M. Münster, Analysis on Electrofuels in Future Energy Systems: A 2050 Case Study, Energy 199 (2020) 117408. https://doi.org/10.1016/J.ENERGY.2020.117408.

[107] D. Connolly, H. Lund, B. V. Mathiesen, Smart Energy Europe: The technical and economic impact of one potential 100% renewable energy scenario for the European Union, Renewable and Sustainable Energy Reviews 60 (2016) 1634–1653. https://doi.org/10.1016/J.RSER.2016.02.025.

[108] A.D. Korberg, I.R. Skov, B.V. Mathiesen, The role of biogas and biogas-derived fuels in a 100% renewable energy system in Denmark, Energy 199 (2020) 117426. https://doi.org/10.1016/J.ENERGY.2020.117426.

[109] K. Dahal, S. Brynolf, C. Xisto, J. Hansson, M. Grahn, T. Grönstedt, M. Lehtveer, Techno-economic review of alternative fuels and propulsion systems for the aviation sector, Renewable and Sustainable Energy Reviews 151 (2021) 111564. https://doi.org/10.1016/J.RSER.2021.111564.

[110] M. Kopp, D. Coleman, C. Stiller, K. Scheffer, J. Aichinger, B. Scheppat, Energiepark Mainz: Technical and economic analysis of the worldwide largest Power-to-Gas plant with PEM electrolysis, Int J Hydrogen Energy 42 (2017) 13311–13320. https://doi.org/10.1016/J.IJHYDENE.2016.12.145.

[111] H. Zhang, L. Wang, J. Van herle, F. Maréchal, U. Desideri, Techno-economic comparison of green ammonia production processes, Appl Energy 259 (2020) 114135. https://doi.org/10.1016/J.APENERGY.2019.114135.

[112] K. Shi, B. Guan, Z. Zhuang, J. Chen, Y. Chen, Z. Ma, C. Zhu, X. Hu, S. Zhao, H. Dang, J. Guo, L. Chen, K. Shu, Y. Li, Z. Guo, C. Yi, J. Hu, Z. Huang, Perspectives and Outlook of E-fuels: Production, Cost Effectiveness, and Applications, Energy and Fuels 38 (2024) 7665–7692. https://doi.org/10.1021/ACS.ENERGYFUELS.4C00409

[113] I. D'Adamo, M. Gastaldi, M. Giannini, A.S. Nizami, Environmental implications and levelized cost analysis of E-fuel production under photovoltaic energy, direct air capture, and hydrogen, Environ Res 246 (2024) 118163. https://doi.org/10.1016/J.ENVRES.2024.118163.

[114] S. Kromus, B. Kamm, M. Kamm, P. Fowler, M. Narodoslawsky, Green Biorefineries: The Green Biorefinery Concept – Fundamentals and Potential, Biorefineries-Industrial Processes and Products: Status Quo and Future Directions 1 (2008) 253–294. https://doi.org/10.1002/9783527619849.CH12.

[115] E. Koukios, D. Koullas, I.D. Koukios, E. Avgerinos, Critical parameters for optimal biomass refineries: The case of biohydrogen, Clean Technol Environ Policy 12 (2010) 147–151. https://doi.org/10.1007/S10098-009-0239-Y/TABLES/1.

[116] N. Mosier, C. Wyman, B. Dale, R. Elander, Y.Y. Lee, M. Holtzapple, M. Ladisch, Features of promising technologies for pretreatment of lignocellulosic biomass, Bioresour Technol 96 (2005) 673–686. https://doi.org/10.1016/J.BIORTECH.2004.06.025.

[117] S. Brethauer, C.E. Wyman, Review: Continuous hydrolysis and fermentation for cellulosic ethanol production, Bioresour Technol 101 (2010) 4862–4874. https://doi.org/10.1016/J.BIORTECH.2009.11.009.

[118] G. Stephanopoulos, G. V. Reklaitis, Process systems engineering: From Solvay to modern bio- and nanotechnology.. A history of development, successes and prospects for the future, Chem Eng Sci 66 (2011) 4272–4306. https://doi.org/10.1016/J.CES.2011.05.049.

[119] A. Voll, W. Marquardt, Reaction network flux analysis: Optimization-based evaluation of reaction pathways for biorenewables processing, AIChE Journal 58 (2012) 1788–1801. https://doi.org/10.1002/AIC.12704.

[120] V. Pham, M. El-Halwagi, Process synthesis and optimization of biorefinery configurations, AIChE Journal 58 (2012) 1212–1221. https://doi.org/10.1002/AIC.12640.

[121] M.A. Fox, M.T. Dulay, Heterogeneous Photocatalysis, Chem Rev 93 (1993) 341–357. https://doi.org/10.1021/CR00017A016

[122] A. Mills, S. Le Hunte, An overview of semiconductor photocatalysis, J Photochem Photobiol A Chem 108 (1997) 1–35. https://doi.org/10.1016/S1010-6030(97)00118-4.

[123] K. Nakata, A. Fujishima, TiO_2 photocatalysis: Design and applications, Journal of Photochemistry and Photobiology C: Photochemistry Reviews 13 (2012) 169–189. https://doi.org/10.1016/J.JPHOTOCHEMREV.2012.06.001.

[124] S. Gisbertz, B. Pieber, Heterogeneous Photocatalysis in Organic Synthesis, ChemPhotoChem 4 (2020) 456–475. https://doi.org/10.1002/cptc.202000014.

[125] M. Bellardita, S. Yurdakal, B.S. Tek, Ç. Değirmenci, G. Palmisano, V. Loddo, L. Palmisano, J. Soria, J. Sanz, V. Augugliaro, Tuning the selectivity to aldehyde via pH regulation in the photocatalytic oxidation of 4-methoxybenzyl alcohol and vanillyl alcohol by TiO_2 catalysts, J Environ Chem Eng 9 (2021) 105308. https://doi.org/10.1016/j.jece.2021.105308.

[126] T. Gupta, R.P. Chauhan, Photocatalytic degradation of water pollutants using II-VI semiconducting catalysts: A comprehensive review, J Environ Chem Eng 9 (2021) 106734. https://doi.org/10.1016/j.jece.2021.106734.

[127] Y. Zhao, Y. Li, L. Sun, Recent advances in photocatalytic decomposition of water and pollutants for sustainable application, Chemosphere 276 (2021) 130201. https://doi.org/10.1016/j.chemosphere.2021.130201.

[128] K. Maeda, K. Domen, Photocatalytic Water Splitting: Recent Progress and Future Challenges, J Phys Chem Lett 1 (2010) 2655–2661. https://doi.org/10.1021/jz1007966.

[129] D. Zhao, Y. Wang, C.-L. Dong, Y.-C. Huang, J. Chen, F. Xue, S. Shen, L. Guo, Boron-doped nitrogen-deficient carbon nitride-based Z-scheme heterostructures for photocatalytic overall water splitting, Nat Energy 6 (2021) 388–397. https://doi.org/10.1038/s41560-021-00795-9.

[130] C.Y. Toe, C. Tsounis, J. Zhang, H. Masood, D. Gunawan, J. Scott, R. Amal, Advancing photoreforming of organics: highlights on photocatalyst and system designs for selective oxidation reactions, Energy Environ Sci 14 (2021) 1140–1175. https://doi.org/10.1039/D0EE03116J.

[131] Y.-H. Chung, K. Han, C.-Y. Lin, D. O'Neill, G. Mul, B. Mei, C.-M. Yang, Photocatalytic hydrogen production by photo-reforming of methanol with one-pot synthesized Pt-containing TiO_2 photocatalysts, Catal Today 356 (2020) 95–100. https://doi.org/10.1016/j.cattod.2019.07.042.

[132] J.A. Rengifo-Herrera, C. Pulgarin, Why five decades of massive research on heterogeneous photocatalysis, especially on TiO_2, has not yet driven to water disinfection and detoxification

applications? Critical review of drawbacks and challenges, Chemical Engineering Journal 477 (2023) 146875. https://doi.org/10.1016/J.CEJ.2023.146875.

[133] L.G. Devi, R. Kavitha, A review on non metal ion doped titania for the photocatalytic degradation of organic pollutants under UV/solar light: Role of photogenerated charge carrier dynamics in enhancing the activity, Appl Catal B 140–141 (2013) 559–587. https://doi.org/10.1016/J.APCATB.2013.04.035.

[134] Q. Shi, H. Duan, Recent progress in photoelectrocatalysis beyond water oxidation, Chem Catalysis 2 (2022) 3471–3496. https://doi.org/10.1016/j.checat.2022.11.007.

[135] J. Yu, J. González-Cobos, F. Dappozze, F.J. López-Tenllado, J. Hidalgo-Carrillo, A. Marinas, P. Vernoux, A. Caravaca, C. Guillard, WO_3-based materials for photoelectrocatalytic glycerol upgrading into glyceraldehyde: Unravelling the synergistic photo- and electro-catalytic effects, Appl Catal B 318 (2022) 121843. https://doi.org/10.1016/J.APCATB.2022.121843.

[136] L. Fan, B. Liu, X. Liu, N. Senthilkumar, G. Wang, Z. Wen, Recent Progress in Electrocatalytic Glycerol Oxidation, Energy Technology 9 (2021) 2000804. https://doi.org/10.1002/ENTE.202000804.

[137] M. Bellardita, V. Loddo, V. Augugliaro, L. Palmisano, S. Yurdakal, Selective photocatalytic and photoelectrocatalytic synthesis of valuable compounds in aqueous medium, Catal Today 432 (2024) 114587. https://doi.org/10.1016/J.CATTOD.2024.114587.

[138] S.Y. Li, K.F. Huang, Z.Y. Tang, J.H. Wang, Photoelectrocatalytic organic synthesis: a versatile method for the green production of building-block chemicals, J Mater Chem A Mater 11 (2023) 3281–3296. https://doi.org/10.1039/D2TA09430D.

[139] P. Lianos, Review of recent trends in photoelectrocatalytic conversion of solar energy to electricity and hydrogen, Appl Catal B 210 (2017) 235–254. https://doi.org/10.1016/J.APCATB.2017.03.067.

[140] M. Bellardita, V. Loddo, F. Parrino, L. Palmisano, (Photo)electrocatalytic Versus Heterogeneous Photocatalytic Carbon Dioxide Reduction, ChemPhotoChem 5 (2021) 767–791. https://doi.org/10.1002/CPTC.202100030.

[141] G.G. Bessegato, T.T. Guaraldo, J.F. de Brito, M.F. Brugnera, M.V.B. Zanoni, Achievements and Trends in Photoelectrocatalysis: from Environmental to Energy Applications, Electrocatalysis 2015 6:5 6 (2015) 415–441. https://doi.org/10.1007/S12678-015-0259-9.

[142] S. Pitchaimuthu, K. Sridharan, S. Nagarajan, S. Ananthraj, P. Robertson, M.F. Kuehnel, Á. Irabien, M. Maroto-Valer, Solar Hydrogen Fuel Generation from Wastewater—Beyond

Photoelectrochemical Water Splitting: A Perspective, Energies (Basel) 15 (2022) 7399. https://doi.org/10.3390/EN15197399.

[143] M. Grätzel, Photoelectrochemical cells, Nature 414 (2001) 338–344.

[144] Y.H. Li, F. Zhang, Y. Chen, J.Y. Li, Y.J. Xu, Photoredox-catalyzed biomass intermediate conversion integrated with H_2 production over Ti_3C_2Tx/CdS composites, Green Chemistry 22 (2020) 163–169. https://doi.org/10.1039/C9GC03332G.

[145] T. Yao, X. An, H. Han, J.Q. Chen, C. Li, Photoelectrocatalytic Materials for Solar Water Splitting, Adv Energy Mater 8 (2018) 1800210. https://doi.org/10.1002/AENM.201800210.

[146] A. Mehtab, S.M. Alshehri, T. Ahmad, Photocatalytic and Photoelectrocatalytic Water Splitting by Porous g-C3N4Nanosheets for Hydrogen Generation, ACS Appl Nano Mater 5 (2022) 12656–12665. https://doi.org/10.1021/ACSANM.2C02460/SUPPL_FILE/AN2C02460_SI_001.PDF.

[147] H. Zhou, D. Zhang, H. Xie, Y. Liu, C. Meng, P. Zhang, F. Fan, R. Li, C. Li, Modulating Oxygen Vacancies in Lead Chromate for Photoelectrocatalytic Water Splitting, Advanced Materials 35 (2023) 2300914. https://doi.org/10.1002/ADMA.202300914.

[148] H. Wang, Y. Liang, L. Liu, J. Hu, P. Wu, W. Cui, Enriched photoelectrocatalytic degradation and photoelectric performance of BiOI photoelectrode by coupling rGO, Appl Catal B 208 (2017) 22–34. https://doi.org/10.1016/J.APCATB.2017.02.055.

[149] P. Alulema-Pullupaxi, P.J. Espinoza-Montero, C. Sigcha-Pallo, R. Vargas, L. Fernández, J.M. Peralta-Hernández, J.L. Paz, Fundamentals and applications of photoelectrocatalysis as an efficient process to remove pollutants from water: A review, Chemosphere 281 (2021) 130821. https://doi.org/10.1016/J.CHEMOSPHERE.2021.130821.

[150] W. Chen, S. Liu, Y. Fu, H. Yan, L. Qin, C. Lai, C. Zhang, H. Ye, W. Chen, F. Qin, F. Xu, X. Huo, H. Qin, Recent advances in photoelectrocatalysis for environmental applications: Sensing, pollutants removal and microbial inactivation, Coord Chem Rev 454 (2022) 214341. https://doi.org/10.1016/J.CCR.2021.214341.

[151] F.Y. Yu, Y.J. Zhou, H.Q. Tan, Y.G. Li, Z.H. Kang, Versatile Photoelectrocatalysis Strategy Raising Up the Green Production of Hydrogen Peroxide, Adv Energy Mater 13 (2023) 2300119. https://doi.org/10.1002/AENM.202300119.

[152] P. Li, Y. Liu, M.A. Mushtaq, D. Yan, Recent progress in ammonia synthesis based on photoelectrocatalysis, Inorg Chem Front 10 (2023) 4650–4667. https://doi.org/10.1039/D3QI00683B.

[153] X. Feng, X. Feng, F. Zhang, Enhanced photoelectrochemical oxidation of glycerol to dihydroxyacetone coupled with hydrogen generation via accelerative middle hydroxyl dehydrogenation over a Bi0/Bi3+ interface of a cascade heterostructure, J Mater Chem A Mater 11 (2023) 20242–20253. https://doi.org/10.1039/D3TA04326F.

[154] J. Yu, J. González-Cobos, F. Dappozze, P. Vernoux, A. Caravaca, C. Guillard, Basic comprehension and recent trends in photoelectrocatalytic systems, Green Chemistry 26 (2024) 1682–1708. https://doi.org/10.1039/D3GC03371F.

[155] C.M. Pecoraro, F. Di Franco, M. Bellardita, V. Loddo, M. Santamaria, Enhancing H_2 production rate in PGM-free photoelectrochemical cells by glycerol photo-oxidation, Int J Hydrogen Energy 49 (2024) 322–336. https://doi.org/10.1016/j.ijhydene.2023.08.011.

[156] Z. Tian, Y. Da, M. Wang, X. Dou, X. Cui, J. Chen, R. Jiang, S. Xi, B. Cui, Y. Luo, H. Yang, Y. Long, Y. Xiao, W. Chen, Selective photoelectrochemical oxidation of glucose to glucaric acid by single atom Pt decorated defective TiO_2, Nature Communications 2023 14:1 14 (2023) 1–12. https://doi.org/10.1038/s41467-023-35875-9.

[157] D.A. Tryk, A. Fujishima, K. Honda, Recent topics in photoelectrochemistry: achievements and future prospects, Electrochim Acta 45 (2000) 2363–2376. https://doi.org/10.1016/S0013-4686(00)00337-6.

[158] M.X. Tan, P.E. Laibinis, S.T. Nguyen, J.M. Kesselman, C.E. Stanton, N.S. Lewis, Principles and Applications of Semiconductor Photoelectrochemistry, Progress in Inorganic Chemistry 41 (2007) 21–144. https://doi.org/10.1002/9780470166420.CH2.

[159] A. Dey, F.A. Houle, C.E. Lubner, M. Sevilla, W.J. Shaw, Introduction to (photo)electrocatalysis for renewable energy, Chemical Communications 57 (2021) 1540–1542. https://doi.org/10.1039/D0CC90530E.

[160] T. Yao, X. An, H. Han, J.Q. Chen, C. Li, Photoelectrocatalytic Materials for Solar Water Splitting, Adv Energy Mater 8 (2018) 1800210. https://doi.org/10.1002/AENM.201800210.

[161] S. Yurdakal, O. Alagöz, L. Özcan, L. Palmisano, Selective photoelectrocatalytic transformations of organic compounds, Photoelectrocatalysis: Fundamentals and Applications (2023) 361–420. https://doi.org/10.1016/B978-0-12-823989-6.00001-1.

[162] L. Liang, L. Shi, F. Wang, H. Wang, P. Yan, Y. Cong, L. Yao, Z. Yang, W. Qi, g-C3N4 nano-fragments as highly efficient hydrogen evolution photocatalysts: Boosting effect of nitrogen vacancy, Appl Catal A Gen 599 (2020) 117618. https://doi.org/10.1016/J.APCATA.2020.117618.

[163] Y. Liu, W. Zhang, Y. Wang, R. Tian, J. Wang, Innovations in Photocatalytic and Photoelectrocatalytic Water Splitting: Pathways to Efficiently Convert Biomass into Renewable Energy and Chemicals, ChemCatChem 2024 (2024) e202400413. https://doi.org/10.1002/CCTC.202400413.

[164] J. Yu, J. González-Cobos, F. Dappozze, N. Grimaldos-Osorio, P. Vernoux, A. Caravaca, C. Guillard, First PEM photoelectrolyser for the simultaneous selective glycerol valorization into value-added chemicals and hydrogen generation, Appl Catal B 327 (2023) 122465. https://doi.org/10.1016/J.APCATB.2023.122465.

[165] T. Li, J.Y. Mo, D.M. Weekes, K.E. Dettelbach, R.P. Jansonius, G.M. Sammis, C.P. Berlinguette, Photoelectrochemical Decomposition of Lignin Model Compound on a BiVO4 Photoanode, ChemSusChem 13 (2020) 3622–3626. https://doi.org/10.1002/CSSC.202001134.

[166] Y. Sun, G. Han, L. Du, C. Du, X. Zhou, Q. Sun, Y. Gao, G. Yin, Y. Li, Y. Wang, Photoelectrochemistry-driven selective hydroxyl oxidation of polyols: Synergy between Au nanoparticles and C3N4 nanosheets, Chem Catalysis 1 (2021) 1260–1272. https://doi.org/10.1016/J.CHECAT.2021.09.001.

[167] K. Jakubow-Piotrowska, B. Witkowski, J. Augustynski, Photoelectrocatalytic hydrogen generation coupled with reforming of glucose into valuable chemicals using a nanostructured WO_3 photoanode, Commun Chem 5 (2022). https://doi.org/10.1038/s42004-022-00745-w.

[168] P. Lianos, Review of recent trends in photoelectrocatalytic conversion of solar energy to electricity and hydrogen, Appl Catal B 210 (2017) 235–254. https://doi.org/10.1016/j.apcatb.2017.03.067.

[169] Y. Miao, Z. Li, Y. Song, K. Fan, J. Guo, R. Li, M. Shao, Surface active oxygen engineering of photoanodes to boost photoelectrochemical water and alcohol oxidation coupled with hydrogen production, Appl Catal B 323 (2023). https://doi.org/10.1016/j.apcatb.2022.122147.

[170] A. Govind Rajan, J.M.P. Martirez, E.A. Carter, Why Do We Use the Materials and Operating Conditions We Use for Heterogeneous (Photo)Electrochemical Water Splitting?, ACS Catal 10 (2020). https://doi.org/10.1021/ACSCATAL.0C01862.

[171] J. Yu, J. González-Cobos, F. Dappozze, N. Grimaldos-Osorio, P. Vernoux, A. Caravaca, C. Guillard, First PEM photoelectrolyser for the simultaneous selective glycerol valorization into value-added chemicals and hydrogen generation, Appl Catal B 327 (2023). https://doi.org/10.1016/j.apcatb.2023.122465.

[172] Y. Han, M. Chang, Z. Zhao, F. Niu, Z. Zhang, Z. Sun, L. Zhang, K. Hu, Selective Valorization of Glycerol to Formic Acid on a BiVO4 Photoanode through NiFe Phenolic Networks, ACS Appl Mater Interfaces 15 (2023) 11678–11690. https://doi.org/10.1021/acsami.2c20516.

[173] L.L. Nascimento, J.Z. Marinho, A.L.R. dos Santos, A.M. de Faria, R.A.C. Souza, C. Wang, A.O.T. Patrocinio, Photoelectrochemical reforming of glycerol by Bi_2WO_6 photoanodes: Role of the electrolyte pH on the H_2 evolution efficiency and product selectivity, Appl Catal A Gen 646 (2022). https://doi.org/10.1016/j.apcata.2022.118867.

[174] C. Lin, C. Dong, S. Kim, Y. Lu, Y. Wang, Z. Yu, Y. Gu, Z. Gu, D.K. Lee, K. Zhang, J.H. Park, Photo-Electrochemical Glycerol Conversion over a Mie Scattering Effect Enhanced Porous BiVO4 Photoanode, Advanced Materials (2023). https://doi.org/10.1002/adma.202209955.

[175] A. Fujishima, K. Honda, Electrochemical Photolysis of Water at a Semiconductor Electrode, Nature 238 (1972) 37–38. https://doi.org/10.1038/238037a0.

[176] Wiley-VCH - Semiconductor Electrochemistry, (n.d.). https://www.wiley-vch.de/de/fachgebiete/ingenieurwesen/materialwissenschaften-10ms/elektronische-materialien-10ms4/semiconductor-electrochemistry-978-3-527-31281-8 (accessed July 17, 2024).

[177] V.A. Myamlin, Y. V. Pleskov, Electrochemistry of Semiconductors, Electrochemistry of Semiconductors (1967). https://doi.org/10.1007/978-1-4899-6533-2.

[178] H.G.-(No Title), undefined 1984, Advances in electrochemistry and electrochemical engineering, Cir.Nii.Ac.Jp (n.d.). https://cir.nii.ac.jp/crid/1130000797742967424 (accessed July 23, 2024).

[179] H. Gerischer, Electrode Processes, Annu Rev Phys Chem 12 (1961) 227–254. https://doi.org/10.1146/ANNUREV.PC.12.100161.001303.

[180] M. Stern, H. Wissenberg, The Influence of Noble Metal Alloy Additions on the Electrochemical and Corrosion Behavior of Titanium, J Electrochem Soc 106 (1959) 759. https://doi.org/10.1149/1.2427493/XML.

[181] E. V. Kondratenko, G. Mul, J. Baltrusaitis, G.O. Larrazábal, J. Pérez-Ramírez, Status and perspectives of CO2 conversion into fuels and chemicals by catalytic, photocatalytic and electrocatalytic processes, Energy Environ Sci 6 (2013) 3112–3135. https://doi.org/10.1039/C3EE41272E.

[182] J. Artz, T.E. Müller, K. Thenert, J. Kleinekorte, R. Meys, A. Sternberg, A. Bardow, W. Leitner, Sustainable Conversion of Carbon Dioxide: An Integrated Review of Catalysis and Life Cycle

Assessment, Chem Rev 118 (2018) 434–504. https://doi.org/10.1021/ACS.CHEMREV.7B00435

[183] B.-Q. Li, C.-X. Zhao, J.-N. Liu, Q. Zhang, B. Li, C. Zhao, J. Liu, Q. Zhang, Electrosynthesis of Hydrogen Peroxide Synergistically Catalyzed by Atomic Co–Nx–C Sites and Oxygen Functional Groups in Noble-Metal-Free Electrocatalysts, Advanced Materials 31 (2019) 1808173. https://doi.org/10.1002/ADMA.201808173.

[184] A. Lenarda, M. Bevilacqua, C. Tavagnacco, L. Nasi, A. Criado, F. Vizza, M. Melchionna, M. Prato, P. Fornasiero, Selective Electrocatalytic H_2O_2 Generation by Cobalt@N-Doped Graphitic Carbon Core–Shell Nanohybrids, ChemSusChem 12 (2019) 1664–1672. https://doi.org/10.1002/CSSC.201900238.

[185] A.J. Nozik, R. Memming, Physical chemistry of semiconductor-liquid interfaces, Journal of Physical Chemistry 100 (1996) 13061–13078. https://doi.org/10.1021/JP953720E

[186] Encyclopedia of Electrochemistry, Encyclopedia of Electrochemistry (2010). https://doi.org/10.1002/9783527610426.

[187] Electrochemical Methods: Fundamentals and Applications, 2nd Edition | Wiley, (n.d.). https://www.wiley.com/en-us/Electrochemical+Methods%3A+Fundamentals+and+Applications%2C+2nd+Edition-p-9780471043720 (accessed July 23, 2024).

[188] K.J. Lee, N. Elgrishi, B. Kandemir, J.L. Dempsey, Electrochemical and spectroscopic methods for evaluating molecular electrocatalysts, Nature Reviews Chemistry 2017 1:5 1 (2017) 1–14. https://doi.org/10.1038/s41570-017-0039.

[189] N. Elgrishi, K.J. Rountree, B.D. McCarthy, E.S. Rountree, T.T. Eisenhart, J.L. Dempsey, A Practical Beginner's Guide to Cyclic Voltammetry, J Chem Educ 95 (2018) 197–206. https://doi.org/10.1021/ACS.JCHEMED.7B00361/SUPPL_FILE/ED7B00361_SI_002.DOCX.

[190] A. Ohma, K. Shinohara, A. Iiyama, T. Yoshida, A. Daimaru, Membrane and Catalyst Performance Targets for Automotive Fuel Cells by FCCJ Membrane, Catalyst, MEA WG, ECS Trans 41 (2011) 775–784. https://doi.org/10.1149/1.3635611/XML.

[191] P. Roy, S. Berger, P. Schmuki, TiO_2 Nanotubes: Synthesis and Applications, Angewandte Chemie International Edition 50 (2011) 2904–2939. https://doi.org/10.1002/anie.201001374.

[192] A. Nitta, M. Takase, M. Takashima, N. Murakami, B. Ohtani, A fingerprint of metal-oxide powders: energy-resolved distribution of electron traps, Chemical Communications 52 (2016) 12096–12099. https://doi.org/10.1039/C6CC04999K.

[193] M. Kobielusz, K. Pilarczyk, E. Święt ek, K. Szaciłowski, W. Macyk, Spectroelectrochemical analysis of TiO_2 electronic states – Implications for the photocatalytic activity of anatase and rutile, Catal Today 309 (2018) 35–42. https://doi.org/10.1016/J.CATTOD.2017.11.013.

[194] R. Memming, Photoinduced charge transfer processes at semiconductor electrodes and particles, (1994) 105–181. https://doi.org/10.1007/3-540-57565-0_75.

[195] J.I. Pankove, Optical processes in semiconductors / Jacques I. Pankove., (1971). https://books.google.com/books/about/Optical_Processes_in_Semiconductors.html?hl=tr&id=zK7vAAAAMAAJ (accessed July 23, 2024).

[196] Y. V Pleskov, Y.Y. Gurevich, Semiconductor photoelectrochemistry, (1986).

[197] J. Georgieva, E. Valova, S. Armyanov, N. Philippidis, I. Poulios, S. Sotiropoulos, Bi-component semiconductor oxide photoanodes for the photoelectrocatalytic oxidation of organic solutes and vapours: A short review with emphasis to TiO_2–WO_3 photoanodes, J Hazard Mater 211–212 (2012) 30–46. https://doi.org/10.1016/J.JHAZMAT.2011.11.069.

[198] A. Heller, Conversion of Sunlight into Electrical Power and Photoassisted Electrolysis of Water in Photoelectrochemical Cells, Acc. Chem. Res 14 (1981) 154–162. https://pubs.acs.org/sharingguidelines (accessed July 23, 2024).

[199] P. Lianos, Review of recent trends in photoelectrocatalytic conversion of solar energy to electricity and hydrogen, Appl Catal B 210 (2017) 235–254. https://doi.org/10.1016/J.APCATB.2017.03.067.

[200] V. Kumaravel, J. Bartlett, S.C. Pillai, Photoelectrochemical Conversion of Carbon Dioxide (CO2) into Fuels and Value-Added Products, ACS Energy Lett (2020) 486–519. https://doi.org/10.1021/ACSENERGYLETT.9B02585

[201] J. Liu, L. Lu, D. Wood, S. Lin, New Redox Strategies in Organic Synthesis by Means of Electrochemistry and Photochemistry, ACS Cent Sci 6 (2020) 1317–1340. https://doi.org/10.1021/ACSCENTSCI.0C00549

[202] J. Li, N. Wu, Semiconductor-based photocatalysts and photoelectrochemical cells for solar fuel generation: a review, Catal Sci Technol 5 (2015) 1360–1384. https://doi.org/10.1039/C4CY00974F.

[203] K. Shankar, J.I. Basham, N.K. Allam, O.K. Varghese, G.K. Mor, X. Feng, M. Paulose, J.A. Seabold, K.S. Choi, C.A. Grimes, Recent advances In the use of TiO 2 nanotube and nanowire arrays for oxidative photoelectrochemistry, Journal of Physical Chemistry C 113 (2009) 6327–6359. https://doi.org/10.1021/JP809385X

[204] M.G. Walter, E.L. Warren, J.R. McKone, S.W. Boettcher, Q. Mi, E.A. Santori, N.S. Lewis, Solar water splitting cells, Chem Rev 110 (2010) 6446–6473. https://doi.org/10.1021/CR1002326

[205] S. Chen, L.W. Wang, Thermodynamic oxidation and reduction potentials of photocatalytic semiconductors in aqueous solution, Chemistry of Materials 24 (2012) 3659–3666. https://doi.org/10.1021/CM302533S/SUPPL_FILE/CM302533S_SI_001.PDF.

[206] A. Di Paola, M. Bellardita, L. Palmisano, Z. Barbieriková, V. Brezová, Influence of crystallinity and OH surface density on the photocatalytic activity of TiO_2 powders, J Photochem Photobiol A Chem Complete (2014) 59–67. https://doi.org/10.1016/J.JPHOTOCHEM.2013.09.008.

[207] Y. Wang, M. Zu, X. Zhou, H. Lin, F. Peng, S. Zhang, Designing efficient TiO_2-based photoelectrocatalysis systems for chemical engineering and sensing, Chemical Engineering Journal 381 (2020) 122605. https://doi.org/10.1016/J.CEJ.2019.122605.

[208] D. Kowalski, D. Kim, P. Schmuki, TiO_2 nanotubes, nanochannels and mesosponge: Self-organized formation and applications, Nano Today 8 (2013) 235–264. https://doi.org/10.1016/j.nantod.2013.04.010.

[209] X. Chen, S.S. Mao, Titanium dioxide nanomaterials: Synthesis, properties, modifications and applications, Chem Rev 107 (2007) 2891–2959. https://doi.org/10.1021/CR0500535.

[210] G. Ognibene, D.A. Cristaldi, R. Fiorenza, I. Blanco, G. Cicala, S. Scirè, M.E. Fragalà, Photoactivity of hierarchically nanostructured ZnO–PES fibre mats for water treatments, RSC Adv 6 (2016) 42778–42785. https://doi.org/10.1039/C6RA06854E.

[211] S.M. Wu, I. Hwang, B. Osuagwu, J. Will, Z. Wu, B.B. Sarma, F.F. Pu, L.Y. Wang, Z. Badura, G. Zoppellaro, E. Spiecker, P. Schmuki, Fluorine Aided Stabilization of Pt Single Atoms on TiO_2 Nanosheets and Strongly Enhanced Photocatalytic H_2 Evolution, ACS Catal 13 (2023) 33–41. https://doi.org/10.1021/ACSCATAL.2C04481

[212] H. Eidsvåg, S. Bentouba, P. Vajeeston, S. Yohi, D. Velauthapillai, TiO_2 as a Photocatalyst for Water Splitting—An Experimental and Theoretical Review, Molecules 26 (2021) 1687. https://doi.org/10.3390/molecules26061687.

[213] Y. Zhao, W. Chang, Z. Huang, X. Feng, L. Ma, X. Qi, Z. Li, Enhanced removal of toxic Cr(VI) in tannery wastewater by photoelectrocatalysis with synthetic TiO_2 hollow spheres, Appl Surf Sci 405 (2017) 102–110. https://doi.org/10.1016/J.APSUSC.2017.01.306.

[214] A.M. Djaballah, M. Bellardita, L. Palmisano, V. Loddo, M. Umair, C.M. Pecoraro, R. Bagtache, M. Trari, Facile preparation of $CuBi_2O_4/TiO_2$ hetero-systems employed for

simulated solar-light selective oxidation of 4-methoxybenzyl alcohol model compound, Molecular Catalysis 546 (2023) 113251. https://doi.org/10.1016/j.mcat.2023.113251.

[215] F. Di Quarto, F. Di Franco, A. Zaffora, M. Santamaria, Photocurrent Spectroscopy in Passivity Studies, Encyclopedia of Interfacial Chemistry: Surface Science and Electrochemistry (2018) 361–371. https://doi.org/10.1016/B978-0-12-409547-2.13578-4.

[216] Yu. V. Pleskov, Yu.Ya. Gurevich, Semiconductor Photoelectrochemistry, (1986). https://doi.org/10.1007/978-1-4684-9078-7.

[217] A. Zaffora, M. Santamaria, F. Di Franco, H. Habazaki, F. Di Quarto, Photoelectrochemical evidence of inhomogeneous composition at nm length scale of anodic films on valve metals alloys, Electrochim Acta 201 (2016) 333–339. https://doi.org/10.1016/J.ELECTACTA.2015.12.157.

[218] M. Umair, C.M. Pecoraro, F. Di Franco, M. Santamaria, L. Palmisano, V. Loddo, M. Bellardita, Efficient Photocatalytic Partial Oxidation of Aromatic Alcohols by Using ZnIn2S4 under Green Conditions, ChemSusChem (2024) e202400404. https://doi.org/10.1002/cssc.202400404.

[219] C.M. Pecoraro, M. Bellardita, V. Loddo, F. Di Franco, L. Palmisano, M. Santamaria, A facile way to synthesize noble metal free TiO_2 based catalysts for glycerol photoreforming, Journal of Industrial and Engineering Chemistry 118 (2023) 247–258. https://doi.org/10.1016/j.jiec.2022.11.010.

[220] C.M. Pecoraro, L. Mino, E. Kozyr, L. Palmisano, F. di Franco, V. Loddo, M. Santamaria, M. Bellardita, Pt–TiO_2 catalysts for glycerol photoreforming: comparison of anatase, brookite and rutile polymorphs, Chemical Communications 60 (2024) 3782–3785. https://doi.org/10.1039/D4CC00353E.

[221] C.M. Pecoraro, F. Di Franco, V. Loddo, M. Bellardita, M. Santamaria, Effect of Ph and Applied Bias on H_2 and HVA Products Through Photoelectrocatalytic Glycerol Oxidation, Chem Eng Trans 109 (2024) 283–288. https://doi.org/10.3303/CET24109048.

[222] C.M. Pecoraro, S. Wu, M. Santamaria, P. Schmuki, Bandgap Engineering of TiO_2 for Enhanced Selectivity in Photoelectrochemical Glycerol Oxidation, Adv Mater Interfaces (2024) 2400583. https://doi.org/10.1002/ADMI.202400583.

[223] C.M. Pecoraro, F. Di Franco, V. Loddo, M. Bellardita, M. Santamaria, Photoelectrolysis of glucose and fructose containing solution in PGM-free cells for hydrogen and valuable chemicals production, Int J Hydrogen Energy 87 (2024) 1277–1287. https://doi.org/10.1016/J.IJHYDENE.2024.09.124.

[224] S. Çetinkaya, G. Khamidov, L. Özcan, L. Palmisano, S. Yurdakal, Selective Photocatalytic Oxidation of Glycerol and 3-Pyridinemethanol by Nanotube/Nanowire-Structured TiO_2 Powders Obtained by Breakdown Anodization, Front Chem 10 (2022). https://doi.org/10.3389/fchem.2022.856947.

[225] J. Corredor, M.J. Rivero, C.M. Rangel, F. Gloaguen, I. Ortiz, Comprehensive review and future perspectives on the photocatalytic hydrogen production, Journal of Chemical Technology & Biotechnology 94 (2019) 3049–3063. https://doi.org/10.1002/jctb.6123.

[226] P.S. Kong, M.K. Aroua, W.M.A.W. Daud, Conversion of crude and pure glycerol into derivatives: A feasibility evaluation, Renewable and Sustainable Energy Reviews 63 (2016) 533–555. https://doi.org/10.1016/j.rser.2016.05.054.

[227] R. Ciriminna, A. Fidalgo, L.M. Ilharco, M. Pagliaro, Dihydroxyacetone: An Updated Insight into an Important Bioproduct, ChemistryOpen 7 (2018) 233–236. https://doi.org/10.1002/open.201700201.

[228] L. Luo, W. Chen, S.-M. Xu, J. Yang, M. Li, H. Zhou, M. Xu, M. Shao, X. Kong, Z. Li, H. Duan, Selective Photoelectrocatalytic Glycerol Oxidation to Dihydroxyacetone via Enhanced Middle Hydroxyl Adsorption over a Bi_2O_3 -Incorporated Catalyst, J Am Chem Soc 144 (2022) 7720–7730. https://doi.org/10.1021/jacs.2c00465.

[229] L. Fan, B. Liu, X. Liu, N. Senthilkumar, G. Wang, Z. Wen, Recent Progress in Electrocatalytic Glycerol Oxidation, Energy Technology 9 (2021) 2000804. https://doi.org/10.1002/ente.202000804.

[230] A.M. Verma, L. Laverdure, M.M. Melander, K. Honkala, Mechanistic Origins of the pH Dependency in Au-Catalyzed Glycerol Electro-oxidation: Insight from First-Principles Calculations, ACS Catal 12 (2022) 662–675. https://doi.org/10.1021/ACSCATAL.1C03788

[231] Y. Liu, M. Wang, B. Zhang, D. Yan, X. Xiang, Mediating the Oxidizing Capability of Surface-Bound Hydroxyl Radicals Produced by Photoelectrochemical Water Oxidation to Convert Glycerol into Dihydroxyacetone, ACS Catal 12 (2022) 6946–6957. https://doi.org/10.1021/ACSCATAL.2C01319

[232] Q. Guo, Z. Ma, C. Zhou, Z. Ren, X. Yang, Single Molecule Photocatalysis on TiO_2 Surfaces, Chem Rev 119 (2019) 11020–11041. https://doi.org/10.1021/acs.chemrev.9b00226.

[233] V. Kumaravel, S. Mathew, J. Bartlett, S.C. Pillai, Photocatalytic hydrogen production using metal doped TiO_2: A review of recent advances, Appl Catal B 244 (2019) 1021–1064. https://doi.org/10.1016/j.apcatb.2018.11.080.

[234] M. Bellardita, E.I. García-López, G. Marcì, G. Nasillo, L. Palmisano, Photocatalytic Solar Light H_2 Production by Aqueous Glucose Reforming, Eur J Inorg Chem 2018 (2018) 4522–4532. https://doi.org/10.1002/EJIC.201800663.

[235] Y.H. Chung, K. Han, C.Y. Lin, D. O'Neill, G. Mul, B. Mei, C.M. Yang, Photocatalytic hydrogen production by photo-reforming of methanol with one-pot synthesized Pt-containing TiO_2 photocatalysts, Catal Today 356 (2020) 95–100. https://doi.org/10.1016/j.cattod.2019.07.042.

[236] K.K. Mandari, J.Y. Do, S.V.P. Vattikuti, A.K.R. Police, M. Kang, Solar light response with noble metal-free highly active copper(II) phosphate/titanium dioxide nanoparticle/copper(II) oxide nanocomposites for photocatalytic hydrogen production, J Alloys Compd 750 (2018) 292–303. https://doi.org/10.1016/j.jallcom.2018.03.294.

[237] N.S. Gultom, H. Abdullah, D.H. Kuo, Enhanced photocatalytic hydrogen production of noble-metal free Ni-doped Zn(O,S) in ethanol solution, Int J Hydrogen Energy 42 (2017) 25891–25902. https://doi.org/10.1016/j.ijhydene.2017.08.198.

[238] S. ichiro Fujita, H. Kawamori, D. Honda, H. Yoshida, M. Arai, Photocatalytic hydrogen production from aqueous glycerol solution using NiO/TiO_2 catalysts: Effects of preparation and reaction conditions, Appl Catal B 181 (2016) 818–824. https://doi.org/10.1016/j.apcatb.2015.08.048.

[239] E. Wierzbicka, M. Altomare, M. Wu, N. Liu, T. Yokosawa, D. Fehn, S. Qin, K. Meyer, T. Unruh, E. Spiecker, L. Palmisano, M. Bellardita, J. Will, P. Schmuki, Reduced grey brookite for noble metal free photocatalytic H_2 evolution, J Mater Chem A Mater 9 (2021) 1168–1179. https://doi.org/10.1039/d0ta09066b.

[240] M. Muscetta, S. al Jitan, G. Palmisano, R. Andreozzi, R. Marotta, S. Cimino, I. di Somma, Visible light – driven photocatalytic hydrogen production using Cu_2O/TiO_2 composites prepared by facile mechanochemical synthesis, J Environ Chem Eng 10 (2022) 107735. https://doi.org/10.1016/j.jece.2022.107735.

[241] K.K. Mandari, J.Y. Do, S.V.P. Vattikuti, A.K.R. Police, M. Kang, Solar light response with noble metal-free highly active copper(II) phosphate/titanium dioxide nanoparticle/copper(II) oxide nanocomposites for photocatalytic hydrogen production, J Alloys Compd 750 (2018) 292–303. https://doi.org/10.1016/j.jallcom.2018.03.294.

[242] N.S. Gultom, H. Abdullah, D.-H. Kuo, Enhanced photocatalytic hydrogen production of noble-metal free Ni-doped Zn(O,S) in ethanol solution, Int J Hydrogen Energy 42 (2017) 25891–25902. https://doi.org/10.1016/j.ijhydene.2017.08.198.

[243] A.M. Mohammed, S.S. Mohtar, F. Aziz, S.A. Mhamad, M. Aziz, Review of various strategies to boost the photocatalytic activity of the cuprous oxide-based photocatalyst, J Environ Chem Eng 9 (2021). https://doi.org/10.1016/j.jece.2021.105138.

[244] J. Low, J. Yu, M. Jaroniec, S. Wageh, A.A. Al-Ghamdi J X Low, J.G. Yu, S. Wageh, A.A. Al-Ghamdi, M. Jaroniec, Heterojunction Photocatalysts, Advanced Materials 29 (2017) 1601694. https://doi.org/10.1002/ADMA.201601694.

[245] M.E. Aguirre, R. Zhou, A.J. Eugene, M.I. Guzman, M.A. Grela, Cu_2O/TiO_2 heterostructures for CO2 reduction through a direct Z-scheme: Protecting Cu2O from photocorrosion, Appl Catal B 217 (2017) 485–493. https://doi.org/10.1016/J.APCATB.2017.05.058.

[246] T. Wei, Y.N. Zhu, X. An, L.M. Liu, X. Cao, H. Liu, J. Qu, Defect Modulation of Z-Scheme TiO_2/Cu_2O Photocatalysts for Durable Water Splitting, ACS Catal 9 (2019) 8346–8354. https://doi.org/10.1021/ACSCATAL.9B01786

[247] K. Yang, G. Cheng, R. Chen, K. Zhao, Y. Liang, W. Li, C. Han, Simply Coupling TiO_2 Nanospheres with Cu2O Particles to Boost the Photocatalytic Hydrogen Evolution through p–n Heterojunction-Induced Charge Transfer, Energy Technology 10 (2022) 2100259. https://doi.org/10.1002/ENTE.202100259.

[248] M. Muscetta, R. Andreozzi, L. Clarizia, I. Di Somma, R. Marotta, Hydrogen production through photoreforming processes over Cu_2O/TiO_2 composite materials: A mini-review, Int J Hydrogen Energy 45 (2020) 28531–28552. https://doi.org/10.1016/J.IJHYDENE.2020.07.225.

[249] A.M. Mohammed, S.S. Mohtar, F. Aziz, S.A. Mhamad, M. Aziz, Review of various strategies to boost the photocatalytic activity of the cuprous oxide-based photocatalyst, J Environ Chem Eng 9 (2021) 105138. https://doi.org/10.1016/J.JECE.2021.105138.

[250] A. Petala, E. Ioannidou, A. Georgaka, K. Bourikas, D.I. Kondarides, Hysteresis phenomena and rate fluctuations under conditions of glycerol photo-reforming reaction over CuO_x/TiO_2 catalysts, Appl Catal B 178 (2015) 201–209. https://doi.org/10.1016/j.apcatb.2014.09.021.

[251] K. Sekar, C. Chuaicham, B. Vellaichamy, W. Li, W. Zhuang, X. Lu, B. Ohtani, K. Sasaki, Cubic Cu2O nanoparticles decorated on TiO_2 nanofiber heterostructure as an excellent synergistic photocatalyst for H_2 production and sulfamethoxazole degradation, Appl Catal B 294 (2021) 120221. https://doi.org/10.1016/J.APCATB.2021.120221.

[252] Y.H. Zhang, M.M. Liu, J.L. Chen, K.F. Xie, S.M. Fang, Dendritic branching Z-scheme Cu_2O/TiO_2 heterostructure photocatalysts for boosting H_2 production, Journal of Physics and Chemistry of Solids 152 (2021) 109948. https://doi.org/10.1016/J.JPCS.2021.109948.

[253] M. Jung, J.N. Hart, J. Scott, Y.H. Ng, Y. Jiang, R. Amal, Exploring Cu oxidation state on TiO_2 and its transformation during photocatalytic hydrogen evolution, Appl Catal A Gen 521 (2016) 190–201. https://doi.org/10.1016/J.APCATA.2015.11.013.

[254] M.O. Segovia-Guzmán, M. Román-Aguirre, J.Y. Verde-Gomez, V.H. Collins-Martínez, G. Zaragoza-Galán, V.H. Ramos-Sánchez, Green Cu_2O/TiO_2 heterojunction for glycerol photoreforming, Catal Today 349 (2020) 88–97. https://doi.org/10.1016/J.CATTOD.2018.05.031.

[255] M. Jung, J.N. Hart, D. Boensch, J. Scott, Y.H. Ng, R. Amal, Hydrogen evolution via glycerol photoreforming over Cu–Pt nanoalloys on TiO_2, Appl Catal A Gen 518 (2016) 221–230. https://doi.org/10.1016/J.APCATA.2015.10.040.

[256] J. Martín-Gómez, J. Hidalgo-Carrillo, V. Montes, R.C. Estévez-Toledano, J.C. Escamilla, A. Marinas, F.J. Urbano, EPR and CV studies cast further light on the origin of the enhanced hydrogen production through glycerol photoreforming on CuO:TiO_2 physical mixtures, J Environ Chem Eng 9 (2021) 105336. https://doi.org/10.1016/J.JECE.2021.105336.

[257] J.L. Chen, M.M. Liu, S.Y. Xie, L.J. Yue, F.L. Gong, K.M. Chai, Y.H. Zhang, Cu2O-loaded TiO_2 heterojunction composites for enhanced photocatalytic H_2 production, J Mol Struct 1247 (2022) 131294. https://doi.org/10.1016/J.MOLSTRUC.2021.131294.

[258] F. Parrino, S.F. Corsino, M. Bellardita, V. Loddo, L. Palmisano, M. Torregrossa, G. Viviani, Sequential biological and photocatalysis based treatments for shipboard slop purification: A pilot plant investigation, Process Safety and Environmental Protection 125 (2019) 288–296. https://doi.org/10.1016/j.psep.2019.03.025.

[259] R. Fiorenza, M. Bellardita, T. Barakat, S. Scirè, L. Palmisano, Visible light photocatalytic activity of macro-mesoporous TiO 2 -CeO 2 inverse opals, J Photochem Photobiol A Chem 352 (2018) 25–34. https://doi.org/10.1016/j.jphotochem.2017.10.052.

[260] R. Fiorenza, M. Bellardita, S. Scirè, L. Palmisano, Photocatalytic H_2 production over inverse opal TiO_2 catalysts, Catal Today 321–322 (2019) 113–119. https://doi.org/10.1016/J.CATTOD.2017.12.011.

[261] Z.H.N. Al-Azri, V. Jovic, W.T. Chen, D. Sun-Waterhouse, J.B. Metson, G.I.N. Waterhouse, Performance evaluation of Pd/TiO_2 and Pt/TiO_2 photocatalysts for hydrogen production from ethanol-water mixtures, Int J Nanotechnol 11 (2014) 695–703. https://doi.org/10.1504/IJNT.2014.060592.

[262] F.J. López-Tenllado, J. Hidalgo-Carrillo, V. Montes, A. Marinas, F.J. Urbano, J.M. Marinas, L. Ilieva, T. Tabakova, F. Reid, A comparative study of hydrogen photocatalytic production

from glycerol and propan-2-ol on M/TiO_2 systems (M=Au, Pt, Pd), Catal Today 280 (2017) 58–64. https://doi.org/10.1016/J.CATTOD.2016.05.009.

[263] V. Augugliaro, H.A.H. el Nazer, V. Loddo, A. Mele, G. Palmisano, L. Palmisano, S. Yurdakal, Partial photocatalytic oxidation of glycerol in TiO_2 water suspensions, Catal Today 151 (2010) 21–28. https://doi.org/10.1016/j.cattod.2010.01.022.

[264] M. Bellardita, D. Virtù, F. di Franco, V. Loddo, L. Palmisano, M. Santamaria, Heterogeneous photocatalytic aqueous succinic acid formation from maleic acid reduction, Chemical Engineering Journal 431 (2022). https://doi.org/10.1016/j.cej.2021.134131.

[265] D. Reyes-Coronado, G. Rodríguez-Gattorno, M.E. Espinosa-Pesqueira, C. Cab, R. de Coss, G. Oskam, Phase-pure TiO 2 nanoparticles: anatase, brookite and rutile, Nanotechnology 19 (2008) 145605. https://doi.org/10.1088/0957-4484/19/14/145605.

[266] J. Zhu, Z. Deng, F. Chen, J. Zhang, H. Chen, M. Anpo, J. Huang, L. Zhang, Hydrothermal doping method for preparation of Cr3+-TiO 2 photocatalysts with concentration gradient distribution of Cr 3+, Appl Catal B 62 (2006) 329–335. https://doi.org/10.1016/j.apcatb.2005.08.013.

[267] R. Fiorenza, M. Bellardita, S. Scirè, L. Palmisano, Effect of the addition of different doping agents on visible light activity of porous TiO_2 photocatalysts, Molecular Catalysis 455 (2018) 108–120. https://doi.org/10.1016/j.mcat.2018.06.002.

[268] C.-M. Wang, C.-Y. Wang, Photocorrosion of plasmonic enhanced Cu x O photocatalyst, (2014). https://doi.org/10.1117/1.

[269] K. Phiwdang, S. Suphankij, W. Mekprasart, W. Pecharapa, Synthesis of CuO Nanoparticles by Precipitation Method Using Different Precursors, Energy Procedia 34 (2013) 740–745. https://doi.org/10.1016/j.egypro.2013.06.808.

[270] Md.J. Nine, B. Munkhbayar, M.Sq. Rahman, H. Chung, H. Jeong, Highly productive synthesis process of well dispersed Cu2O and Cu/Cu2O nanoparticles and its thermal characterization, Mater Chem Phys 141 (2013) 636–642. https://doi.org/10.1016/j.matchemphys.2013.05.032.

[271] U. Balachandran, N.G. Eror, Raman spectra of titanium dioxide, J Solid State Chem 42 (1982) 276–282. https://doi.org/10.1016/0022-4596(82)90006-8.

[272] K. Yang, G. Cheng, R. Chen, K. Zhao, Y. Liang, W. Li, C. Han, Simply Coupling TiO_2 Nanospheres with Cu2O Particles to Boost the Photocatalytic Hydrogen Evolution through p–n Heterojunction-Induced Charge Transfer, Energy Technology 10 (2022). https://doi.org/10.1002/ente.202100259.

[273] J.L. Chen, M.M. Liu, S.Y. Xie, L.J. Yue, F.L. Gong, K.M. Chai, Y.H. Zhang, Cu2O-loaded TiO_2 heterojunction composites for enhanced photocatalytic H_2 production, J Mol Struct 1247 (2022). https://doi.org/10.1016/j.molstruc.2021.131294.

[274] R. Fiorenza, M. Bellardita, S. Scirè, L. Palmisano, Photocatalytic H_2 production over inverse opal TiO_2 catalysts, Catal Today (2019) 113–119. https://doi.org/10.1016/j.cattod.2017.12.011.

[275] G.G. Lenzi, C.V.B. Fávero, L.M.S. Colpini, H. Bernabe, M.L. Baesso, S. Specchia, O.A.A. Santos, Photocatalytic reduction of Hg(II) on TiO_2 and Ag/TiO_2 prepared by the sol–gel and impregnation methods, Desalination 270 (2011) 241–247. https://doi.org/10.1016/J.DESAL.2010.11.051.

[276] H. Adamu, A.J. McCue, R.S.F. Taylor, H.G. Manyar, J.A. Anderson, Simultaneous photocatalytic removal of nitrate and oxalic acid over Cu_2O/TiO_2 and Cu_2O/TiO_2-AC composites, Appl Catal B 217 (2017) 181–191. https://doi.org/10.1016/J.APCATB.2017.05.091.

[277] F. Boccuzzi, A. Chiorino, G. Martra, M. Gargano, N. Ravasio, B. Carrozzini, Preparation, Characterization, and Activity of Cu/TiO_2Catalysts. I. Influence of the Preparation Method on the Dispersion of Copper in Cu/TiO_2, J Catal 165 (1997) 129–139. https://doi.org/10.1006/JCAT.1997.1475.

[278] P.A. Bharad, A. V. Nikam, F. Thomas, C.S. Gopinath, CuO_x-TiO_2 Composites: Electronically Integrated Nanocomposites for Solar Hydrogen Generation, ChemistrySelect 3 (2018) 12022–12030. https://doi.org/10.1002/SLCT.201802047.

[279] N.D. Abazović, M.I. Čomor, M.D. Dramićanin, D.J. Jovanović, S.P. Ahrenkiel, J.M. Nedeljković, Photoluminescence of anatase and rutile TiO_2 particles, Journal of Physical Chemistry B 110 (2006) 25366–25370. https://doi.org/10.1021/JP064454F.

[280] J. Bandara, C.P.K. Udawatta, C.S.K. Rajapakse, Highly stable CuO incorporated TiO_2 catalyst for photocatalytic hydrogen production from H_2O, Photochemical & Photobiological Sciences 2005 4:11 4 (2005) 857–861. https://doi.org/10.1039/B507816D.

[281] J. Yu, Y. Hai, M. Jaroniec, Photocatalytic hydrogen production over CuO-modified titania, J Colloid Interface Sci 357 (2011) 223–228. https://doi.org/10.1016/J.JCIS.2011.01.101.

[282] M. Tavakolian, K. Keshavarz, M. Hosseini-Sarvari, Cu_2O/TiO_2 as a sustainable and recyclable photocatalyst for gram-scale synthesis of phenols in water, Molecular Catalysis 514 (2021) 111810. https://doi.org/10.1016/J.MCAT.2021.111810.

[283] M. Bellardita, E.I. García-López, G. Marcì, G. Nasillo, L. Palmisano, Photocatalytic Solar Light H $_2$ Production by Aqueous Glucose Reforming, Eur J Inorg Chem 2018 (2018) 4522–4532. https://doi.org/10.1002/ejic.201800663.

[284] M. Muscetta, S. Al Jitan, G. Palmisano, R. Andreozzi, R. Marotta, S. Cimino, I. Di Somma, Visible light – driven photocatalytic hydrogen production using Cu_2O/TiO_2 composites prepared by facile mechanochemical synthesis, J Environ Chem Eng 10 (2022) 107735. https://doi.org/10.1016/J.JECE.2022.107735.

[285] Z. Xi, C. Li, L. Zhang, M. Xing, J. Zhang, Synergistic effect of Cu_2O/TiO_2 heterostructure nanoparticle and its high H_2 evolution activity, Int J Hydrogen Energy 39 (2014) 6345–6353. https://doi.org/10.1016/J.IJHYDENE.2014.01.209.

[286] J. Duan, H. Zhao, Z. Zhang, W. Wang, The Z-scheme heterojunction between TiO_2 nanotubes and Cu2O nanoparticles mediated by Ag nanoparticles for enhanced photocatalytic stability and activity under visible light, Ceram Int 44 (2018) 22748–22759. https://doi.org/10.1016/J.CERAMINT.2018.09.062.

[287] S. Lv, Y. Wang, Y. Zhou, Q. Liu, C. Song, D. Wang, Oxygen vacancy stimulated direct Z-scheme of mesoporous Cu_2O/TiO_2 for enhanced photocatalytic hydrogen production from water and seawater, J Alloys Compd 868 (2021) 159144. https://doi.org/10.1016/J.JALLCOM.2021.159144.

[288] M. Jung, J.N. Hart, D. Boensch, J. Scott, Y.H. Ng, R. Amal, Hydrogen evolution via glycerol photoreforming over Cu–Pt nanoalloys on TiO_2, Appl Catal A Gen 518 (2016) 221–230. https://doi.org/10.1016/J.APCATA.2015.10.040.

[289] C.K. Nuo Peh, X.-Q. Wang, G.W. Ho, Increased photocatalytic activity of CuO/TiO_2 through broadband solar absorption heating under natural sunlight, Procedia Eng 215 (2017) 171–179. https://doi.org/10.1016/J.PROENG.2017.11.006.

[290] Y. Li, B. Wang, S. Liu, X. Duan, Z. Hu, Synthesis and characterization of Cu_2O/TiO_2 photocatalysts for H_2 evolution from aqueous solution with different scavengers, Appl Surf Sci 324 (2015) 736–744. https://doi.org/10.1016/J.APSUSC.2014.11.027.

[291] M. Zhang, T. Chen, Y. Wang, Insights into TiO_2 polymorphs: highly selective synthesis, phase transition, and their polymorph-dependent properties, RSC Adv 7 (2017) 52755–52761. https://doi.org/10.1039/C7RA11515F.

[292] A. Di Paola, G. Cufalo, M. Addamo, M. Bellardita, R. Campostrini, M. Ischia, R. Ceccato, L. Palmisano, Photocatalytic activity of nanocrystalline TiO_2 (brookite, rutile and brookite-based) powders prepared by thermohydrolysis of $TiCl_4$ in aqueous chloride solutions, Colloids Surf

A Physicochem Eng Asp 317 (2008) 366–376. https://doi.org/10.1016/J.COLSURFA.2007.11.005.

[293] C. Günnemann, C. Haisch, M. Fleisch, J. Schneider, A. V. Emeline, D.W. Bahnemann, Insights into Different Photocatalytic Oxidation Activities of Anatase, Brookite, and Rutile Single-Crystal Facets, ACS Catal 9 (2019) 1001–1012. https://doi.org/10.1021/ACSCATAL.8B04115

[294] L. Mino, G. Spoto, S. Bordiga, A. Zecchina, Rutile surface properties beyond the single crystal approach: New insights from the experimental investigation of different polycrystalline samples and periodic DFT calculations, Journal of Physical Chemistry C 117 (2013) 11186–11196. https://doi.org/10.1021/JP401916Q/SUPPL_FILE/JP401916Q_SI_001.PDF.

[295] M. Bellardita, M. Feilizadeh, R. Fiorenza, S. Scirè, L. Palmisano, V. Loddo, Selective aqueous oxidation of aromatic alcohols under solar light in the presence of TiO_2 modified with different metal species, Photochemical and Photobiological Sciences 21 (2022) 2139–2151. https://doi.org/10.1007/S43630-022-00284-2

[296] Z. Li, S. Cong, Y. Xu, Brookite vs anatase TiO_2 in the photocatalytic activity for organic degradation in water, ACS Catal 4 (2014) 3273–3280. https://doi.org/10.1021/CS500785Z

[297] F. Pellegrino, F. Sordello, L. Mino, C. Minero, V.D. Hodoroaba, G. Martra, V. Maurino, Formic Acid Photoreforming for Hydrogen Production on Shape-Controlled Anatase TiO_2 Nanoparticles: Assessment of the Role of Fluorides, {101}/{001} Surfaces Ratio, and Platinization, ACS Catal 9 (2019) 6692–6697. https://doi.org/10.1021/ACSCATAL.9B01861

[298] L. Mino, A. Zecchina, G. Martra, A.M. Rossi, G. Spoto, A surface science approach to TiO_2 P25 photocatalysis: An in situ FTIR study of phenol photodegradation at controlled water coverages from sub-monolayer to multilayer, Appl Catal B 196 (2016) 135–141. https://doi.org/10.1016/J.APCATB.2016.05.029.

[299] J.G. Li, T. Ishigaki, X. Sun, Anatase, brookite, and rutile nanocrystals via redox reactions under mild hydrothermal conditions: Phase-selective synthesis and physicochemical properties, Journal of Physical Chemistry C 111 (2007) 4969–4976. https://doi.org/10.1021/JP0673258.

[300] E. Wierzbicka, M. Altomare, M. Wu, N. Liu, T. Yokosawa, D. Fehn, S. Qin, K. Meyer, T. Unruh, E. Spiecker, L. Palmisano, M. Bellardita, J. Will, P. Schmuki, Reduced grey brookite for noble metal free photocatalytic H_2 evolution, J Mater Chem A Mater 9 (2021) 1168–1179. https://doi.org/10.1039/D0TA09066B.

[301] R. Kaplan, B. Erjavec, G. Dražić, J. Grdadolnik, A. Pintar, Simple synthesis of anatase/rutile/brookite TiO_2 nanocomposite with superior mineralization potential for

photocatalytic degradation of water pollutants, Appl Catal B 181 (2016) 465–474. https://doi.org/10.1016/J.APCATB.2015.08.027.

[302] L. Jing, S. Li, S. Song, L. Xue, H. Fu, Investigation on the electron transfer between anatase and rutile in nano-sized TiO_2 by means of surface photovoltage technique and its effects on the photocatalytic activity, Solar Energy Materials and Solar Cells 92 (2008) 1030–1036. https://doi.org/10.1016/J.SOLMAT.2008.03.003.

[303] M. Addamo, V. Augugliaro, M. Bellardita, A. Di Paola, V. Loddo, G. Palmisano, L. Palmisano, S. Yurdakal, Environmentally friendly photocatalytic oxidation of aromatic alcohol to aldehyde in aqueous suspension of brookite TiO_2, Catal Letters 126 (2008) 58–62. https://doi.org/10.1007/S10562-008-9596-0/FIGURES/3.

[304] M.R. Karimi Estahbanati, M. Feilizadeh, F. Attar, M.C. Iliuta, Current developments and future trends in photocatalytic glycerol valorization: process analysis, React Chem Eng 6 (2021) 197–219. https://doi.org/10.1039/D0RE00382D.

[305] S. ichiro Fujita, H. Kawamori, D. Honda, H. Yoshida, M. Arai, Photocatalytic hydrogen production from aqueous glycerol solution using NiO/TiO_2 catalysts: Effects of preparation and reaction conditions, Appl Catal B 181 (2016) 818–824. https://doi.org/10.1016/J.APCATB.2015.08.048.

[306] A. Di Paola, M. Addamo, M. Bellardita, E. Cazzanelli, L. Palmisano, Preparation of photocatalytic brookite thin films, Thin Solid Films 515 (2007) 3527–3529. https://doi.org/10.1016/J.TSF.2006.10.114.

[307] M. Monai, T. Montini, P. Fornasiero, Brookite: Nothing New under the Sun?, Catalysts 2017, Vol. 7, Page 304 7 (2017) 304. https://doi.org/10.3390/CATAL7100304.

[308] L. Mino, F. Pellegrino, S. Rades, J. Radnik, V.D. Hodoroaba, G. Spoto, V. Maurino, G. Martra, Beyond Shape Engineering of TiO_2 Nanoparticles: Post-Synthesis Treatment Dependence of Surface Hydration, Hydroxylation, Lewis Acidity and Photocatalytic Activity of TiO_2 Anatase Nanoparticles with Dominant {001} or {101} Facets, ACS Appl Nano Mater 1 (2018) 5355–5365. https://doi.org/10.1021/ACSANM.8B01477

[309] G. Iervolino, V. Vaiano, J.J. Murcia, A.E. Lara, J.S. Hernández, H. Rojas, J.A. Navío, M.C. Hidalgo, Photocatalytic production of hydrogen and methane from glycerol reforming over $Pt/TiO_2–Nb_2O_5$, Int J Hydrogen Energy 46 (2021) 38678–38691. https://doi.org/10.1016/J.IJHYDENE.2021.09.111.

[310] R. Chong, J. Li, X. Zhou, Y. Ma, J. Yang, L. Huang, H. Han, F. Zhang, C. Li, Selective photocatalytic conversion of glycerol to hydroxyacetaldehyde in aqueous solution on facet

tuned TiO_2-based catalysts, Chemical Communications 50 (2013) 165–167. https://doi.org/10.1039/C3CC46515B.

[311] V. Augugliaro, H.A.H. El Nazer, V. Loddo, A. Mele, G. Palmisano, L. Palmisano, S. Yurdakal, Partial photocatalytic oxidation of glycerol in TiO_2 water suspensions, Catal Today 151 (2010) 21–28. https://doi.org/10.1016/J.CATTOD.2010.01.022.

[312] Slamet, D. Tristantini, Valentina, M. Ibadurrohman, Photocatalytic hydrogen production from glycerol–water mixture over Pt-N-TiO_2 nanotube photocatalyst, Int J Energy Res 37 (2013) 1372–1381. https://doi.org/10.1002/ER.2939.

[313] U. Nwosu, A. Wang, B. Palma, H. Zhao, M.A. Khan, M. Kibria, J. Hu, Selective biomass photoreforming for valuable chemicals and fuels: A critical review, Renewable and Sustainable Energy Reviews 148 (2021) 111266. https://doi.org/10.1016/J.RSER.2021.111266.

[314] Y. Wang, L. Mino, F. Pellegrino, N. Homs, P. Ramírez de la Piscina, Engineered Mo_xC/TiO_2 interfaces for efficient noble metal-free photocatalytic hydrogen production, Appl Catal B 318 (2022) 121783. https://doi.org/10.1016/J.APCATB.2022.121783.

[315] G. Iervolino, V. Vaiano, G. Pepe, P. Campiglia, V. Palma, Degradation of Acid Orange 7 Azo Dye in Aqueous Solution by a Catalytic-Assisted, Non-Thermal Plasma Process, Catalysts 10 (2020) 888. https://doi.org/10.3390/catal10080888.

[316] M. Yasuda, T. Matsumoto, T. Yamashita, Sacrificial hydrogen production over TiO_2-based photocatalysts: Polyols, carboxylic acids, and saccharides, Renewable and Sustainable Energy Reviews 81 (2018) 1627–1635. https://doi.org/10.1016/J.RSER.2017.05.243.

[317] M. Falk, The frequency of the H□O□H bending fundamental in solids and liquids, Spectrochim Acta A 40 (1984) 43–48. https://doi.org/10.1016/0584-8539(84)80027-6.

[318] L. Mino, Á. Morales-García, S.T. Bromley, F. Illas, Understanding the nature and location of hydroxyl groups on hydrated titania nanoparticles, Nanoscale 13 (2021) 6577–6585. https://doi.org/10.1039/D1NR00610J.

[319] L. Mino, C. Negri, R. Santalucia, G. Cerrato, G. Spoto, G. Martra, Morphology, Surface Structure and Water Adsorption Properties of TiO_2 Nanoparticles: A Comparison of Different Commercial Samples, Molecules 2020, Vol. 25, Page 4605 25 (2020) 4605. https://doi.org/10.3390/MOLECULES25204605.

[320] M. Bellardita, A. Di Paola, L. Palmisano, F. Parrino, G. Buscarino, R. Amadelli, Preparation and photoactivity of samarium loaded anatase, brookite and rutile catalysts, Appl Catal B 104 (2011) 291–299. https://doi.org/10.1016/J.APCATB.2011.03.016.

[321] L. Mino, G. Spoto, S. Bordiga, A. Zecchina, Particles morphology and surface properties as investigated by HRTEM, FTIR, and periodic DFT calculations: From pyrogenic TiO 2 (P25) to nanoanatase, Journal of Physical Chemistry C 116 (2012) 17008–17018. https://doi.org/10.1021/JP303942H/SUPPL_FILE/JP303942H_SI_001.PDF.

[322] S. Pantaleone, F. Pellegrino, V. Maurino, M. Corno, P. Ugliengo, L. Mino, Disclosing the true atomic structure of {001} facets in shape-engineered TiO 2 anatase nanoparticles, J Mater Chem A Mater 12 (2024) 4325–4332. https://doi.org/10.1039/D3TA06694K.

[323] K.I. Hadjiivanov, IR study of CO and H 2 O coadsorption on Pt n+ /TiO 2 and Pt/TiO 2 samples, Journal of the Chemical Society, Faraday Transactions 94 (1998) 1901–1904. https://doi.org/10.1039/A801892H.

[324] L. Lan, H. Daly, Y. Jiao, Y. Yan, C. Hardacre, X. Fan, Comparative study of the effect of TiO_2 support composition and Pt loading on the performance of Pt/TiO_2 photocatalysts for catalytic photoreforming of cellulose, Int J Hydrogen Energy 46 (2021) 31054–31066. https://doi.org/10.1016/J.IJHYDENE.2021.06.043.

[325] R.M. Navarro, J. Arenales, F. Vaquero, I.D. González, J.L.G. Fierro, The effect of Pt characteristics on the photoactivity of Pt/TiO_2 for hydrogen production from ethanol, Catal Today 210 (2013) 33–38. https://doi.org/10.1016/J.CATTOD.2013.01.006.

[326] M. Carosso, T. Fovanna, A. Ricchebuono, E. Vottero, M. Manzoli, S. Morandi, R. Pellegrini, A. Piovano, D. Ferri, E. Groppo, Gas phase vs. liquid phase: monitoring H_2 and CO adsorption phenomena on Pt/Al_2O_3 by IR spectroscopy, Catal Sci Technol 12 (2022) 1359–1367. https://doi.org/10.1039/D1CY02233D.

[327] H.V. Thang, G. Pacchioni, L. DeRita, P. Christopher, Nature of stable single atom Pt catalysts dispersed on anatase TiO_2, J Catal 367 (2018) 104–114. https://doi.org/10.1016/J.JCAT.2018.08.025.

[328] M. Bowker, H. Bahruji, J. Kennedy, W. Jones, G. Hartley, C. Morton, The photocatalytic window: Photo-reforming of organics and water splitting for sustainable hydrogen production, Catal Letters 145 (2015) 214–219. https://doi.org/10.1007/S10562-014-1443-X/FIGURES/8.

[329] H. Ahmad, S.K. Kamarudin, L.J. Minggu, M. Kassim, Hydrogen from photo-catalytic water splitting process: A review, Renewable and Sustainable Energy Reviews 43 (2015) 599–610. https://doi.org/10.1016/J.RSER.2014.10.101.

[330] M. Bellardita, V. Loddo, L. Palmisano, Formation of High Added Value Chemicals by Photocatalytic Treatment of Biomass, Mini Rev Org Chem 17 (2020) 884–901. https://doi.org/10.2174/1570193X17666200131112856.

[331] G. Han, Y.H. Jin, R.A. Burgess, N.E. Dickenson, X.M. Cao, Y. Sun, Visible-Light-Driven Valorization of Biomass Intermediates Integrated with H_2 Production Catalyzed by Ultrathin Ni/CdS Nanosheets, J Am Chem Soc 139 (2017) 15584–15587. https://doi.org/10.1021/JACS.7B08657/SUPPL_FILE/JA7B08657_SI_001.PDF.

[332] Z. Fang, P. Zhang, M. Wang, F. Li, X. Wu, K. Fan, L. Sun, Selective Electro-oxidation of Alcohols to the Corresponding Aldehydes in Aqueous Solution via Cu(III) Intermediates from CuO Nanorods, ACS Sustain Chem Eng 9 (2021) 11855–11861. https://doi.org/10.1021/acssuschemeng.1c03691.

[333] X. Li, J. Hu, T. Yang, X. Yang, J. Qu, C.M. Li, Efficient photocatalytic H_2-evolution coupled with valuable furfural-production on exquisite 2D/2D $LaVO_4$/g-C_3N_4 heterostructure, Nano Energy 92 (2022) 106714. https://doi.org/10.1016/j.nanoen.2021.106714.

[334] H. Wang, Y. Song, J. Xiong, J. Bi, L. Li, Y. Yu, S. Liang, L. Wu, Highly selective oxidation of furfuryl alcohol over monolayer titanate nanosheet under visible light irradiation, Appl Catal B 224 (2018) 394–403. https://doi.org/10.1016/j.apcatb.2017.10.069.

[335] S. Dhingra, M. Sharma, V. Krishnan, C.M. Nagaraja, Design of noble metal-free CoTiO3/Zn0.5Cd0.5S heterostructure photocatalyst for selective synthesis of furfuraldehyde combined with H_2 production, J Colloid Interface Sci 608 (2022) 1040–1050. https://doi.org/10.1016/J.JCIS.2021.10.031.

[336] C.-L. Tan, M.-Y. Qi, Z.-R. Tang, Y.-J. Xu, Cocatalyst decorated ZnIn2S4 composites for cooperative alcohol conversion and H_2 evolution, Appl Catal B 298 (2021) 120541. https://doi.org/10.1016/j.apcatb.2021.120541.

[337] S. Huang, B. Gong, Y. Jin, P.H.L. Sit, J.C.H. Lam, The Structural Phase Effect of MoS2 in Controlling the Reaction Selectivity between Electrocatalytic Hydrogenation and Dimerization of Furfural, ACS Catal 12 (2022) 11340–11354. https://doi.org/10.1021/ACSCATAL.2C02137

[338] J. Zhang, D. Mao, D. Wu, Industrially Applicable Aqueous-Phase Selective Hydrogenation of Furfural on an Efficient TiOx-Modified Ni Nanocatalyst, ACS Sustain Chem Eng 9 (2021) 13902–13914. https://doi.org/10.1021/ACSSUSCHEMENG.1C05098

[339] W. Tolek, N. Nanthasanti, B. Pongthawornsakun, P. Praserthdam, J. Panpranot, Effects of TiO_2 structure and Co addition as a second metal on Ru-based catalysts supported on TiO_2 for selective hydrogenation of furfural to FA, Scientific Reports 2021 11:1 11 (2021) 1–14. https://doi.org/10.1038/s41598-021-89082-x.

[340] X. Chen, L. Zhang, B. Zhang, X. Guo, X. Mu, Highly selective hydrogenation of furfural to furfuryl alcohol over Pt nanoparticles supported on g-C3N4 nanosheets catalysts in water, Scientific Reports 2016 6:1 6 (2016) 1–13. https://doi.org/10.1038/srep28558.

[341] D.I. Kondarides, V.M. Daskalaki, A. Patsoura, X.E. Verykios, Hydrogen Production by Photo-Induced Reforming of Biomass Components and Derivatives at Ambient Conditions, Catal Letters 122 (2008) 26–32. https://doi.org/10.1007/s10562-007-9330-3.

[342] J.C. Colmenares, A. Magdziarz, M.A. Aramendia, A. Marinas, J.M. Marinas, F.J. Urbano, J.A. Navio, Influence of the strong metal support interaction effect (SMSI) of Pt/TiO_2 and Pd/TiO_2 systems in the photocatalytic biohydrogen production from glucose solution, Catal Commun 16 (2011) 1–6. https://doi.org/10.1016/J.CATCOM.2011.09.003.

[343] H.C. Yang, H.Y. Lin, Y.S. Chien, J.C.S. Wu, H.H. Wu, Mesoporous TiO_2/SBA-15, and Cu/TiO_2/SBA-15 composite photocatalysts for photoreduction of CO2 to methanol, Catal Letters 131 (2009) 381–387. https://doi.org/10.1007/S10562-009-0076-Y

[344] J. Yan, G. Wu, N. Guan, L. Li, Nb_2O_5/TiO_2 heterojunctions: Synthesis strategy and photocatalytic activity, Appl Catal B 152–153 (2014) 280–288. https://doi.org/10.1016/J.APCATB.2014.01.049.

[345] A. Di Paola, M. Bellardita, B. Megna, F. Parrino, L. Palmisano, Photocatalytic oxidation of trans-ferulic acid to vanillin on TiO_2 and WO_3-loaded TiO_2 catalysts, Catal Today 252 (2015) 195–200. https://doi.org/10.1016/J.CATTOD.2014.09.012.

[346] M. Santamaria, G. Conigliaro, F. Di Franco, F. Di Quarto, Photoelectrochemical Evidence of Cu_2O/TiO_2 Nanotubes Hetero-Junctions formation and their Physicochemical Characterization, Electrochim Acta 144 (2014) 315–323. https://doi.org/10.1016/j.electacta.2014.07.154.

[347] L. Palmisano, V. Augugliaro, M. Bellardita, A. Di Paola, E. García López, V. Loddo, G. Marcì, G. Palmisano, S. Yurdakal, Titania Photocatalysts for Selective Oxidations in Water, ChemSusChem 4 (2011) 1431–1438. https://doi.org/10.1002/CSSC.201100196.

[348] S. Yurdakal, G. Palmisano, V. Loddo, V. Augugliaro, L. Palmisano, Nanostructured rutile TiO_2 for selective photocatalytic oxidation of aromatic alcohols to aldehydes in water, J Am Chem Soc 130 (2008) 1568–1569. https://doi.org/10.1021/JA709989E/

[349] V. Augugliaro, T. Caronna, V. Loddo, G. Marcì, G. Palmisano, L. Palmisano, S. Yurdakal, Oxidation of Aromatic Alcohols in Irradiated Aqueous Suspensions of Commercial and Home-Prepared Rutile TiO_2: A Selectivity Study, Chemistry – A European Journal 14 (2008) 4640–4646. https://doi.org/10.1002/CHEM.200702044.

[350] M. Bellardita, A. Di Paola, E. García-López, V. Loddo, G. Marcì, L. Palmisano, Photocatalytic CO2 Reduction in Gas-Solid Regime in the Presence of Bare, SiO2 Supported or Cu-Loaded TiO_2 Samples, Curr Org Chem 17 (2013) 2440–2448. https://doi.org/10.2174/13852728113179990057.

[351] J. Kou, C. Lu, J. Wang, Y. Chen, Z. Xu, R.S. Varma, Selectivity Enhancement in Heterogeneous Photocatalytic Transformations, Chem Rev 117 (2017) 1445–1514. https://doi.org/10.1021/ACS.CHEMREV.6B00396

[352] F. Parrino, M. Bellardita, E.I. García-López, G. Marcì, V. Loddo, L. Palmisano, Heterogeneous Photocatalysis for Selective Formation of High-Value-Added Molecules: Some Chemical and Engineering Aspects, ACS Catal 8 (2018) 11191–11225. https://doi.org/10.1021/ACSCATAL.8B03093

[353] R. Chong, J. Li, Y. Ma, B. Zhang, H. Han, C. Li, Selective conversion of aqueous glucose to value-added sugar aldose on TiO_2-based photocatalysts, J Catal 314 (2014) 101–108. https://doi.org/10.1016/J.JCAT.2014.03.009.

[354] K. Su, H. Liu, Z. Gao, P. Fornasiero, F. Wang, Nb2O5-Based Photocatalysts, Advanced Science 8 (2021) 2003156. https://doi.org/10.1002/ADVS.202003156.

[355] J. Araña, C. Fernández Rodríguez, O. González Díaz, J.A. Herrera Melián, J. Pérez Peña, Role of Cu in the Cu-TiO_2 photocatalytic degradation of dihydroxybenzenes, Catal Today 101 (2005) 261–266. https://doi.org/10.1016/J.CATTOD.2005.03.006.

[356] M. Santamaria, G. Conigliaro, F. Di Franco, B. Megna, F. Di Quarto, Electronic Properties of Thermal Oxides on Ti and Their Influence on Impedance and Photoelectrochemical Behavior of TiO_2 Nanotubes, J Electrochem Soc 164 (2017) C113–C120. https://doi.org/10.1149/2.0601704jes.

[357] S.P. Albu, H. Tsuchiya, S. Fujimoto, P. Schmuki, TiO_2 Nanotubes – Annealing Effects on Detailed Morphology and Structure, Eur J Inorg Chem 2010 (2010) 4351–4356. https://doi.org/10.1002/ejic.201000608.

[358] M. Hunsom, P. Saila, Product Distribution of Electrochemical Conversion of Glycerol via Pt Electrode: Effect of Initial pH, Int. J. Electrochem. Sci 8 (2013) 11288–11300. www.electrochemsci.org (accessed December 15, 2023).

[359] M.R. Karimi Estahbanati, N. Mahinpey, M. Feilizadeh, F. Attar, M.C. Iliuta, Kinetic study of the effects of pH on the photocatalytic hydrogen production from alcohols, Int J Hydrogen Energy 44 (2019) 32030–32041. https://doi.org/10.1016/J.IJHYDENE.2019.10.114.

[360] V. Grozovski, V. Climent, E. Herrero, J.M. Feliu, Intrinsic activity and poisoning rate for HCOOH oxidation at Pt(100) and vicinal surfaces containing monoatomic (111) steps, ChemPhysChem 10 (2009) 1922–1926. https://doi.org/10.1002/cphc.200900261.

[361] S. Çetinkaya, G. Khamidov, L. Özcan, L. Palmisano, S. Yurdakal, Selective photoelectrocatalytic oxidation of glycerol by nanotube, nanobelt and nanosponge structured TiO_2 on Ti plates, J Environ Chem Eng 10 (2022) 107210. https://doi.org/10.1016/j.jece.2022.107210.

[362] M. Motola, L. Hromadko, J. Prikryl, H. Sopha, M. Krbal, J.M. Macak, Intrinsic properties of high-aspect ratio single- and double-wall anodic TiO_2 nanotube layers annealed at different temperatures, Electrochim Acta 352 (2020) 136479. https://doi.org/10.1016/j.electacta.2020.136479.

[363] J.C. Parker, R.W. Siegel, Calibration of the Raman spectrum to the oxygen stoichiometry of nanophase TiO_2, Appl Phys Lett 57 (1990) 943–945. https://doi.org/10.1063/1.104274.

[364] F. di Franco, A. Zaffora, D. Pupillo, L. Iannucci, S. Grassini, M. Santamaria, The Effect of Electronic Properties of Anodized and Hard Anodized Ti and Ti6Al4V on Their Reactivity in Simulated Body Fluid, J Electrochem Soc 169 (2022) 071506. https://doi.org/10.1149/1945-7111/AC8316.

[365] A. Zaffora, F. di Franco, F. di Quarto, M. Santamaria, Optimization of anodizing process of tantalum for Ta2O5-based capacitors, Journal of Solid State Electrochemistry 24 (2020) 2953–2962. https://doi.org/10.1007/S10008-020-04704-0

[366] L.W. Huang, T.G. Vo, C.Y. Chiang, Converting glycerol aqueous solution to hydrogen energy and dihydroxyacetone by the $BiVO_4$ photoelectrochemical cell, Electrochim Acta 322 (2019) 134725. https://doi.org/10.1016/J.ELECTACTA.2019.134725.

[367] Y.H. Wu, D.A. Kuznetsov, N.C. Pflug, A. Fedorov, C.R. Müller, Solar-driven valorisation of glycerol on BiVO4 photoanodes: effect of co-catalyst and reaction media on reaction selectivity, J Mater Chem A Mater 9 (2021) 6252–6260. https://doi.org/10.1039/D0TA10480A.

[368] F. Di Franco, A. Zaffora, M. Santamaria, Photoelectrochemical characterization of photocatalysts, in: Materials Science in Photocatalysis, Elsevier, 2021: pp. 115–123. https://doi.org/10.1016/B978-0-12-821859-4.00005-2.

[369] B. Hirschorn, M.E. Orazem, B. Tribollet, V. Vivier, I. Frateur, M. Musiani, Determination of effective capacitance and film thickness from constant-phase-element parameters, Electrochim Acta 55 (2010) 6218–6227. https://doi.org/10.1016/j.electacta.2009.10.065.

[370] S. Miraghaei, M. Santamaria, F. Di Quarto, Red Shift in the Light Absorption Threshold of Anodic TiO_2 Films Induced by Nitrogen Incorporation, Electrochim Acta 134 (2014) 150–158. https://doi.org/10.1016/J.ELECTACTA.2014.04.151.

[371] J.M. Macak, A. Ghicov, R. Hahn, H. Tsuchiya, P. Schmuki, Photoelectrochemical properties of N-doped self-organized titania nanotube layers with different thicknesses, J Mater Res 21 (2006) 2824–2828. https://doi.org/10.1557/JMR.2006.0344.

[372] T. Chankhanittha, S. Nanan, Visible-light-driven photocatalytic degradation of ofloxacin (OFL) antibiotic and Rhodamine B (RhB) dye by solvothermally grown ZnO/Bi_2MoO_6 heterojunction, J Colloid Interface Sci 582 (2021) 412–427. https://doi.org/10.1016/j.jcis.2020.08.061.

[373] F. Guo, X. Lin, Y. Hong, W. Fang, L. Wang, S-Scheme Heterojunction Photocatalyst for Photocatalytic H_2O_2 Production: A Review, Catalysts 2023, Vol. 13, Page 1325 13 (2023) 1325. https://doi.org/10.3390/CATAL13101325.

[374] R.P.V. Faria, C.S.M. Pereira, V.M.T.M. Silva, J.M. Loureiro, A.E. Rodrigues, Glycerol valorization as biofuel: Thermodynamic and kinetic study of the acetalization of glycerol with acetaldehyde, Ind Eng Chem Res 52 (2013) 1538–1547. https://doi.org/10.1021/ie302935w.

[375] N.T. Nguyen, S. Ozkan, O. Tomanec, R. Zboril, P. Schmuki, Spaced Titania Nanotube Arrays Allow the Construction of an Efficient N-Doped Hierarchical Structure for Visible-Light Harvesting, ChemistryOpen 7 (2018) 131–135. https://doi.org/10.1002/OPEN.201700199.

[376] M.P. Kumar, R. Jagannathan, S. Ravichandran, Photoelectrochemical System for Unassisted High-Efficiency Water-Splitting Reactions Using N-Doped TiO_2 Nanotubes, Energy and Fuels 34 (2020) 9030–9036. https://doi.org/10.1021/ACS.ENERGYFUELS.0C00634

[377] D. Regonini, A. Groff, G.D. Sorarù, F.J. Clemens, Photoelectrochemical study of anodized TiO_2 Nanotubes prepared using low and high H_2O contents, Electrochim Acta 186 (2015) 101–111. https://doi.org/10.1016/J.ELECTACTA.2015.10.162.

[378] E. Baran, B. YazIcI, Effect of different nano-structured Ag doped TiO_2-NTs fabricated by electrodeposition on the electrocatalytic hydrogen production, Int J Hydrogen Energy 41 (2016) 2498–2511. https://doi.org/10.1016/J.IJHYDENE.2015.12.028.

[379] D. Gao, Z. Lu, C. Wang, W. Li, P. Dong, Enhanced Photocatalytic Properties of Ag-Loaded N-Doped TiO_2 Nanotube Arrays, Autex Research Journal 18 (2018) 67–72. https://doi.org/10.1515/AUT-2017-0005

[380] W. Deng, Q. Zhang, Y. Wang, Catalytic transformations of cellulose and cellulose-derived carbohydrates into organic acids, Catal Today 234 (2014) 31–41. https://doi.org/10.1016/j.cattod.2013.12.041.

[381] F. Olivito, V. Algieri, M.A. Tallarida, A. Jiritano, P. Costanzo, L. Maiuolo, A. De Nino, High-yield synthesis of HMF from glucose and fructose by selective catalysis with water-tolerant rare earth metal triflates assisted by choline chloride, Green Chemistry 25 (2023) 1679–1689. https://doi.org/10.1039/D2GC04046H.

[382] S. Zhang, J. Sun, D. Feng, H. Sun, J. Cui, X. Zeng, Y. Wu, G. Luan, X. Lu, Unlocking the potentials of cyanobacterial photosynthesis for directly converting carbon dioxide into glucose, Nature Communications 2023 14:1 14 (2023) 1–14. https://doi.org/10.1038/s41467-023-39222-w.

[383] K.R. Hwang, W. Jeon, S.Y. Lee, M.S. Kim, Y.K. Park, Sustainable bioplastics: Recent progress in the production of bio-building blocks for the bio-based next-generation polymer PEF, Chemical Engineering Journal 390 (2020) 124636. https://doi.org/10.1016/J.CEJ.2020.124636.

[384] S. Shinde, K. Tarade, G. Mitra, C. Rode, Integration of Heterogeneous Acid and Base Catalysis for Clean Synthesis of Jet-Fuel Precursor from Carbohydrates, ChemistrySelect 5 (2020) 392–400. https://doi.org/10.1002/SLCT.201903735.

[385] K. Alamgir Ahmad, M. Haider Siddiqui, K.K. Pant, K.D.P. Nigam, N.P. Shetti, T.M. Aminabhavi, E. Ahmad, A critical review on suitability and catalytic production of butyl levulinate as a blending molecule for green diesel, Chemical Engineering Journal 447 (2022) 137550. https://doi.org/10.1016/J.CEJ.2022.137550.

[386] K. Karádi, T.T. Nguyen, A.A. Ádám, K. Baán, A. Sápi, Á. Kukovecz, Z. Kónya, P. Sipos, I. Pálinkó, G. Varga, Structure–activity relationships of LDH catalysts for the glucose-to-fructose isomerisation in ethanol, Green Chemistry 25 (2023) 5741–5755. https://doi.org/10.1039/D3GC01860A.

[387] H. Guo, J. Li, S. Xu, J. Yang, G.H. Chong, F. Shen, Mo-modified MnOx for the efficient oxidation of high-concentration glucose to formic acid in water, Fuel Processing Technology 242 (2023) 107662. https://doi.org/10.1016/J.FUPROC.2023.107662.

[388] D. Álvarez-Hernández, S. Ivanova, A. Penkova, M.Á. Centeno, Influence of vanadium species on the catalytic oxidation of glucose for formic acid production, Catal Today 441 (2024) 114906. https://doi.org/10.1016/J.CATTOD.2024.114906.

[389] T. Xia, M. Ju, H. Qian, X. Bai, R. Lai, C. Xie, G. Yu, Y. Tang, C. Wang, Q. Hou, Photocatalytic fenton-like system with atomic Fe on carbon nitride boost selective glucose oxidation towards gluconic acid, J Catal 429 (2024) 115257. https://doi.org/10.1016/J.JCAT.2023.115257.

[390] J. Wang, L. Chen, H. Zhao, P. Kumar, S.R. Larter, M.G. Kibria, J. Hu, In Situ Photo-Fenton-Like Tandem Reaction for Selective Gluconic Acid Production from Glucose Photo-Oxidation, ACS Catal 13 (2023) 2637–2646. https://doi.org/10.1021/ACSCATAL.2C05931

[391] S. Ramachandran, P. Fontanille, A. Pandey, C. Larroche, Gluconic acid: Properties, applications and microbial production, Food Technol Biotechnol 44 (2006) 185–195.

[392] J.V. Machado, M.L.A. da Silva, C.L.S. Silva, M.C.G. Correia, A.D. da Silva Ruy, L.A.M. Pontes, Catalysts and processes for gluconic and glucaric acids production: A comprehensive review of market and chemical routes, Catal Commun 182 (2023) 106740. https://doi.org/10.1016/J.CATCOM.2023.106740.

[393] Y. Chen, Y. Yang, X. Liu, X. Shi, C. Wang, H. Zhong, F. Jin, Sustainable production of formic acid and acetic acid from biomass, Molecular Catalysis 545 (2023) 113199. https://doi.org/10.1016/J.MCAT.2023.113199.

[394] D.O. Wasik, A. Martín-Calvo, J.J. Gutiérrez-Sevillano, D. Dubbeldam, T.J.H. Vlugt, S. Calero, Enhancement of formic acid production from carbon dioxide hydrogenation using metal-organic frameworks: Monte Carlo simulation study, Chemical Engineering Journal 467 (2023) 143432. https://doi.org/10.1016/J.CEJ.2023.143432.

[395] W. Deng, Y. Feng, J. Fu, H. Guo, Y. Guo, B. Han, Z. Jiang, L. Kong, C. Li, H. Liu, P.T.T. Nguyen, P. Ren, F. Wang, S. Wang, Y. Wang, Y. Wang, S.S. Wong, K. Yan, N. Yan, X. Yang, Y. Zhang, Z. Zhang, X. Zeng, H. Zhou, Catalytic conversion of lignocellulosic biomass into chemicals and fuels, Green Energy & Environment 8 (2023) 10–114. https://doi.org/10.1016/J.GEE.2022.07.003.

[396] H. Zhang, K. Yang, Y. Tao, Q. Yang, L. Xu, C. Liu, L. Ma, R. Xiao, Biomass directional pyrolysis based on element economy to produce high-quality fuels, chemicals, carbon materials – A review, Biotechnol Adv 69 (2023) 108262. https://doi.org/10.1016/J.BIOTECHADV.2023.108262.

[397] B. Zhang, B.K. Biswal, J. Zhang, R. Balasubramanian, Hydrothermal Treatment of Biomass Feedstocks for Sustainable Production of Chemicals, Fuels, and Materials: Progress and Perspectives, Chem Rev 123 (2023) 7193–7294. https://doi.org/10.1021/ACS.CHEMREV.2C00673

[398] J. Yun, G. Yao, F. Jin, H. Zhong, A. Kishita, K. Tohji, H. Enomoto, L. Wang, Low-temperature and highly efficient conversion of saccharides into formic acid under hydrothermal conditions, AIChE Journal 62 (2016) 3657–3663. https://doi.org/10.1002/AIC.15287.

[399] C. Wang, X. Chen, M. Qi, J. Wu, G. Gözaydin, N. Yan, H. Zhong, F. Jin, Room temperature, near-quantitative conversion of glucose into formic acid, Green Chemistry 21 (2019) 6089–6096. https://doi.org/10.1039/C9GC02201E.

[400] A. Liu, Z. Huang, X. Wang, Efficient Oxidation of Glucose into Gluconic Acid Catalyzed by Oxygen-Rich Carbon Supported Pd Under Room Temperature and Atmospheric Pressure, Catal Letters 148 (2018) 2019–2029. https://doi.org/10.1007/S10562-018-2409-1/TABLES/5.

[401] A. Onda, T. Ochi, K. Kajiyoshi, K. Yanagisawa, A new chemical process for catalytic conversion of d-glucose into lactic acid and gluconic acid, Appl Catal A Gen 343 (2008) 49–54. https://doi.org/10.1016/J.APCATA.2008.03.017.

[402] I.T. Bae, X. Xing, C.C. Liu, E. Yeager, In situ Fourier transform infrared reflection absorption spectroscopic studies of glucose oxidation on platinum in acid *, Elsevier Sequoia S.A, 1990.

[403] G.A.B. Mello, W. Cheuquepán, V. Briega-Martos, J.M. Feliu, Glucose electro-oxidation on Pt(100) in phosphate buffer solution (pH 7): A mechanistic study, Electrochim Acta 354 (2020). https://doi.org/10.1016/j.electacta.2020.136765.

[404] G. Moggia, T. Kenis, N. Daems, T. Breugelmans, Electrochemical Oxidation of <scp>d</scp> -Glucose in Alkaline Medium: Impact of Oxidation Potential and Chemical Side Reactions on the Selectivity to <scp>d</scp> -Gluconic and <scp>d</scp> -Glucaric Acid, ChemElectroChem 7 (2020) 86–95. https://doi.org/10.1002/celc.201901592.

[405] T. Faverge, B. Gilles, A. Bonnefont, F. Maillard, C. Coutanceau, M. Chatenet, In Situ Investigation of d-Glucose Oxidation into Value-Added Products on Au, Pt, and Pd under Alkaline Conditions: A Comparative Study, ACS Catal 13 (2023) 2657–2669. https://doi.org/10.1021/acscatal.2c05871.

[406] K. Lee, A. Mazare, P. Schmuki, One-dimensional titanium dioxide nanomaterials: Nanotubes, Chem Rev 114 (2014) 9385–9454. https://doi.org/10.1021/CR500061M

[407] F. La Mantia, J. Stojadinović, M. Santamaria, F. Di Quarto, Dynamic Response of Thin-Film Semiconductors to AC Voltage Perturbations, ChemPhysChem 13 (2012) 2910–2918. https://doi.org/10.1002/CPHC.201200226.

[408] L. Lan, H. Daly, R. Sung, F. Tuna, N. Skillen, P.K.J. Robertson, C. Hardacre, X. Fan, Mechanistic Study of Glucose Photoreforming over TiO_2-Based Catalysts for H_2 Production, ACS Catal 13 (2023) 8574–8587. https://doi.org/10.1021/acscatal.3c00858.

[409] C. Shi, M. Eqi, J. Shi, Z. Huang, H. Qi, Constructing 3D hierarchical TiO_2 microspheres with enhanced mass diffusion for efficient glucose photoreforming under modulated reaction conditions, J Colloid Interface Sci 650 (2023) 1736–1748. https://doi.org/10.1016/j.jcis.2023.07.081.

[410] Y. Zhu, R. Tan, C. Yang, B. Zhang, K. Deng, D. Tang, D. Ding, Efficient visible light photocatalytic performance of bismuth trioxide/titanium dioxide composite for selective conversion of glucose to arabinose and formic acid, Molecular Catalysis 554 (2024). https://doi.org/10.1016/j.mcat.2024.113818.

[411] Y. Ding, Y. Cao, D. Chen, J. Li, H. Wu, Y. Meng, J. Huang, J. Yuan, Y. Su, J. Wang, H. Li, Relay photo/thermal catalysis enables efficient cascade upgrading of sugars to lactic acid: Mechanism study and life cycle assessment, Chemical Engineering Journal 452 (2023). https://doi.org/10.1016/j.cej.2022.139687.

[412] M. Zhou, Y. Li, S. Peng, G. Lu, S. Li, Effect of epimerization of d-glucose on photocatalytic hydrogen generation over Pt/TiO 2, Catal Commun 18 (2012) 21–25. https://doi.org/10.1016/j.catcom.2011.11.017.

[413] K. Bubacz, B. Tryba, A.W. Morawski, The role of adsorption in decomposition of dyes on TiO_2 and N-modified TiO_2 photocatalysts under UV and visible light irradiations, Mater Res Bull 47 (2012) 3697–3703. https://doi.org/10.1016/J.MATERRESBULL.2012.06.038.

[414] L. Fan, B. Liu, X. Liu, N. Senthilkumar, G. Wang, Z. Wen, Recent Progress in Electrocatalytic Glycerol Oxidation, Energy Technology 9 (2021). https://doi.org/10.1002/ENTE.202000804.